

PROTEIN INTERACTIONS WITH NITROGEN-DOPED  
AMORPHOUS CARBON SURFACES

A Thesis Submitted to the  
College of Graduate and Postdoctoral Studies  
In Partial Fulfillment of the Requirements  
For the Degree of Doctor of Philosophy  
In the Division of Biomedical Engineering  
University of Saskatchewan  
Saskatoon

By

Jason Michael Maley

## **PERMISSION TO USE**

In presenting this thesis in partial fulfilment of the requirements for a Postgraduate degree from the University of Saskatchewan, I agree that the Libraries of this University may make it freely available for inspection. I further agree that permission for copying of this thesis in any manner, in whole or in part, for scholarly purposes may be granted by Prof. Wenjun (Chris) Zhang who co-supervised my thesis work or, in their absence, by the Head of the Division of Biomedical Engineering or the Dean of the College of Graduate and Postdoctoral Studies (CGPS) in which my thesis was done. It is understood that any copying or publication or use of this thesis or parts thereof for financial gain shall not be allowed without my written permission. It is also understood that due recognition shall be given to me and to the University of Saskatchewan in any scholarly use which may be made of any material in my thesis.

Requests for permission to copy or to make other use of material in this thesis in whole or part should be addressed to:

Head of the Division of Biomedical Engineering  
57 Campus Drive,  
University of Saskatchewan  
Saskatoon, Saskatchewan, Canada S7N 5A9

OR

Dean of College of Graduate and Postdoctoral Studies  
University of Saskatchewan  
116 Thorvaldson Building  
110 Science Place  
Saskatoon, Saskatchewan, Canada S7N 5C9

## ABSTRACT

Amorphous carbon is a very promising material for biocompatible devices. It can be made by a variety of plasma-assisted deposition techniques and is readily doped with other elements, such as nitrogen, which allows tuneable mechanical and tribological properties, including high hardness, low coefficient of friction, and high chemical resistance. It has also been applied to polymer surfaces like poly(tetrafluoroethylene) which gives it the potential for coating applications to hemocompatible devices such as vascular grafts.

Although advances in biomaterials used in both surgical and biomedical applications have steadily improved over the past 30 years, improvements towards their biocompatibility and longevity are still needed. Proteins immediately adsorb to the biomaterial interface when it is exposed to bodily fluids such as blood, and this protein layer mediates cellular adsorption on the biomaterial, ultimately playing a major role in the overall success of the biomaterial. Despite advances over the past 40 years in understanding protein interactions at biomaterial interface, there is still a lack of understanding on many of the mechanisms and factors affecting protein adsorption. The main objective of the work presented in this thesis is to (1) develop a surface plasmon resonance (SPR) assay to measure the initial binding kinetics of two major serum proteins, human serum albumin (HSA) and fibrinogen (Fib), to amorphous carbon films prepared with different amounts of nitrogen incorporation. The nitrogen incorporation was controlled by adjusting the %N<sub>2</sub> plasma discharge gas during plasma enhanced chemical sputtering using a graphite target onto a Au sensor surface. The initial binding kinetics measurements from SPR experiments found the dissociation kinetics ( $k_d$ ) for both Fib and HSA were comparable onto fullerene-like carbon nitride films (FL-CN<sub>x</sub>). The association kinetics ( $k_a$ ) was determined to be an important factor for protein adsorption, and the  $k_a$  was an order of magnitude larger for Fib than HSA. In addition, nitrogen incorporation into the FL-CN<sub>x</sub> initially decreased  $k_a$  for both Fib and HSA. However, increasing the nitrogen incorporation due to higher %N<sub>2</sub> plasma discharge gas ratios during FL-CN<sub>x</sub> film deposition increased the  $k_a$  values for both Fib and HSA. Atomic force microscopy, Raman spectroscopy, and sessile contact angle measurements on the FL-CN<sub>x</sub> films indicated that the surface hydrophobicity, and the film structure played roles in the changes in protein binding kinetics.

The FL-CN<sub>x</sub> films prepared in the original deposition chamber were also found to contain trace amounts of metals, mainly Fe, incorporated into the films during the deposition process. A second objective (2) of the thesis was to characterize the trace Fe in FL-CN<sub>x</sub> films deposited onto poly(tetrafluoroethylene). X-ray photoelectron spectroscopy, Fe L-edge x-ray absorption near edge spectroscopy, and electron spin resonance spectroscopy were used to elucidate the Fe structure in the FL-CN<sub>x</sub> films. The Fe was found to exist in different Fe(III)-oxide and Fe(II) oxide forms, and the Fe valency and concentration was dependent on the %N<sub>2</sub> plasma discharge gas during film deposition, and differences were observed for the Fe in the surface and bulk regions of the film.

A third objective (3) of this thesis was to design a “metal free” plasma deposition chamber. The films generated using this new chamber were amorphous carbon nitride (a-C:N), and the nitrogen incorporation was controlled by changing the %N<sub>2</sub> plasma discharge during a-C:N film deposition. The SPR measurements on the a-C:N films found that the  $k_d$  values were very similar for HSA and Fib, indicating that the protein/surface interaction is very stable and independent of the protein. The  $k_a(\text{Fib}) > k_a(\text{HSA})$  by an order of magnitude. The incorporation of nitrogen into a-C:N film initially decreased the  $k_a$  for both HSA and Fib, but incorporation of nitrogen using higher %N<sub>2</sub> plasma discharge gas during a-C:N film formation increased the  $k_a$  values for both HSA and Fib. Film characterization suggested that changes in the a-C:N film surface wettability, the type of nitrogen functionalization within the film matrix, and the electronic workfunction may play a role in the changes in  $k_a$  values measured for HSA and Fib. In addition, it was found that Fe-doping (1.3 at.% Fe) into a-C:N film did not change the HSA and Fib binding kinetics compared to the “metal-free” a-C:N film.

Overall, a SPR assay was successfully developed and the initial binding kinetics of HSA and Fib onto amorphous carbon surfaces prepared with different amounts of nitrogen incorporation are reported for the first time. The kinetic results show that the major differences in the binding strength between the two different proteins are the differences in the protein's  $k_a$  (recognition rate) towards the surface. This fundamental assay can be expanded in future experiments to study specific surface properties and quantitatively measure the effects of protein binding.

## ACKNOWLEDGMENTS

I greatly appreciate the love, support, and encouragement from my wife Sharleen and children Alexandra, and Stephen. They have put up with my evening and weekend absences for many years, and I do not know how they will adjust with me being around! I am also grateful for the ongoing love and support from my parents and mother-in-law. Also to our cats Tigger and Ziggy.

I would like to thank my co-supervisors Dr. Wenjun (Chris) Zhang and Dr. Akira Hirose for allowing me to take this journey on a part-time basis. Unfortunately, Dr. Hirose passed away November 2017, and did not see the completion of this work. However, I am truly grateful for his support and the access to the Plasma Physics Laboratory.

I would also like to thank my committee members for sticking with me through this long journey. Their insight and encouragement will not be forgotten.

I am grateful that the University of Saskatchewan has a facility like the Saskatchewan Structural Sciences Center (SSSC). This facility allowed access to the AFM, Raman spectroscopy, FTIR spectroscopy, XPS, UPS, and SPR measurements completed in this work.

I would like to thank Dr. Renfei Feng from the VESPERS beamline at the Canadian Light Source for assisting with the XRF measurements. Rick Elvin in the Department of Chemistry glass shop for constructing the new deposition chamber. I would also like to thank Ted and Blair from the Physics Machine shop and David McColl from the Plasma Physics Lab for assistance. And of course, I would like to thank my colleagues past and present.

## TABLE OF CONTENTS

PERMISSION TO USE .....	i
ABSTRACT .....	ii
ACKNOWLEDGMENTS .....	iv
LIST OF TABLES .....	vii
LIST OF FIGURES .....	viii
LIST OF ABBREVIATIONS.....	xii
CHAPTER 1 - INTRODUCTION.....	1
1.1. Biomaterials and Biocompatibility.....	1
1.2. Blood Material Interactions.....	2
1.3. Surface Plasmon Resonance.....	5
1.4. Amorphous Carbon .....	8
1.4.1. Carbon Properties.....	8
1.4.2. Amorphous Carbon Synthesis.....	9
1.4.3. Amorphous Carbon Clustering .....	12
1.4.4. Amorphous Carbon Doping.....	13
1.4.4.1. Amorphous Carbon Nitride (a-C:N).....	14
1.4.4.2. Fullerene-Like Amorphous Carbon Nitride (FL-CN <sub>x</sub> ).....	15
1.5. Research Proposal .....	16
1.5.1. Thesis Objectives .....	16
CHAPTER 2 - LITERATURE REVIEW .....	18
2.1. Biocompatibility Studies of Amorphous Carbon .....	18
2.1.1. Clinically Tested a-C Devices for Hemocompatible Applications.....	18
2.1.1.1. Cardiovascular Stents .....	20
2.1.1.2. Heart Valves and Pumps.....	22
2.1.2. Amorphous Carbon Plasma Deposition on Polymeric Substrate .....	23
2.1.3. Nitrogen-Doped Amorphous Carbon Biocompatibility.....	25
2.2. Protein Adsorption at Biomaterial Interface .....	27
2.2.1. The Role of Protein Properties.....	29
2.2.2. Role of Surface Properties .....	30
2.2.3. Environmental Roles.....	31
2.2.4. Transient Adsorption Model .....	32
2.2.5. Multi-protein Adsorption .....	34
2.3. Protein Layer Mediates Cell Adhesion .....	35
2.4. Protein/Amorphous Carbon Interactions.....	36
2.5. Initial Surface/Protein Interactions Measured by SPR.....	38
CHAPTER 3 - MATERIALS AND METHODS .....	42
3.1. Amorphous Carbon Film Preparation .....	42
3.1.1. Metal-Containing FL-CN <sub>x</sub> Films .....	42
3.1.1.1. FL-CN <sub>x</sub> Coated SPR Sensor Chips.....	42
3.1.2. Metal-Free a-C:N Film Apparatus .....	43

3.1.2.1.	a-C:N Film Deposition .....	44
3.2.	Characterization Methods .....	45
3.2.1.	Atomic Force Microscopy .....	45
3.2.2.	Raman Spectroscopy and FTIR Spectroscopy.....	45
3.2.3.	Contact Angle Measurements .....	46
3.2.4.	X-ray Photoelectron Spectroscopy .....	46
3.2.4.1.	FL-CN <sub>x</sub> Films on PTFE Substrate.....	46
3.2.4.2.	a-C:N Films on Au Substrate.....	46
3.2.5.	Micro-X-ray Fluorescence (μ-XRF).....	47
3.2.6.	X-ray Absorption Near-Edge Spectroscopy (XANES) .....	47
3.2.7.	Electron Spin Resonance (ESR) .....	47
3.3.	Protein Surface Interactions .....	47
3.3.1.	Chemicals.....	47
3.3.2.	Surface Plasmon Resonance .....	48
3.3.2.1.	FL-CN <sub>x</sub> Protein Interactions.....	48
3.3.2.2.	a-C:N Protein Interactions .....	48
3.3.3.	Scanning Transmission X-ray Microscopy (STXM).....	49
CHAPTER 4 - RESULTS AND DISCUSSION .....		51
4.1.	Metal Containing FL-CN <sub>x</sub> .....	51
4.1.1.	General FL-CN <sub>x</sub> Films on PTFE Substrate Characterization .....	51
4.1.2.	Metal Incorporation into FL-CN <sub>x</sub> Matrix .....	66
4.1.2.1.	FL-CN <sub>x</sub> Film Discussion .....	73
4.1.3.	Protein Interactions with Metal Incorporated FL-CN <sub>x</sub> .....	76
4.1.3.1.	SPR .....	76
4.1.3.2.	Scanning Transmission X-ray Spectroscopy (STXM) .....	85
4.2.	Metal Free a-C:N Films.....	89
4.2.1.	Verification of Metal-Free a-C:N Deposition.....	89
4.2.2.	a-C:N Film Characterization on Au Substrate .....	90
4.2.3.	SPR of a-C:N Protein Interactions .....	98
4.2.4.	a-C:N Protein Interaction Discussion .....	105
CHAPTER 5 - CONCLUSIONS .....		109
5.1.	Summary .....	109
5.2.	Proposed Future Work .....	111
REFERENCES .....		113

## LIST OF TABLES

<b>Table 1.1.</b> Physical properties for different types of crystalline allotropes and amorphous carbon thin films. <sup>9-10</sup> .....	10
<b>Table 2.1.</b> Summary of Commercially Available Biomedical Devices using a-C Coatings. ....	19
<b>Table 3.1.</b> Sample notation for FL-CN <sub>x</sub> samples prepared by hot filament graphite sputtering plasma deposition. ....	42
<b>Table 3.2.</b> Sample notation for a-C:N samples prepared in “metal-free” deposition chamber. ....	45
<b>Table 4.1.</b> AFM, contact angle and Raman spectroscopy data for FL-CN <sub>x</sub> films deposited on PTFE. ....	51
<b>Table 4.2.</b> ATR-FTIR spectroscopy band assignments for FL-CN <sub>x</sub> samples deposited on PTFE. <sup>182-183</sup> ..	56
<b>Table 4.3.</b> XPS survey scans for FL-CN <sub>x</sub> films deposited onto PTFE substrate. ....	58
<b>Table 4.4.</b> High resolution XPS (C1s, N1s, O1s) band deconvolution of FL-CN <sub>x</sub> films. ....	60
<b>Table 4.5.</b> Valence band XPS (Al K $\alpha$ = 1486.6 eV) for FL-CN <sub>x</sub> films. ....	66
<b>Table 4.6.</b> Fe L-edge XANES analysis for FL-CN <sub>x</sub> films prepared with different %N <sub>2</sub> plasma discharge gas. ....	70
<b>Table 4.7.</b> FL-CN <sub>x</sub> Film characterization prepared with different %N <sub>2</sub> plasma discharge gas and deposited on Au sensor surfaces. ....	78
<b>Table 4.8.</b> Kinetic analysis of (a) HSA and (b) Fib binding with FL-CN <sub>x</sub> films prepared with different %N <sub>2</sub> plasma discharge gas. Standard deviations are given in brackets. ....	80
<b>Table 4.9.</b> NEXAFS bands for C1s, N1s, and O1s for FL-CN <sub>x</sub> films prepared with different %N <sub>2</sub> plasma discharge gas. ....	87
<b>Table 4.10.</b> Film Characterization of metal-free a-C:N films prepared with different N <sub>2</sub> % plasma discharge gas and deposited on Au sensor surfaces. ....	90
<b>Table 4.11.</b> XPS and UPS measurements of a-C:N films prepared on Au substrate. ....	93
<b>Table 4.12.</b> Peak deconvolution of high resolution XPS measurements of a-C:N films prepared with different %N <sub>2</sub> plasmas discharge gas. ....	95
<b>Table 4.13.</b> Binding Kinetics <sup>a</sup> of HSA and Fib onto a-C:N Films. ....	103

## LIST OF FIGURES

<b>Figure 1.1.</b> Suggested tests for new potential biocompatible devices as recommended by ISO 10993-1:2018. <sup>3</sup> .....	2
<b>Figure 1.2.</b> Schematic representation of the protein/film interface in a biological system. ....	4
<b>Figure 1.3.</b> (a) General overview of SPR instrumentation. (b) Typical designs of micro-fluidics for commercially available instruments. Commercially available Biacore® SPR instruments use a serial flow cell design where liquid delivery flows through each flow cell in a serial manner. The Proteon XPR36 instrument from Biorad Laboratories uses a 6 parallel flow channel that can be rotated in the horizontal (A1-A6) and vertical direction (L1-L6). ....	6
<b>Figure 1.4.</b> (a) General overview of an SPR sensorgram. (b) SPR sensorgrams of showing the changes in binding kinetics ( $k_a$ , $k_d$ ) profiles for different biomolecular interactions having the same affinity ( $K_D = 5.0$ nM) and same analyte concentration (50 nM). ....	7
<b>Figure 1.5.</b> (a) Carbon has 3 different types of hybridization: $sp^3$ -hybridization contains 4 s-bonds; $sp^2$ contains 3 $sp^2$ bonds, and a weaker p-bond; $sp^1$ -hybridization contains a s-bond and 2 $\pi$ -bonds. (b) Different allotropes of carbon can contain an exclusive type of carbon hybridization (ex. Diamond, graphite) or a combination of hybridizations (ex. Graphdiyne, amorphous carbon). ....	9
<b>Figure 1.6.</b> Ternary diagram of a-C composed of different $sp^2$ , $sp^3$ , and H content. <sup>11</sup> .....	10
<b>Figure 1.7.</b> Common plasma deposition methods for a-C. ....	11
<b>Figure 1.8.</b> Basic configuration of plasma-assisted sputtering. ....	12
<b>Figure 1.9.</b> There are 3 stages of amorphization of carbon from graphitic state. Stage 1 finds the graphitic crystalline size ( $L_a$ ) decrease until small 1-2 nm clusters are formed. Stage 2 sees the conversion of the small $sp^2$ clusters to amorphous carbon. Some $sp^3$ content will be introduced. Stage 3 sees the aromatic $sp^2$ clusters are converted to chains, and the % $sp^3$ content dramatically increases to approximately 100%. ...	13
<b>Figure 1.10.</b> Nitrogen has many different bonding configurations in the $sp^3$ , $sp^2$ , and $sp^1$ hybridization. Nitrogen incorporation into the aromatic a-C matrix may be pyridinic, pyrrolic, and graphitic nitrogen substitutions. ....	15
<b>Figure 2.1.</b> Schematic of protein adsorption that may occur at various stages. Native protein ( $P_N$ ) adsorb onto the surface. If given enough time ( $\tau_{r1}$ ), the adsorbed protein may structurally relax. This relaxed protein intermediate ( $P_{R1}$ ) may desorb and set up an equilibrium with solution interface. If the adsorbed $P_{R1}$ is given enough time, it may structurally relax to the protein's final relaxed state ( $P_S$ ). ....	33
<b>Figure 3.1.</b> (a) Basic design of metal-free deposition chamber. (b) Basic set-up of DC plasma deposition chamber with graphite target. ....	44
<b>Figure 3.2.</b> FL-CN <sub>x</sub> films were deposited onto Si <sub>3</sub> N <sub>4</sub> windows using different masks. Left: Carbon tape; Middle: Si wafer; Right: Kapton™ tape. ....	50
<b>Figure 4.1.</b> AFM topography images (1 $\mu$ m x 1 $\mu$ m) of FL-CN <sub>x</sub> films prepared with different amounts of N <sub>2</sub> plasma discharge gas. (a) FL-CN <sub>x</sub> -00 (b) FL-CN <sub>x</sub> -03 (c) FL-CN <sub>x</sub> -06 (d) FL-CN <sub>x</sub> -10 (e) FL-CN <sub>x</sub> -20. ....	52

**Figure 4.2.** Static contact angle measurements using water for FL-CN<sub>x</sub> films prepared with different N<sub>2</sub> amounts in plasma discharge gas. For each sample, contact angle measurements were replicated 3-5 times. .... 53

**Figure 4.3.** (a) Raman spectroscopy ( $\lambda_{\text{ex}} = 514.5$  nm) of FL-CN<sub>x</sub> films deposited on PTFE. (1) PTFE (2) FL-CN<sub>x</sub>-00 (3) FL-CN<sub>x</sub>-03 (4) FL-CN<sub>x</sub>-06 (5) FL-CN<sub>x</sub>-10 (6) FL-CN<sub>x</sub>-20. (b) Peak deconvolution of the G-Band and D-Band show differences in the G-Band position (-■-), G-Band peak width at FWHM (-■-) and the I<sub>D</sub>/I<sub>G</sub> peak intensity ratio (-■-). .... 54

**Figure 4.4.** ATR-FTIR spectra of the FL-CN<sub>x</sub> films deposited on PTFE. (1) PTFE (2) FL-CN<sub>x</sub>-00 (3) FL-CN<sub>x</sub>-03 (4) FL-CN<sub>x</sub>-06 (5) FL-CN<sub>x</sub>-10 (6) FL-CN<sub>x</sub>-20. .... 56

**Figure 4.5.** (a) XPS (Al K $\alpha$  = 1486.6 eV) survey scans of FL-CN<sub>x</sub> films “as received” and after surface cleaning (1 min 4 keV, 15 mA Ar<sup>+</sup> sputtering). (b) The at.% N/C and O/C ratios for “as received” and after surface cleaning. .... 58

**Figure 4.6.** High resolution XPS of the FL-CN<sub>x</sub> films. (1) PTFE (2) FL-CN<sub>x</sub>-00 (3) FL-CN<sub>x</sub>-03 (4) FL-CN<sub>x</sub>-06 (5) FL-CN<sub>x</sub>-10 (6) FL-CN<sub>x</sub>-20. (a) C1s (b) C1s at.% ratios for different films (c) N1s (d) N1/N2 and N3/N1 at.% ratios for different films (e) O1s (f) (O3+O4)/(O2+O1) at.% ratio for different films. ... 59

**Figure 4.7.** XANES FLY spectra of FL-CN<sub>x</sub> films prepared under different %N<sub>2</sub> plasma discharge gas. (2) FL-CN<sub>x</sub>-00 (3) FL-CN<sub>x</sub>-03 (4) FL-CN<sub>x</sub>-06 (5) FL-CN<sub>x</sub>-010 (6) FL-CN<sub>x</sub>-020. (a) N1s FLY spectra (b) The N1s  $\pi^*_1/\pi^*_2$  intensity ratio as a function of %N<sub>2</sub> plasma discharge gas used during film preparation. (c) O1s FLY spectra. (d) Relative K-edge FLY XANES  $\pi^*/\sigma^*$  areas for films prepared with different %N<sub>2</sub> plasma discharge. .... 64

**Figure 4.8.** Valence Band XPS (Al K $\alpha$  = 1486.6 eV) measurements for the FL-CN<sub>x</sub> films prepared with different %N<sub>2</sub> plasma discharge gas. (1) PTFE (2) FL-CN<sub>x</sub>-00 (3) FL-CN<sub>x</sub>-03 (4) FL-CN<sub>x</sub>-06 (5) FL-CN<sub>x</sub>-10 (6) FL-CN<sub>x</sub>-20. .... 65

**Figure 4.9.** (a) XRF spectra of FL-CN<sub>x</sub> films indicating the presence of different transition metals within the FL-CN<sub>x</sub> matrix. (b) The distribution of metals within samples decreases as a function of the %N<sub>2</sub> discharge gas used during film deposition. .... 67

**Figure 4.10.** High resolution XPS of W4f region shows the presence of WO<sub>x</sub> in the FL-CN<sub>x</sub> films prepared with different %N<sub>2</sub> in the plasma discharge: (2) FL-CN<sub>x</sub>-00 (3) FL-CN<sub>x</sub>-03 (4) FL-CN<sub>x</sub>-06 (5) FL-CN<sub>x</sub>-10 (6) FL-CN<sub>x</sub>-20. (b) The composition of the WO<sub>x</sub> is dependent on the %N<sub>2</sub> in the plasma discharge gas. . 68

**Figure 4.11.** (a) High resolution XPS of Fe2p region for FL-CN<sub>x</sub> films prepared with different %N<sub>2</sub> in the plasma discharge gas: (2) FL-CN<sub>x</sub>-00 (3) FL-CN<sub>x</sub>-03 (4) FL-CN<sub>x</sub>-06. .... 69

**Figure 4.12.** (a) Fe L-edge XANES measurements of FL-CN<sub>x</sub> films prepared with different %N<sub>2</sub> in the plasma discharge: (2) FL-CN<sub>x</sub>-00 (3) FL-CN<sub>x</sub>-03 (4) FL-CN<sub>x</sub>-06 (5) FL-CN<sub>x</sub>-10 (6) FL-CN<sub>x</sub>-20. The XANES spectra were normalized to the L<sub>3</sub> region’s inflection point. (b) Electron energy loss spectroscopy reference spectra for some different iron oxides.<sup>205</sup> (c) The energy difference between band B and band A as a function of the peak height intensity ratio I<sub>A</sub>/I<sub>B</sub>. (d) the I as a function of N<sub>2</sub> in the plasma discharge gas. .... 71

**Figure 4.13.** ESR spectra (6 K) of FL-CN<sub>x</sub> samples prepared under different %N<sub>2</sub> plasma discharge environment. (2) FL-CN<sub>x</sub>-00 (4) FL-CN<sub>x</sub>-06 (5) FL-CN<sub>x</sub>-10 (6) FL-CN<sub>x</sub>-20. .... 73

<b>Figure 4.14.</b> The relative indexes of platelet adhesion of uncoated PTFE and FL-CN <sub>x</sub> films prepared using different %N <sub>2</sub> plasma discharge gas. Platelets adsorbed onto surfaces were classified as (I) Single nonactivated; (II) Slightly activated cells with pseudopodia; (III) fully spread platelets; (IV) aggregated platelets. Figure is adapted from results presented in Dr. M. Foursa's PhD dissertation. <sup>114</sup> .....	75
<b>Figure 4.15.</b> SPR reflectance curves for Au sensor substrate and FL-CN <sub>x</sub> films prepared from different amounts of N <sub>2</sub> plasma discharge gas ratios.....	77
<b>Figure 4.16.</b> AFM topography images of FL-CN <sub>x</sub> films prepared with different amounts of N <sub>2</sub> plasma discharge gas: (a) FL-CN <sub>x</sub> -00; (b) FL-CN <sub>x</sub> -10; (c) FL-CN <sub>x</sub> -20; (d) FL-CN <sub>x</sub> -30. Images are 1 μm x 1 μm. The FL-CN <sub>x</sub> sample images are displayed in the same height and color scale.....	78
<b>Figure 4.17.</b> Raman spectroscopy of various FL-CN <sub>x</sub> films prepared with %N <sub>2</sub> plasma discharge gas. (2) FL-CN <sub>x</sub> -00; (5) FL-CN <sub>x</sub> -10; (6) FL-CN <sub>x</sub> -20; (7) FL-CN <sub>x</sub> -30.....	79
<b>Figure 4.18.</b> SPR sensorgrams of FL-CN <sub>x</sub> films interaction with (a-d) HSA and (e-h) Fib. (a,e) FL-CN <sub>x</sub> -00 (b, f) FL-CN <sub>x</sub> -10(c, g) FL-CN <sub>x</sub> -20 (d, h) FL-CN <sub>x</sub> -30.....	81
<b>Figure 4.19.</b> SPR kinetics for HSA and Fib for the FL-CN <sub>x</sub> films prepared with different %N <sub>2</sub> plasma discharge gas. (a) k <sub>a</sub> (b) k <sub>d</sub> .....	82
<b>Figure 4.20.</b> Comparison of the k <sub>a</sub> kinetics of Fib and HSA with the wettability of the FL-CN <sub>x</sub> films prepared with different %N <sub>2</sub> plasma discharge gas.....	83
<b>Figure 4.21.</b> SPR sensorgrams of Fib (500 nM) binding to FL-CN <sub>x</sub> -00 film for the unmodified surface (red) and HSA saturated FL-CN <sub>x</sub> -00 surface (1200 RU HSA immobilized).....	84
<b>Figure 4.22.</b> NEXAFS for (a) C1s (b) N1s (c) O1s for FL-CN <sub>x</sub> films prepared with different N <sub>2</sub> /Ar plasma discharge gas ratios. (d) The at.% of N and O within the films are determined by the integrated area ratios for different films.....	85
<b>Figure 4.23.</b> NEXAFS of HSA immobilized on FL-CN <sub>x</sub> film prepared with 10% N <sub>2</sub> plasma discharge gas. (a) C1s (b) N1s (c) O1s. An HSA solution (0.1mg/mL in PBS, pH7.4) was dropped onto the FL-CN <sub>x</sub> film for 2-3min, gently rinsed with PBS, then water, and then dried.....	88
<b>Figure 4.24.</b> (a) μ-XRF of a-C:N-00 prepared film deposited on Si from new chamber is compared to the FL-CN <sub>x</sub> -00 film prepared from the old chamber. (b) XPS survey scans for the a-C:N films deposited on Si shows no additional metals co-deposited into a-C:N films.....	89
<b>Figure 4.25.</b> AFM topography images of a-C:N films prepared with different amounts of N <sub>2</sub> plasma discharge gas: (a) a-C:N-00Fe (b) a-C:N-00; (c) a-C:N-05; (d) a-C:N-10; (e) a-C:N-20, (f) a-C:N-30. Images are 2 μm x 2 μm.....	91
<b>Figure 4.26.</b> (a) Raman measurements (λ <sub>ex</sub> = 514.5 nm) of a-C:N-00Fe (1) and metal-free (2-6) a-C:N films prepared with different %N <sub>2</sub> plasma discharge gas. (2) a-C:N-00; (3) a-C:N-05; (4) a-C:N-10; (5) a-C:N-20; (6) a-C:N-30. (b) The I <sub>D</sub> /I <sub>G</sub> peak intensity ratio and the contact angle measurements for the Fe-doped and "metal free" a-C:N films.....	92
<b>Figure 4.27.</b> High resolution XPS of the a-C:N films prepared with different %N <sub>2</sub> plasma discharge gas. (1) a-C:N-00Fe (2) a-C:N-00 (3) a-C:N-05 (4) a-C:N-1 (5) a-C:N-20 (6) a-C:N-30. (a) The at.% ratios of N/C and O/C as a function of plasma discharge gas during film preparation. High resolution XPS spectra were collected for (b) C1s; (c) N1s; (d) O1s; (e) Fe2p.....	94

<b>Figure 4.28.</b> The N1/N2 at.% peak ratio from N1s spectral deconvolution as a function of a-C:N films prepared with different %N <sub>2</sub> plasma discharge gas. ....	97
<b>Figure 4.29.</b> (a) UPS (He <sup>I</sup> = 21.22 eV) spectra of the Fe-doped (1) and metal-free (2-6) a-C:N films prepared with different %N <sub>2</sub> plasma discharge gas. (1) a-C:N-00Fe (2) a-C:N-00 (3) a-C:N-05% (4) a-C:N-10 (5) a-C:N-20 (6) a-C:N-30. (b) The $\Phi$ of each a-C:N film calculated from the secondary electron cut-off.....	98
<b>Figure 4.30.</b> Representative SPR reflectance curves of cleaned Au sensor chip and a-C:N film. ....	99
<b>Figure 4.31.</b> SPR sensorgrams of using casein and BSA to block non-specific binding sites to be used as a suitable reference surface.....	100
<b>Figure 4.32</b> SPR sensorgrams for HSA (0-179 nM) interaction with a-C:N-10 film. (a) HSA sensorgrams over the a-C:N-10 surface (L1) (b) HSA sensorgrams over the BSA-coated reference surface shown in Figure 4.31. (c) HSA “reference” subtracted sensorgrams (L1-L6) will correct for refractive index changes from protein solutions (d) double reference subtracted sensorgrams after subtracting the “buffer blank”(A6). This concentration profile sensorgrams are ready for kinetics modelling. ....	101
<b>Figure 4.33.</b> SPR sensorgrams of HSA (top) and Fib (bottom) interaction with a-C:N surfaces prepared with different %N <sub>2</sub> plasma discharge. HSA solutions (179 nM, 1X PBS, pH 7.4) were diluted 2-fold, and injected for 2 min at 30 $\mu\text{L min}^{-1}$ , followed by a 5-10 min dissociation. Fib (7.5 nM, 1X PBS pH 7.4) was diluted 2-fold and injected under the same conditions as HSA. Sensorgrams were evaluated with a 1:1 Langmuir model to determine kinetic parameters. (a,g) a-C:N-00; (b,h) a-C:N-05; (c,i) a-C:N-10; (d,j) a-C:N-20; (e,k) a-C:N-30; (f,l) a-C:N-00Fe.....	102
<b>Figure 4.34.</b> Isoaffinity plot for the HSA (black) and Fib (red) for a-C:N films prepared with different %N <sub>2</sub> plasma discharge gas. The kinetic parameters for FL-CN <sub>x</sub> interaction with HSA (blue) and Fib (purple) are also shown.....	104
<b>Figure 4.35.</b> The comparison of $k_a$ values for a-C:N-00 and a-C:N-00Fe film interaction with HSA and Fib. ....	105

## LIST OF ABBREVIATIONS

a-C	Amorphous carbon
a-C:H	Hydrogenated amorphous carbon
a-C:N	Amorphous carbon nitride
a-C:N:H	Hydrogenated amorphous carbon nitride
AFM	Atomic force microscopy
ATR	Attenuated total reflectance
BSA	Bovine serum albumin
CVD	Chemical vapour deposition
dc	Direct current
DLC	Diamond like carbon
$\Delta E$	Energy difference
ESR	Electron Spin Resonance
Fib	Fibrinogen
FL-CN <sub>x</sub>	Fullerene-like carbon nitride
FLY	X-ray fluorescent yield
FTIR	Fourier transform infrared
HSA	Human serum albumin
I	Intensity
IB	Intensity branching ratio
ISO	International Organization of Standardization
L <sub>a</sub>	Graphitic cluster size
LTIC	Low temperature isotropic carbon
K <sub>D</sub>	Dissociation constant
k <sub>a</sub>	Association kinetic rate constant
k <sub>d</sub>	Dissociation kinetic rate constant
NEXAFS	Near Edge X-ray Absorption Fine Structure
P, P <sub>N</sub>	Native protein
P <sub>RI</sub>	Protein structurally relaxed intermediate
P <sub>S</sub>	Protein structurally relaxed final state

P'S	protein surface binding complex
PBS	Phosphate-buffered saline
PET	Poly(ethylene terephthalate)
pI	Isoelectric point
PTFE	Poly(tetrafluoroethylene)
PVD	Physical vapour deposition
rf	Radio frequency
RGD	Arginine glycine aspartic acid amino acid sequence
R <sub>max</sub>	Response maximum
R <sub>RMS</sub>	Root mean square surface roughness
SDS	Sodium dodecyl sulfate
SGM	Spherical grating monochromator
S	Surface
SPR	Surface plasmon resonance
STXM	Scanning transmission x-ray microscopy
t	Time
$\tau_{1/2}$	Half-life
$\tau_{RI}$	Time needed for P <sub>N</sub> to structurally relax to P <sub>RI</sub>
$\tau_f$	Overall time need to fill protein layer
ta-C	tetrahedral amorphous carbon
ta-C:H	Hydrogenated tetrahedral amorphous carbon
TEY	Total electron yield
ULTIC	Ultralow-temperature isotropic carbon
UPS	Ultraviolet photoelectron spectroscopy
VESPER	Very sensitive element and structural probe employing radiation from asynchrotron
$\mu$ -XRF	Micro-x-ray fluorescence
$\Phi$	Workfunction
XANES	X-ray absorption near edge spectroscopy
XPS	X-ray photoelectron spectroscopy
$\chi^2$	Chi <sup>2</sup> or goodness-to-fit parameter

# CHAPTER 1 - INTRODUCTION

## 1.1. Biomaterials and Biocompatibility

Biomaterials are man-made materials and devices used to replace/repair parts of the human body in order to extend the longevity and/or improve the quality of life.<sup>1</sup> These materials are broadly referred to as biomaterials, since they are involved in a wide range of applications, including drug delivery, tissue regeneration/compatibility, medical devices, and surface coating applications. Advances in biomaterials have steadily increased over the past 30 years for both surgical and medical applications. This is evidenced by the global market being approximately \$30 billion in 2000.

Biomaterials are generally classified into 3 categories: (1) metal and alloys; (2) ceramics and glasses; (3) polymers.<sup>2</sup> Mechanical properties dictate the types of applications, and the biomedical devices in which they are used. For instance, metals like titanium-alloys and stainless steel have strong mechanical properties which make them suitable materials for hip and knee replacements. Ceramic materials such as aluminum oxide or hydroxyapatite are used for dental and bone repairs. Some polymers are flexible and mouldable, and thus suitable for applications in vascular grafts, blood vessel prosthesis, and intraocular lens.

Although a newly synthesized material may have desirable mechanical properties for a biomedical application, the material must be biocompatible. The interactions between a biomaterial's surface and a host organism are extremely complex, and the biomedical device must not cause any adverse effects to the host organism. There are many different types of adverse effects ranging from short term to long term or chronic effects. It is therefore of high importance to evaluate a new biomedical device from a wide spectrum of tests before approval. A more recent ISO 10993-1 guideline was recently updated in 2018 by the International Organization of Standardization (ISO).<sup>3</sup> This guideline outlines the standard practises used to for the “biological evaluation of medical devices Part 1: Evaluation and testing within a risk management process”. The suggested test-specific considerations when evaluating a new biomedical device are shown in Figure 1.1. Depending on the final application of the finished biomedical device product, some or all of the suggested tests will have to be completed.

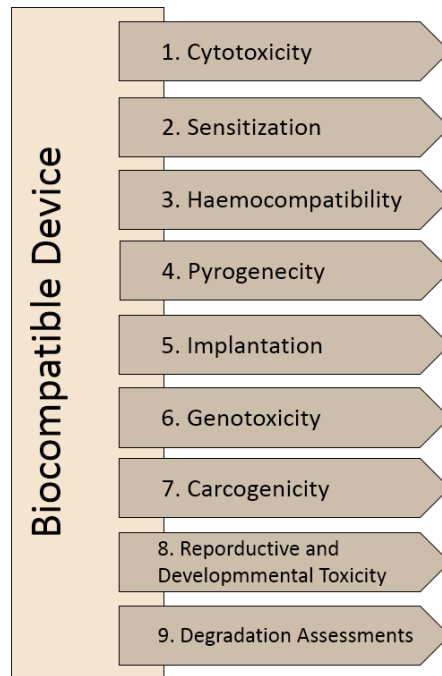


**Figure 1.1.** Suggested tests for new potential biocompatible devices as recommended by ISO 10993-1:2018.<sup>3</sup>

These tests mainly measure the response of the host to the foreign biomaterial, and include inflammation, coagulation, mutagenicity, carcinogenicity, immune surveillance, and healing. However, the specific testing for the biomedical device will depend on its intended use, and the duration and types of biological interactions that may be encountered during the biomedical device's contact with surface and bodily fluids. The present research will be focussed more towards the hemocompatibility of materials.

## 1.2. Blood Material Interactions

Blood is a very important and complex substance within the body. The major components include important cells such as erythrocytes (red blood cells), lymphocytes (white blood cells), and platelets (thrombocytes). The other major component in blood is the plasma which is the aqueous component that contains major proteins, electrolytes, nutrients, lipids, and dissolved gases. The circulatory system plays a significant part in maintaining homeostasis within the body and can be thought of a closed network of blood vessels that transports blood throughout the body, delivering nutrients and transporting wastes away.

In the event of vascular injury, hemostasis may be initiated in the event of a damaged or broken lining within a blood vessel. Vasoconstriction immediately occurs near the injury to reduce

the amount of blood flow. Thrombosis almost immediately begins with platelets binding to freshly exposed collagen in surrounding tissue outside the endothelial cells forming the blood vessel. The platelets aggregate and form a temporary plug at the damaged region. A second step initiates the coagulation cascade in thrombosis using fibrinogen, a naturally occurring protein in blood plasma. Within the damaged region, the coagulation cascade activates thrombin, which interacts with fibrinogen and activates it to fibrin. The activated fibrin units polymerize in an end-to-end fashion, interacting with the platelets, and forming a complex network which strengthens the temporary platelet plug and causes a blood clot.

The assessment of the hemocompatible characteristics of a new biomaterial device that will be in contact with blood is very important. The ISO 10993-4:2017 provides the most recent guidelines for biological evaluation of medical device interactions with blood.<sup>4</sup> It is applicable to devices with either an indirect (cannulae, blood storage bags, etc.) or direct contact (guidewires, catheters, hemodialysis equipment, etc.) with blood as well as implant device (heart valves, stents, endovascular grafts, etc.). There are 5 primary processes that should be tested: thrombosis, coagulation, platelet adherence, hematology, and complement system (component of the innate immune system that helps eliminate microorganisms and damaged cells by attacking the plasma membrane). Ideally, the testing should simulate the clinical conditions for the device as much as possible.

Thrombosis evaluation consists of exposing the device to blood, and evaluating adhered platelets, leucocytes, aggregates, fibrin, etc. on the surface through light microscopy or scanning electron microscopy. This evaluation is suggested for both *in vitro* and *in vivo* assessments, although *in vitro* testing may be only performed if it is properly justified (blood contact time and clinical use of material). Coagulation can be measured *in vitro* by determining the rate of clot formation or partial thromboplastin time of plasma exposed to the biomaterial during a set incubation period. Platelet studies can be measured using electron microscopy or light microscopy by counting the number of platelets adhered to a surface and how many are activated, or irregular shaped (pseudoactivated) after a set incubation time. Hematology evaluation may involve measuring leucocytes and activation, hemolysis, and cell counts. Complement activation typically measures small proteins that can be used to monitor the activation of the complement system. This is typically done using enzyme-linked immunosorbent assay measurements.

An important feature that is not mentioned in the recommended tests mentioned above is that upon exposure to bodily fluids, proteins will adsorb onto a biomaterial's surface within seconds.<sup>5</sup> It is this protein adsorbed interface that will initiate platelet and other cell adhesion onto the biomaterial surface. This protein/interface adsorption is extremely complex and will be influenced by several factors outlined in Figure 1.2 Surface properties such as surface tomography, crystallinity, roughness, hydrophobicity, and composition have a large influence on protein adsorption. On the other hand, proteins have charged surfaces (charged side chains) and hydrophobic patches on its surface, so the interaction with surfaces will be governed by electrostatic interactions, hydrophobic interactions, hydrogen bonding, and Van der Waals forces as well as solvent composition (ionic strength, salt ions, pH, etc.).

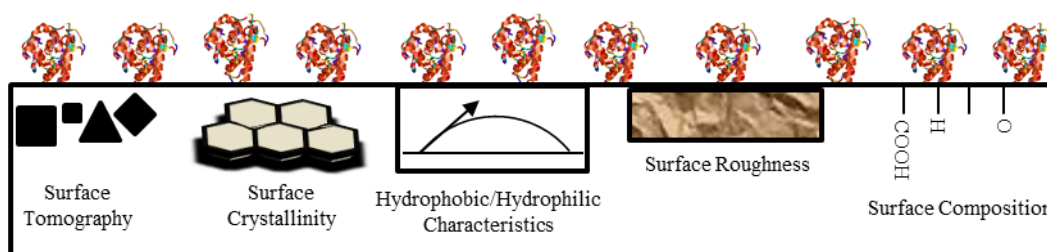


**Figure 1.2.** Schematic representation of the protein/film interface in a biological system.

When blood serum proteins are exposed to a fresh biomaterial surface, blood serum proteins will interact with the surface. The general theory, commonly referred to as the Vroman effect, is that proteins will associate and dissociate continuously with the surface, and the highest mobility proteins, such as serum albumins, will generally adsorb first. The less mobile proteins (higher molecular weights), such as fibrinogen, fibronectin, and high molecular weight kininogen, tend to have a higher affinity for the surface and will displace the smaller proteins.<sup>6</sup>

Protein adsorption is generally accepted to be a 2-step process, where the first step (order of minutes) involves the protein adsorbing onto the surface through non-covalent interactions (electrostatic, hydrophobic, hydrogen, and Van der Waals). This is followed by a reorganization step (minutes to hours) where the protein may alter its conformation (changes in secondary, tertiary structure), undergo a denaturing process, and spreading.

The platelet adherence, and other cells that are used to evaluate the blood compatibility tests outlined in ISO-10993-4 are not directly interacting with the biomaterial surface. The blood cells are interacting with the adsorbed protein film, and therefore any platelet activation, etc. will be as a result of the proteins adsorbed onto the biomaterial surface, and not a direct interaction

with the biomaterial surface. Thus, understanding the roles of the various surface properties on protein binding will ultimately aid the development and design of better biocompatible materials.

Blood plasma contains approximately  $90 \text{ mg mL}^{-1}$  protein that includes hundreds of different proteins. These proteins include serum albumins (55%), globulins (38%), fibrinogen (7%), and other regulatory proteins. In general, protein-surface interactions have been focused on 2 major proteins found in the blood plasma: (1) human serum albumin (HSA) and (2) fibrinogen (Fib). The HSA:Fib ratio is approximately 10:1 in serum.

HSA is small globular protein (66 kDa, pI = 4.8, 4 nm x 4 nm x 14 nm) that is the most abundant protein in serum plasma (approximately  $40 \text{ mg mL}^{-1}$ ). It's mainly responsible for transporting fatty acids and small molecules around the body. The secondary structure of HSA is approximately 60%  $\alpha$ -helix, 40%  $\beta$ -sheet,  $\beta$ -turns and has 16 disulfide bonds. HSA has been generally seen as a good protein for surface adsorption due to its minimal interaction with platelets.<sup>7</sup>

Fib is a large elongated glycoprotein (340 kDa; pI = 5.8; 5 nm x 5 nm x 47 nm) that is the highest abundance protein (approximately  $3 \text{ mg mL}^{-1}$ ) involved in the coagulation process. Fib is converted to fibrin by the enzyme thrombin during a vascular injury event. Fib is composed of 2 sets of 3 non-identical polypeptide chains referred to as the  $A_\alpha$ ,  $B_\beta$  and C. The amino termini of all 6 chains are disulfide linked forming its central region. After cleavage of fibrinopeptides, the A domains become untethered (aa392-610) which can promote lateral fiber assembly and endothelial cell adhesion.

### **1.3. Surface Plasmon Resonance**

Surface plasmon resonance (SPR) is a biophysical technique that measures real-time kinetic interactions between two species. In this technique, outlined in Figure 1.3, polarized incoherent light is totally internally reflected off a dielectric-dielectric interface, such as glass-water, in which a thin film of Au is located. Under these conditions, the p-polarized component of the light penetrates the Au film, and the energy is transferred to the metal electrons, creating surface plasmon polaritons. The surface plasmon wave propagates in all directions and enhances the evanescent wave in the z-direction and penetrates the lower refractive index medium (water). This evanescent field is very sensitive to refractive index change (as much as  $10^{-6}$  refractive index units) at the metal-dielectric interface, where adsorption/desorption of molecules changes the

refractive index at the metal-dielectric interface, resulting in a change in the minimum SPR deflection angle.

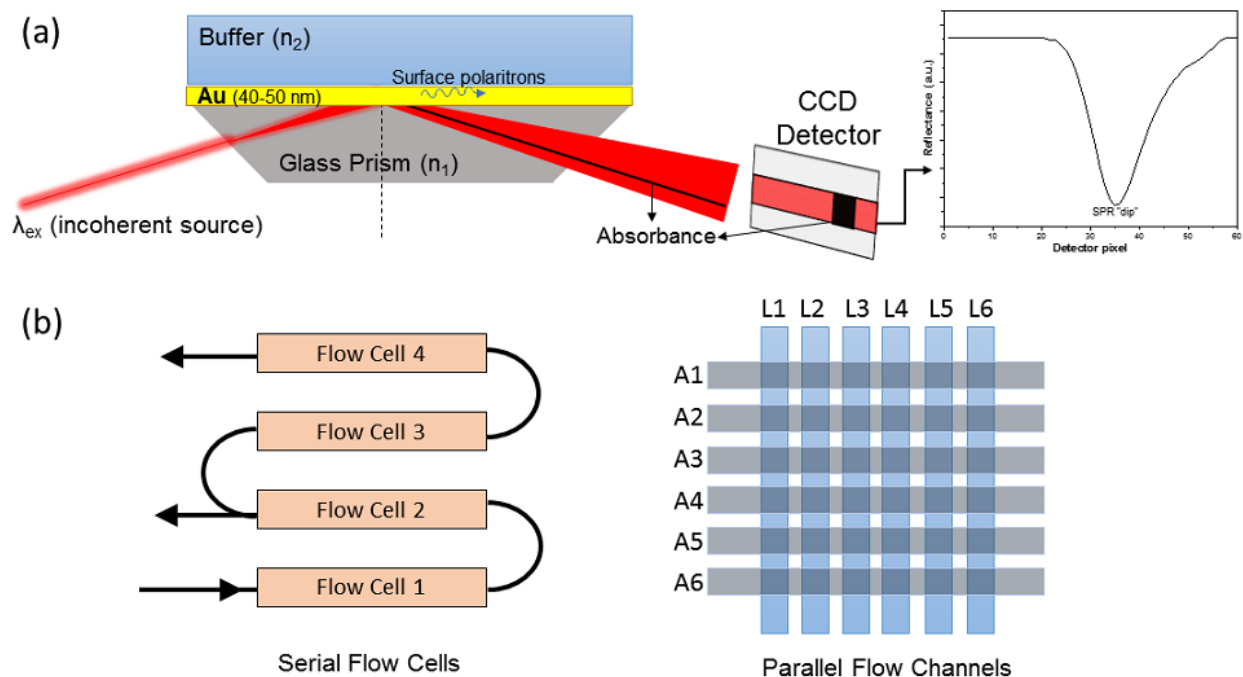


**Figure 1.3.** (a) General overview of SPR instrumentation. (b) Typical designs of micro-fluidics for commercially available instruments. Commercially available Biacore® SPR instruments use a serial flow cell design where liquid delivery flows through each flow cell in a serial manner. The Proteon XPR36 instrument from Biorad Laboratories uses a 6 parallel flow channel that can be rotated in the horizontal (A1-A6) and vertical direction (L1-L6).

Commercially available SPR instrument have become common place in research laboratories, and they are an integral part in pharmaceutical drug discovery. The common advantages of SPR instruments include low sample consumption due to the use of microfluidics, real-time biomolecular interaction monitoring, and there is no need to fluorescently label biomolecules. Commercial SPR instruments use micro-fluidic channels and pneumatic valves to deliver liquid to sensor surfaces in a very consistent and reliable way. Different manufacturers have different sensor surface design outlined in Figure 1.3(b). The serial flow channel design is used by Biacore® instruments. Here, a single liquid injection is delivered to the flow channels and flows across each flow cell in a serial manner. There is a small dead volume between each flow cell, and there are generally 2-4 flow cells depending on the instrument model. For each solution injection, 1-3 sensorgrams can be obtained (1 flow cell is used as a reference surface). The Biorad

Proteon XPR36 instrument uses 6 independent flow channels that can be rotated both horizontally and vertically. This allows for 36 sensorgrams to be measured during one sample cycle.

A typical sensorgram is shown in Figure 1.4(a). In a typical experiment, running buffer is continuously flowing through the flow cells (A). A protein would have been previously immobilized on the surface, and commonly referred to as the ligand. A solution containing a second biomolecule, referred to as the analyte, is injected into the flow cells and marks the beginning of the association phase (B). An increase in the response signal corresponds to a change in refractive index at the surface due to the mass increase at the surface due to protein binding. At the end of the association phase (C), the analyte solution stops flowing over the flow channel, and it is replaced by the running buffer. This marks the start of the dissociation phase (D), where a decrease in the response signal is associated with the desorption of the analyte biomolecule from the surface. After a suitable dissociation time, the remaining analyte can be removed using various types of regeneration solutions (E). The type of regeneration solution used will depend on the type of binding interaction present. For example, an electrostatic interaction can be disrupted by a large concentration of salt solution (ex. 4 M NaCl).

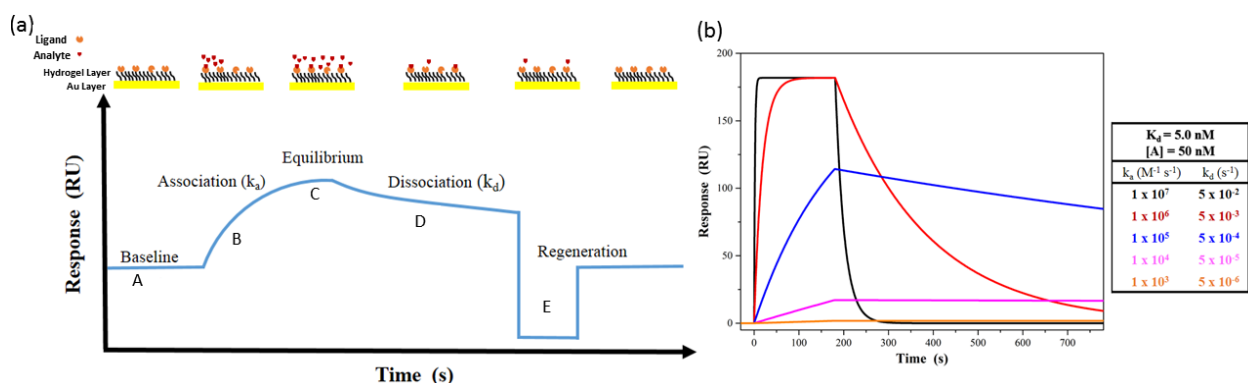


**Figure 1.4.** (a) General overview of an SPR sensorgram. (b) SPR sensorgrams of showing the changes in binding kinetics ( $k_a$ ,  $k_d$ ) profiles for different biomolecular interactions having the same affinity ( $K_D = 5.0 \text{ nM}$ ) and same analyte concentration ( $50 \text{ nM}$ ).

The dissociation constant ( $K_D$ ) is generally used to assess the strength of a biomolecular binding interaction. However, the association ( $k_a$ ) and dissociation ( $k_d$ ) kinetics for a biomolecular interaction can be extracted from SPR measurements and they provide meaningful information. The  $K_D$  is related to  $k_a$  and  $k_d$  by Equation 1.1.

$$K_D = \frac{k_d}{k_a} \quad (1.1)$$

In Figure 1.4(b), the SPR sensorgrams for a simulated biomolecular interaction that has a  $K_D$  of 5.0 nM, but different  $k_a$  and  $k_d$  kinetics for a single injection of analyte (50 nM). The SPR sensorgram lineshapes look very different depending on the of  $k_a$  and  $k_d$  values. The  $k_a$  will measure how fast the biomolecular species recognize each other, where larger  $k_a$  values show an increase in the rate of response and reach a maximum when the analyte solution and the surface are in dynamic equilibrium. On the other hand, the larger  $k_d$  value measures the stability of the biomolecular complex. The larger  $k_d$  curves shown in Figure 1.4(b) show a sharp decay back to the baseline. However, as the  $k_d$  values decrease, the rate of decay decreases until the dissociation curve looks comparable to a straight line.

## 1.4. Amorphous Carbon

### 1.4.1. Carbon Properties

Carbon is a unique element in the periodic table in that carbon has three different bonding configurations and results in the existence of many different carbon allotropes, as shown in Figure 1.5. In the  $sp^3$  configuration, each of the 4 valence electrons form a tetrahedral  $sp^3$  hybridized orbital with the adjacent carbon atoms, resulting in the formation of 4 very strong  $\sigma$ -bonds. These four  $\sigma$ -bonds are responsible for diamond's high hardness and large band gap (5.5 eV). On the other hand, the  $sp^2$  configuration contains three  $\sigma$ -bonds that adopt a trigonal in-plane structure. The  $p_z$  orbital contains the last valence electron, and it remains unhybridized and slightly higher energy compared to the 3  $sp^2$  orbitals. This orbital is generally referred to as the  $\pi$ -orbital and it is arranged perpendicular to the plane of the  $sp^2$   $\sigma$  orbitals. It is involved in a weaker  $\pi$ -bond due to side-to-side overlap with another  $\pi$ -orbital on an adjacent C atom, resulting in the  $\pi$ -electrons to be delocalized between the adjacent C atoms. Graphite is an example of a trigonal  $sp^2$  network that forms 6-membered rings containing alternating single and double bonds. Strong intermolecular forces, from the delocalized electrons of the  $\pi$ -bonds between the sheets or planes give rise to a zero bandgap. Fullerenes and carbon nanotubes are other examples of carbon allotropes containing  $sp^2$ -networks of carbon. The  $sp^1$  configuration is composed of 2  $\sigma$  bonds directed along the x-axis, and the  $p_y$ ,  $p_z$  orbitals for  $\pi$ -bonding. The resulting  $C\equiv C$  bond has recently been found in a newer allotrope of carbon called graphdiyne, which is a flat material composed of  $sp^2$ - and  $sp^1$ -hybridized carbon atoms with a high degree of  $\pi$ -conjugation and uniformly distributed pores.<sup>8</sup>

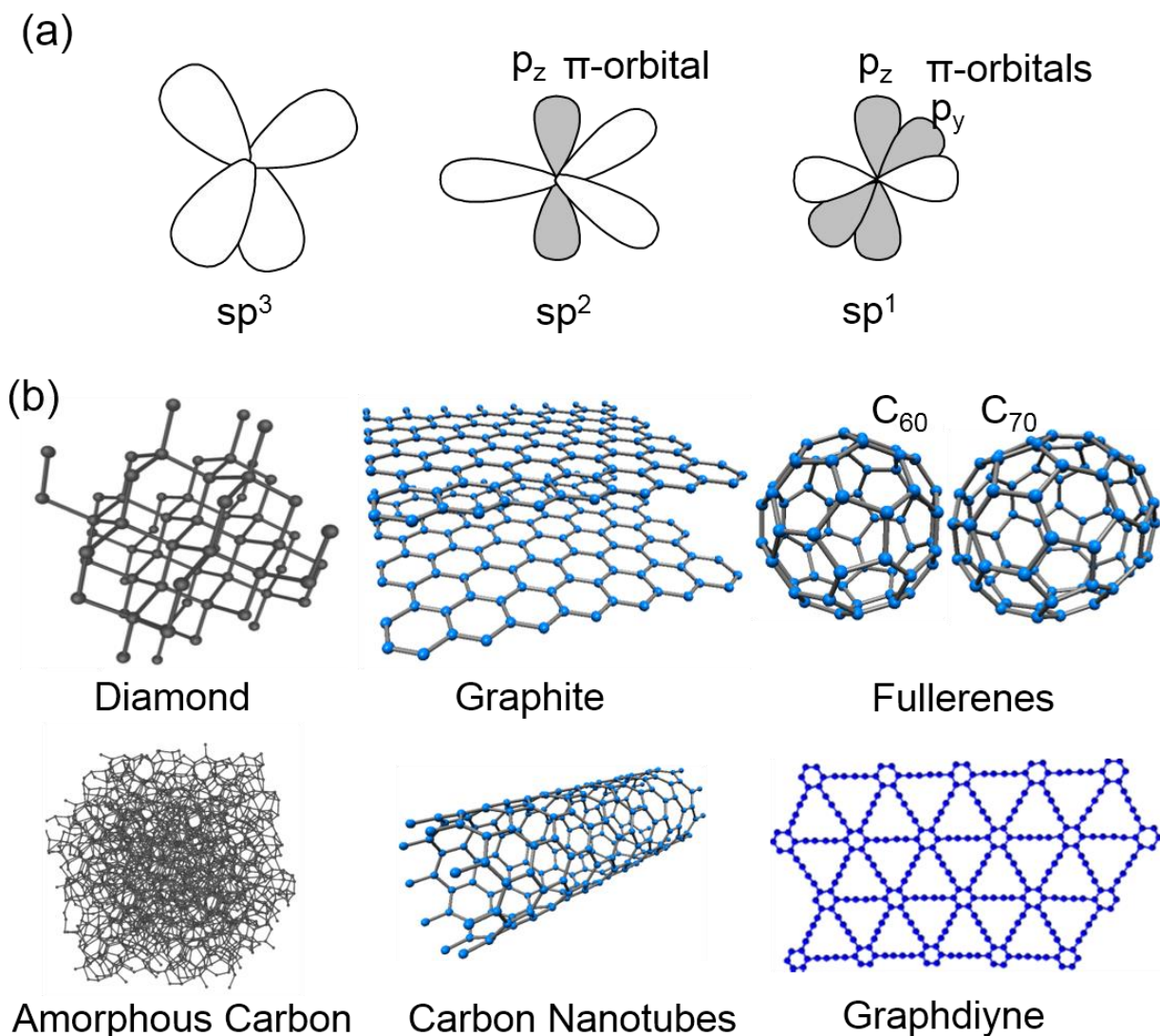


**Figure 1.5.** (a) Carbon has 3 different types of hybridization:  $sp^3$ -hybridization contains 4 s-bonds;  $sp^2$  contains 3  $sp^2$  bonds, and a weaker p-bond;  $sp^1$ -hybridization contains a s-bond and 2  $\pi$ -bonds. (b) Different allotropes of carbon can contain an exclusive type of carbon hybridization (ex. Diamond, graphite) or a combination of hybridizations (ex. Graphdiyne, amorphous carbon).

#### 1.4.2. Amorphous Carbon Synthesis

Amorphous carbon (a-C) films can have a mixture of  $sp^3$  (diamond-like),  $sp^2$  (graphite-like), and even  $sp^1$  bond hybridizations, and the resulting combinations can lead to some interesting forms of a-C microstructure, some of which are outlined in Table 1.1.<sup>9-10</sup> In addition, the disorder within a-C films also allows other impurities/dopants to be built into the microstructure, which may further alter the physical properties of the film. The key parameters that will highly influence the properties of an a-C film includes the  $sp^3$  content, the clustering and orientation of the  $sp^2$

phase, the cross-sectional nanostructure, and the H content.<sup>11</sup> The common types of amorphous carbon are summarized in the ternary diagram shown in Figure 1.6.

**Table 1.1.** Physical properties for different types of crystalline allotropes and amorphous carbon thin films.<sup>9-10</sup>

Carbon Material	Hardness (Gpa)	sp <sup>3</sup> (%)	Optical Bandgap (eV)	Density (g cm <sup>-1</sup> )	H (at. %)
Diamond	Hard	100	5.5	3.515	0
Graphite	Soft	0	0	2.1-2.3	0
Diamond-Like Amorphous Carbon	20-40	40-60	0.8-4.0	1.8-3.0	20-40
Tetrahedral Amorphous Carbon	40-65	65-90	1.6-2.6	2.5-3.5	0-30
Polymer-Like Amorphous Carbon	Soft	60-80	2.0-5.0	0.6-1.5	40-65
Graphitic Amorphous Carbon	Soft	0-30	0.0-0.6	1.2-2.0	0-40
Nanocomposite Amorphous Carbon	20-40	30-80	0.8-2.6	2.0-3.2	0-30

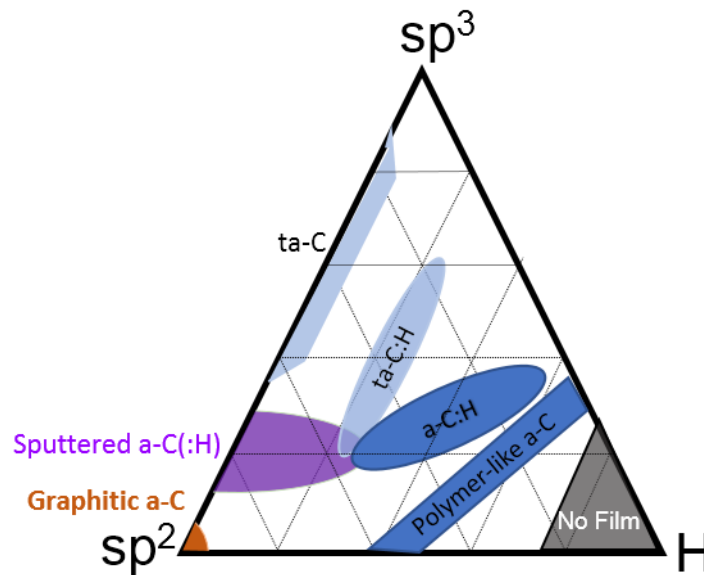


**Figure 1.6.** Ternary diagram of a-C composed of different sp<sup>2</sup>, sp<sup>3</sup>, and H content.<sup>11</sup>

The a-C film surface coatings are generated from the vapour phase using either chemical vapour deposition (CVD) or physical vapour deposition (PVD) methods and are summarized in Figure 1.7. The simplest CVD methods typically involve high temperatures which are used to decompose chemicals and then recombine to form on the hot substrate. The use of high temperatures limits the type of substrates to be used for a-C surface coating. Plasma enhanced chemical vapour deposition is a hybrid process in which energetic electrons (100-300 eV) are

activated within a plasma, allowing for lower substrate temperatures (100-600 °C) and high vacuum pressures (0.01-5 Torr).<sup>12</sup> Plasmas can be generated using direct current (dc), radio frequency (rf) (13-56 MHz) or microwave (2.45 GHz) fields.

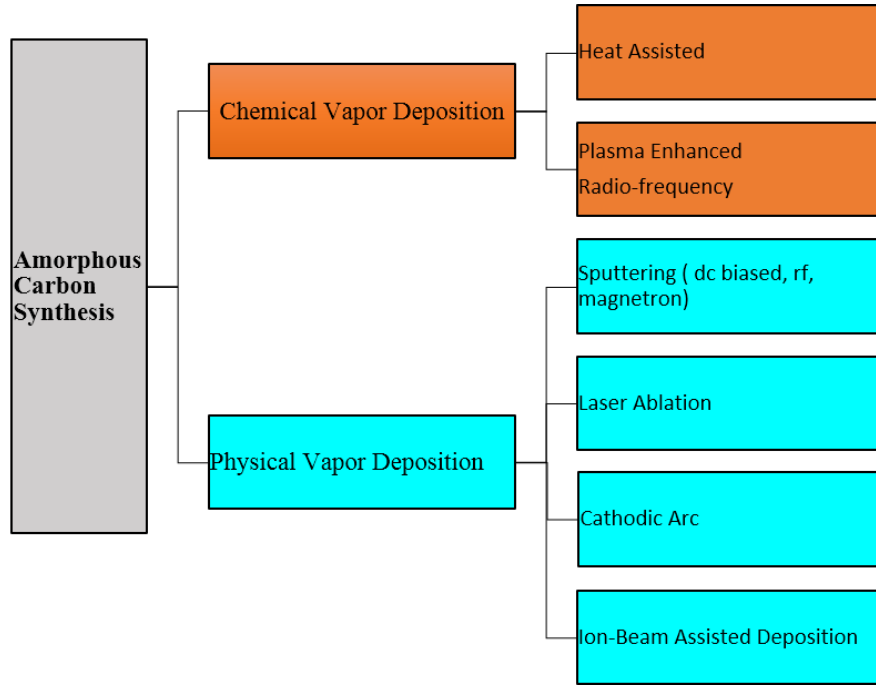


**Figure 1.7.** Common plasma deposition methods for a-C.

The PVD deposition techniques include sputtering, evaporation, ion beam assisted deposition, cathodic arc, and pulsed laser deposition processes. These techniques all include the condensation of a vapour onto the substrate under a relatively high vacuum. PVD techniques will only deposit films that are within “sight” of the vapours, so substrates with complex geometries, holes, etc. may have difficulties obtaining uniform coatings. This research will be using sputtering deposition, so this PVD method will be discussed in more detail.

Plasma assisted sputtering is one of the most widely used deposition methods for a-C due to its versatility ease of use. The general configuration is shown in Figure 1.8. In this method, an inert gas, typically Ar, is ionized by electrons emitted from a cathode target normally composed of graphite. The graphite target is biased with a dc voltage or a rf source. The  $\text{Ar}^+$  then accelerate and ablates the graphite surface, producing  $\text{C}^+$  and  $\text{C}_n^+$  ions. The ions can have a wide energy distribution (up to  $10^1$  eV) which can then move towards the substrate. Depending on their energy, the ions may adsorb (stick) onto the substrate, reflect off the surface (too low of energy), or sputter the surface (too high of energy). Once on the surface, the ions may undergo chemical reactions

with other ions forming more complex structures. In general, graphite has a low yield for sputtering (ratio of energetic ions to neutrals is  $< 1\%$ ). In some cases, magnets may be added behind the substrate to increase the mean-free path of the ions, increasing the number of ions within the plasma. In addition, a dc bias may be applied to the substrate, resulting in changes in the film properties due to the alteration of the ratio of ions, electrons, neutrals, etc. bombarding the substrate.

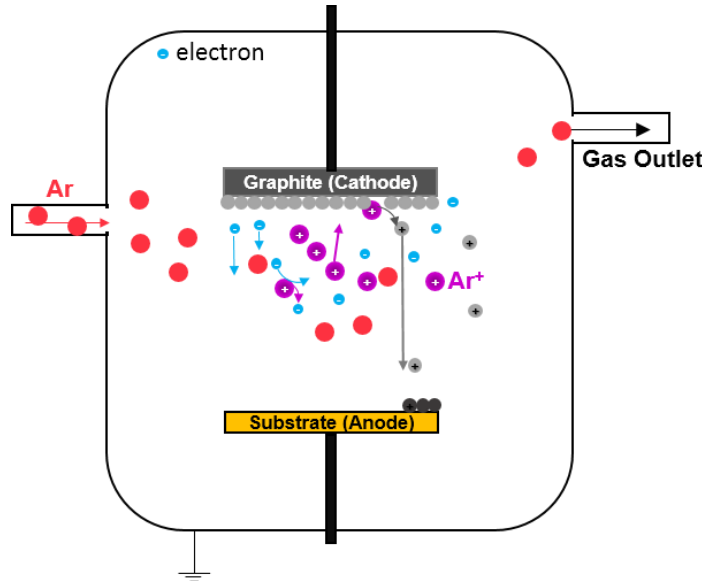


**Figure 1.8.** Basic configuration of plasma-assisted sputtering.

### 1.4.3. Amorphous Carbon Clustering

The evolution of  $sp^2$  clustering has been proposed to occur in 3 different stages of amorphization as outlined in Figure 1.9.<sup>13-14</sup> All of these stages can be identified by Raman spectroscopy in the so-called D and G regions. The first stage begins with well-ordered, large crystallites of graphite. Graphite will be broken down into smaller crystallite sizes ( $L_a$ ) of nanocrystalline graphite materials, eventually reduces to 1-2 nm  $sp^2$  clusters. Stage 2 introduces disorder within the  $sp^2$  structure as the nanocrystalline graphite transforms into a-C. Bond lengths will change and the bond angles within aromatic structures will become more strained. There will also be a loss of % $sp^2$  content within the material (down to approximately 80%  $sp^2$ ). The third stage shows a dramatic increase in the  $sp^3$  content as the aromatic rings are transformed to more chain configurations, eventually forming tetrahedral amorphous carbon (ta-C) also known as diamond like carbon (DLC).

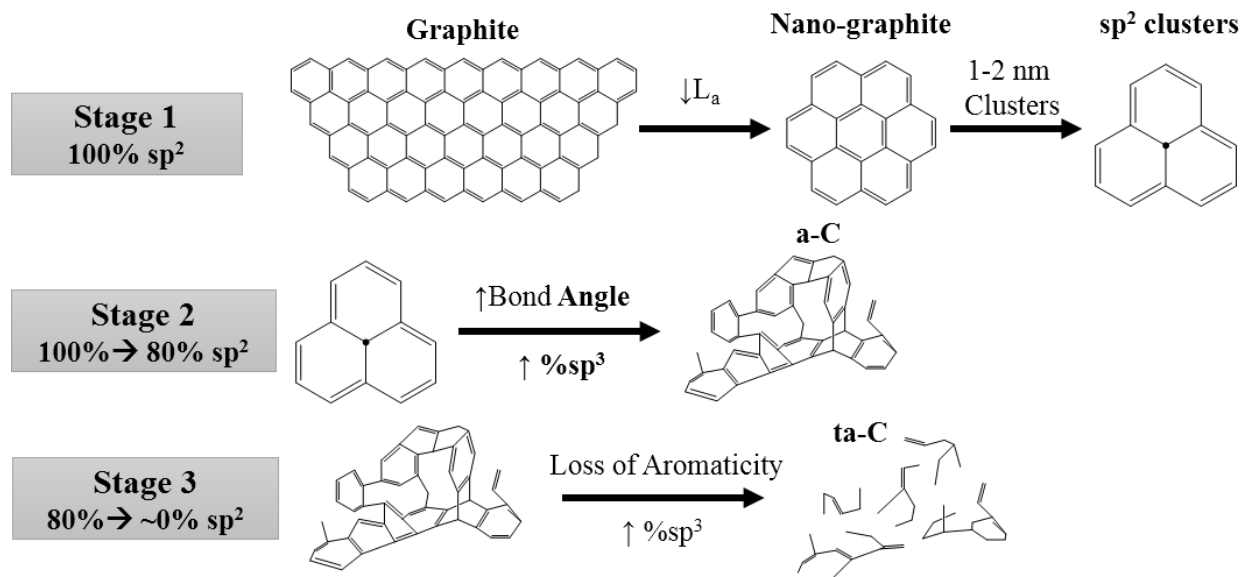


**Figure 1.9.** There are 3 stages of amorphization of carbon from graphitic state. Stage 1 finds the graphitic crystalline size ( $L_a$ ) decrease until small 1-2 nm clusters are formed. Stage 2 sees the conversion of the small  $sp^2$  clusters to amorphous carbon. Some  $sp^3$  content will be introduced. Stage 3 sees the aromatic  $sp^2$  clusters are converted to chains, and the  $sp^3$  content dramatically increases to approximately 100%.

#### 1.4.4. Amorphous Carbon Doping

The physical properties of a-C coatings doped with different elements has been extensively studied and reviewed.<sup>11, 15</sup> The addition of different elements has added an additional dimension to controlling the a-C coating properties while maintaining its amorphous structure. The different types of elements studied can be subdivided into metals (Ti, Cu, W, Nb, Au, Cr, Ni, Mo, Ta, etc.) and light elements (B, N, Si, O, F, P).<sup>16</sup>

Metal doping into a-C has been mainly formed by magnetron sputtering metallic targets in the presence of Ar/hydrocarbon gas<sup>17-18</sup> or simultaneous sputtering of graphite and metal targets.<sup>19</sup> The metals have been generally observed to be dispersed within the a-C network as small nanocrystallites of pure metal, or metal carbides.<sup>16, 19-20</sup> The general coating properties that are altered include the internal stress, adhesion, as well as tribological properties like friction and wear. For instance, Ti and Cr have been used as an interlayer to improve a-C/DLC adhesion onto different steel alloys.<sup>21-22</sup> In addition, the inclusion of Cr into the a-C matrix was found to decrease the internal stress within the coating which ensured sufficient adhesion strength by developing a strong chromium carbide interface.<sup>23</sup> Another study found that the incorporation of Ta and W into DLC reduced their frictional coefficients and had a better wear resistance compared to TiN and TiAlN surfaces under the same conditions.<sup>24</sup>

Incorporating lighter elements (B, N, Si, O, F, P) into a-C matrix has been extensively studied. In most cases, the lighter element incorporation improves specific properties of the a-C films.<sup>16</sup> These include field emission and electrical conductivity,<sup>25-27</sup> surface energy,<sup>28</sup> friction and wear,<sup>29-30</sup> and biocompatibility.<sup>28, 31-35</sup> The present research is focused on nitrogen incorporation into the amorphous carbon.

#### ***1.4.4.1. Amorphous Carbon Nitride (a-C:N)***

Nitrogen incorporation into a-C films is interesting due to the many different possible bonding configurations it can adopt with carbon and is outlined in Figure 1.10. Bonding configurations include  $sp^3$ -like amino structures, chain terminating  $sp^1$  nitrile groups, and  $sp^2$ -like bonding found in ring systems (pyridine, pyrrole) and/or double bonded olefinic variants. In addition, some bonding configurations may contain lone pair electrons and represent possible substitutional doping configurations. Nitrogen can incorporate into aromatic carbon clusters through pyridinic and pyrrolic aromatic rings. In addition, nitrogen can incorporate through graphitic substitution and pyridinic oxides.

Nitrogen and carbon have a very similar atomic size, so nitrogen incorporation does not induce a significant lattice mismatch. In addition, the additional electron in nitrogen provides an opportunity of a n-type electronic modification of the carbon structure. Several research studies have shown that the a-C:N properties (tribological, biocompatibility, electrical, etc.) generally show an improvement compared to the equivalent prepared a-C. For example, a-C:N films have been shown as a potential protective coating for magnetic storage disks.<sup>36-37</sup> Nitrogen incorporation has also been shown to reduce the internal stress of the a-C:N coating without significantly altering the tribological properties compared to undoped a-C.<sup>38</sup> The improved adhesion has led to potential coating for biomedical devices/materials.<sup>31, 39-42</sup>

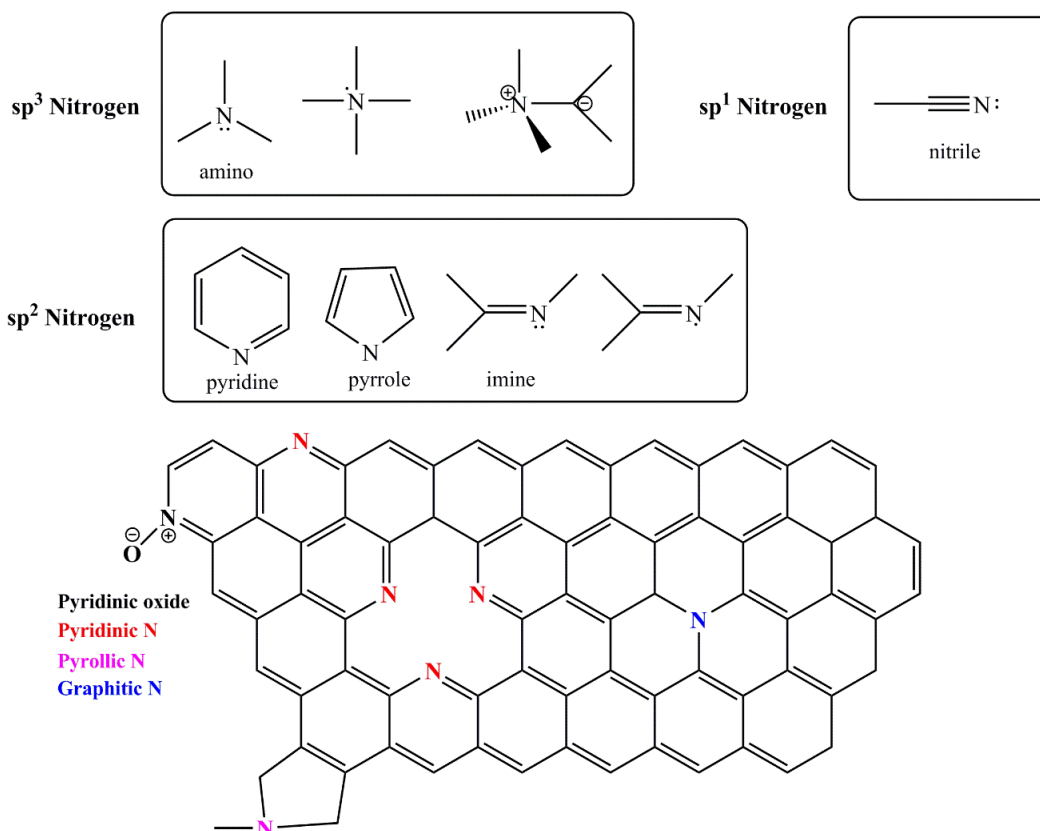


**Figure 1.10.** Nitrogen has many different bonding configurations in the sp<sup>3</sup>, sp<sup>2</sup>, and sp<sup>1</sup> hybridization. Nitrogen incorporation into the aromatic a-C matrix may be pyridinic, pyrrolic, and graphitic nitrogen substitutions.

#### 1.4.4.2. Fullerene-Like Amorphous Carbon Nitride (FL-CN<sub>x</sub>)

Fullerene-like carbon nitride (FL-CN<sub>x</sub>) is a subclass of a-C:N that is characterized by its high at.% N concentration (>15%), and its high degree of sp<sup>2</sup> bonding from the graphite plane bending and cross-linking which gives these films its fullerene-like character.<sup>29, 43</sup> Some of the unique characteristics include its flexibility and high hardness for materials composed of a high degree of sp<sup>2</sup> carbon.<sup>44</sup> These films have also been found to provide better thermal stability compared to DLC films, but its thermal stability is dependent on the substrate temperature and type of nitrogen bonding within the coating during synthesis. Other tribological properties such as wear and friction have also been evaluated.<sup>45</sup> The frictional coefficient was dependent on the nitrogen content within the coating, where a general increase of the friction coefficients increased with increase nitrogen content within the film. It was also found that the wear rates of the FL-CN<sub>x</sub> was generally lower compared to a tungsten carbide/carbon reference. The wear rates were also dependent on the humidity.

## 1.5. Research Proposal

To date, low temperature isotropic carbon (LTIC), glassy carbon, and ultralow-temperature isotropic carbon (ULTIC) have been very successfully applied in biomedical devices, including mitral and aortic heart valves, blood access devices, Dacron and Teflon vascular grafts, and blood oxygenator microporous membranes.<sup>46</sup> There has been much research to improve upon LTIC and ULTIC success by using a-C coated materials. It is biocompatible *in vitro* and *in vivo* in simple orthopedic applications.<sup>47-48</sup> It has also been found to promote less platelet activation than metallic substrates used for cardiovascular applications.<sup>49</sup> In addition, there have been some positive results showing nitrogen incorporation into the a-C films improves its biocompatible properties.<sup>41, 50</sup> However, it was found that films prepared with too much N<sub>2</sub>/Ar plasma discharge gas actually decreased the film's biocompatibility properties.<sup>41</sup>

One major issue regarding the biocompatibility of a-C films is the inconsistent results found in the literature. Some of the biocompatibility results for some a-C materials have been positive.<sup>31, 51-52</sup> However, there have been instances where biocompatibility results have been worse than that obtained for LTIC.<sup>53</sup> Most biocompatible studies have focussed on cellular adhesion to the a-C film. Hemocompatible studies have also focussed on evaluating the number, size and shape of adhered red blood cells. More recently, there have been some studies on protein adsorption onto a-C films.<sup>54</sup>

It is well known that protein adsorption onto implant devices happens immediately upon exposure to biological fluids.<sup>55</sup> there has been much gain in the understanding regarding protein adsorption at the surface.<sup>6, 56-58</sup> However, there still remains some unanswered questions. It was recently suggested that rather than chase the holy grail of a perfect hemocompatible biomaterial, efforts should be focussed on answering some of the basic unknown questions surrounding blood-biomaterial interactions.<sup>59</sup> It was suggested that these questions could be achieved using existing techniques using good experimental models.

### 1.5.1. Thesis Objectives

The main objective of this thesis is to (1) develop an SPR assay to measure the initial surface interactions of 2 major proteins found in serum, HSA and Fib, to a-C films prepared with different amounts of nitrogen incorporation. Nitrogen incorporation into the films was varied by

changing the %N<sub>2</sub> plasma discharge gas during plasma assisted chemical sputtering using a graphite target.

The original plasma deposition chamber produced FL-CN<sub>x</sub> films that contained trace amounts of metals, mainly Fe. A second objective was to determine (2) the metal composition and whether it influenced the FL-CN<sub>x</sub> film structure/properties.

The third objective was (3) to design a “metal-free” deposition chamber to prepare used to was designed, and different %N<sub>2</sub> plasma discharge gas from plasma-assisted chemical sputtering deposition using a graphite target. Films were prepared at a lower temperature and were regular a-C:N films. The “metal-free” a-C:N films were prepared on SPR sensor chips and the film properties were characterized using various spectroscopic techniques. In addition, an a-C:N film was purposely doped with Fe in order (4) to investigate whether the incorporation of Fe into the a-C:N films changed the binding interactions with HSA and Fib.

The FL-CN<sub>x</sub> and a-C:N films were characterized using a variety of techniques, including atomic force microscopy, Raman spectroscopy, sessile contact angle measurements, x-ray photoelectron spectroscopy, ultraviolet photoelectron spectroscopy, x-ray absorption near edge spectroscopy, electron spin resonance spectroscopy, and Fourier transform infrared spectroscopy.

## CHAPTER 2 - LITERATURE REVIEW

### 2.1. Biocompatibility Studies of Amorphous Carbon

Carbon materials such as LTIC, glassy carbon, and ultralow-temperature isotropic carbon ULTIC have been successfully applied to biomedical devices, including mitral and aortic heart valves, blood access devices, Dacron and Teflon vascular grafts, and blood oxygenator microporous membranes.<sup>46</sup> The biocompatible properties of LTIC has been known for some time. It has been used in prosthetic heart valves since 1969, and it had greatly reduced the incidence of thrombogenic incidences and mechanical failures.<sup>60</sup> In addition, it has been used successfully in some upper limb joint prostheses such as the metacarpophalangeal joint and the proximal interphalangeal joint.<sup>61</sup>

LTIC biomedical devices have provided good hemocompatibility results, but they do eventually fail over time. Plasma-generated a-C coatings, with their ability to alter the physical/mechanical properties and ease of doping additional elements into the a-C matrix, has been a highly researched area. One of the main issues that has limited the commercialization of a-C coatings are that the biocompatibility results in the literature are inconsistent. Some studies have revealed improved biocompatible results compared to other materials while other studies have shown no difference and/or reduced biocompatible results. Several studies have been summarized in literature reviews on the biocompatibility of a-C coatings.<sup>15, 51-52, 62-65</sup>

#### 2.1.1. Clinically Tested a-C Devices for Hemocompatible Applications

There have been some a-C coated materials using in blood-interfacing applications that have been clinically tested with some that are commercially available, and they are summarized in Table 2.1. In general, the main goal for blood-interfacing devices is to prevent biomaterial associated thrombosis. This will critically depend on the biomaterial's surface composition, surface texture, local flow conditions, etc. It has been generally observed that the high ratio of albumin/fibrinogen adsorbed at the surface correlates with a lower platelet adherence, which reduces the chances of thrombus formation.

**Table 2.1.** Summary of Commercially Available Biomedical Devices using a-C Coatings.

<b>Device/Company</b>	<b>Instrument Type</b>	<b>Comments</b>
Phytis Medical Devices GmbH, Germany	DiamondFlex AS™ (stent)	
PlasmaChem GmbH., Germany	BioDiamond™ (stent)	
Sorin Biomedical, Italy (<2008) CID, Italy (2008-2013) Alvimedica, Turkey (2013-)	CarbonStent™ (stent) Chrono™ (stent) Avantgard™ (polymer-free drug eluting stent) Cre8™ (polymer-free drug eluting stent)	Coated with 0.5 mm CarboFilm™ coating described as turbostratic structure Avantgard and Cre8™
Bekaert, Belgium Blue Medical Devices BV, Netherlands (2004-2013)	Dylyn™ (stent) XTRM-FIT (stent)	Nanocomposite consisting of a-C and amorphous silicon oxide coated on stent.
ENDOCOR GmbH, Germany	SEQUENCE™ (drug eluting stent)	“Inert Carbon Technology” is a plasma assisted a-C coating....
Japan Stent Technology Co Ltd., Japan	MOMO® (Stent)	Uses a 35nm DLC coating on stent
Sun Medical Technology Research Corporation, Japan	Centrifugal ventricular blood pump device	
Sorin Biomedical, Italy	Biocarbon™ mechanical heart valve	CarboFilm™ turbostratic carbon structure
Ventracor Pty Ltd., Australia	VentraAssist™ (ventricular assist device)	DLC coated cardiac devices
Cardio Carbon Company Ltd., United Kingdom	‘Angelini Valvuloplasty’ ring valve repair ‘Angelini Lamina-flo’ mechanical heart valve	DLC coated Ti implant

### **2.1.1.1. Cardiovascular Stents**

Phytis Medical Devices GmbH (Germany) was cofounded in 1997 by Dr. Alexei Kalachev and Dr. Franz Herbst in 1997 and was a distributor of DLC coated stents which were created according to the owner's patented plasma deposition process.<sup>66</sup> This process deposited a uniform DLC coating on both the inside and outside surfaces of the stent. The initial *in vitro* tests found that the DLC coating reduced the amounts of Ni, Cr, Mn, and Mo over a 96 hr period in human plasma compared to uncoated stainless steel stents.<sup>67</sup> Flow cytometry analysis for CD62p and CD63 antigens (platelet activation markers) showed a higher fluorescent intensity compared to the DLC-coated stents. The study suggested that the DLC coating reduced the metal release and had a lower overall platelet activation compared to the uncoated stainless-steel stents. However, a clinical trial study involving the Diamond Flex AS™ stent and stainless steel stent randomly compared in 347 patients (520 lesions) found that there was no differences observed for in-hospital major cardiac events.<sup>68</sup> During the 6-month follow-up, both the Diamond Flex AS™ and stainless-steel stents showed a similar rate of binary restenosis and cumulative major adverse cardiac events (31.8%/30.5% and 35.9%/32.7%, respectively). Their conclusions were that the DLC-coating did not provide statistically significant improvements over the stainless-steel stents with the same design. Furthermore, an additional randomized study of the DLC-coated stent manufactured from Phytis Medical Devices GmbH was compared to an uncoated stent for patients diagnosed with coronary artery disease.<sup>69</sup> Their conclusions also found that there were no differences in the restenosis and major cardiac event rates after 6 months.

Kalachev and Herbst also cofounded another company called Biodiamond in 1999 which was the exclusive licensee for the technology and distribution for their DLC coated stents. The BioDiamond™ stent as well as a BioDiamond™ urinary tract stent was distributed by PlasmaChem GmbH, Germany (owned and managed by Dr. Alexey Kalachev). A clinical trial centred at CHP Beauregard, Marseille, France had 163 patients undergo 248 implants for 233 coronary lesions.<sup>66</sup> The Biodiamond™ (PlasmaChem GmbH, Germany) coronary stent was effective in 98% of the coronary lesions, showing a minimum lumen increase from 0.76 mm to 2.57 mm after the procedure. The 6-month follow-up revealed that 98.6% of patients did not have a major adverse clinical event.

The CarboStent™ (Sorin Biomedical, Italy) is a balloon-expandable stainless steel tubular stent with a turbostratic carbon coating. A clinical study involving 112 patients and 132 coronary

lesions underwent CarboStent™ implantation.<sup>70</sup> The preliminary clinical study showed a high procedural success rate, and a low rate of angiographic restenosis and clinical related results. There was no observed stent thrombosis, and a 6-month follow-up found the restenosis rate was 11%, and 10% of the patients had repeat revascularization. This clinical study was limited to the Carbostent™, and it did not compare it to other commercially available stents. Another pilot clinical study looked at the effect of aspirin alone treatment given post-operation of a Carbostent™ intracoronary implantation.<sup>71</sup> This study included 110 patients and a total of 129 lesions showed no stent thrombosis during in-hospital stay, and no adverse events were observed within 30 days despite the reduced antiplatelet regimen.

The Carbostent™ and vascular therapy business from Sorin Biomedical became an independent company called CID (Carbostent & Implantable Devices) in 2008. They continued to develop the CarboFilm™ onto Co-Cr alloyed stent called the Chrono™.<sup>72</sup> In 2013, CID and Alvimedica (Turkey) merged and continue to develop new medical devices. A more recent carbon coating called iCarbofilm™ is less than 300 nm thickness and is marketed as a “Bio Inducer Surface”.

The Dylun™ coated stent manufactured by Bekaert (Belgium) is a nanocomposite coating consisting of amorphous carbon and a amorphous silicon oxide network.<sup>73</sup> promising DLC nanocomposited coatings (single layer and double layer). Initial animal studies were performed on porcine coronary arteries using 2 different Dylun™ coatings (single and double coating) and compared to uncoated stents.<sup>74</sup> After a six week period, the pigs were sacrificed, and the results found that the stenosis area was lower for the Dylun™ coated stent compared to uncoated stents. In addition, the thrombus formation was significantly decreased and the neointimal hyperplasia was also decreased but not significantly different from the uncoated stent. Overall, the second layer of DLC offered not additional advantage over the single layer. Initial clinical tests for the Dylun™ coated coronary stents found excellent short-term results, but the amount of angiographic restenosis at 6 months was comparable to other non-drug eluting stent systems.<sup>75</sup> No further studies were found for this device. However, Blue Medical Devices BV (Netherlands) has marketed a Dylun™ coated stent called XTRM-FIT. Unfortunately, Blue Medical Devices BV declared bankruptcy in 2013, and was incorporated into Wellingq Holding BV (Switzerland). The XTRM-FIT is not available.

The MOMO® coronary stent manufactured by the Japan Stent Technology Co Ltd. (Japan) uses a 35 nm DLC coating deposited on a Co-Cr stent. It has been clinically tested, and preliminary results suggest that it has a lower target vessel failure rate after 9 months compared to uncoated metal stent.<sup>76</sup> Drug-eluting stents have become an important advance that shows large potential in preventing restenosis. Typically, drugs are contained within a polymer film deposited onto a stent and then released over a time period, reducing adverse effects from the stent. More recently, ENDOCOR GmbH (Germany) has marketed the SEQUENCE™ which is a drug eluting stent using a biodegradable polymer carrier. It uses a carbonized stainless steel surface formed by C<sup>+</sup> ion implantation, so that after the biodegradable polymer carrier is removed, the carbonized surface is more biocompatible. Alvimedica (Turkey) has a very effective polymer-free drug-eluting stent called the Cre8™ EVO. It uses the iCarboFilm™, marketed as a “Bio Inducer Surface”, that ensures effective neointima suppression and rapid endothelialisation. It was found to have equivalent efficacy in both the general population and diabetics.<sup>77</sup>

#### ***2.1.1.2. Heart Valves and Pumps***

The Sun Medical Technology Research Corporation (Japan) developed a centrifugal blood pump that was composed of a Ti-alloy which contained a DLC coating (ion beam sputtering) in areas of blood-contact.<sup>54</sup> The pump demonstrated excellent hemocompatibility in the long-term *in vivo* experiments performed in calves. The device showed good success rates in clinical trial studies situated in Japan.<sup>78-79</sup> More recently, Evaheart Inc. was established in the United States to gain regulatory approval and commercialize the EVAHEART®2 Left Ventricular Assist System. This device is currently undergoing pre-clinical trials.<sup>80-81</sup>

The Bicarbon™ mechanical heart valve manufactured by Sorin Biomedical (Italy) uses the same tubostratic CarboFilm™ as the Carbostent™ detailed above. This device has been around since the early 1990s, and the initial clinical results found no structural deterioration (mechanical fracture, non-structural dysfunction) or acute thrombosis of the prosthesis, or other thromboembolic events were found.<sup>82</sup> This device has been used for many years, and several publications after 5 years to 15 years of use have concluded that the device has continued to perform satisfactorily over the long term with a low incidence of valve-related mortality and morbidity.<sup>83-85</sup>

The VentraAssist™ left ventricular assist device was developed by Ventracor Pty Ltd. (Australia).<sup>86</sup> This device has a DLC coating on all blood-contacting surfaces. The initial animal

study indicated that the device showed low levels of hemolysis, and no clinical evidence of renal or hepatic dysfunction.<sup>86-87</sup> It was determined that the prototype needed some modifications regarding the inflow and outflow cannulae. The VentraAssist was eventually implanted into 400 patients worldwide as of 2009. However, Ventracor ran into financial problems during its final stages of clinical testing, and a potential buyout from Siqro (United States), a subsidiary of Orqis Medical, fell through and the company was eventually liquidated.

The Cardio Carbon Company Ltd. (United Kingdom) was formed in the early 1990s and it was based on a patent based on a mechanical heart valve composed of vitreous carbon.<sup>88</sup> The company marketed the vitreous carbon as “Turboform Carbon”.<sup>89</sup> A second patent describing the use of DLC-coating for Ti medical devices was issued.<sup>90</sup> According to the patent, it used a multi-layered coating that included a TiN, TiC, followed by DLC. Two medical devices called the *Angelini Lamina-flo*<sup>™</sup> (a mechanical heart valve) and the *Angelini Valvuloplasty*<sup>™</sup> (a ring valve repair) were marketed and clinical trials were underway.<sup>91-92</sup> However, there were no supporting clinical studies found for these devices, and the company was disbanded in 2001.

### **2.1.2. Amorphous Carbon Plasma Deposition on Polymeric Substrate**

Many biomedical prostheses are made of polymeric materials, and the most common polymers used are poly(ethyleneterephthalate) (PET or Dacron®) and poly(tetrafluoroethylene) (PTFE or Teflon®). The PTFE is a low cost, machinable fluorocarbon polymer that has low chemical inertness, non-biodegradable, and has a low coefficient of friction. Biomedical devices such as vascular grafts, catheters, and sutures have taken advantage of PTFE properties.

Vascular graft prostheses have continued to improve with new techniques and materials. For example, larger vascular prostheses with diameters greater than 6 mm have a 5-year survival rate of 95%, and their patency rates continue to improve.<sup>93</sup> However, the patency rate for vascular grafts with diameters less than 6 mm are still very low. The preferred choice for smaller vascular grafts is to use autologous blood vessels due to their mechanical stability, low risk of infection, and natural antithrombogenic properties of the intima (innermost endothelial cell layer of the blood vessel in contact with blood). Unfortunately, many patients have limited autologous veins due to pre-existing diseases, damage, etc., making the use of polymeric vascular prosthesis the best route of treatment.

The poor long-term patency rates for smaller vascular grafts is due to intimal hyperplasia at the anastomotic site (surgical connection between two structures).<sup>93-95</sup> Although the mechanism

is not understood well, smooth muscle cells tend to migrate and proliferate in these regions. In addition, polymer surfaces may be biocompatible in nature during initial blood exposure, but they turn inherently thrombogenic in the long-term. Methods to improve PTFE biocompatibility has included modifying the PTFE surface through O<sub>2</sub> plasma, creating different surface hydrophobicity depending on the etching power.<sup>96</sup> Another strategy has been to modify the PTFE surface through CO<sub>2</sub> plasma initiated grafting polymerization of acrylic acid, which was further modified with human thrombomodulin, a glycoprotein that is a direct anticoagulant that tightly binds to thrombin, preventing Fib to form a clot.<sup>97</sup>

One of the more recent strategies to improve the patency rate of polymeric vascular grafts has been to seed the inner polymeric surface with endothelial cells.<sup>98-99</sup> Since the endothelial cells are the innermost cell lining in a natural blood vessel, this would be best case scenario for a synthetic vascular graft. However, the rapid loss of endothelial cells due to the exposure to sheer stress *in vitro*<sup>100</sup> or *in vivo* due to a loss in cellular mitogenic proliferation.<sup>101</sup>

It was shown that a-C coatings could be deposited onto polymer surfaces by plasma deposition methods.<sup>102</sup> Today, there are many commercial companies that specialize in a-C coating on polymer surfaces for many different applications, including biomedical materials. Some have attempted to coat PTFE and other polymers with amorphous carbon layers.<sup>103-109</sup> New plasma-assisted deposition designs have been applied to directly deposit a-C layers within the inner wall of a synthetic vascular graft using a cylindrical electrode.<sup>110</sup> Recently, the inner wall of a 4 mm expanded-PTFE vascular graft was successfully coated with an a-C:H layer.<sup>111</sup> The vascular graft was implanted into a carotid artery of a beagle and evaluated after 8 weeks. The pathology analysis of the vascular grafts showed that the a-C:H coated graft had a more uniform and thinner vascular intima compared to an inconsistent intimal thickening observed for the uncoated expanded-PTFE vascular graft.

One of the concerns during amorphous carbon deposition is the compressive stress that can form within films, especially tetrahedral amorphous carbon films, which can lead to films buckling under stress or even delamination from the substrate.<sup>16</sup> Reducing the compressive stress within films can usually be achieved by increasing the deposition temperature or using lower energy deposition methods. In addition, doping a-C films with nitrogen has also been shown to relieve internal stress within the films,<sup>38</sup> making it a potential candidate to coat soft biomaterials.

### 2.1.3. Nitrogen-Doped Amorphous Carbon Biocompatibility

There have been no commercial hemocompatible biomedical devices on the market containing a-C:N coatings. However, there has been many *in vitro* studies investigating the influence of nitrogen incorporation into the a-C matrix and its influence on cell adhesion and overall hemocompatibility. There have been several reviews on biocompatible characterizations of a-C:N coatings.<sup>40, 53, 112</sup> The biocompatibility and hemocompatibility properties were generally assessed by endothelial cell attachment, and platelet adhesion/activation. Other hemocompatibility studies have been assessed by serum protein adsorption and will be discussed in Section 2.4.

The attachment of human endothelial cells has been evaluated for different types of nitrogen-doped a-C prepared by different plasma deposition methods. Hydrogen-free a-C:N prepared by magnetron sputtering using different N<sub>2</sub> partial pressures (5% N<sub>2</sub>/Ar and 25% N<sub>2</sub>/Ar corresponding to 8.8 at.% N and 14.9 at.% N, respectively) and evaluated for human endothelial cells and mouse fibroblast attachment.<sup>50</sup> The resulting coatings were very smooth and possessed a very low coefficient of friction. They observed that the mouse fibroblast cells showed much better cell filopodia for the a-C:N coating containing the higher nitrogen content. In addition, both coatings showed long filopodia extending from the endothelial cell bodies, indicating good adhesion and stability on the a-CN<sub>x</sub> coating.

The biocompatible properties of a-C:H coating and hydrogenated amorphous carbon nitride (a-C:N:H) were evaluated *in vitro*.<sup>113</sup> The incorporation of nitrogen (12.7 at.% N) into the a-C:H matrix increased the surface roughness and hydrophilic character of the surface. Human micro-vascular endothelial cells were incubated on the coatings and both films showed well-polymerized actin skeleton and vinculin adhesion complexes. There were no morphological differences for the coatings, although there seemed to be a higher cell density on the a-C:N:H coating. The a-C:N:H coating also had approximately half the number of adhered platelets compared to the a-C:H coating, but the percentage of inactivated platelets were higher for the carbon coatings. The author's concluded that the biocompatible properties improved with the nitrogen incorporation, and it was a factor of surface composition, wettability, and surface roughness.

There have been several studies investigating the hemocompatibility properties of nitrogen-doped amorphous carbon. Kwok et al.<sup>41</sup> implanted nitrogen into hydrogen free a-C coatings by plasma immersion ion implantation. They found that the incorporation of some

nitrogen into the a-C coating increased the hydrophilicity of the coating surface, and this also correlated with a decrease in the adherent platelet activation compared to LTIC. However, higher amounts of nitrogen-doping turned the coating's surface more hydrophobic, and the resulting adherent platelet activation was 4 times higher compared to the LTIC.

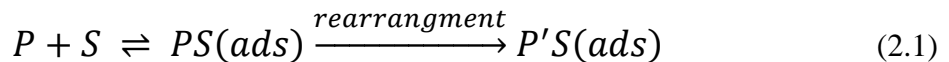
Nitrogen-doped a-C coatings deposited onto PTFE substrates were previously made using a hot-filament plasma deposition chamber in the Plasma Physics Laboratory at the University of Saskatchewan.<sup>114</sup> Initial studies showed that the nitrogen content was uniform throughout the deposited film, and the oxygen content was higher near the surface.<sup>103</sup> Synchrotron-based X-ray Absorption Near Edge Spectroscopy (XANES) analysis of the C1s found that the coatings contained high amounts of %sp<sup>2</sup>, and increased with the incorporation of nitrogen.<sup>104-105</sup> Interestingly, the %sp<sup>2</sup> content for the coatings prepared on PTFE was much lower than the Si substrate (74% sp<sup>2</sup> vs 88% sp<sup>2</sup>, respectively) for 0% N<sub>2</sub> plasma discharge gas. However, the %sp<sup>2</sup> were comparable when the %N<sub>2</sub> gas increased (3-20% N<sub>2</sub> plasma discharge gas). The biocompatibility of the coatings prepared on PTFE prepared by different N<sub>2</sub>/Ar plasma discharge gas ratios were evaluated by platelet adhesion/activation and endothelial cell adhesion.<sup>114</sup> In general, radio-labelled platelets displayed a much lower radioactive signal for the a-C coatings compared to the PTFE substrate, suggesting an overall lower number of platelets adsorbed on the a-C coatings. In addition, it was observed that the overall adhered platelets (> 80%) were in an inactivated form for the films prepared with less than 10% N<sub>2</sub> discharge gas. However, coatings prepared with ≥10% N<sub>2</sub> discharge gas showed less inactivated platelets (<65%), and the amount of spread/pseudo-spread platelet increased to the point where it was larger than the PTFE substrate for the coating prepared with 20% N<sub>2</sub> plasma discharge gas.

a-C:N:H films were deposited onto PTFE substrates using an ion-beam beam deposition technique.<sup>106, 115</sup> Raman measurements showed differences in the coatings prepared on PTFE and Si substrate. The wettability of the a-C:H film was also very hydrophobic (contact angle of 130° for water) compared to the substrate (89° for PTFE). The incorporation of 10 at.% N into the a-C:H film decreased the contact angle to 111°, which was still higher hydrophobicity compared to the PTFE substrate. The radio-labelled platelet adhesion studies found that both the a-C:H and nitrogen-doped a-C:H coatings had more platelets adhered to the surface compared to the PTFE substrate. However, the authors indicated that there were less activated platelets on the a-C:H and a-C:H:N films compared the PTFE substrate (no statistical analysis completed).

Hydrogen-free a-C:N was deposited onto PTFE substrates using inductively coupled plasma deposition.<sup>108-109</sup> Interestingly, x-ray photoelectron spectroscopy (XPS) measurements showed a high at.% O on the coating surface (42 at.% O) for 0% N<sub>2</sub> plasma discharge gas and then drops with the addition of N<sub>2</sub> in the plasma discharge gas (approximately 25 at.% O). At the same time, the at.% N increased from 5 to 35 at.% N in the films prepared from nitrogen-free plasma discharge gas to 10-40% N<sub>2</sub> plasma discharge gas. The XANES measurements for the coatings also found that the %sp<sup>2</sup> fraction initially decreased from 92% to 81% with the addition of N<sub>2</sub> plasma discharge. However, higher %N<sub>2</sub> plasma discharge gas (>20% N<sub>2</sub>) increased the %sp<sup>2</sup> to 91-94%, indicating a sensitivity to the compositional structure of the coatings with the N<sub>2</sub>/Ar plasma discharge gas ratio. Biocompatible studies showed that the a-C:N coatings had more cytotoxic response compared to the PTFE, and there was no apparent difference in blood clotting time between the a-C:N coatings and the PTFE substrate. The number of platelets adhered to the 0%N<sub>2</sub> a-C:N coating was approximately 2X lower compared to the PTFE substrate, and the a-C:N coatings prepared from 10-20% N<sub>2</sub> plasma discharge gas was approximately 3-4X lower compared to the PTFE control sample. However, a-C:N coatings prepared from 30-40% N<sub>2</sub> plasma discharge gas had approximately 2X more platelets adhered compared to the PTFE control. It was concluded that the sp<sup>2</sup> and sp<sup>3</sup> content within the film as well as the %N<sub>2</sub> plasma discharge gas value used during the coating deposition may play a role in the hemocompatibility properties of the a-C:N coating.

## 2.2. Protein Adsorption at Biomaterial Interface

The adsorption of proteins at the interface has been a very active field for many years. Despite the advances in the research over the years, the exact process/mechanism is still not completely understood, especially when it comes to blood-surface interactions and hemocompatibility. In general, proteins-surface interactions have a two-step process outlined in Equation 2.1:



where the protein (P) interacts with the surface (S). This interaction is very fast and spontaneous. The second reaction involves a protein “relaxation” event where it undergoes a conformational rearrangement and will spread itself onto the interface. At this point, the adsorbed protein forms a very strong binding complex with the surface (P’S), and it is essentially irreversible.

Protein adsorption is for the most part an entropy driven process at the surface interface, with the main contributions coming from a combination of electrostatic, dispersion and hydrophobic forces.<sup>56, 116-117</sup> Electrostatic forces will occur between positive and/or negative charged amino acid side-chains on the surface of the protein with oppositely charged surface charges. They are most effective within the so-called Debye length which is dependent on the ionic strength of solution (ex. 3 nm in a 10mM ionic strength solution). Dispersion forces are the weakest intermolecular force, and although they are present in protein surface interactions, their overall contribution is small.

The hydration or water layer plays a significant role for hydrophobic interactions between the protein and surface. A water layer will exist on both the protein surface and the interface, and the hydrophilic/hydrophobic character will influence the strength of this hydration layer. For example, if both the protein and surface are polar, it is likely that some water molecules will remain in contact after adsorption (lower entropy gain). In the other hand, protein adsorption is highly favored when both the protein and surface are hydrophobic due to the removal of the adjacent water layer (high gain in entropy). Given that the Gibbs energy of dehydration of one alkyl group is approximately the same as the Gibbs energy of adsorption of one monovalent ion at the surface, the hydrophobic interaction will override electrostatic energy barrier and protein adsorption may occur.<sup>56</sup>

The interior of a protein contains ordered secondary structures ( $\alpha$ -helix,  $\beta$ -sheet) linked though extended hydrogen bonding from the more hydrophobic amino acid side chains, whereas the surface of the protein may contain more hydrophilic amino acid side chains. After the initial contact on the surface, the protein may undergo a structural rearrangement protein that effectively shields a portion of the protein surface from the aqueous solution and exposes hydrophobic portions near the protein surface without complete unfolding and exposing the hydrophobic residues from interior of the protein. In the event that that structural rearrangement causes changes that reduce or destabilize the interior secondary structure of the protein which results in hydrogen bonding with the surface, this would imply a higher conformational energy and would favor adsorption.<sup>56</sup>

In general, interfaces cannot easily resist protein adsorption. For a hydrophobic surface, the adsorption of any type of protein is very likely due to the loss of a water layer at the interface which outweighs the contributions from electrostatic repulsion. Conversely, hydrophilic surfaces

may facilitate protein adsorption by electrostatic interactions and/or protein structural changes.<sup>56</sup> Other factors that drive protein adsorption at an interface can be summarized into the following categories: (1) Protein properties (size, shape, surface charge, aggregation, etc.); (2) surface properties (topography, tomography, surface charge, surface composition, etc.); (3) environmental factors (solution composition, pH, temperature, ionic conductivity, salt composition, etc.).

### **2.2.1. The Role of Protein Properties**

Proteins are complex polymers composed of a polyamide backbone and a combination of 20 different amino acid side chains. These side chains are a combination of cationic, anionic, and uncharged groups. Depending on the sequence of amino acids, the polypeptide forms a secondary structure ( $\alpha$ -helix,  $\beta$ -sheets,  $\beta$ -turns, etc.) which are arranged to form the tertiary structure of the protein. Some proteins may contain multiple domains (individual units composed of a tertiary structure) and this is referred to as its quaternary structure.

For proteins in aqueous media such as plasma serum, proteins are folded such that the hydrophobic side chains are found in the interior of the protein, shielding these apolar moieties from water. The surface of the proteins will contain the cationic and anionic side chains to interact with the aqueous media. These surface charges located on the protein surface can electrostatically interact with opposite charges located at the surface interface.

The protein size and its shape contribute to its adsorption behaviour. Proteins have been defined as to being “hard” or “soft” structures.<sup>58</sup> A “hard” protein has a strong internal cohesion that would permit limited structural changes upon surface adsorption, whereas a “soft” protein has weaker internal cohesion that makes it more structurally labile and open towards surface-induced structural changes. For example, lysozyme (MW 14 kDa) is a small protein which appears to have a prolate ellipsoid shape, is generally considered a “hard” protein due to its structural rigidity upon surface adsorption. Intermediately sized proteins, such as those found in blood plasma, generally have the structural flexibility that would allow surface-induced structural changes. In addition, the function of the protein may also provide insight into its adsorption behaviour. For example, lipoproteins would be attracted to hydrophobic surfaces and adsorb quite favorably onto the surface, whereas glycoprotein adsorption onto a hydrophobic surface would be inhibited due to the presence of hydrophilic glycans.

### 2.2.2. Role of Surface Properties

The protein-surface interaction will be influenced by the surface properties of the biomaterial. There are many surface parameters including the wettability, surface energy, chemical composition, charge, polarity, and morphology.<sup>117-118</sup> In general, the affinity of proteins towards hydrophobic surfaces (surfaces that do not have an extended water layer) is much larger compared to hydrophilic surfaces (surfaces that can promote water binding through hydrogen bonding). This trend was confirmed by observing higher protein adsorption onto hydrophobic portions of a hydrophobic gradient surface.<sup>119</sup> The surface composition at the interface will also contribute to the wettability property of the surface. It is generally known that surface oxides will exist on metallic surfaces under normal conditions. Oxygen functional groups or other types of functional groups (depending on the material) are generally present at the surface. The presence of surface hydroxyl groups can promote hydrogen binding with water and improve the hydrophilic properties of a surface. Similarly, carboxyl or amino functional groups can contribute to the surface charge depending on the solution pH.

The effect of nanoscale surface topographical features has been recognized to play an effect over micron scale surface topography.<sup>120-121</sup> Rechendorff *et al.* used quartz crystal microbalance measurements to study Fib and HSA adsorption onto Ta thin films with varying surface roughness in the 2-33 nm range. They found that Fib adsorption increased as much as 70% with the increase in surface roughness and was much larger than the increase in surface area (20%). In contrast, the bovine serum albumin (BSA) adsorption increased proportional to the increase in surface area. Lord *et al.* measured Fib and fibronectin adsorption onto substrates treated with different sizes of colloidal silica and variable surface roughness.<sup>122</sup> There was no significant difference in Fib and fibronectin adsorption onto the different colloidal silica samples. However, they did find that the colloidal silica treated surfaces reduced endothelial cell attachment, suggesting a conformational change of the fibronectin layer and burying the arginine-glycine-aspartic acid (RDG) tag within the protein film.

Protein adsorption and cell adhesion has been improved for some biomaterials by using nanopatterning techniques.<sup>123-124</sup> Sommerfeld *et al.* created periodic ripples on Si and TiO<sub>2</sub> surfaces by Xe ion irradiation.<sup>125</sup> Fib was found to adsorb onto the surfaces (untreated and irradiated) in a globular form, with no aggregation or extended protein networks observed. The addition of ripples with varying periodicity showed changes in Fib adsorption behavior, where

nanopatterned TiO<sub>2</sub> surfaces with periodicity (<50 nm) showed no apparent Fib adsorption. Protein adsorption has also been studied on a-C:H surfaces that were nanopatterned using focused ion beam milling, and nanoindentation.<sup>123</sup> The a-C:H surfaces had similar nanoscale topography, but different local composition. In general, both Fib and BSA adsorbed differently onto a-C:H, with Fib adsorbing in a rougher and denser layer. BSA-coated AFM tips were used to measure local binding adhesion and found that the focused ion beam nanopatterns showed a significantly larger adhesion force compared to unpatterned surfaces.

### **2.2.3. Environmental Roles**

The major environmental parameters that can influence protein adsorption include temperature, pH, ionic composition, and salt concentration. It is obvious that using standard physiological buffers such as phosphate-buffered saline (PBS) at a constant pH and temperature can minimize the influence of environmental parameters towards protein adsorption. Temperature will influence the adsorption rates of a protein as an increase in temperature will increase kinetic rates. Elevated temperatures will also increase the diffusivity of proteins in solution (diffusion coefficients are proportional to temperature). The pH of the solution will determine the protein's electrostatic state. The amino acid side chains on the surface of protein will contribute to the protein's overall positive/negative charge at a given pH. The isoelectric point (pI) is the pH at which the protein has net neutral charge (number of positive charges equals number of negative charges). In addition, the electrostatic repulsion between protein-protein interactions are minimized at the pI. This can allow increased packing densities at the surface. Adsorption rates are increased with the protein and surface when there is an electrostatic attraction between the protein and surface. The ionic strength of the buffer solution and it plays a significant role in the double layer present at surfaces (both proteins and surface). The Debye length is characteristic of the double layer thickness and increasing the number of ions in solution will compress the double layer and increase the electrical potential gradient. The salt concentration and type of salts present in a buffer solution will also influence protein adsorption. It is well known in biochemical methods that increasing the concentration of kosmotropic (strongly hydrated) ions can accelerate protein precipitation (SO<sub>4</sub><sup>2-</sup>, Ca<sup>2+</sup>, Mg<sup>2+</sup>, etc.), whereas other chaotropic (weakly hydrated) ions will decelerate protein precipitation (ClO<sub>4</sub><sup>-</sup>, NH<sub>4</sub><sup>+</sup>, etc.).

#### 2.2.4. Transient Adsorption Model

The affinity of single protein adsorption has been generally presented as adsorption isotherms, where a protein adsorbed vs. protein concentration is plotted, yielding an “apparent” protein adsorption affinity. Protein adsorption isotherms tend to show a “high affinity” type in which a steep initial rise in adsorption is observed and a strong resistance to desorption is observed. It would be assumed that the isotherm would not follow the Langmuir type isotherm because this model assumes a fully reversible reaction, no lateral interactions, and the surface attachment is site-determined. However, in some cases such as globular albumin proteins show defined saturation points indicating a closed packed monolayer of protein which suggests a Langmuir type isotherm. In order to account for these types of interactions, it is important to note that the evolution of the protein’s final state on the surface depends on some preceding events.

There have been different models developed for the kinetics and dynamics of protein adsorption and have been summarized by Norde *et al.*<sup>56</sup> The common theme for the different models has been accounting for the generally observed partial irreversibility of the protein adsorption process and/or deceleration of adsorption with increasing coverage of the surface.<sup>56</sup> The most successful (and least popular) description of protein adsorption has been the random sequential adsorption model, or slight modifications of it.<sup>126</sup>

Protein adsorption at the interface appears to be an overall irreversible reaction over longer time scales, but the evolution of the adsorbed protein’s final state depends on some preceding events. This was investigated by the Norde research group and outlined in Figure 2.1.<sup>58, 127</sup> In general, a dynamic equilibrium will be established between the proteins in its native state ( $P_N$ ) in both solution and adsorbed at the surface. This equilibrium was observed for Fib adsorption onto polymer surfaces where different desorption rates were observed suggesting three populations of a non-exchanging, fast exchanging, and slow exchanging processes occurring simultaneously.<sup>128-</sup><sup>129</sup> Single molecule fluorescence spectroscopy measurements for BSA adsorption onto fused silica revealed that the majority of BSA did not adsorb onto the surface, and desorb within minutes.<sup>130</sup> However, a small fraction (<1%) of BSA adsorbed quite strongly over time, indicating some type of protein solution heterogeneity.

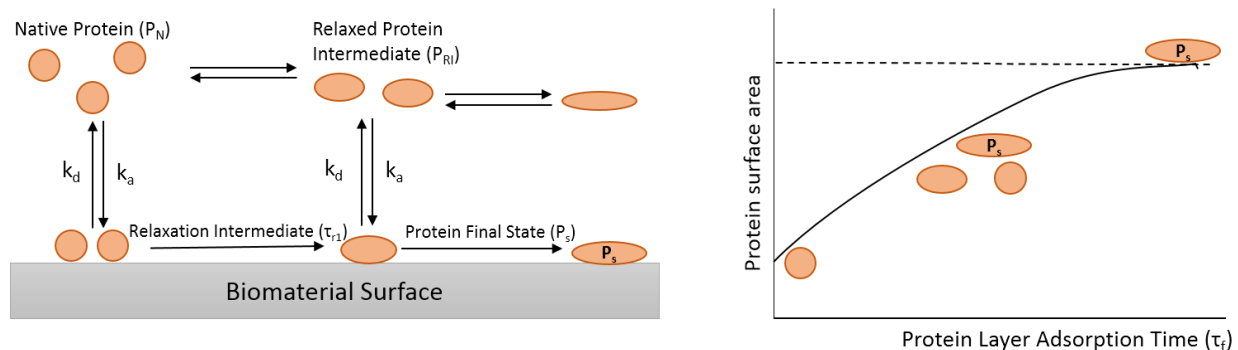


**Figure 2.1.** Schematic of protein adsorption that may occur at various stages. Native protein ( $P_N$ ) adsorb onto the surface. If given enough time ( $\tau_{r1}$ ), the adsorbed protein may structurally relax. This relaxed protein intermediate ( $P_{RI}$ ) may desorb and set up an equilibrium with solution interface. If the adsorbed  $P_{RI}$  is given enough time, it may structurally relax to the protein's final relaxed state ( $P_S$ ).

The overall time needed to fill the protein layer,  $\tau_f$ , will be controlled by the flux of proteins that arrive at the surface and are able to deposit. This  $\tau_f$  is inversely proportional to the protein concentration and linearly proportional to the resistance for a protein to reach the surface. If given enough time and enough space, the  $P_N$  can structurally perturb to a relaxed intermediate ( $P_{RI}$ ). The time needed for a protein to convert into its relaxed form,  $\tau_{r1}$ , will be dependent on a protein's resistance against deformation – the so-called hard and soft proteins. This value is also highly dependent by the interfacial tension where surfaces having higher interfacial surface tension (hydrophobic surfaces) has a higher tendency to spread.

The  $P_{RI}$  also has a potential for the altered protein to desorb back into solution setting up a dynamic equilibrium. Circular dichroism and differential scanning calorimetry measurements found that BSA released from a hydrophobic polystyrene surface showed an increase in  $\beta$ -sheet structure at the expense of  $\alpha$ -helix.<sup>131</sup> This new structure was found to be more stable than the  $P_N$ , and even more pronounced when pre-adsorbed BSA had undergone more spreading at the surface. Similar results were found for BSA on a hydrophobic PTFE surface.<sup>127</sup> On the other hand, it was found that although BSA had a secondary structure changes upon binding to a hydrophilic silica surface, the BSA reverted back to its native secondary structure when exchanged in solution.<sup>131</sup> In addition, lysozyme tends to regain its native secondary structure regardless of the surface hydrophobicity.<sup>127</sup>

Figure 2.1 shows that the average protein surface area will linearly increase as  $\tau_f$  progresses. The protein film will initially resemble  $P_N$  at low  $\tau_f$ . The biological activity of the protein film will be higher when more  $P_N$  proteins are adsorbed and may be achieved by increasing

the solution concentration of  $P_N$ . As  $\tau_f$  progresses, the surface heterogeneity will be a mixture of  $P_N$  and  $P_{RI/PS}$ . This portion of the interaction is often referred to as the surface jamming, and it eventually plateaus as the fully spread final state ( $P_S$ ) is achieved and the major population on the surface. Proteins arriving late to the pre-adsorbed protein layer may still deposit in interstitial sites which may be still open due to pre-adsorbed protein in their PS conformation. These late arriving proteins may have the highest biological activity.<sup>56</sup>

### **2.2.5. Multi-protein Adsorption**

Biomaterials will encounter multi-protein adsorption upon exposure to biological fluids. For instance, blood has been estimated to contain hundreds of proteins, lipoproteins, lipids, ions, and other species. For a given protein layer that adsorbs to the biomaterial surface, the exact composition of proteins on a given surface is still not exactly known, though partial profiles have been compiled using mass spectrometry and gel electrophoresis methods.<sup>132-134</sup> It is generally believed that limiting the amount of proteins involved in the thrombus cascade (Fib, fibronectin, vitronectin, and von Willebrand factor) will reduce platelet adhesion and improve hemocompatibility of the biomaterial.

One early feature that was observed from analyzing the multi-protein adsorption from blood onto a surface was that initial protein adsorption was dominated by higher mobility proteins. These proteins may be of higher concentration in serum but have a lower affinity towards the surface. After a given amount of time, these lower affinity proteins are replaced by larger, less mobile proteins that have low concentration in serum, but have a higher affinity towards the surface. This is known as the Vroman effect, and it was first observed when adsorbed Fib was replaced by the larger plasminogen protein.<sup>6</sup> This transient adsorption phenomena was found to be diffusion limited, and it was also observed that pre-adsorbed Fib was found to have dissociation rates that were considerably slower compared to Fib that was adsorbed *in situ* during blood plasma exposure.<sup>135</sup>

More recently, it was suggested that an initial protein layer may interact with a second protein layer that forms and/or embeds onto the initial protein layer.<sup>136</sup> This interaction may involve several proteins that form a complex or multiprotein aggregate with the initial protein layer, causing it to structurally turn. This subsequently exposes the initial protein layer to the solution phase, resulting in protein desorption from the surface.

### 2.3. Protein Layer Mediates Cell Adhesion

The initial adsorbed protein layer plays a significant role in cell adhesion. After the protein layer has been established, it then directs the subsequent cellular response, particularly platelet adhesion and activation in blood.<sup>137-138</sup> It is believed that some proteins within the adsorbed protein layer are unfavorable due to their involvement in the thrombus cycle. These proteins, commonly referred to as the “adhesion” proteins include Fib, fibronectin, vitronectin, and von Willebrand’s factor. These proteins which contain the specific RGD amino acid sequence are specifically bound by integrin receptors on the surface of cells. These sequences are eventually exposed on the adsorbed protein film’s surface allowing platelets and other cells containing integrin receptors contact points to bind to a surface.

Fib adsorption to the biomaterial surface is the typical protein used to assess the hemocompatible properties of a biomaterial surface. Since Fib helps mediate platelet adhesion, it would be logical to assume that platelet adhesion and the amount of Fib adsorbed on surface would be well correlated. However, it was recently found that there was a strong correlation with platelet adhesion and the conformational change in adsorbed Fib.<sup>139</sup> In the same study, they found essentially no correlation with the amount of surface adsorbed Fib and platelet adhesion. In another study, Zhang *et al.* found that Fib bound to both hydrophilic and hydrophobic polymeric surfaces.<sup>140</sup> However, the hydrophobic surfaces were found to induce Fib to form fibers, and these fibers were found to induce platelet adhesion and possible aggregation in isolated areas. In the absence of Fib fibers, the platelets would bind uniformly across the surface. It was also reported that platelets adsorb to a HSA protein layer, but only under special circumstances.<sup>141-142</sup> The interaction was found to occur only when the adsorbed HSA had lost at least 34% of its  $\alpha$ -helix structure, and when HSA concentrations were less than 10 mg mL<sup>-1</sup>. This is well below *in vivo* concentrations.

An opposite research strategy has been to promote cellular interactions with the biomaterial surface, as it is known that the vascular endothelium is the only known surface that is truly blood compatible. The endothelium consists of an integrated layer of endothelium cells that are attached to a membrane. The properties of these cells provide the function of this layer, which includes regulation of inflammation, thrombosis and fibrinolysis. Therefore, enhancing the growth and migration of an endothelial layer onto a vascular graft for example could extend its patency rate.

## 2.4. Protein/Amorphous Carbon Interactions

The first investigations into protein adsorption from blood plasma was first investigated on LTIC.<sup>134, 143-146</sup> Interestingly, LTIC has properties that are opposite of commonly accepted blood compatibility properties. LTIC has a hydrophobic surface, it is hard (high modulus) and has a relatively high surface energy. It is also electrically conductive, and it has a positive resting potential (vs NHE). Feng et al. proposed that its biocompatible properties was due to an inactive adsorbed protein layer.

The plasma protein adsorption was studied from LTIC properties. For example, the changes in the double-layer capacitance for the LTIC found that proteins adsorbed on more negatively charged surface at near neutral or acidic solution, independent of the charge on the proteins for a given pH, and variation of the ionic strength did not alter this trend.<sup>144</sup> They observed that the electrostatic interaction between the protein and surface was not a major significant force in the protein-LTIC interaction, but rather hypothesized that the hydrophobic interactions played a more critical role and considered it an importance to consider the competitive competition of proteins and water for surface sites.

Radioactively labelling both HSA and Fib was done to study the protein adsorption onto LTIC.<sup>145</sup> The HSA and Fib adsorption saturated to approximately  $5.8 \text{ mg m}^{-2}$  and  $23 \text{ mg m}^{-2}$  surface concentrations, respectively. They also found that a pre-adsorbed HSA layer on the LTIC suppressed both HSA and Fib adsorption by 77% and 23%, respectively after 60 min post-adsorption. However, a more compact layer of HSA using a higher protein concentration was able to reduce the Fib binding by 80%, likely due to fewer voids in the HSA protein layer. A comparison of single protein adsorption versus diluted plasma also found that competitive protein adsorption takes place, and the HSA surface concentration reduced by approximately 55%. Since HSA accounts for approximately 50% of the total mass of plasma proteins, it suggests that there is no preferential adsorption on LTIC. The Fib surface concentration reduced by approximately 35% from single protein to diluted plasma adsorption, which was still rather significant given that Fib constitutes about 3% of total plasma proteins. It was suggested that the Fib may adsorb onto the HSA layer rather than LTIC surface. Using a constant binary mixture of HSA and Fib, proportional amounts of proteins on the surface were found, suggesting the absence of preferential adsorption on LTIC. The reversibility of the protein adsorption was also completed in this study. They found that there was very little protein eluted off the surface and less than 10% of the adsorbed protein

film (HSA, Fib, or diluted plasma) eluted off the LTIC surface. It was found that less than 2 minutes was enough to stabilize the adsorbed protein. On the other hand, post-adsorbed proteins needed much more time to strengthen their adsorption to a protein surface or finding small voids in the initial protein film.

The adsorption of HSA and Fib onto a-C coatings was investigated with spectroscopic ellipsometry and atomic force microscopy (AFM) techniques.<sup>147-150</sup> A series of a-C and a-C:H coatings were prepared with floating and negative biased magnetron sputtering. The spectroscopic ellipsometry measurements of the a-C coatings were determined and differences between the ellipsometry spectra for adsorbed HSA and Fib contained information regarding the amount and density of the adsorbed protein layers. Based on these differences, an HSA/Fib ratio was generated and the hemocompatible properties were concluded from this ratio. The highest HSA/Fib ratio was found on coatings prepared under floating bias conditions, which also produced rougher protein surface layers as measured by AFM. It was also observed that the protein layer thickness for both HSA and Fib showed variations in the protein layer thickness, though samples were incubated for a period, rinsed and dried with N<sub>2</sub>. The authors did not comment on any effects this may have played with the protein layer measurements.

Ellipsometry measurements were also used to investigate HSA and plasma adsorption onto different types of a-C and a-C:N coatings prepared from magnetron sputtering.<sup>151-152</sup> These films included a-C, a-C:N, FL-CN<sub>x</sub>, and graphitic carbon nitride coatings. The ellipsometry measurements showed different surface concentrations and thickness of the adsorbed HSA film for the different films. The lower surface mass density was correlated with samples that had larger surface roughness values. However, radioactive labelled HSA measurements done on the same samples found that the surface coverage of adsorbed HSA were very similar. The elutability of the adsorbed HSA layer was also very low for all samples, with approximately 60-80% of the original HSA remaining on the surface.

The hemocompatibility suitability of boron carbonitride films were investigated using different amounts of nitrogen in the films and compared to a-C:H films and stainless steel.<sup>32</sup> The incorporation of nitrogen into the boron carbon coatings increased the crystallinity of the films. The boron carbonitride films showed a decrease in HSA and Fib adsorption compared to a stainless steel reference, as well as a-C:H films, but Fib preferentially adsorbed to all surfaces compared to HSA. This study did not demonstrate that the HSA and Fib adsorption was independent of surface

energy of the films. It was also determined that the higher Fib:HSA ratio resulted in a higher blood platelet adherence compared to stainless steel. However, it seems as though a higher amount of adsorbed Fib did not necessarily correlate with a higher blood platelet adherence.

Kwok et al.<sup>41</sup> investigated the hemocompatibility properties of hydrogen free a-C coatings prepared by different N<sub>2</sub>/Ar plasma discharge gas ratios. This study showed that nitrogen incorporation improved the hemocompatibility properties of the coating compared to LTIC, but excess nitrogen within the coating degraded the blood compatibility. The interfacial energies for adsorbed HSA and Fib films were lower for coatings that showed less platelet activation. In addition, the ratio of the polar and dispersive components of surface tension was also lower for the samples showing better hemocompatibility. It was suggested that protein adhesion was strong when both the polar and dispersive components of surface adhesion showed similar contributions. The polar to dispersion component ratio for Fib was approximately 5-7 times lower compared to the values for HSA, suggesting Fib has much stronger surface adhesion compared to HSA.

## **2.5. Initial Surface/Protein Interactions Measured by SPR**

SPR has been a technique used to study protein interactions with different surface chemistries prepared from self-assembled monolayers.<sup>153-155</sup> SPR uses a Au sensor surface and alkylthiolates containing different functional end groups (-CH<sub>3</sub>, -NH<sub>2</sub>, -COOH, -OH, etc.) provide a means to study the surface chemistry effects on protein adsorption. The different functional end groups could be correlated with the surface wettability (ie. interfacial surface energy). In general, large proteins such as Fib and  $\gamma$ -globulins were not selective and adsorbed to surfaces with different surface energies. Small proteins such as RNase and lysozyme showed selectivity. BSA showed sensitivity towards the different surface chemistries that was intermediate between the large proteins and the small proteins. The adsorbed protein surfaces were kinetically stable, and it was observed that within 1 hour, less than 5% of protein desorbed from the surface. The wettability of the surfaces appeared to have no influence over the stability of the films once they were formed. However, the addition of sodium dodecyl sulfate (SDS) in concentrations above its critical micelle concentration (1mM) was effective in desorbing the majority (>90%) within a 1 min exposure.

Carbon based films have been successfully deposited onto metal films. For instance, a-C films were deposited onto Au films, hydrogen plasma annealed, and chemically modified to successfully immobilize nucleotides for DNA array technology.<sup>156</sup> The thickness of the a-C film was found to play a role in the SPR surface sensitivity, where increasing a-C film thickness

broadens the SPR curve as well as decreases in the photon-plasmon coupling efficiency play a role.

Home-built SPR instruments have also been used to report different types and compositions of a-C coatings on Au substrates.<sup>157-158</sup> The a-C:H coatings were prepared on Au-substrates using rf-sputtering of a graphite target. The reflectance at different angles using a 635 nm laser diode, and the reflectivity minimum shifted to higher incidence angles, indicating protein adsorption. One major issue with using a coherent light source is the production of localized electromagnetic field enhancement “hot spots” on the SPR active Au film that may occur if Au nanoparticles of certain size and shape may be present during Au film formation.<sup>159</sup> In addition, the home-built SPR system was limited to measuring changes in the SPR angle shifts upon HSA, Fib, and lysozyme adsorption, and only positive/negative (yes/no) signal confirmation was obtained for protein adsorption on the different a-C surfaces.

Commercially available SPR instruments offer an advantage for the following reasons: (1) SPR sensor chips are manufactured of high quality and consistency (2) the liquid delivery systems are generally micro-fluidics with high specifications regarding the rise-time and fall time during a liquid injection and (3) data acquisition is high quality. An SPR instrument manufactured by Biacore (Uppsala, Sweden) was used to measure the adsorption of blood plasma proteins onto a Au sensor chip coated with a “nanocrystalline diamond” surface.<sup>160</sup> However, the Raman spectrum indicated an a-C like film structure. The preliminary results showed that a small amount of protein plasma adsorbed to the a-C coating (<100RU) and there was no noticeable adsorption difference compared to the bare Au sensor surface. However, an injection of anti-Fib was followed up after the plasma protein adsorption and there was a smaller response on the a-C compared to the Au surface. This indicated that the Fib adsorption on the a-C coating was less compared to the bare Au. These results demonstrated that commercial SPR instrument were useful for protein adsorption measurements on different surfaces.

Commercial SPR instruments have been used to study the adsorption kinetics of amino acid interactions with molecularly imprinted polymer films.<sup>161</sup> Quantitative kinetic values were extracted from the resulting sensorgrams by fitting the data to a 1:1 Langmuir binding model, where biomolecule (P) binds to single and independent site (S):



The net rate expression can be expressed by Equation 2.3:

$$\frac{d[PS]}{dt} = k_a[P][S] - k_d[PS] \quad (2.3)$$

where  $k_a$  is the association rate,  $k_d$  is the dissociation rate, and  $[P]$ ,  $[S]$ , and  $[PS]$  are the concentrations of the biomolecule, surface binding site, and biomolecule-surface complex, respectively. The integrated forms of the association and dissociation equations can be expressed by the forms of Equation 2.4 and Equation 2.5, respectively:

$$R = \frac{[P]k_a R_{max} [1 - e^{-(k_a + k_d)t}]}{[P]k_a + k_d} \quad (2.4)$$

$$R = R_{max} e^{-k_d(t-t_0)} \quad (2.5)$$

where  $R$  is the surface uptake response, and  $R_{max}$  is the maximum equilibrium capacity. However, the curve fitting to this model showed high  $\chi^2$  or goodness-to-fit ( $\chi^2$ ) values. The sensorgram data was further modelled using a dual-site Langmuir model that offered 2 binding sites on the surface. This dual-site Langmuir model allows for 2 independent binding sites on the surface, and the sensorgram data showed lower  $\chi^2$  values, suggesting a better fit using this model. However, it has been advisable from SPR application scientists to resist the urge to incorporate more complicated kinetic models for specific biomolecular interactions, unless of course it is known for the interaction under study.

Other protein interaction assays have studied HSA and Fib interactions to various metal oxide nanoparticles that were directly immobilized onto commercial sensor chips.<sup>162</sup> The Proteon XPR36 instrument (Biorad Laboratories Ltd) had a 6 x 6 independent flow channels that could be run in the vertical or horizontal position. The metal nanoparticles were immobilized in the vertical direction. The sensor chip was then rotated 90° and 6 concentrations of Fib or HSA could be flowed across the sensor surfaces, resulting in 36 sensorgrams in a single pass. The Fib-metal nanoparticle interactions fit well to a 1:1 Langmuir model where  $k_a$  and  $k_d$  values were approximately  $10^4$ - $10^6$  M<sup>-1</sup> s<sup>-1</sup> and  $10^{-4}$  s<sup>-1</sup>, respectively. The HSA-nanoparticle interaction was found not to fit as well to the 1:1 Langmuir model, and it was fit to a conformational change model because it was previously found that some of the metal oxide NPs induced conformational changes to HSA.<sup>163</sup> The  $k_a$  and  $k_d$  values for HSA interactions with the metal nanoparticles were in general a magnitude lower compared to the Fib values.

Both graphene and graphene oxide layers have been found to enhance the SPR signal when added to the metal sensor surface.<sup>164-166</sup> The addition of graphene oxide/Au composite was flowed onto a Au film in PBS. It was found that the wavelength shifts in the detected light were much more sensitive to protein binding. The graphene oxide/Au nanocomposite was modified with staphylococcal protein A, and its detection of different immunoglobulins was lowered by approximately 16-fold with the addition of the graphene oxide/Au composite.<sup>166</sup> In a separate study, it was found that a single layer of graphene oxide or reduced graphene oxide enhanced the SPR signal, but the addition of multiple layers reduced the SPR signal.<sup>164</sup> The deposition of single layer graphene via chemical vapor deposition showed an enhancement of the SPR signal.<sup>165</sup> In addition, non-covalent functionalization using molecules with an extended  $\pi$ -system (ex. Pyrene and its derivatives) were used to preserve the unique properties of graphene. The use of pyrene-NTA layer was further stabilized by electropolymerization of the pyrene groups. The resulting layer improved the SPR sensor response by approximately 80%. The limit of detection for anti-cholera toxin antigen detection was approximately  $4 \text{ pg mL}^{-1}$ .

Nanoplasmonic sensing has been recently used to study the protein adsorption of BSA and bovine Fib onto a-C prepared surfaces.<sup>167</sup> These measurements were conducted on a commercially available XNano instrument (Insplorion, Sweden). The sensor chips use very small Au nanodisks ( $\sim 50 \text{ nm}$ ) which incorporates localized surface plasmon resonance due to the incident light wavelength interacting with much smaller metal nanoparticles of specific sizes and shapes. Interestingly, the surface coverage of Au nanodisks is only approximately 8% of the glass sensor surface. There were no kinetic adsorption measurements from this study, but they were able to estimate surface concentrations of  $3.8 \text{ mg m}^{-2}$  for bovine Fib on both a-C and a-C:H surfaces. The BSA surface coverage for BSA was  $2.6 \text{ mg m}^{-2}$  and  $2.1 \text{ mg m}^{-2}$  for the a-C and a-C:H coatings, respectively. The differences in the BSA surface coverages was due to the differing wettability property of the coatings, where the a-C coating showed more hydrophilic surface from contact angle measurements.

## CHAPTER 3 - MATERIALS AND METHODS

### 3.1. Amorphous Carbon Film Preparation

#### 3.1.1. Metal-Containing FL-CN<sub>x</sub> Films

The FL-CN<sub>x</sub> films were prepared by Dr. M. Foursa using a home built hot-wire plasma assisted deposition chamber described previously.<sup>114</sup> Briefly, a W wire (0.3 mm) glowing white-hot (1950-2100 K) was biased to -40 V as a cathode emitting electrons. Specific mixtures of Ar and N<sub>2</sub> gases using a total gas flow rate of 25 sccm and a working pressure of 50 mTorr was used as the discharge gas. A graphite target (2.5 cm x 2.5 cm x 1 cm) biased to -250 V was used as the carbon source in the sputtering process.

The FL-CN<sub>x</sub> films were deposited onto commercially available 60 μm skived PTFE substrate (CHEMFILM®, Saint Gobain, USA). The nitrogen content in the FL-CN<sub>x</sub> films were varied by adjusting the N<sub>2</sub> flow rate using mass flow controllers in the range of 0-20% N<sub>2</sub> of the total gas flow rate. The substrate bias was -40 V, and the sample deposition time was 2 hr. The substrate temperature was approximately 195 °C ±15 °C during plasma deposition and measured by a thermocouple located on the underside of the substrate holder.

The FL-CN<sub>x</sub> sample notation is summarized in Table 3.1 for the FL-CN<sub>x</sub> films are described by the %N<sub>2</sub> partial flow rate used during film deposition, and it does not necessarily reflect or relate to the amount of nitrogen incorporated in the FL-CN<sub>x</sub> film.

**Table 3.1.** Sample notation for FL-CN<sub>x</sub> samples prepared by hot filament graphite sputtering plasma deposition.

Sample	FL-CN <sub>x</sub> -00	FL-CN <sub>x</sub> -03	FL-CN <sub>x</sub> -06	FL-CN <sub>x</sub> -10	FL-CN <sub>x</sub> -20	FL-CN <sub>x</sub> -30
N <sub>2</sub> Flow Rate (sccm)	0	0.75	1.5	2.5	5.0	7.5
Ar Flow Rate (sccm)	25	24.25	23.5	22.5	20	17.5
%N <sub>2</sub>	0	3	6	10	20	30

##### 3.1.1.1. FL-CN<sub>x</sub> Coated SPR Sensor Chips

FL-CN<sub>x</sub> films were deposited onto commercially available SPR Au sensor chips (SIA kit Au, Biacore Inc., Pitascaway, NJ). Prior to FL-CN<sub>x</sub> film deposition, the Au surfaces were cleaned in a piranha solution (3:1 H<sub>2</sub>SO<sub>4</sub>:H<sub>2</sub>O<sub>2</sub> (v/v)) for 10 min, rinsed with ultra-pure water, and

sonicated in ethanol. The nitrogen content in the FL-CN<sub>x</sub> film was varied by adjusting the N<sub>2</sub> flow rate to 0-30% N<sub>2</sub> of the total gas flow rate. The substrate bias was set at -40 V, and the sample deposition time was adjusted between 2-5 min in order to achieve similar film thickness according to the deposition rates determined previously.<sup>114</sup> The substrate temperature was 195 °C ±15 °C.

### **3.1.2. Metal-Free a-C:N Film Apparatus**

Metal free a-C:N films were prepared using a home built hot-wire plasma assisted deposition chamber shown in Figure 3.1. The chamber was constructed from pyrex, and the dimensions were minimized to a 2” diameter to minimize the volume inside the chamber (faster evacuation). The endcaps were also made of pyrex and they were connected to the main T-chamber by an o-ring flange. Each endcap had 2 glass compression feedthroughs. No grease was used on the o-rings. The metal parts inside the chamber were all composed of W, Ta, or Mo – metals with high melting temperatures and commonly used in vacuum chambers. When possible, the metal components were covered with ceramic tubes to minimize their exposure.

The substrate holder was made of MACOR®, a machinable glass ceramic that is stable up to 800 °C and is a good electrical and thermal insulator. The electrical contact to the substrate was achieved by a small Ta clip (only exposed metal component in the system). A MACOR® shield was also placed on the backside of the graphite target which helped focus the plasma towards the substrate. Gas mixtures were premixed (ratios determined by partial pressures) in a 20L air tank, and gas flow was maintained by a needle valve. The W filament (10 cm, 0.3 mm diameter) was spot welded onto W rods that were also shielded. The W filament was operated at 90° to the target, and it was operated at a red glow and used to pump additional electrons into the plasma. The W filament was far enough (3-6 cm) as to not to influence the temperature on the substrate.

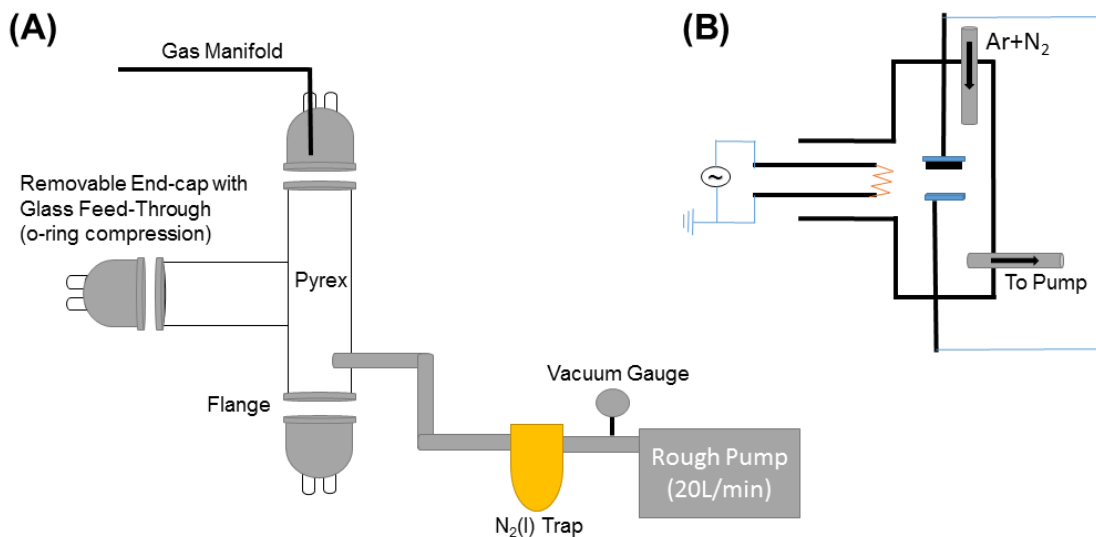


**Figure 3.1.** (a) Basic design of metal-free deposition chamber. (b) Basic set-up of DC plasma deposition chamber with graphite target.

### 3.1.2.1. *a-C:N Film Deposition*

The a-C:N films were deposited onto commercially available SPR Au-coated sensor chips (BioRad, Hercules, CA) and Au-coated Si wafer (Platypus Technologies, Madison, WI) for film characterization methods. Prior to a-C:N film deposition, the Au surfaces were cleaned using a previously published method to remove organic materials.<sup>168-170</sup> Briefly, Au substrates were placed in a 0.5 M NaBH<sub>4</sub> 50% ethanolic solution for 5-10 min, rinsed with Millipore water, and followed up with ozone for 5-10min. Au substrates were then stored in a dust free environment until use.

The a-C:N films were prepared on the SPR Au coated sensor chip using the deposition apparatus described in Figure 3.1. The substrate was biased to -40V, and a working pressure of 900 mTorr in the pre-mixture of Ar and N<sub>2</sub> plasma discharge gas. The nitrogen content in the a-C:N films were varied by premixing N<sub>2</sub> and Ar in a manifold which corresponded to 0-30% N<sub>2</sub> of the total gas flow rate. A graphite target (2.5 cm x 2.5 cm x 0.125 cm) biased to -420 V was used as the carbon source in the sputtering process. The sample deposition time was approximately 3-4 min for SPR sensor chips, and 30-40 min for Au-coated Si wafers.

The sample notation summarized in Table 3.2 for the a-C:N films are described by the %N<sub>2</sub> partial pressure prepared by pre-mixing the N<sub>2</sub> and Ar gases in the storage manifold. The %N<sub>2</sub> does not necessarily reflect or relate to the amount of nitrogen incorporated in the a-C:N film.

**Table 3.2.** Sample notation for a-C:N samples prepared in “metal-free” deposition chamber.

<b>Sample</b>	<b>a-C:N-00</b>	<b>a-C:N-05</b>	<b>a-C:N-10</b>	<b>a-C:N-20</b>	<b>a-C:N-30</b>
N <sub>2</sub> Partial Pressure (psi)	0	5	10	20	30
Ar Partial Pressure (psi)	100	95	90	80	70
%N <sub>2</sub>	0	5	10	20	30

## **3.2. Characterization Methods**

### **3.2.1. Atomic Force Microscopy**

AFM measurements were carried out on a Model 4500 AFM instrument (Agilent Technologies, Chandler, AZ) operating in intermittent contact mode. A conical silicon cantilever (Applied NanoScience, Tempe, AZ) with a force constant of approximately 40 N m<sup>-1</sup>, resonant frequency of approximately 190 kHz, and a with a curvature radius of <10 nm was used for AFM measurements. All measurements were taken with the ratio of the set-point oscillation amplitude to free air oscillation amplitude of 0.85, and resonant amplitude in the range of 6-10 V. In addition, all measurements were performed at ambient conditions with the instrument mounted in a vibration isolation system. The scan rate was 1.0-1.5 Hz (512 pixels per line) for all images.

### **3.2.2. Raman Spectroscopy and FTIR Spectroscopy**

Raman spectroscopy measurements were carried out on a Renishaw InVia Raman microscope using an Ar<sup>+</sup> laser (Modulaser Spectra Physics, Model 812) operating at 514.5 nm, and an 1800 lines mm<sup>-1</sup> grating. The microscope was focused onto the sample using a Leica 20X N PLAN objective (NA = 0.40) (FL-CN<sub>x</sub> samples on PTFE substrate) or Leica 100X NPLAN objective (NA = 0.85) (FL-CN<sub>x</sub> or a-C:N films on SPR sensor surface), and the backscattered Raman signals were collected with a Peltier cooled CCD detector. Spectra were captured in static mode, where the grating was centered at 1400 cm<sup>-1</sup> and data points were collected in the range of 1100-1700 cm<sup>-1</sup>. The laser was focused onto the sample using the linefocus confocal mode with a 10 s detector exposure time. The laser power was 350 μW (20X objective), or 22 μW (100X objective) measured at the sample. The instrument’s calibration was verified using an internal Si (110) sample, which was measured at 520 cm<sup>-1</sup>.

FTIR spectroscopy was performed on an IlluminatIR spectrometer (Smith’s Detection, MA) attached to a Renishaw Invia Reflex microscope (Renishaw Inc., Chicago, Il). Samples were

secured onto borosilicate slides and the IR beam was focused onto the sample using a 36X diamond attenuated total reflectance (ATR) objective ( $NA=\infty$ ; Smiths Detection, MA). Minor baseline correction and smoothing of the spectra were done with Grams32 V8.1 software.

### **3.2.3. Contact Angle Measurements**

Sessile contact angle measurements were done on a home-built apparatus by dropping 2-3  $\mu\text{L}$  of water onto the a-C:N or FL-CN<sub>x</sub> films. Optical pictures of the liquid drops were collected by a DynaPro 90X long working distance USB optical microscope, and angles were measured using the DinoCapture V2.0 included with the microscope.

### **3.2.4. X-ray Photoelectron Spectroscopy**

#### ***3.2.4.1. FL-CN<sub>x</sub> Films on PTFE Substrate***

XPS measurements were completed at Surface Science Western located at the University of Western Ontario. The samples were measured on a Kratos Axis Ultra XPS spectrometer using an AlK $\alpha$  source (1486.7 eV). Survey scan analyses were carried out with an analysis area of 300 x 700 microns and a pass energy of 160 eV. High resolution and valence band analyses were carried out with an analysis area of 300 x 700 microns and a pass energy of 20 eV. Survey scans of the samples were taken again after a 1 min Ar<sup>+</sup> beam sputter etch (4 keV, 15 mA). Data analysis was completed using CASA XPS software (V.2.3.16).

#### ***3.2.4.2. a-C:N Films on Au Substrate***

a-C:N samples prepared on Au-coated Si substrates were measured at the Saskatchewan Structural Sciences Centre, University of Saskatchewan, using a Kratos Axis Supra-HP X-ray photoelectron spectrometer using an AlK $\alpha$  source (1486.7 eV). Survey scan analyses were carried out with an analysis area of 300 x 700 microns and a pass energy of 160 eV. Survey scans of the samples were taken again after a 30 s argon ion beam sputter etch (500 eV, 15 mA). High resolution measurements were carried out with an analysis area of 300 x 700 microns and a pass energy of 20 eV. Ultraviolet Photoelectron Spectroscopy (UPS) measurements were carried out using a He(I) source (20.22 eV) using a 55  $\mu\text{m}$  collimation and a 10 eV pass energy. Data analysis was completed using CASA XPS software (V.2.3.16).

### **3.2.5. Micro-X-ray Fluorescence ( $\mu$ -XRF)**

Single-acquisition and two dimensional  $\mu$ -XRF images were collected using Beamline 07B2-1 'Very Sensitive Elemental and Structural Probe Employing Radiation from a Synchrotron' (VESPERS) located at the Canadian Light Source, Saskatoon, Canada.<sup>171</sup> A polychromatic 'pink beam' (5-30 keV) was used as an excitation source and was focussed down in the microprobe setup to acquire step sizes of 5  $\mu$ m x 5  $\mu$ m in the horizontal and vertical directions. A single Vortex Silicon Drift Detector mounted 45° and 80 mm from sample collected the resulting fluorescence emission from the samples. The dwell time during image acquisition was 1-2 s.

### **3.2.6. X-ray Absorption Near-Edge Spectroscopy (XANES)**

XANES measurements for the C, N, O K-edge and Fe L<sub>1</sub>,L<sub>2</sub>-edge were collected at spherical grating monochromator (SGM) undulator beamline at the CLS, Saskatoon, Canada. The energy resolution ( $E/\Delta E$ ) is >5000 in the 250-1500 eV region. XANES were obtained using the total electron yield (TEY), which measures the sample current, and the X-ray fluorescence yield (FLY) using a channel plate detector. Both the TEY and FLY were obtained simultaneously, providing the electronic structures of the near-surface (few nm) and bulk (~100nm) respectively. All spectra are normalized to the incident photon flux,  $I_0$ , by using an Au mesh.

### **3.2.7. Electron Spin Resonance (ESR)**

ESR measurements were acquired on a Bruker EMX ESR spectrometer equipped with an Oxford cryostat ESR900 operating at 4 K. The typical operating parameters were as follows: microwave frequency 9.388 GHz, microwave power 2.00 mW, centre field 3349.88 G, sweep widths of 6000.0 and 200.0 G, conversion time 163.84 ms, time constant 81.92 ms, sweep time 167.77 s, modulation frequency 100 kHz, modulation amplitude 1.0 G, receiver gain  $3.56 \times 10^4$ .

## **3.3. Protein Surface Interactions**

### **3.3.1. Chemicals**

HSA and Fib were purchased from Sigma (Mississauga, ON), and used as received. All other chemicals were reagent grade and used as received. Stock solutions of proteins were made in PBS buffer (10mM Na<sub>2</sub>HPO<sub>4</sub>, 2mM NaH<sub>2</sub>PO<sub>4</sub>, 137mM NaCl, 2.7 mM KCl), pH=7.4, filtered with 0.1  $\mu$ m Anodisk filter (Whatman), and stored at -20 °C until use. Concentrations of stock

protein solutions were determined from absorbance measurements at 280 nm. Millipore water (18.2 MΩ cm<sup>-1</sup>) was used for all solution preparation.

### **3.3.2. Surface Plasmon Resonance**

#### ***3.3.2.1. FL-CN<sub>x</sub> Protein Interactions***

SPR experiments were done on a BiacoreX instrument (Biacore Inc., Pitascaway, NJ) operating at 25 °C. The FL-CN<sub>x</sub> films were made in the home-built deposition chamber were found to have small metal oxide (at.%<1%) contamination, and were subsequently conditioned by 10mM HCl injections. Prior to protein binding experiments, the sensor chips were pretreated with 30 s injections of 70% EtOH, and 0.5% SDS at 50 μL min<sup>-1</sup>, followed by equilibration with the PBS (pH=7.4) running buffer for approximately 60 min before experiments.

For kinetic binding experiments, HSA (0.1-10 μM) and Fib (0.1-500 nM) in PBS, pH=7.4, were injected over a single flow cell at a flow rate of 30 μL min<sup>-1</sup>. The protein binding was allowed to associate for 120 s, and dissociate for 180 s. The surface was regenerated using 0.5% (w/v) SDS. Duplicate injections (in random order) of each protein and a buffer blank were flowed over the surface. Data were collected at a rate of 10 Hz and was fit to a simple 1:1 interaction model available within the Biaevaluation 4.1 software (Biacore Inc., Pitascaway, NJ).

#### ***3.3.2.2. a-C:N Protein Interactions***

SPR experiments were performed at 25 °C on a Proteon XPR36 instrument (Biorad Laboratories, Hercules, CA), which consists of 6 independent parallel flow channels that can be run in the horizontal and vertical directions, providing up to 36 individual sensorgrams in a single run. Prior to protein binding experiments, a-C:N films were conditioned with 1 min injections of 0.5% SDS, 50mM NaOH, and 100mM HCl at 30 μL min<sup>-1</sup> in both the horizontal and vertical directions. A suitable reference surface was created by two 6 min injections of 0.2-0.3% (w/v) casein or BSA (1X PBS, pH 7.4) at 25 μL min<sup>-1</sup> in the vertical direction. The sensor chip was rotated to the horizontal position and 5-6 injections of running buffer (1X PBS, pH 7.4) were injected to stabilize the sensor surface. HSA and Fib concentration series dissolved in the running buffer were injected over the a-C:N surfaces for 2 min at 30 μL min<sup>-1</sup>. The instrument then switched to running buffer, and the dissociation was monitored for 600 s. The surfaces were then regenerated using injections of 0.5% SDS and 100mM HCl. Kinetic parameters were extracted using a 1:1 interaction model using the Proteon XPR36 software.

### 3.3.3. Scanning Transmission X-ray Microscopy (STXM)

STXM experiments were performed on the 10ID-1 (SM) beamline at the Canadian Light Source in Saskatoon, Canada. The beamline is equipped with an APPLE II type elliptically polarizing undulator which provides circular polarized or linear polarized light with an  $E/\Delta E > 3000$ . Briefly, a monochromatic x-ray beam is focussed by Fresnel zone plate down to 30 nm spot on the FL-CN<sub>x</sub> film. The sample is raster scanned with synchronized detection of transmitted x-rays in order to generate images. Chemical imaging and Near Edge X-ray Absorption Fine Structure (NEXAFS) spectra are obtained using image sequence (stack) scans over a range of energies near an element's edge (ie. 1 image per energy point). The x-ray energy scale at the beamline was calibrated with N<sub>2</sub> (g) for N1s measurements, and CO<sub>2</sub> (g) for C1s and O1s measurements. STXM data was analyzed using aXis2000, software developed at McMaster University, Canada, and freely available for non-commercial applications (<http://unicorn.mcmaster.ca/aXis2000.html>).

The FL-CN<sub>x</sub> films were deposited onto 75nm thick Si<sub>3</sub>N<sub>4</sub> windows (Norcanda, Edmonton, Canada) using the original hot filament sputtering deposition apparatus located in the Plasma Physics Laboratory. The STXM measurements require a suitable I<sub>0</sub> region that does not contain the FL-CN<sub>x</sub> film that is measured simultaneously with the region of interest. The most efficient way to do this with thin films is at an interface between the Si<sub>3</sub>N<sub>4</sub> substrate and thin film. Carbon tape, Si wafer, and Kapton<sup>TM</sup> tape were tested for potential masks on the Si<sub>3</sub>N<sub>4</sub> window during FL-CN<sub>x</sub> deposition, and the resulting Si<sub>3</sub>N<sub>4</sub> coated windows are shown in Figure 3.2. The Kapton<sup>TM</sup> film provided the “cleanest” interface between the FL-CN<sub>x</sub> film and the Si<sub>3</sub>N<sub>4</sub> window. The sample thickness was estimated at approximately 60-100 nm from the film's interference colours. The C1s (280-320 eV), N1s (395-430 eV) and O1s (520-560 eV) NEXAFS spectra had energy step sizes of 0.1eV employed around the near-edge, and a 1eV step size in the pre-edge and post-edge regions.

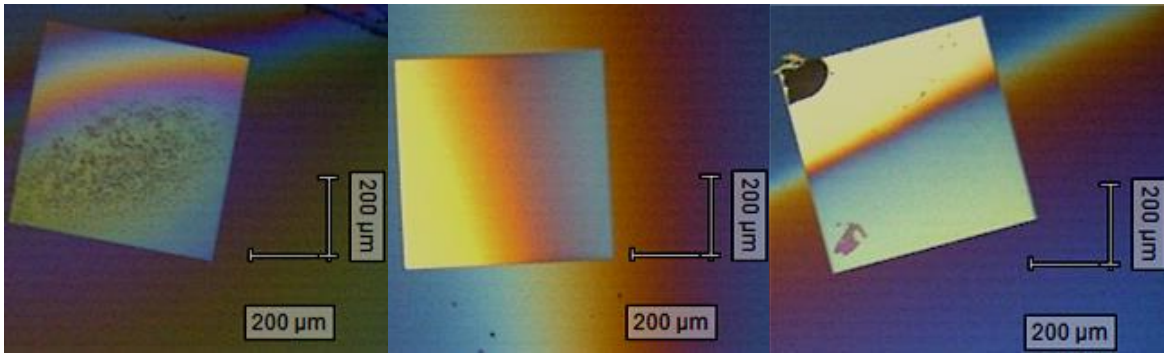


**Figure 3.2.** FL-CN<sub>x</sub> films were deposited onto Si<sub>3</sub>N<sub>4</sub> windows using different masks. Left: Carbon tape; Middle: Si wafer; Right: Kapton™ tape.

## CHAPTER 4 - RESULTS AND DISCUSSION

### 4.1. Metal Containing FL-CN<sub>x</sub>

#### 4.1.1. General FL-CN<sub>x</sub> Films on PTFE Substrate Characterization

The FL-CN<sub>x</sub> films were uniform and their adhesion onto the PTFE substrate were confirmed by the adhesion tape test.<sup>103</sup> The FL-CN<sub>x</sub> samples were evaluated using AFM, contact angle and Raman spectroscopy techniques, and the measurements are summarized in and the data is summarized in Table 4.1.

**Table 4.1.** AFM, contact angle and Raman spectroscopy data for FL-CN<sub>x</sub> films deposited on PTFE.

Sample	AFM <sup>1</sup>	Contact Angle <sup>2</sup>	Raman Spectroscopy <sup>3</sup>		
	R <sub>RMS</sub> (nm)	(Deg)	G-Band (cm <sup>-1</sup> )	D-Band (cm <sup>-1</sup> )	I <sub>D</sub> /I <sub>G</sub> <sup>4</sup>
PTFE	22.9 (±3.5)	107.3 (±2.2)	--	--	--
FL-CN <sub>x</sub> -00	22.1 (±3.1)	72.8 (±2.6)	1576 (118)	1361 (237)	0.80 (0.02)
FL-CN <sub>x</sub> -03	14.3 (±3.6)	58.7 (±2.6)	1577 (155)	1366 (224)	1.25 (0.01)
FL-CN <sub>x</sub> -06	12.5 (±3.7)	53.9 (±3.5)	1575 (160)	1364 (212)	1.20 (0.01)
FL-CN <sub>x</sub> -10	8.7 (±2.3)	63.6 (±2.7)	1573 (155)	1367 (229)	1.20 (0.01)
FL-CN <sub>x</sub> -20	10.3 (±2.9)	64.8 (±2.6)	1570 (170)	1364 (206)	1.10 (0.01)

<sup>1</sup> R<sub>RMS</sub> values were taken from 2 μm x 2 μm areas over n = 3-4 areas.

<sup>2</sup> Contact angles were taken from n = 5-7 measurements.

<sup>3</sup> Peak linewidth at full width half maximum (FWHM) given in brackets.

<sup>4</sup> The standard error for the peak height ratio is given in brackets.

High resolution AFM topography images are shown in Figure 4.1. The samples all reveal an aggregated cluster morphology with the smallest measurable cluster was approximately 20 nm. However, it is likely that these features are much smaller due to lateral AFM tip-sample convolution effects, which are significant when the surface features are smaller than the AFM probe curvature of radius (probes used <10 nm). The root-mean square roughness (R<sub>RMS</sub>) for the PTFE substrate was 22.9 ± 3.5 nm, and the R<sub>RMS</sub> was 22.1 nm for the FL-CN<sub>x</sub>-00 sample. The addition of N<sub>2</sub> into the plasma discharge gas decreased the R<sub>RMS</sub> of the films which were measured in the range of 8.7 nm to 14.3 nm for FL-CN<sub>x</sub>-03 to FL-CN<sub>x</sub>-20 samples.

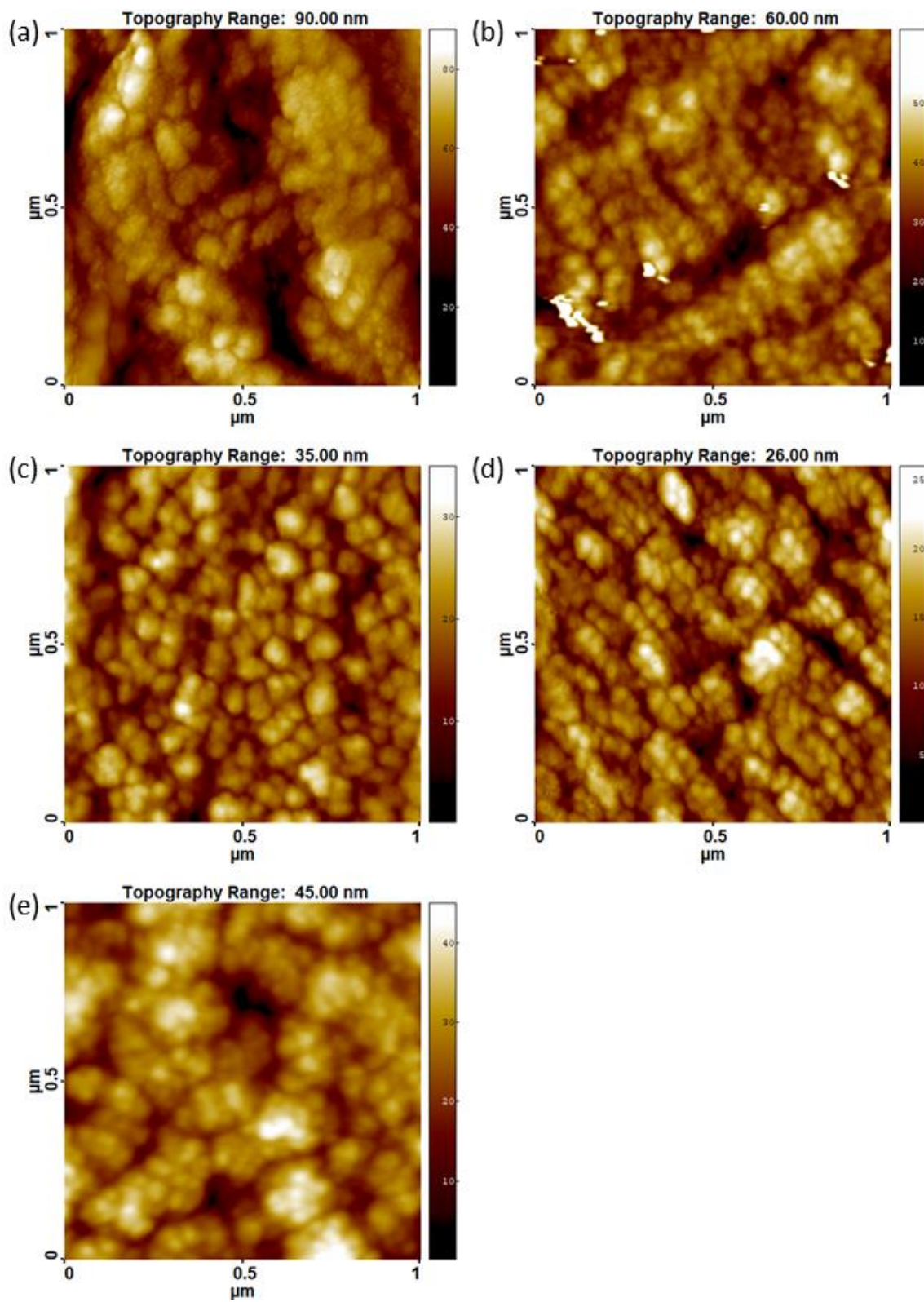


**Figure 4.1.** AFM topography images (1 μm x 1 μm) of FL-CN<sub>x</sub> films prepared with different amounts of N<sub>2</sub> plasma discharge gas. (a) FL-CN<sub>x</sub>-00 (b) FL-CN<sub>x</sub>-03 (c) FL-CN<sub>x</sub>-06 (d) FL-CN<sub>x</sub>-10 (e) FL-CN<sub>x</sub>-20.

The wettability can provide information regarding the hydrophilic and hydrophobic properties of surfaces. The wettability of the different FL-CN<sub>x</sub> films was assessed by static sessile contact angle measurements. Contact angle measurements using Millipore water on the different surfaces are shown in Figure 4.2 and summarized in Table 4.1. The FL-CN<sub>x</sub> films have a much lower contact angle compared to PTFE. The introduction of nitrogen (3-6% N<sub>2</sub>) into the a-C matrix initially decreases the contact angle, indicating a more hydrophilic surface. However, increasing the plasma discharge gas to ≥10% N<sub>2</sub> during film deposition increases the contact angle revealing a more hydrophobic surface.

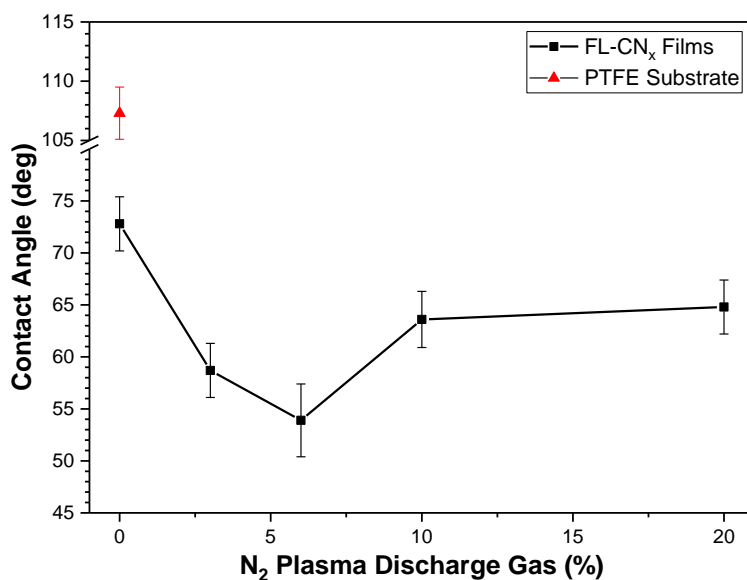


**Figure 4.2.** Static contact angle measurements using water for FL-CN<sub>x</sub> films prepared with different N<sub>2</sub> amounts in plasma discharge gas. For each sample, contact angle measurements were replicated 3-5 times.

Raman spectra for the FL-CN<sub>x</sub> films are shown in Figure 4.3 and summarized Table 4.1. The Raman spectroscopy measurements include 2 large bands at approximately 1575 cm<sup>-1</sup> and 1360 cm<sup>-1</sup>, which corresponds to the G and D bands, respectively. The G and D bands arise from sp<sup>2</sup> sites of carbon, where the G band is associated with the symmetrical stretching of all sp<sup>2</sup> carbon atom pairs in aromatic and olefinic molecules, and the D band is associated with the breathing modes of the aromatic ring-like sp<sup>2</sup> atoms.<sup>172</sup> This mode is forbidden in perfect graphite, and become active in the presence of disorder. In addition, nitrogen containing a-C structures tend to be delocalized over both carbon and nitrogen sites due to nitrogen's tendency to sp<sup>2</sup> clustering of the Raman bands of different types of molecules. It is difficult to separate the -C=N- and -C=C-

vibrational modes in the G and D band region, The general bonding trends may be analyzed and compared to nitrogen-free a-Cs.<sup>173</sup>

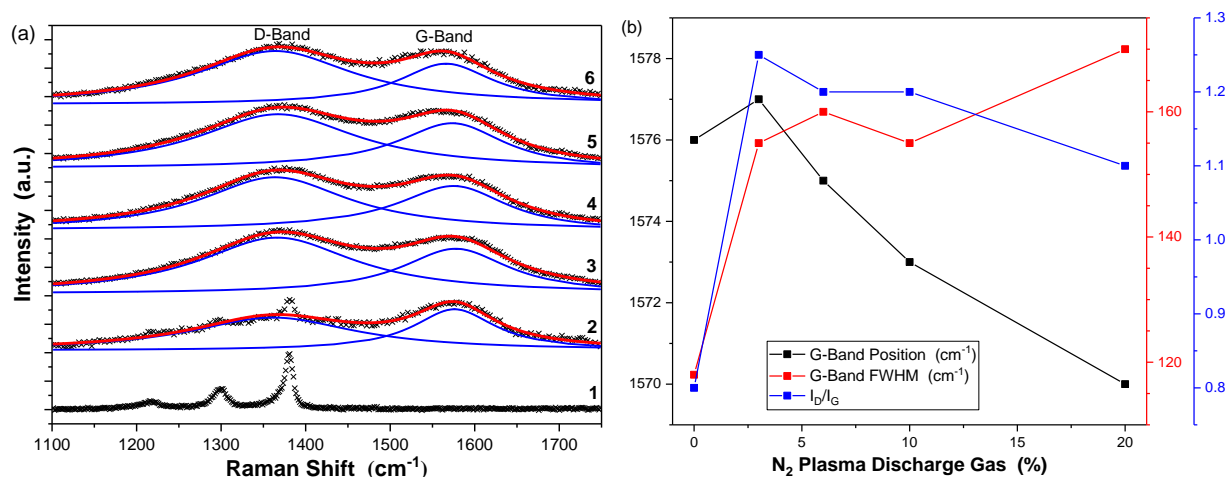


**Figure 4.3.** (a) Raman spectroscopy ( $\lambda_{\text{ex}} = 514.5 \text{ nm}$ ) of FL-CN<sub>x</sub> films deposited on PTFE. (1) PTFE (2) FL-CN<sub>x</sub>-00 (3) FL-CN<sub>x</sub>-03 (4) FL-CN<sub>x</sub>-06 (5) FL-CN<sub>x</sub>-10 (6) FL-CN<sub>x</sub>-20. (b) Peak deconvolution of the G-Band and D-Band show differences in the G-Band position (-■-), G-Band peak width at FWHM (-■-) and the I<sub>D</sub>/I<sub>G</sub> peak intensity ratio (-■-).

Raman spectroscopy peak deconvolution for a-C materials can be complex, and a generally accepted method has been reported by Ferrari *et al.*<sup>172-177</sup> A Lorentzian lineshape is often used for crystals and disordered graphite, and arise from finite lifetime broadening of phonons whereas a Gaussian lineshape is expected for a random distribution of phonon lifetimes in disordered materials. It would be apparent that Gaussian lineshapes would be preferred for a-C. However, there are some residual bands that may be present at 1100-1200 cm<sup>-1</sup> and 1400-1500 cm<sup>-1</sup>. To account for the residual Raman peaks without performing a 4-peak deconvolution, the most widely used alternative to a Gaussian fit is the use of a Breit-Wigner-Fano lineshape for G-band deconvolution.<sup>178-179</sup> The Breit-Wigner-Fano lineshape appears in Raman scattering through the interaction between discrete Raman-active phonon modes and a continuum of Raman-active excitations. The Breit-Wigner-Fano lineshape's asymmetry tails at lower wavenumbers and can account for the Raman intensity at 1100 cm<sup>-1</sup> and 1400 cm<sup>-1</sup> without deconvoluting the spectrum with 2 additional bands. The D-band is fit with a Lorentzian lineshape.<sup>172</sup>

The G-band peak positions for all of the FL-CN<sub>x</sub> films suggest that the films are stage 2 amorphous carbon.<sup>172, 176</sup> Initially, the G-band peak position is centered at 1576 cm<sup>-1</sup> for FL-CN<sub>x</sub>-00 and it fluctuates  $\pm 1 \text{ cm}^{-1}$  with small amounts N<sub>2</sub> (3-6 %) in the plasma discharge gas during film deposition. This small fluctuation is within the spectral resolution ( $\pm 4\text{-}5 \text{ cm}^{-1}$ ) of the Raman

instrument. For FL-CN<sub>x</sub>-10 and FL-CN<sub>x</sub>-20 samples, there is a measurable downshift of the G-band peak position to 1573-1570 cm<sup>-1</sup>. This G-band down shift indicates a small increase in the %sp<sup>3</sup> carbon, as the trajectory of stage 2 a-C towards stage 3 a-C shows a decrease in G-band peak position as well as a decrease in I<sub>D</sub>/I<sub>G</sub> peak intensity ratio.<sup>172-173</sup> The G-band FWHM is 118 cm<sup>-1</sup> for FL-CN<sub>x</sub>-00 sample and it increases to 155 cm<sup>-1</sup> for the FL-CN<sub>x</sub>-03 sample, even though the peak position does not change. This suggests that the sp<sup>2</sup> sites do not order into graphitic-like clusters, but the variation of sp<sup>2</sup> bonding becomes larger.<sup>180 173</sup> The I<sub>D</sub>/I<sub>G</sub> ratio, which is proportional to the number of ordered aromatic rings as well as the cluster size squared (L<sub>a</sub><sup>2</sup>) for Stage 2 a-C,<sup>172, 176</sup> increases for the FL-CN<sub>x</sub> sample. Nitrogen incorporation into a-C generally helps cross-linking between graphitic planes, increasing the aromatic clustering size.<sup>173</sup> However, the I<sub>D</sub>/I<sub>G</sub> ratio decreases for the FL-CN<sub>x</sub>-06 to FL-CN<sub>x</sub>-20 samples suggesting that the saturation of nitrogen into a-C matrix decreases the number of aromatic rings which is also in combination with the G-peak downshift.

ATR-FTIR spectra shown in Figure 4.4 reveal the different functional groups within the films. The vibrational assignments for the FTIR bands are summarized in Table 4.2. In the absence of N<sub>2</sub> in the plasma discharge gas during film deposition, the FTIR spectrum is unrevealing as the vibrational bands are small and indicate the presence of oxygen containing functional groups such as carboxyl (1730 cm<sup>-1</sup>) and carbonyl (1630 cm<sup>-1</sup>) groups. The 1650 cm<sup>-1</sup> and 1570 cm<sup>-1</sup> bands indicate that the small amount of nitrogen in this film is in the amide form. The broad bands in the 1750-1300 cm<sup>-1</sup> region also increased in intensity with the incorporation of nitrogen into the a-C matrix. Although the nitrogen helps break the electronic symmetry of the π system, the more significant role in the increased intensity is likely from its contribution to increase the sp<sup>2</sup> fraction and clustering.<sup>173</sup> In addition, the N-incorporation increases the O-H band found around 3000-3300 cm<sup>-1</sup>, indicating the these films may contain a high porosity and incorporate water and an extended H-bonding network.<sup>173, 181</sup>

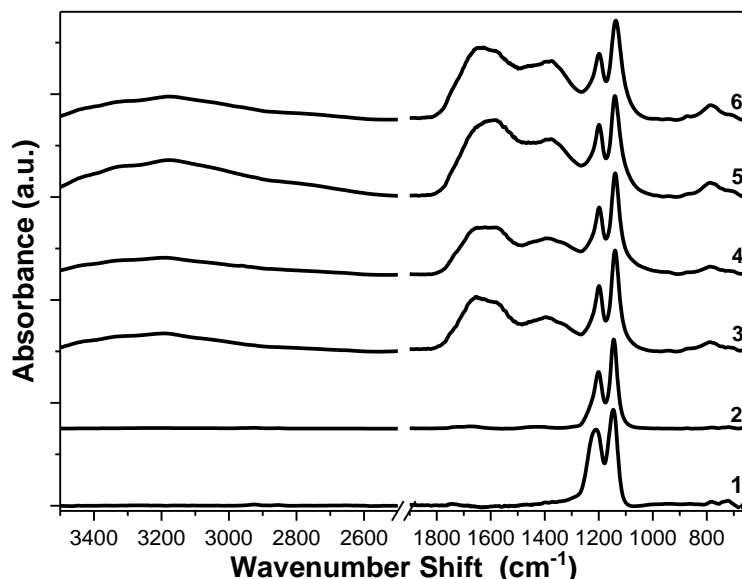


**Figure 4.4.** ATR-FTIR spectra of the FL-CN<sub>x</sub> films deposited on PTFE. (1) PTFE (2) FL-CN<sub>x</sub>-00 (3) FL-CN<sub>x</sub>-03 (4) FL-CN<sub>x</sub>-06 (5) FL-CN<sub>x</sub>-10 (6) FL-CN<sub>x</sub>-20.

**Table 4.2.** ATR-FTIR spectroscopy band assignments for FL-CN<sub>x</sub> samples deposited on PTFE. <sup>182-183</sup>

Vibrational Band Assignment	PTFE	FL-CN <sub>x</sub> -00	FL-CN <sub>x</sub> -03	FL-CN <sub>x</sub> -06	FL-CN <sub>x</sub> -10	FL-CN <sub>x</sub> -20
<i>O-H Stretch</i>		3000-3500	3000-3500	3000-3500	3000-3500	3000-3500
<i>Carbonyl Stretch</i>	1742	1720*	1740	1729*	1740*	1730*
<i>C=O (Amide)</i>		1665	1653	1650	1644*	1644*
<i>Amorphous Carbon</i>			1588	1580	1581	1581
<i>Amorphous Carbon</i>		1420	1395	1392	1380	1372
<i>C-F<sub>2</sub> asymmetric stretch</i>	1210	1200	1199	1199	1199	1199
<i>C-F<sub>2</sub> symmetric stretch</i>	1146	1144	1139	1139	1140	1137
<i>PTFE-Amorphous</i>	861	861	861	869	863*	871
<i>PTFE-Amorphous</i>	782	782	788	787	787	786
<i>PTFE-Amorphous</i>	735*	735*	743*	744*	741*	741*
<i>PTFE-Amorphous</i>	720	720	720	720	724	719
<i>PTFE-Amorphous</i>	702	702	703*	704*	704	706*
$I_{(782\text{cm}^{-1})}/I_{(1146\text{cm}^{-1})} (x10^{-2})$	14.6	4.1	1.2	8.8	7.2	11.8

\*peak shoulder

The large bands located at 1201 cm<sup>-1</sup> and 1147 cm<sup>-1</sup> are associated with the CF<sub>2</sub> stretches of PTFE. The addition of the FL-CN<sub>x</sub> film resulted in the CF<sub>2</sub> bands downshift by up to 9 cm<sup>-1</sup> suggesting that the PTFE substrate structure has been altered during the deposition process. The bands located in the range of 700-800 cm<sup>-1</sup> are associated with amorphous structures within the PTFE. <sup>182-183</sup> It has been suggested that the CF<sub>2</sub> stretch at 1147 cm<sup>-1</sup> is independent of the crystalline

or amorphous structure of PTFE.<sup>184</sup> The  $I_{782\text{cm}^{-1}}/I_{1146\text{cm}^{-1}}$  peak intensity ratio shown Table 4.2 shows a lower value for the FL-CN<sub>x</sub> samples compared to the PTFE substrate, suggesting a loss in amorphous structures with the addition of FL-CN<sub>x</sub> films. This may be a consequence of the higher temperature exposure during film deposition as the crystallinity of PTFE for a given molecular weight is a function of heat treatment.

XPS measurements were used to assess the composition of the FL-CN<sub>x</sub> films. This technique is very surface sensitive, and the emitted electrons originate from within approximately 10 nm from the surface. The XPS survey spectra shown in Figure 4.5 were acquired for the FL-CN<sub>x</sub> samples for both with and without surface sputtering. The at.% of different elements observed is summarized in Table 4.3. The addition of N<sub>2</sub> to the plasma gas discharge shows an increase in the N/C ratio, whereas the O/C ratio decreases slightly, but it can be considered constant. The at.% O has been previously shown to be slightly higher at the surface, but it is found throughout the film.<sup>103</sup> Films were sputtered for 1 min, and the O/C ratio was found to decrease by a factor of 2, indicating a higher oxide content on the surface. In addition, the N/C ratio slightly increased, likely due to the decreased presence of the oxide layer and surface contaminants removed. Small amounts of transition metals, mainly Fe and W, were also observed in the FL-CN<sub>x</sub> films. Other elements such as F and Si were identified in the films. The F could be due to small pinholes within the films, whereas the Si could be from sputtering Si substrates that were also being used to simultaneously deposit FL-CN<sub>x</sub> films. Another possibility could be from pump oil contamination due to back flow. There was no N<sub>2</sub>(l) trap used in on this coater apparatus. Both Fe and Si signals decreased as a function of N<sub>2</sub>/Ar or decrease of corrosivity of the plasma.

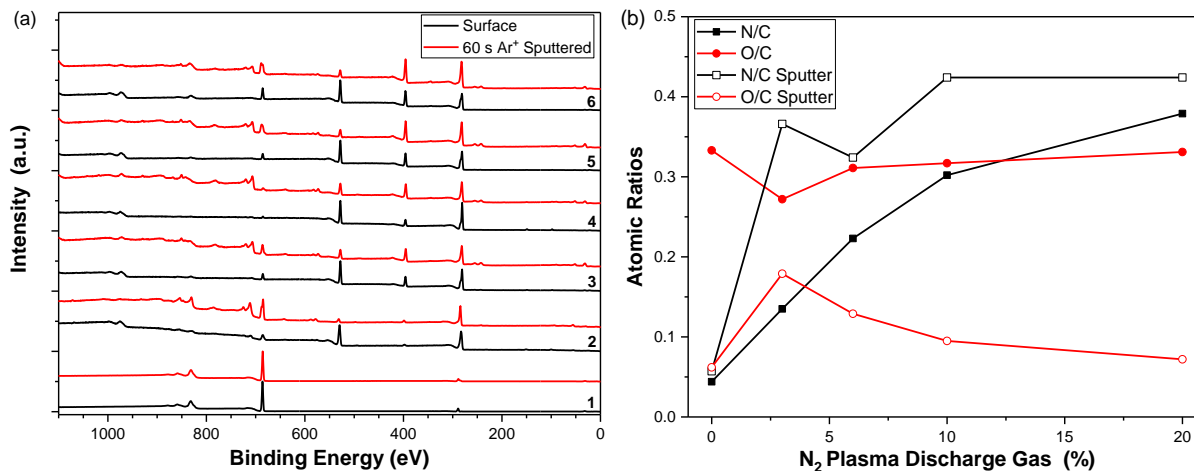


**Figure 4.5.** (a) XPS (Al K $\alpha$  = 1486.6 eV) survey scans of FL-CN $_x$  films “as received” and after surface cleaning (1 min 4 keV, 15 mA Ar $^+$  sputtering). (b) The at.% N/C and O/C ratios for “as received” and after surface cleaning.

**Table 4.3.** XPS survey scans for FL-CN $_x$  films deposited onto PTFE substrate.

Sample	XPS (at.%) <sup>a</sup>								
	C	N	O	FF	Fe	W	Si	Cr	Other
PTFE	29.1		0.1	70.8					
FL-CN $_x$ -00	66.0	2.9	22.0	5.5	0.9	0.1	2.1	0.4	0.2 (Na)
FL-CN $_x$ -03	68.8	9.3	18.7	1.0	0.7	0.1	1.9		
FL-CN $_x$ -06	62.0	13.8	19.3	3.5	0.3	0.1	1.9		
FL-CN $_x$ -10	59.6	18.0	18.9	3.2		0.1	0.3		
FL-CN $_x$ -20	54.4	20.6	18.0	6.4		0.1	0.2		
<b>(b) After 1 min sputter</b>									
PTFE	33.0			67.0					
FL-CN $_x$ -00	59.9	3.4	3.7	21.1	8.6	0.1		1.8	
FL-CN $_x$ -03	55.2	18.4	7.3	8.0	7.5	0.8	0.9	1.5	
FL-CN $_x$ -06	56.8	20.3	9.9	1.8	5.9	0.9	0.1	1.4	
FL-CN $_x$ -10	55.6	23.6	5.3	8.1	4.2	1.0	0.3	0.9	
FL-CN $_x$ -20	57.3	24.3	4.1	9.6	2.9	0.5	0.1	0.5	

<sup>a</sup> Relative errors in XPS area measurements are approximately 5-10%.

High resolution XPS for the C1s, N1s and O1s are shown in Figure 4.6 and the deconvoluted bands are summarized in Table 4.4.

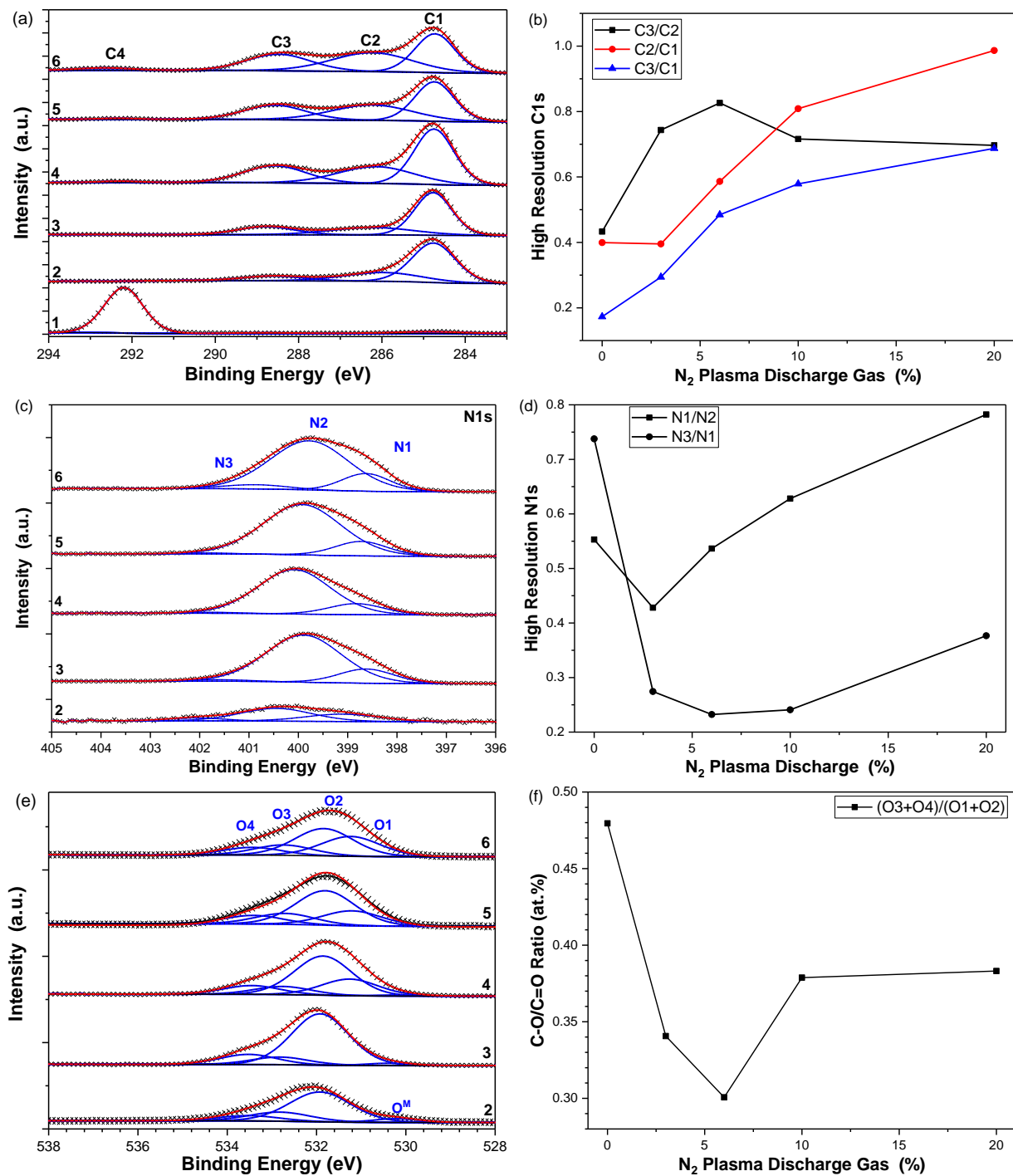


**Figure 4.6.** High resolution XPS of the FL-CN<sub>x</sub> films. (1) PTFE (2) FL-CN<sub>x</sub>-00 (3) FL-CN<sub>x</sub>-03 (4) FL-CN<sub>x</sub>-06 (5) FL-CN<sub>x</sub>-10 (6) FL-CN<sub>x</sub>-20. (a) C1s (b) C1s at.% ratios for different films (c) N1s (d) N1/N2 and N3/N1 at.% ratios for different films (e) O1s (f) (O3+O4)/(O2+O1) at.% ratio for different films.

**Table 4.4.** High resolution XPS (C1s, N1s, O1s) band deconvolution of FL-CN<sub>x</sub> films.

<b>(a) C1s<sup>a</sup></b>								
Sample	C1 <i>C=C, C-H</i> (eV)	At.%	C2 <i>C=N; C-O</i> (eV)	At.%	C3 <i>C-N; C=O</i> (eV)	At.%	C4 <i>-CF<sub>2</sub></i> (eV)	At.%
PTFE	284.8 (1.8)	5.8	286.3 (1.8)	0.6	287.9 (1.8) 288.9 (1.8)	0.2 2.0	292.2 (1.1)	91.4
FL-CN <sub>x</sub> -00	284.5 (1.2)	63.6	286.0 (2.2)	25.4	288.6 (1.8)	11.0	--	0
FL-CN <sub>x</sub> -03	284.8 (1.1)	59.2	286.2 (2.4)	23.4	288.8 (1.6)	17.4	--	0
FL-CN <sub>x</sub> -06	284.7 (1.1)	48.1	286.1 (2.2)	28.2	288.6 (1.8)	23.3	292.3 (1.2)	0.3
FL-CN <sub>x</sub> -10	284.7 (1.1)	41.8	286.2 (2.3)	33.8	288.6 (1.8)	24.2	292.3 (1.1)	0.3
FL-CN <sub>x</sub> -20	284.7 (1.1)	37.1	286.2 (2.1)	36.6	288.5 (1.8)	25.5	292.6 (1.6)	0.9

<sup>a</sup> The standard deviation for C1s area is  $\pm 1.0$  at.%.

<b>(b) N1s<sup>a</sup></b>						
Sample	N1 <i>Pyridinic N</i> (eV)	At.%	N2 <i>Pyrolic N</i> (eV)	At.%	N3 <i>Graphitic N</i> (eV)	At.%
FL-CN <sub>x</sub> -00	399.0 (1.7)	28.2	400.2 (1.7)	51.0	401.4 (1.7)	20.8
FL-CN <sub>x</sub> -03	399.0 (1.5)	27.7	400.1 (1.5)	64.7	401.2 (1.5)	7.6
FL-CN <sub>x</sub> -06	398.8 (1.5)	32.3	400.0 (1.5)	60.2	401.1 (1.5)	7.5
FL-CN <sub>x</sub> -10	398.9 (1.5)	35.3	400.0 (1.5)	56.2	401.0 (1.5)	8.5
FL-CN <sub>x</sub> -20	398.9 (1.4)	37.7	399.9 (1.4)	48.2	400.8 (1.4)	14.2

<sup>a</sup> The standard deviation for N1s area is  $\pm 0.3$  at.%.

<b>(c) O1s<sup>a</sup></b>										
Sample	O <sup>M</sup> <i>M<sub>x</sub>O<sub>y</sub></i> (eV)	At.%	O1 <i>Quinone</i> (eV)	At.%	O2 <i>C=O</i> (eV)	At.%	O3 <i>C-O-C</i> (eV)	At.%	O4 <i>C-O;Ar-OH</i> (eV)	At.%
FL-CN <sub>x</sub> -00	530.2 (1.2)	5.9	--	--	531.9 (1.6)	63.6	532.8 (1.6)	19.3	533.5 (1.6)	11.2
FL-CN <sub>x</sub> -03	530.2 (1.2)	2.0	531.3 (1.5)	0.5	531.9 (1.5)	72.6	532.8 (1.5)	10.8	533.5 (1.5)	14.1
FL-CN <sub>x</sub> -06	530.2 (1.2)	1.2	531.3 (1.5)	22.6	531.8 (1.5)	53.9	532.8 (1.5)	11.0	533.5 (1.5)	12.0
FL-CN <sub>x</sub> -10			531.2 (1.6)	23.8	531.8 (1.6)	48.8	532.7 (1.6)	14.5	533.4 (1.6)	13.0
FL-CN <sub>x</sub> -20			531.2 (1.6)	30.4	531.8 (1.6)	41.9	532.7 (1.6)	15.9	533.4 (1.6)	11.8

<sup>a</sup> the standard deviation for O1s area is  $\pm 1.1$  at.%.

The C1s region for carbon materials will contain some level of oxygen-containing functional groups on its surface. This region is generally deconvoluted using 4 bands based on the XPS of polymeric materials: the C=C band for graphitic material is generally around 284.5 eV; a band at 1.5 eV above the C=C band is C-OH and C-O-C groups; a band at 3.0 eV above the C=C band is for C=O groups; and a band at 4.5 eV above the C=C band is O=C-OH groups.<sup>185</sup> In addition, materials that contain a high amount of C=C bonding may also show a C=C shake-up band at approximately 290.5-292 eV. Nitrogen-doped carbon materials have reported 2 bands around 285.8-286.3 eV and 287-288.3 eV for sp<sup>2</sup>-N and sp<sup>3</sup>-N, respectively.<sup>186</sup> The C1s spectra shown in Figure 4.5(a) were deconvoluted into 4 main bands: C1 (284.7 eV) is attributed to the sp<sup>2</sup>-C (C=C); C2 (286.1 eV) is a mixture of sp<sup>2</sup>-N (C=N) and sp<sup>3</sup>-C (C-OH); C3 (287.7-288.1eV) is a mixture of sp<sup>3</sup>-N and sp<sup>2</sup>-C (C=O, O=C-OH); C5 (292 eV) is attributed to the -CF<sub>2</sub> groups from the PTFE substrates (this band is not present in all measurements).

The C1s deconvolution shows that the C=C bonding decreases with an increase in the N-incorporation into the films. Similarly, the C2 and C3 bands increase with increasing N-incorporation. In terms of peak area ratios, the C3/C2 band ratio shown in Figure 4.6(b) shows an initial increase in this ratio for the films prepared at different %N<sub>2</sub> plasma discharge. This ratio reaches a maximum for the FL-CN<sub>x</sub>-06 sample, and the C2/C3 ratio then decreases for films prepared with larger %N<sub>2</sub> plasma discharge. The C3/C1 ratio scales linearly with the %N<sub>2</sub> plasma discharge gas. The C2/C1 ratio initially decreased for the FL-CN<sub>x</sub>-03 film, but the ratio increased for somewhat linearly for films prepared with larger N<sub>2</sub> plasma discharge gas.

The band deconvolution for the N1s region for carbon materials has been reviewed, and the N1s region is generally deconvoluted up to 4 different bands, but the band assignments have not been consistent.<sup>187</sup> N1 (398-399 eV) has been generally assigned to pyridinic-N (2-fold sp<sup>2</sup>-coordinated); N2 (399.5-400.5 eV) has generally been pyrrolic-N (3-fold sp<sup>2</sup>-coordinated), although this band has also been assigned to nitriles (399.5 eV), amines (399.4 eV), or even graphitic carbon. The N3 band (401-402.5 eV) is associated with quaternary N or graphitic N, and N4 (403-406 eV) is generally associated with a pyridine-oxide, or adsorbed NO.<sup>187</sup> In addition, a deconvolution of an element will generally have a similar FWHM for all bands, as the common processes that contribute to the FWHM (natural width of incident X-ray source, thermal broadening, pass energy of the instrument analyzer, lifetime of the electron hole, etc.) are the same for each band (and each sample).

The asymmetric band in the N1s region shown in Figure 4.6(c) is centered at approximately 400 eV. The N1s envelope was deconvoluted into 3 major bands (3 bands were also shown in N1s XANES which will be introduced below): N1 was located at 398.9 eV ( $\pm 0.1$  eV) and it is associated with pyridinic N; N2 is located 400.0 eV ( $\pm 0.1$  eV) and it has been assigned to pyrrolic-N (Raman spectra for the FL-CN<sub>x</sub> films did not show the characteristic 2250 cm<sup>-1</sup> band for nitriles); N3 was located at 401.1 ( $\pm 0.3$  eV) and it is assigned to graphitic-N. The FL-CN<sub>x</sub>-00 (2.9 at.% N) pyridinic-N:pyrrolic-N:graphic-N ratio is approximately a 3:5:2 ratio. The addition of more nitrogen into the FL-CN<sub>x</sub>-03 (9.3 at.% N) sample reduced the amount of graphitic-N content and increased the pyrrolic-N content (the pyridinic-N remained approximately the same for this sample). This causes the N1/N2 at.% ratio to decrease to a minimum while the N3/N2 ratio decreased to a minimum as shown in Figure 4.6(d). In addition, the N3/N2 at.% ratio decreased significantly. Further increases of %N<sub>2</sub> into the plasma discharge gas increased the pyridinic-N content, while the pyrrolic-N decreased (ie. N1/N2 at.% ratio increased). The N3/N1 at.% ratio was constant for the FL-CN<sub>x</sub>-03 to FL-CN<sub>x</sub>-10 samples. The FL-CN<sub>x</sub>-20 (20.6 at.% N) showed that at slight increase in the at.% N compared to the FL-CN<sub>x</sub>-10 (18.9 at.%N) showed a significant increase in graphitic-N content at the expense of the pyrrolic-N content. The pyridinic-N increased slightly.

The O1s band deconvolution can be very complex due to the mixtures of adsorbed and bulk oxygen containing species.<sup>188</sup> In addition, the binding energies (BE) for different oxygen functional groups are very close and are not easily separable without careful measurements. For instance, Fe(II/III) oxide/hydroxide surfaces have been found to contain the lattice O<sup>2-</sup> at 530.0  $\pm$  0.1 eV, lattice and adsorbed OH<sup>-</sup> at 531.1  $\pm$  0.1 eV and 532.1  $\pm$  0.1 eV, adsorbed O<sub>2</sub> at 531.6  $\pm$  0.1 eV, and adsorbed H<sub>2</sub>O at 533.3  $\pm$  0.3 eV.<sup>189</sup> The FTIR (Figure 4.2(c)) and the C1s measurements indicate the presence of carbonyls (C=O), which have a binding energy of approximately 531.8 eV, and C-O for non-carbonyl oxygen and aromatic OH groups have a BE of approximately 533.4 eV.<sup>188</sup> Physisorbed H<sub>2</sub>O and H<sub>2</sub>O trapped in microporous have been assigned at higher BE, in the range or 534-536 eV.

The O1s carbon surface chemistry was evaluated on a carbon substrate using temperature desorption in-situ with XPS and mass spectrometry.<sup>188</sup> The use of both XPS and mass spectrometry in tandem was able to identify and correlate different oxygen functional groups and their binding energy from the O1s region as the sample was subjected to temperature change. The O1s XPS

region shown in Figure 4.6(e) was deconvoluted into 5 main peaks: (1) O1 is located at 531.2 eV ( $\pm 0.1$  eV) and is associated with quinone-type structure, (2) O2 is located at 531.8 eV ( $\pm 0.1$  eV) and it is associated with carbonyls, (3) O3 located at 532.7 eV ( $\pm 0.1$  eV) is associated with C-O-C structure, O4 is located at approximately 533.2 eV ( $\pm 0.1$  eV) and is associated with C-O (carboxylic acids) and phenols. Brender *et al.*<sup>188</sup> also observed additional peaks in the 534-536 eV region associated with adsorbed water, but this was not observed for the FL-CN<sub>x</sub> samples.

FL-CN<sub>x</sub>-00 to FLCN<sub>x</sub>-06 also contained a small peak at 530.2 eV and is assigned to the O<sub>2</sub><sup>-</sup> lattice contributions for metal oxides present in the samples. are considered here metal oxides, as the more significant amounts of metal content are associated with these samples. The contribution of the lattice-O from the metal oxides decreased as the at.% of metal decreased in the films. Overall, the at.% O is fairly constant for the different FL-CN<sub>x</sub> films (18-22 at.%O). The addition of nitrogen into the a-C decreased the C-O (ethers, phenols, etc.) to carbonyl (C=O) ratio for the FL-CN<sub>x</sub>-03 and FL-CN<sub>x</sub>-06 samples. However, this ratio increased for the FL-CN<sub>x</sub>-10 and FL-CN<sub>x</sub>-20 samples. This C-O/C=O ratio trend mirrors the surface wettability relation from the contact angle measurements shown in Figure 4.2. The carboxyl and phenol groups are typically the functional groups associated with surface wettability. However, the ether group concentration seems to have a greater influence on the changes in the surface wettability measurements.

XANES spectroscopy of the N1s and O1s regions were also obtained and The N1s K-edge XANES spectra for the films are shown in Figure 4.7(a). The at.% N for the FL-CN<sub>x</sub>-00 sample was very low, so the signal to noise was very poor, so it is not shown. The FLY is more bulk sensitive, and it provides a probing depth on the order of 100nm. The spectral features are the result of transitions from electrons in the N1s core level being excited to the  $\pi$ -like final unoccupied states. The spectra for all films are very similar, and the 3 major  $\pi^*$  bands centered at 398.4 eV, 399.3 eV, and a small band at approximately 401.0 eV can be attributed to pyridinic, nitrogen containing aromatics, and graphitic functional groups respectively. The broad band associated with  $\sigma^*$  (sensitive to bond lengths) is centered at 407 eV. The relative  $\pi^*/\sigma^*$  ratio for the FL-CN<sub>x</sub> films was the range of 0.92-0.98, indicating that there was very little change in the N delocalization within the different films. The peak height intensity  $\pi^*_1/\pi^*_2$  ratio is shown in Figure 4.7(b) is lower for the FL-CN<sub>x</sub>-03 film, indicating a lower pyridinic N in the film. However, the  $\pi^*_1/\pi^*_2$  ratio increases for the FL-CN<sub>x</sub>-06 film and appears to level off for the FL-CN<sub>x</sub>-10 and FL-CN<sub>x</sub>-20

samples. This was also observed from the XPS measurements shown in Figure 4.6, and suggests that the bulk and surface nitrogen configuration is similar.

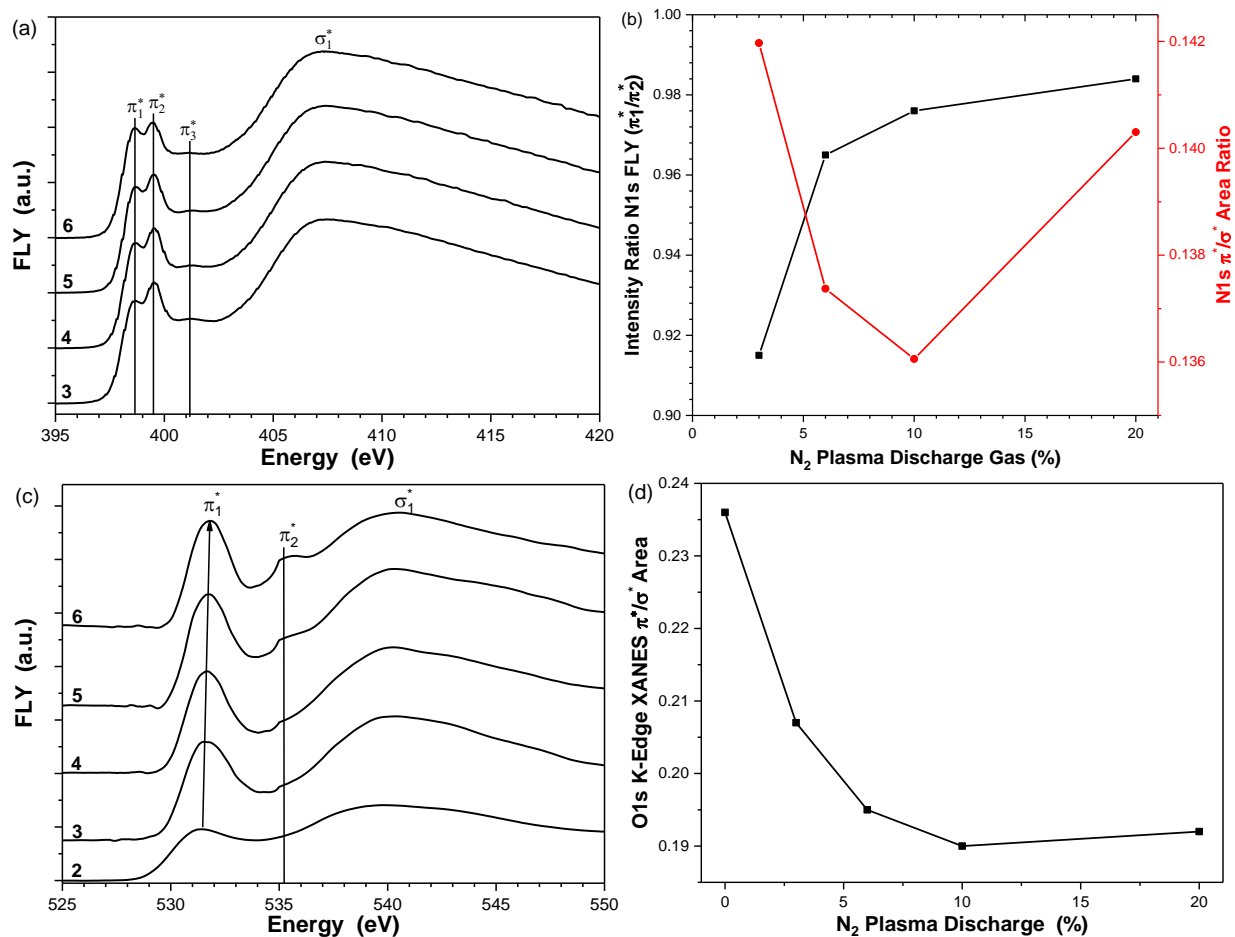


**Figure 4.7.** XANES FLY spectra of FL-CN<sub>x</sub> films prepared under different %N<sub>2</sub> plasma discharge gas. (2) FL-CN<sub>x</sub>-00 (3) FL-CN<sub>x</sub>-03 (4) FL-CN<sub>x</sub>-06 (5) FL-CN<sub>x</sub>-10 (6) FL-CN<sub>x</sub>-20. (a) N1s FLY spectra (b) The N1s  $\pi_1^*/\pi_2^*$  intensity ratio as a function of %N<sub>2</sub> plasma discharge gas used during film preparation. (c) O1s FLY spectra. (d) Relative K-edge FLY XANES  $\pi^*/\sigma^*$  areas for films prepared with different %N<sub>2</sub> plasma discharge.

The O1s K-edge XANES spectra for the films is shown in Figure 4.7(c). The O1s  $\pi^*$  resonances appear around 528-534 eV and the broad  $\sigma^*$  resonances appear from 535-550 eV. The O1s K-edge was 530.1 eV for the FL-CN<sub>x</sub>-00 film and shifts to 530.5-530.7 eV for the FL-CN<sub>x</sub>-03 to FL-CN<sub>x</sub>-20 films. This shift could be due to the at.% (N/C) ratio increasing within the films, or the decrease in metal oxides within the films. The main band is centered at 531.2 eV and it is associated with  $1s \rightarrow \pi^*(C=O)$ . There are gradual shifts to 531.7 eV ( $1s \rightarrow \pi^*(O-C=O)$  carboxyl groups) as the %N<sub>2</sub> plasma discharge gas increases during film formation.<sup>190</sup> The relative  $\pi^*/\sigma^*$

ratio is shown in Figure 4.7(d) decreased with increasing nitrogen in the film at.% (N/C) showing less  $\pi$ -character contribution from O sites as the at.% (N/C) increases within the film.

The valence band spectra for the metal-doped FL-CN<sub>x</sub> films shown in Figure 4.8 provide important information of the electronic structure near the Fermi level. Since the Al x-ray source was used for measurements, the resulting valence band spectra are a mixture of surface and bulk electronic structure. The spectra presented in Figure 4.8 are used for purely qualitative purposes and they show that the electronic structure near the Fermi level are different for the FL-CN<sub>x</sub> films. The valence band spectrum of PTFE shows a relatively flat line in the 0-6 eV region, and the large band in the 10-12 eV region is associated with the C-F bonding (F2p band). The 15-25 eV region also reveals several bands associated C-C bonds.<sup>191</sup>

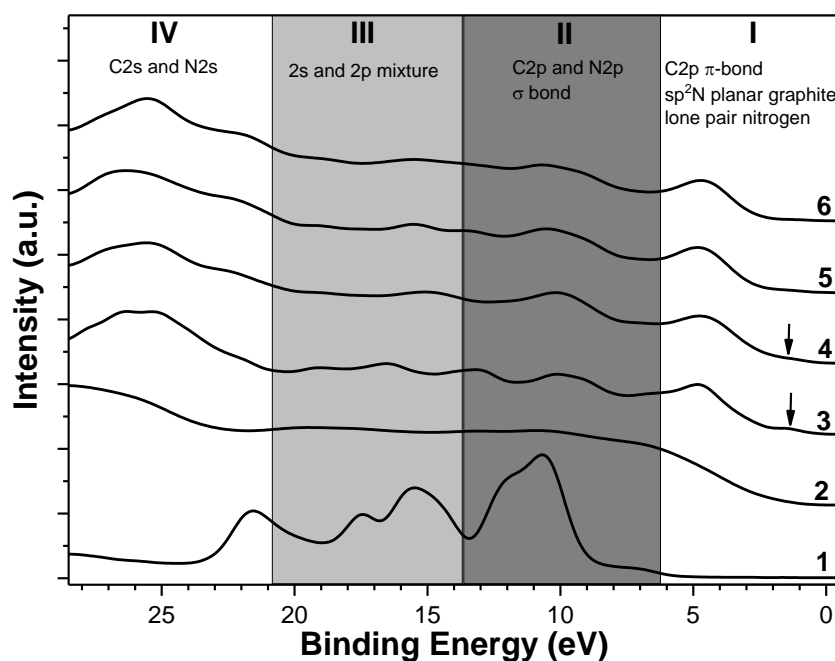


**Figure 4.8.** Valence Band XPS (Al K $\alpha$  = 1486.6 eV) measurements for the FL-CN<sub>x</sub> films prepared with different %N<sub>2</sub> plasma discharge gas. (1) PTFE (2) FL-CN<sub>x</sub>-00 (3) FL-CN<sub>x</sub>-03 (4) FL-CN<sub>x</sub>-06 (5) FL-CN<sub>x</sub>-10 (6) FL-CN<sub>x</sub>-20.

Table 4.5 summarizes the observed valence band peaks for the FL-CN<sub>x</sub> samples. In general, 4 different regions have been identified for a-C:N<sup>192</sup>: (I) 0-6.2 eV is associated with C-C  $\pi$  bonds from C 2p electrons as well as sp<sup>2</sup> N in a planar graphite structure; (II) 6.2-13.7 eV is a contribution of C 2p and N 2p electrons associated with  $\sigma$  bonds; (III) 13.7-20.8 eV is associated with a mixture of 2s and 2p electrons (IV) 20.8-30 eV is due to C 2s and N 2s electrons. The valence band spectrum for the FL-CN<sub>x</sub>-00 has a broad increase in intensity to approximately 7.3 eV, and broad

peaks centered at 10.8 eV, 13.1 eV, and 19.4 eV and are attributed to s-p hybridized states.<sup>192</sup> There is a broad increase beyond 20 eV which is attributed to the C2s electrons. The introduction of nitrogen into the FL-CN<sub>x</sub> films shows significant changes in the FL-CN<sub>x</sub> valence band spectra. The FL-CN<sub>x</sub>-03 and FL-CN<sub>x</sub>-06 films have a new band centered at 1.6 eV that is associated with lone pairs from nitrogen. This band disappears for the FL-CN<sub>x</sub>-10 and FL-CN<sub>x</sub>-20 films. All of the FL-CN<sub>x</sub> films prepared with nitrogen have a band centered at 4.7 eV. The significant differences of the valence band spectra for the FL-CN<sub>x</sub> films are more pronounced in the >7 eV regions. For instance, the FL-CN<sub>x</sub>-06 film has distinguishing bands at 10.1 eV, 13.2 eV, 16.6 eV, and 19.1 eV. There is also a doublet band 25.3 eV and 26.3 eV associated with C2s and N2s electrons. The FL-CN<sub>x</sub>-06 to FL-CN<sub>x</sub>-20 films shows a change in the band structure in areas (II) and (III). For instance, the band centered at 10.12 eV for FL-CN<sub>x</sub>-03 shifts to 10.3 for the FL-CN<sub>x</sub>-06 film and shifts to 10.6 eV for the FL-CN<sub>x</sub>-20 film. Also, a new band found at 15.1 eV for the FL-CN<sub>x</sub>-06 film shifts to 15.5 eV for the FL-CN<sub>x</sub>-20. In addition, a band appearing as a shoulder around 22.5 eV shoulder becomes more predominant as the %N<sub>2</sub> plasma discharge gas was increased in the FL-CN<sub>x</sub> films.

**Table 4.5.** Valence band XPS (Al K $\alpha$  = 1486.6 eV) for FL-CN<sub>x</sub> films.

Valence Band Peaks (eV)					Assignment
FL-CN <sub>x</sub> -00	FL-CN <sub>x</sub> -03	FL-CN <sub>x</sub> -06	FL-CN <sub>x</sub> -10	FL-CN <sub>x</sub> -20	
	1.7	1.7			(I) Nitrogen Lone Pairs, C-C $\pi$ bonds, sp <sup>2</sup> N planar graphite
	4.7	4.7	4.7	4.7	
10.8	10.1	10.3	10.6	10.6	(II) C2p and N2p $\sigma$ bonds
13.1	13.2				
		15.1	15.5	15.5	(III) 2s and 2p electrons
	16.6				
19.4	19.1				
	22.5*	22.5*	22.5*	22.5*	(IV) C2s and N2s electrons
	25.3, 26.3				

\* Shoulder

#### 4.1.2. Metal Incorporation into FL-CN<sub>x</sub> Matrix

It was discovered during XANES experiments that there was some additional metal incorporation, mainly Fe, during film deposition. XRF is a sensitive technique to measure the presence of different metal content within the FL-CN<sub>x</sub> films, so it was employed to find all of the metal present in the films. Samples were mounted on a Si wafer substrate and the spectra were

collected with the pink beam (polychromatic) which produces a broad Compton scattering band at energies greater than 9000 eV. In addition, 3 large bands centered at approximately 10.4 keV, 14.5 keV, and 16.5 keV originate from the single crystal Si wafer substrate used to mount the FL-CN<sub>x</sub> films, and the 10.4 keV band was used to normalize the spectra. Figure 4.1(a) shows the XRF for the different FL-CN<sub>x</sub> samples. The major transition metals found include Fe, Ni, Mn, Cr, Cu, and W. The significant bands shown in Figure 4.9(a) show the presence of Fe ( $K_{\alpha 1} = 6404$  eV,  $K_{\beta 1} = 7058$  eV), Ni ( $K_{\alpha 1} = 7478$  eV), W ( $L_{\alpha 1} = 8398$  eV,  $L_{\beta 1} = 9672$  eV), Cr ( $K_{\alpha 1} = 5899$  eV), and smaller bands show Cr ( $K_{\alpha 1} = 5415$  eV), Mn ( $K_{\alpha 1} = 5899$  eV), and Cu ( $K_{\alpha 1} = 8048$  eV).<sup>193</sup> Integration of the  $K_{\alpha}$  bands shown in Figure 4.9(b) show that the metal band areas decrease as a function of %Ar in the plasma discharge. The Ar<sup>+</sup> ions are very commonly used to sputter surfaces to clean metal oxides and other contaminants from surfaces. Within the deposition chamber, the Ar<sup>+</sup> ions will also be attracted to d.c. biased metal surfaces that have been improperly shielded or should not be present in plasma discharge apparatus. This includes Cu feed-throughs, W filament, Ni substrate holder, stainless steel bolts/nuts (Fe, Mn, Cr).

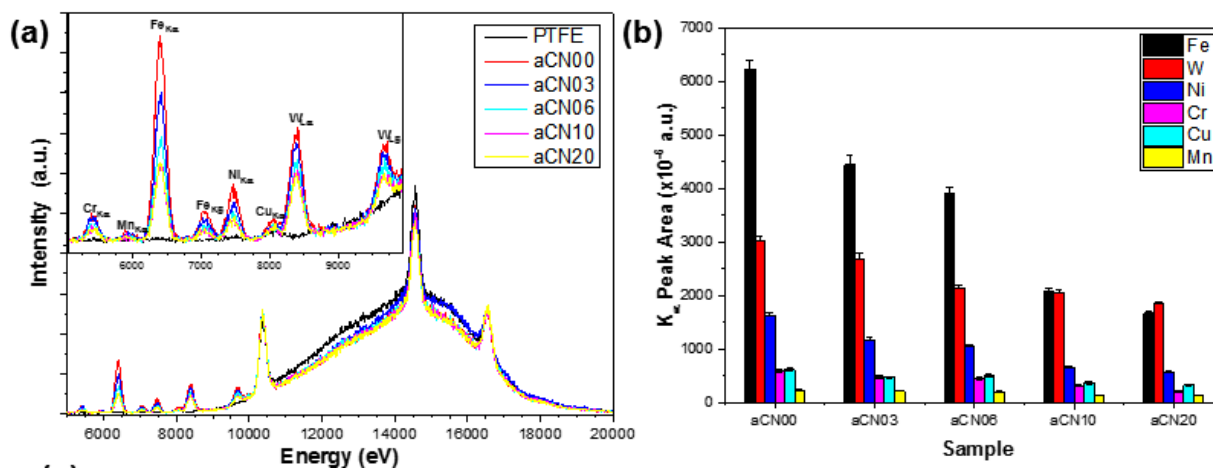


**Figure 4.9.** (a) XRF spectra of FL-CN<sub>x</sub> films indicating the presence of different transition metals within the FL-CN<sub>x</sub> matrix. (b) The distribution of metals within samples decreases as a function of the %N<sub>2</sub> discharge gas used during film deposition.

High resolution XPS measurements of the W4f region are shown in Figure 4.10. The amount of W in the FL-CN<sub>x</sub> samples was approximately 0.1 at.% for all samples and indicates that there are no measurable effects by XPS from the different amounts of N<sub>2</sub> in the plasma discharge. The FL-CN<sub>x</sub>-00 and films showed 2 primary bands centered at 35.8 eV (W1) and 38.0 eV (W2) correspond to the W4f<sub>7/2</sub> and W4f<sub>5/2</sub> bands for WO<sub>3</sub>, respectively.<sup>194-195</sup> These two bands of WO<sub>3</sub> shifted to lower energies of 35.5 eV and 37.7 eV, respectively for the FL-CN<sub>x</sub>-03 film. Two

additional bands centered at 33.6 eV (W3) and 35.8 eV (W4) appeared in the FL-CN<sub>x</sub>-06 film. These new bands correspond to the W4f<sub>7/2</sub> and W4f<sub>5/2</sub> bands for WO<sub>2</sub>.<sup>195</sup> The relative at.% of the WO<sub>2</sub> and WO<sub>3</sub> content shown in Figure 4.10(b) shows that the concentration of WO<sub>2</sub> increased in at the expense of the concentration of WO<sub>3</sub> within the film as the larger amount of %N<sub>2</sub> plasma discharge gas used during FL-CN<sub>x</sub> deposition. There is no evidence of WC<sub>x</sub> or WN<sub>x</sub> which would appear around 31-32 eV.<sup>195</sup> Therefore, it can be concluded that the W incorporated in the FL-CN<sub>x</sub> films are in an oxide state and there is no evidence to suggest some kind of bonding or incorporation into the FL-CN<sub>x</sub> structure.

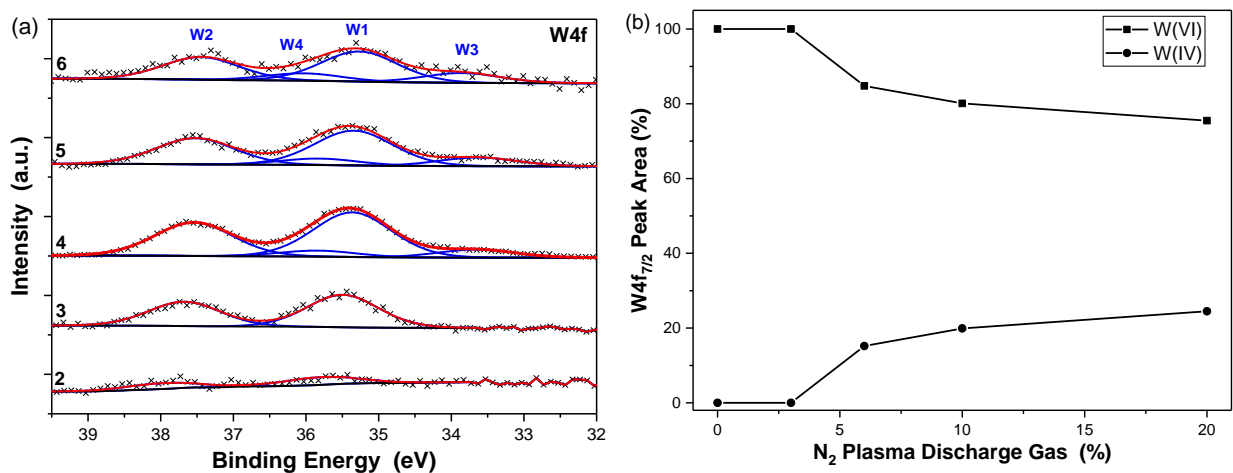


**Figure 4.10.** High resolution XPS of W4f region shows the presence of WO<sub>x</sub> in the FL-CN<sub>x</sub> films prepared with different %N<sub>2</sub> in the plasma discharge: (2) FL-CN<sub>x</sub>-00 (3) FL-CN<sub>x</sub>-03 (4) FL-CN<sub>x</sub>-06 (5) FL-CN<sub>x</sub>-10 (6) FL-CN<sub>x</sub>-20. (b) The composition of the WO<sub>x</sub> is dependent on the %N<sub>2</sub> in the plasma discharge gas.

The high resolution XPS measurements of the Fe2p region is shown in Figure 4.11. There are many types of Fe-oxides that are known to co-exist within deposits, and quantifying the different Fe-oxides, each having overlapping binding energies, can lead to erroneous interpretation.<sup>196</sup> Therefore, the Fe2p XPS spectral interpretation is used for qualitative purposes only. The Fe2p spectrum for FL-CN<sub>x</sub>-00 film (2) showed asymmetric bands centered at approximately 711.4 eV (Fe2p<sub>3/2</sub>) and 724.8 eV (Fe2p<sub>1/2</sub>). These bands are very comparable to Fe(III) hydroxy-oxides such as αFeOOH (goethite), and γFeOOH (lepidocrocite) which have major Fe2p<sub>3/2</sub> core lines at 711.4 eV, and 711.5 eV, respectively.<sup>197-198</sup> A slight shoulder around 714 eV has been attributed to an Fe<sup>3+</sup> surface band, which has been suggested to arise from changes in the crystal field energy of surface versus bulk Fe(III).<sup>199</sup>

The addition of N<sub>2</sub> in the plasma discharge gas during film deposition changed the main band center of symmetry and downshifted the Fe2p<sub>3/2</sub> and Fe2p<sub>1/2</sub> regions to 709.7 eV and 723.3

eV, respectively. These bands P for the FL-CN<sub>x</sub>-03 and FL-CN<sub>x</sub>-06 films. These bands are consistent with FeO (wüstite - band center of symmetry is 709.5 eV).<sup>198, 200</sup> It is also possible for the presence of Fe<sub>3</sub>O<sub>4</sub> (magnetite) which contains a mixture of Fe<sup>2+</sup> and Fe<sup>3+</sup> ions. A second defined band centered at approximately 714 eV can be attributed to a Fe<sup>2+</sup> satellite band.<sup>198, 200</sup>

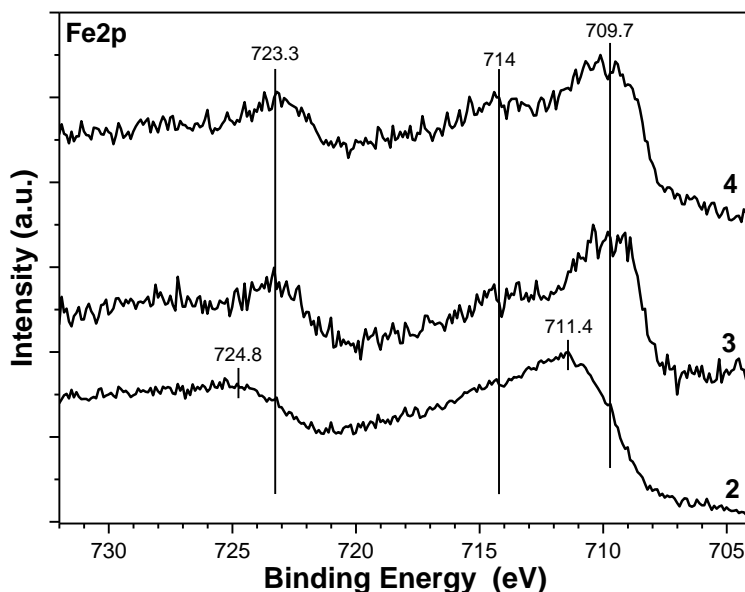


**Figure 4.11.** (a) High resolution XPS of Fe2p region for FL-CN<sub>x</sub> films prepared with different %N<sub>2</sub> in the plasma discharge gas: (2) FL-CN<sub>x</sub>-00 (3) FL-CN<sub>x</sub>-03 (4) FL-CN<sub>x</sub>-06.

The Fe L-edge XANES is a sensitive technique that involves the resonant excitation of electrons from a core 2p level localized on the Fe to partially filled and unoccupied density of electronic states of the 3d in the material from the 2p<sub>1/2</sub>→3d (L<sub>2</sub>) and 2p<sub>3/2</sub>→3d (L<sub>3</sub>) transitions. The 2p→3d transition is localized on the metal center due to the localized nature of the Fe 2p orbital. Therefore, the L-edge intensity is directly proportional to the amount of metal d-character in the unoccupied orbitals. The energy positions and intensities have contributions from the effective nuclear charge of the metal and the ligand field splitting of its d orbitals. In addition, the spectral line shape of the L-edge XANES is sensitive to the ligand field, 2p spin-orbit coupling, 3d spin-orbit coupling, and multiplet effects.

The peak positions, peak differences ( $\Delta E$ ), intensity ratios ( $I_A/I_B$ ), and the branch intensity ratio ( $I_{L3}/(I_{L3}+I_{L2})$ ) are summarized in **Error! Reference source not found.** and measured from the Fe L<sub>2,3</sub>-edge XANES of the Fe present in the films is shown in Figure 4.12(a). The XANES measurements were collected in both TEY and FLY detection modes simultaneously. The Fe-L<sub>3</sub>-edge spectra for the FL-CN<sub>x</sub>-00 film is dominated by 2 main bands labelled A (707.6 eV) and B

(709.0 eV) and have a similar spectral lineshape found for Fe<sub>2</sub>O<sub>3</sub> or FeO(OH) structure.<sup>201-203</sup> In an octahedral environment, the 3d orbitals will be split into the lower energy t<sub>2g</sub> orbitals (band A) and the higher energy e<sub>g</sub> orbitals (band B) which are separated by the crystal field splitting parameter (10Dq). The lineshape of (2) in Figure 4.12(a) and the energy difference between bands A and B can be accounted for by the strong crystal field splitting parameter (10Dq=1.45 eV) for an α-Fe<sub>2</sub>O<sub>3</sub> type structure.<sup>203</sup> The FLY and TEY spectra resemble the reference spectra shown in Figure 4.12(b) for α-Fe<sub>2</sub>O<sub>3</sub>, α-FeOOH, and β-FeOOH. The energy difference for both the TEY and FLY spectra are 1.4 eV, but the peak height intensity ratios (I<sub>A</sub>/I<sub>B</sub>) and the intensity branching ratios (IB) are slightly different (TEY: I<sub>A</sub>/I<sub>B</sub>=0.53, IB = 0.78; FLY: I<sub>A</sub>/I<sub>B</sub>=0.50, IB = 0.70). This slight change in the I<sub>A</sub>/I<sub>B</sub> ratios could be due to the presence of hydroxyl ligands near the more oxygen rich surface. The presence of hydroxyl ligands in the FeOOH structure was found to lower the I<sub>A</sub>/I<sub>B</sub> ratio values relative to pure oxide phases.<sup>204</sup> The higher band ratio for the TEY indicates higher unoccupied 3d states of Fe<sup>3+</sup> near the surface compared the bulk.

**Table 4.6.** Fe L-edge XANES analysis for FL-CN<sub>x</sub> films prepared with different %N<sub>2</sub> plasma discharge gas.

Sample	Fe L <sub>3</sub> Edge				
	A (eV)	B (eV)	ΔE (eV)	I <sub>A</sub> /I <sub>B</sub>	Branch Intensity Ratio I <sub>L3</sub> /(I <sub>L3</sub> +I <sub>L2</sub> )
<b>TEY</b>					
FL-CN <sub>x</sub> -00	707.6	709.0	1.4	0.53	0.78
FL-CN <sub>x</sub> -03	707.4	708.9	1.5	1.32	0.77
FL-CN <sub>x</sub> -06	707.3	709.2	1.9	1.41	0.76
FL-CN <sub>x</sub> -10	707.3	709.2	1.9	1.80	0.74
FL-CN <sub>x</sub> -20	707.3	709.2	1.9	3.06	0.72
<b>FLY</b>					
FL-CN <sub>x</sub> -00	707.6	709.0	1.4	0.50	0.70
FL-CN <sub>x</sub> -03	707.4	709.2	1.8	1.03	0.71
FL-CN <sub>x</sub> -06	707.3	709.2	1.9	1.20	0.69
FL-CN <sub>x</sub> -10	707.3	709.2	1.9	1.37	0.67
FL-CN <sub>x</sub> -20	707.4	709.2	1.8	1.36	0.67

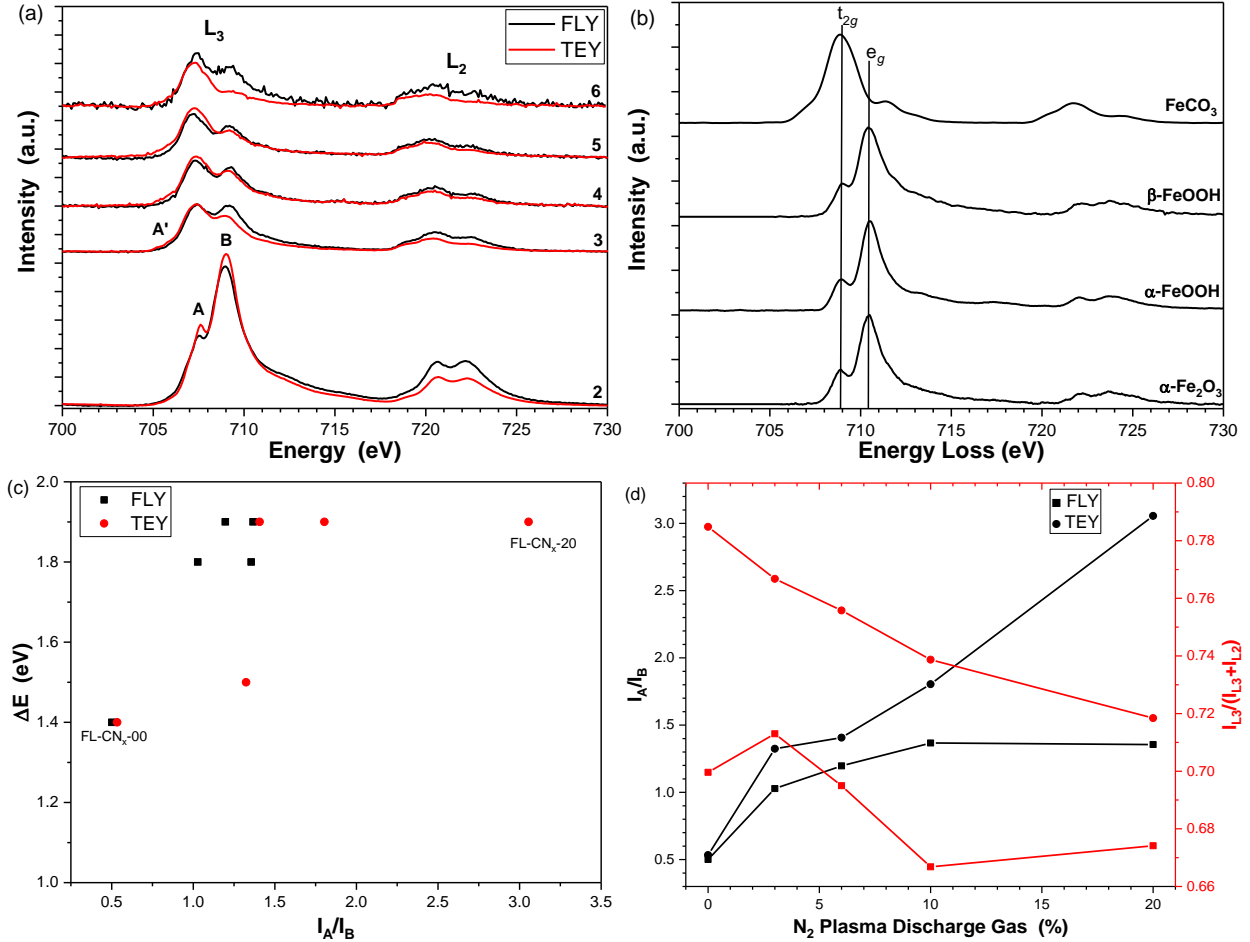


**Figure 4.12.** (a) Fe L-edge XANES measurements of FL-CN<sub>x</sub> films prepared with different %N<sub>2</sub> in the plasma discharge: (2) FL-CN<sub>x</sub>-00 (3) FL-CN<sub>x</sub>-03 (4) FL-CN<sub>x</sub>-06 (5) FL-CN<sub>x</sub>-10 (6) FL-CN<sub>x</sub>-20. The XANES spectra were normalized to the L<sub>3</sub> region's inflection point. (b) Electron energy loss spectroscopy reference spectra for some different iron oxides.<sup>205</sup> (c) The energy difference between band B and band A as a function of the peak height intensity ratio I<sub>A</sub>/I<sub>B</sub>. (d) the I as a function of N<sub>2</sub> in the plasma discharge gas.

The addition of N<sub>2</sub> into the plasma discharge gas during film deposition shows very different Fe-L<sub>3</sub> edge XANES spectra compared to the FL-CN<sub>x</sub>-00 film. There is a lower energy shoulder located at approximately 705.5 eV (band A') which has been observed in Fe<sup>2+</sup> containing oxides such as magnetite (Fe<sub>3</sub>O<sub>4</sub>) and wusite (FeO).<sup>205-207</sup> This shoulder is also present for the FeCO<sub>3</sub> reference spectrum shown in Figure 4.12(b). This shoulder is more prevalent in the TEY compared to the FLY spectra, indicating more surface Fe<sup>2+</sup> compared to bulk Fe<sup>2+</sup>. The high resolution Fe2p XPS measurements from Figure 4.11 indicate the major signal near the surface was from Fe(II)-oxide.

The most significant changes in the Fe L-edge spectra for the FL-CN<sub>03-20</sub> films are the following: (1) the ΔE between the t<sub>eg</sub> and e<sub>g</sub> bands increases to 1.8-1.9 eV (faster rate increase for

the FLY compared to the TEY), (2) the  $I_A/I_B$  ratio increases as a function of %N<sub>2</sub> in the plasma discharge gas during film deposition. This ratio plateaus for the FLY spectra, but it continues to increase for the TEY spectra. The origin of the changing band ratio appears to be a decrease in the intensity of band B for both the FLY and TEY. (3) the branching ratio decreases linearly as a function of %N<sub>2</sub> used in the plasma discharge gas for the TEY spectra, and it decreases and plateaus for the FLY spectra.

The intensity of band A remains relatively the same for both FLY and TEY measurements for a particular N<sub>2</sub> fraction. On the other hand, the intensity of band B is greatly reduced and is different for the FLY and TEY measurements, and it can be the primary cause of the increase in the  $I_A/I_B$  ratio. The  $I_A/I_B$  ratio and  $\Delta E$  have been suggested as a quick evaluation method for iron oxide speciation in minerals, where  $I_A/I_B > 1$  and  $\Delta E = 1.2-1.7$  eV are generally observed for Fe<sup>2+</sup>/Fe<sup>3+</sup> mixed minerals and pure Fe<sup>2+</sup> minerals ( $I_A/I_B = 1.5-2.2$ ,  $\Delta E = 2.1-2.8$  eV).<sup>204, 208</sup> The changes in Fe<sup>2+</sup> and Fe<sup>3+</sup> distributions in the surface and bulk have also been observed for Fe-doped Bi<sub>2</sub>Te<sub>3</sub>.<sup>209</sup> In addition, it was observed that the Fe<sup>2+</sup> concentration increased as the sample aged after 1 year.

ESR is a spectroscopic technique that measures the absorption of the electron spin of unpaired electrons within a substance. It is very useful for studying 3d transition metals that contain unpaired electrons. In general, The Fe<sup>3+</sup> is ESR active when in a 3d<sup>5</sup> high spin configuration (6S ground state, and  $S = 5/2$ ). The ESR spectra for the FL-CN<sub>x</sub> films taken at 10 K are shown in Figure 4.13. The ESR signal is a combination of the FL-CN<sub>x</sub>,<sup>210-211</sup> free radicals trapped within the PTFE matrix during plasma deposition,<sup>212</sup> and Fe<sup>3+</sup> signals.<sup>213</sup> Using an X-band frequencies (9.5 GHz), the Fe<sup>3+</sup> typically give absorption bands at g-factor values around 10, 4.3, and 2. These g-factor values are attributed to the Fe<sup>3+</sup> symmetry. For instance, absorption bands at approximately  $g = 4.3$  are attributed to Fe<sup>3+</sup> in a tetrahedral or octahedral environment with a rhombohedral distortion.<sup>214</sup> The  $g=10$  signal is generally thought to be due to Fe<sup>3+</sup> in an axial distorted environment, whereas the  $g = 2$  absorption has been attributed to Fe<sup>3+</sup> with high octahedral symmetry.

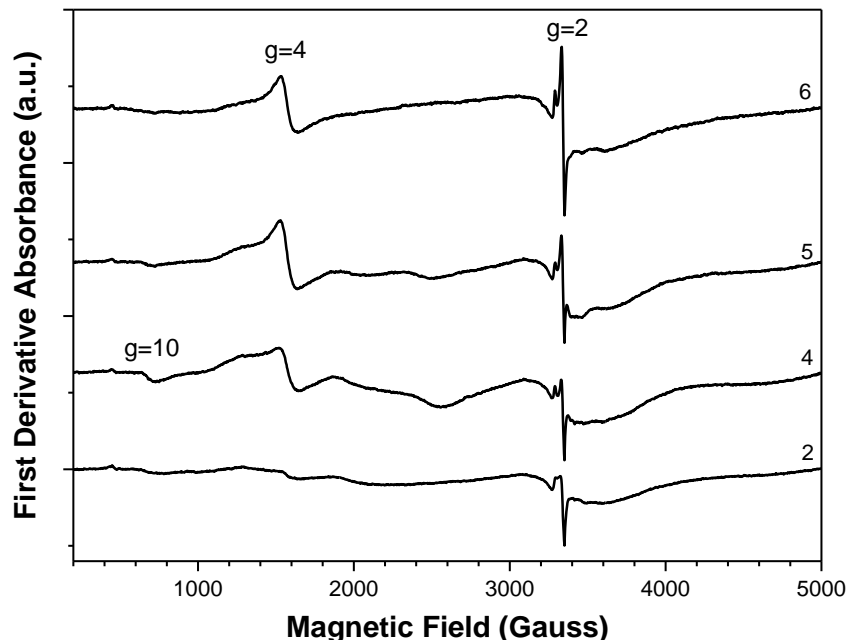


**Figure 4.13.** ESR spectra (6 K) of FL-CN<sub>x</sub> samples prepared under different %N<sub>2</sub> plasma discharge environment. (2) FL-CN<sub>x</sub>-00 (4) FL-CN<sub>x</sub>-06 (5) FL-CN<sub>x</sub>-10 (6) FL-CN<sub>x</sub>-20.

There are very small absorption bands for the FL-CN<sub>x</sub>-00 film observed at  $g = 10$  ( $\Delta H = 143$  G) and an asymmetric peak at approximately  $g = 4.3$  ( $\Delta H = 109$ ) shown in Figure 4.13. The broad band at  $g = 2.05$  ( $\Delta H = 516$  G) also has a sharp peak at  $g=2.009$  ( $\Delta H=24$ ). The broad peak for the  $g = 2$  line may be from Fe<sub>2</sub>O<sub>3</sub>,<sup>213</sup> from the amorphous carbon matrix,<sup>210-211</sup> or from free radicals found in the PTFE film from plasma deposition.<sup>212</sup> The FL-CN<sub>x</sub>-06 film shows changes in the ESR spectrum with an enhancement of the  $g = 10$  ( $\Delta H = 97$ ) and  $g = 4.3$  ( $\Delta H = 120$ ) peaks. The Fe<sup>3+</sup> signal enhancement with decreasing concentration has also been observed in Fe<sup>3+</sup> doped zeolites.<sup>213</sup> The  $g = 4.3$  peak also has a broad shoulder at approximately  $g = 5$ . The FL-CN<sub>x</sub>-10 and FL-CN<sub>x</sub>-20 films showed a gradual disappearance of the  $g = 10$  absorption peak as well as a decrease in the shoulder ( $g = 5$ ) on the  $g = 4.3$  absorption band.

#### **4.1.2.1. FL-CN<sub>x</sub> Film Discussion**

Doping a-C films has been extensively studied and found to improve biocompatible properties of the film. The type of dopant used would depend on the desired improvement. In this research, fullerene-like amorphous carbon was doped primarily with nitrogen, and it was later found out that there were some residual metals incorporated into the coating. The XPS measurements found primarily Fe and W within the coatings ( $\leq 1$  at.%), and the concentration decreased as a function of increased N<sub>2</sub> in the plasma discharge gas. Other metals, including Ni,

Cr, Mn, And Cu were also found using the more sensitive  $\mu$ -XRF technique. The source of this metal contamination is most likely from exposed metal materials that were biased (copper feedthrough, threaded bolt, iron nuts to compress W wire, metal substrate holder). The use of  $\text{Ar}^+$  within the plasma discharge gas will attack and etch any metal material that is not properly shielded, and these metals can be added within the plasma and ultimately be incorporated into the FL-CN<sub>x</sub> film.

Incorporation of transition metals into a-C films has been done to improve the tribological properties of the coating. This is mainly achieved through decreasing the internal stress within the a-C matrix and/or improving the adhesion to the substrate.<sup>16</sup> The metal distribution within metal-incorporated a-C films prepared by magnetron sputtering a metal (Ti, V, Zr, W) and graphite target produced films containing low metal concentrations (< 10 at.%).<sup>19</sup> The metal distribution within the films was suggested to be atomically dispersed within the film, and carbide particles were formed only after annealing the films. Extended x-ray absorption fine structure spectroscopy analysis measurements suggested that the Ti was surrounded by oxygen.<sup>19</sup>

In the present work, the XPS, XANES, and ESR measurements determined that the metal incorporation into the FL-CN<sub>x</sub> films were in oxide form, and there was no indication in the data that suggested there was an interaction with the carbon matrix. The most abundant metal found within the FL-CN<sub>x</sub> films was Fe, and its concentration decreased when the amount of  $\text{Ar}^+$  in the plasma discharge gas decreased. It was interesting to find that the oxidation state of Fe was dependent on the plasma discharge gas content. In the absence of  $\text{N}_2$  in the plasma discharge gas, Fe was primarily in the  $\text{Fe}^{3+}$  oxidation state as an oxide or oxyhydroxide complex. However, the addition of  $\text{N}_2$  to the plasma discharge gas during film deposition found  $\text{Fe}^{2+}$  near the surface, but there are still some  $\text{Fe}^{3+}$  in the film, as suggested from the ESR measurements. It has been reported that iron oxides near the surface of materials can be reduced to  $\text{Fe}^{2+}$ -oxides during  $\text{Ar}^+$  sputtering.<sup>197</sup> Here the  $\text{Fe}^{3+}$ -oxide loses an oxygen atom during the sputtering process, and reduces to an  $\text{Fe}^{2+}$ -oxide. Others have reported autoreduction of  $\text{Fe}^{3+}$  oxide catalysts to  $\text{Fe}^{2+}$  oxides in reducing atmospheres using  $\text{H}_2$  or He environments.<sup>215-216</sup> In a more recent publication, XANES measurements of an Fe-doped topical insulator  $\text{Bi}_2\text{Te}_3$  was found to differ in  $\text{Fe}^{2+}:\text{Fe}^{3+}$  ratio in both the surface and bulk region.<sup>209</sup>

The % $\text{N}_2$  plasma discharge gas used in the preparation of FL-CN<sub>x</sub> was found to change many different properties of the resulting FL-CN<sub>x</sub> films. The %sp<sup>2</sup> content were calculated for

these FL-CN<sub>x</sub> films deposited on PTFE from C1s XANES measurements.<sup>105</sup> In general, nitrogen doping linearly increased the %sp<sup>2</sup> carbon content to a maximum of approximately 92% for FL-CN<sub>x</sub>-10 film. However, further increasing the %N<sub>2</sub> plasma discharge did not change the %sp<sup>2</sup> content.

Biocompatible testing on the FL-CN<sub>x</sub> coatings were summarized in Dr. M. Foursa's PhD dissertation.<sup>114</sup> In general, the FL-CN<sub>x</sub> coatings did not adsorb as much fibrin compared to the uncoated PTFE substrate, resulting in reduced red blood cell adhesion. Similarly, the FL-CN<sub>x</sub> coatings had good endothelial cell and fibroblast adhesion and spreading (generally a sign of low cytotoxicity), whereas there was no adsorption observed on the uncoated PTFE substrate. A quantitative analysis of platelet adsorption and activation was also completed for the FL-CN<sub>x</sub> coatings. The platelet adhesion results presented in Dr. M. Foursa's dissertation is re-plotted and shown in Figure 4.14.<sup>114</sup> In general, the FL-CN<sub>x</sub>-00 to FL-CN<sub>x</sub>-10 films had a larger fraction of non-activated platelets observed on their surface, with a maximum non-activated platelets observed on the FL-CN<sub>x</sub>-03 film. The FL-CN<sub>x</sub>-20 film had less non-activated platelets compared to the uncoated PTFE substrate, but it also had a significant portion of the platelets in the spread and aggregated form compared to any other film. The fully spread and aggregated were also minimized for the FL-CN<sub>x</sub>-03 and FL-CN<sub>x</sub>-06 films.

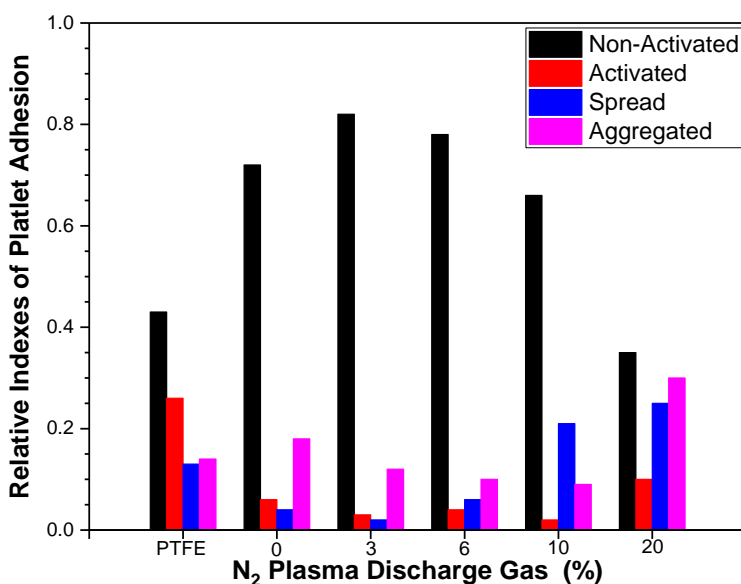


**Figure 4.14.** The relative indexes of platelet adhesion of uncoated PTFE and FL-CN<sub>x</sub> films prepared using different %N<sub>2</sub> plasma discharge gas. Platelets adsorbed onto surfaces were classified as (I) Single nonactivated; (II) Slightly activated cells with pseudopodia; (III) fully spread platelets; (IV) aggregated platelets. Figure is adapted from results presented in Dr. M. Foursa's PhD dissertation.<sup>114</sup>

The incorporation of nitrogen into the FL-CN<sub>x</sub> matrix has shown some biocompatible improvements compared to the nitrogen-free counterpart. Incorporation of smaller amounts of nitrogen correlate with a smaller %N<sub>2</sub> plasma discharge gas during film preparation. These lower amounts of at.% N found in the FL-CN<sub>x</sub>-03 and FL-CN<sub>x</sub>-06 films increased the hydrophilicity of the resulting films (Figure 4.2). However, the FL-CN<sub>x</sub>-10 and FL-CN<sub>x</sub>-20 films became more hydrophobic and increased the number of activated platelets which were observed for these films.

The G-band peak position and the I<sub>D</sub>/I<sub>G</sub> ratio measured from Raman spectroscopy on the FL-CN<sub>x</sub> films provided some additional insight regarding the changes in platelet adhesion for the films prepared with different %N<sub>2</sub> plasma discharge gas. The initial nitrogen incorporation used low %N<sub>2</sub> plasma discharge gas for the FL-CN<sub>x</sub>-03 and FL-CN<sub>x</sub>-06 films did not significantly change the G-band peak position compared to the FL-CN<sub>x</sub>-00 film. The I<sub>D</sub>/I<sub>G</sub> peak ratio also increased to a maximum for the FL-CN<sub>x</sub>-03 film and further %N<sub>2</sub> plasma discharge gas reduced this ratio. The I<sub>D</sub>/I<sub>G</sub> peak ratio for stage-2 type amorphous carbon represents an increase in order as well as an increase in aromatic clusters.<sup>173</sup> It was previously reported that there seemed to be an optimum fraction of %sp<sup>2</sup> content in the films that reduced the amount of activated platelets, but too much nitrogen reversed this trend.<sup>41</sup> Incidentally, the FL-CN<sub>x</sub> film that had the maximum I<sub>D</sub>/I<sub>G</sub> peak intensity ratio also showed the minimum of activated platelets.

The surface reactivity of the films will be a combination of surface topography, microstructure, and functional groups. Understanding the electronic structure may provide insight as to why coatings prepared under similar conditions vary in their biocompatible responses. The contact angle measurements shown in Figure 4.2 show a general trend in which the decrease in contact angle (increase in hydrophilicity) for the small amounts of at.% N in the 3-6%N<sub>2</sub> prepared films. However, the films prepared with larger amounts of %N<sub>2</sub> (10-20%) showed a significant decrease in the number of non-activated platelet cells. An increase in hydrophilicity has been shown to improve the biocompatible properties for coatings prepared under similar conditions, but it is not the sole determining factor.

### **4.1.3. Protein Interactions with Metal Incorporated FL-CN<sub>x</sub>**

#### **4.1.3.1. SPR**

The FL-CN<sub>x</sub> prepared with different amounts of N<sub>2</sub> plasma discharge gas were deposited onto commercially available Au-coated SPR sensor chips. The SPR reflectance curves, commonly

referred to as the SPR “dips”, are shown in Figure 4.15. The minimum SPR deflection angle is very sensitive to refractive index changes and correlates to changes in mass at the Au/PBS interface. The SPR reflectance minimum is centered at 10 pixel units for the bare Au film in PBS. The SPR reflectance minimum is centered at 10 pixel units for the bare Au film in PBS. The x-axis is given in the location of the SPR detector and could be converted to an SPR angle, but the manufacturer does not provide the conversion. The addition of the FL-CN<sub>x</sub> film shifts the SPR deflection angle minima to 28-35 pixel units. The thickness of FL-CN<sub>x</sub> film was approximated by AFM, and found to be approximately 10-15 nm in thickness.

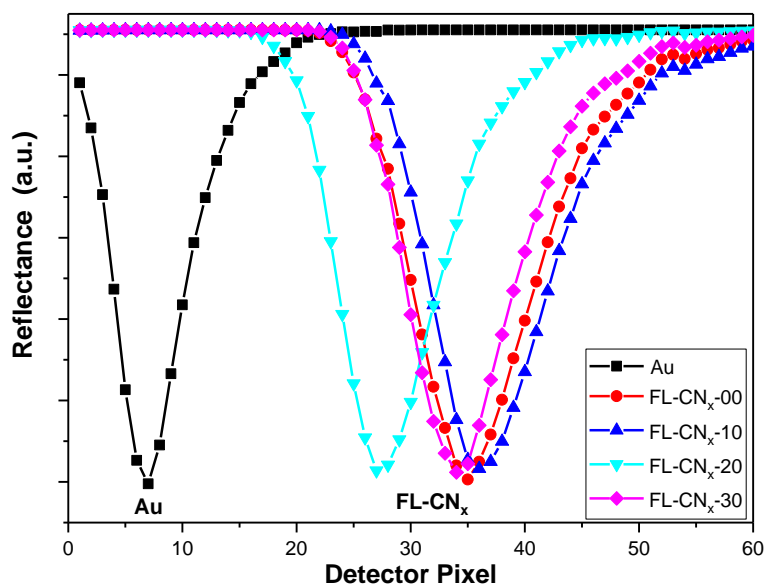


**Figure 4.15.** SPR reflectance curves for Au sensor substrate and FL-CN<sub>x</sub> films prepared from different amounts of N<sub>2</sub> plasma discharge gas ratios.

The FL-CN<sub>x</sub> film’s surface topography was measured with AFM shown in Figure 4.16. The films were very smooth and the R<sub>RMS</sub> roughness values, summarized in Table 4.7, showed a slight decrease for films prepared with N<sub>2</sub> in the plasma discharge gas. The size and shape of the nanoclusters seemed to vary. The FL-CN<sub>x</sub> films contained small individual-like and aggregated nanoclusters. In addition, there is an appearance that the nanoclusters from a more fibril-like structure or a nano-island like structure.

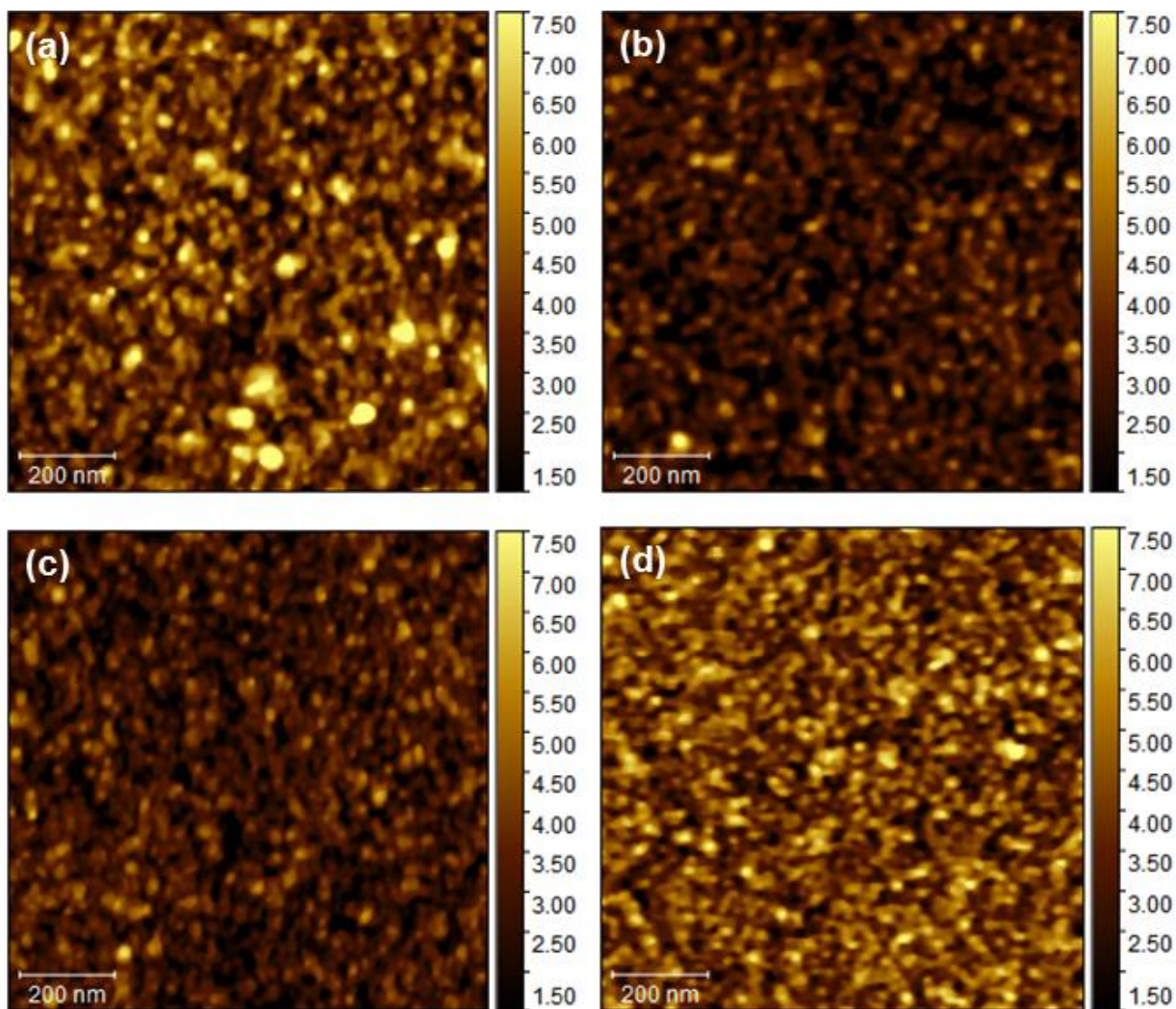


**Figure 4.16.** AFM topography images of FL-CN<sub>x</sub> films prepared with different amounts of N<sub>2</sub> plasma discharge gas: (a) FL-CN<sub>x</sub>-00; (b) FL-CN<sub>x</sub>-10; (c) FL-CN<sub>x</sub>-20; (d) FL-CN<sub>x</sub>-30. Images are 1 μm x 1 μm. The FL-CN<sub>x</sub> sample images are displayed in the same height and color scale.

**Table 4.7.** FL-CN<sub>x</sub> Film characterization prepared with different %N<sub>2</sub> plasma discharge gas and deposited on Au sensor surfaces.

Sample	AFM <sup>1</sup>	Contact Angle <sup>2</sup> (Deg)	Raman <sup>3</sup>		
	R <sub>RMS</sub> (nm)		G-Band (cm <sup>-1</sup> )	D-Band (cm <sup>-1</sup> )	I <sub>D</sub> /I <sub>G</sub> <sup>4</sup>
FL-CN <sub>x</sub> -00	2.1 (±0.3)	72.0 (±1.5)	1558 (117)	1395 (210)	0.71 (0.06)
FL-CN <sub>x</sub> -10	1.2 (±0.3)	58.3 (±3.3)	1554 (151)	1377 (219)	0.80 (0.07)
FL-CN <sub>x</sub> -20	1.6 (±0.2)	68.0 (±1.0)	1558 (139)	1380 (283)	1.09 (0.07)
FL-CN <sub>x</sub> -30	1.4 (±0.2)	70.2 (±3.4)	1556 (178)	1377 (230)	0.93 (0.04)

<sup>1</sup> R<sub>RMS</sub> values were taken from 2 μm x 2 μm areas over n = 4-5 areas.

<sup>2</sup> Contact angles were taken from n = 5-7 measurements.

<sup>3</sup> FWHM values given in brackets.

<sup>4</sup> Standard error from peak height ratios given in brackets.

Raman spectroscopy measurements for the FL-CN<sub>x</sub> films shown in Figure 4.17 and summarized in Table 4.7 revealed that the G-Band is approximately 11-17 cm<sup>-1</sup> downshifted when deposited on Au substrates (1554-1558 cm<sup>-1</sup>) compared to the PTFE substrate (1570-1577 cm<sup>-1</sup>). This G-band position indicates that the FL-CN<sub>x</sub> films are stage 2 a-C containing approximately 10-15% sp<sup>3</sup> bonds and the aromatic cluster size (L<sub>a</sub>) decreases to < 2 nm.<sup>176</sup> The FWHM of the G-band also increased with the incorporation of nitrogen into the a-C matrix, and indicates a larger variation of sp<sup>2</sup> sites within the films.<sup>173, 180</sup> The I<sub>D</sub>/I<sub>G</sub> ratio summarized in Table 4.7 showed that nitrogen incorporation increased the I<sub>D</sub>/I<sub>G</sub> ratio, showing that nitrogen incorporation induces aromatic clustering.<sup>173</sup> However, high amounts of nitrogen in the plasma discharge gas reversed this trend.

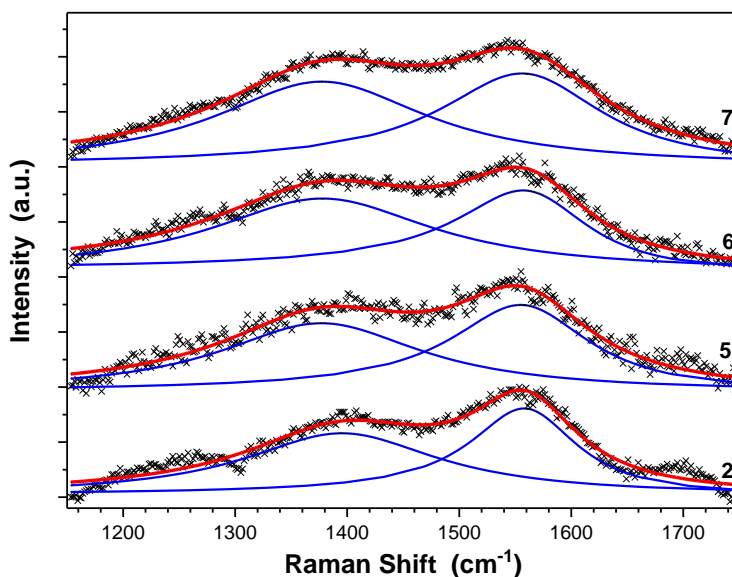


**Figure 4.17.** Raman spectroscopy of various FL-CN<sub>x</sub> films prepared with %N<sub>2</sub> plasma discharge gas. (2) FL-CN<sub>x</sub>-00; (5) FL-CN<sub>x</sub>-10; (6) FL-CN<sub>x</sub>-20; (7) FL-CN<sub>x</sub>-30.

The contact angle measurements were performed on the FL-CN<sub>x</sub> films with water, and the results are summarized in Table 4.7. The contact angle for the FL-CN<sub>x</sub>-10 film decreased compared to the FL-CN<sub>x</sub>-00 film, indicating that the nitrogen incorporation into the films decreased the film's hydrophobicity. This was similarly observed for the FL-CN<sub>x</sub> films on the PTFE substrate. However, the contact angle measurement for the FL-CN<sub>x</sub>-20 and FL-CN<sub>x</sub>-30 films increased and indicated that these films became more hydrophobic. This was also observed for the FL-CN<sub>x</sub> films deposited on the PTFE substrate.

The SPR sensorgrams of FL-CN<sub>x</sub> surface interactions with HSA and Fib are shown in Figure 4.18. The binding kinetics of the protein with the surface were fit with a 1:1 Langmuir binding model and summarized in Table 4.8. For a given protein interaction sensorgram, the running buffer flows through the flow cell continuously ( $t < 0$  s). At the beginning of the association phase, the protein solution is injected through the flow cell and exposed to the FL-CN<sub>x</sub> surface. An initial response ( $< 1$  s) is dominated by the bulk shift in refractive index due to the differences in refractive index between the running buffer and the protein solution. This is followed by an increase in response due to the protein/surface interactions which increases the mass at the surface and causes an increase in refractive index. After the association phase (0-120 s), the protein solution was stopped, and the dissociation phase (120-300 s) is started by flowing the running buffer over the flow cell surface. An initial decrease in response is generally observed near the beginning of the dissociation phase due to the change from higher refractive index protein solution to the lower refractive index running buffer. A slow decrease in the response is observed during the dissociation phase due to protein desorption from the flow cell surface.

**Table 4.8.** Kinetic analysis of (a) HSA and (b) Fib binding with FL-CN<sub>x</sub> films prepared with different %N<sub>2</sub> plasma discharge gas. Standard deviations are given in brackets.

FL-CN <sub>x</sub> Film	k <sub>a</sub> (x 10 <sup>4</sup> ) (M <sup>-1</sup> s <sup>-1</sup> )	k <sub>d</sub> (x 10 <sup>-4</sup> ) (s <sup>-1</sup> )	K <sub>D</sub> (nM)	χ <sup>2</sup>
(a) HSA				
FL-CN <sub>x</sub> -00	9.1 (5.1)	4.5 (2.2)	4.9 (2.4)	9.5
FL-CN <sub>x</sub> -10	2.7 (1.7)	5.6 (2.3)	20.7 (13.5)	4.2
FL-CN <sub>x</sub> -20	3.1 (2.4)	2.3 (0.9)	7.4 (3.8)	11.4
FL-CN <sub>x</sub> -30	9.2 (2.4)	2.8 (1.2)	3.0 (5.0)	9.4
(b) Fib				
FL-CN <sub>x</sub> -00	203 (21)	1.9 (0.7)	0.1 (0.3)	2.6
FL-CN <sub>x</sub> -10	50.6 (20)	8.2 (0.5)	1.6 (0.3)	2.9
FL-CN <sub>x</sub> -20	18.8 (8.4)	1.9 (1.1)	1.0 (1.3)	2.4
FL-CN <sub>x</sub> -30	80.9 (40)	5.2 (3.3)	0.6 (0.8)	4.0

The lateral protein interactions were minimized by keeping the protein adsorption maximum responses to approximately 200-300 RU, which was well below the R<sub>max</sub> for the FL-CN<sub>x</sub> surfaces (R<sub>max</sub> > 1200 RU for HSA). The Chi<sup>2</sup> (χ<sup>2</sup>) values provide an accuracy of the curve fitting (lower values indicate better accuracy).

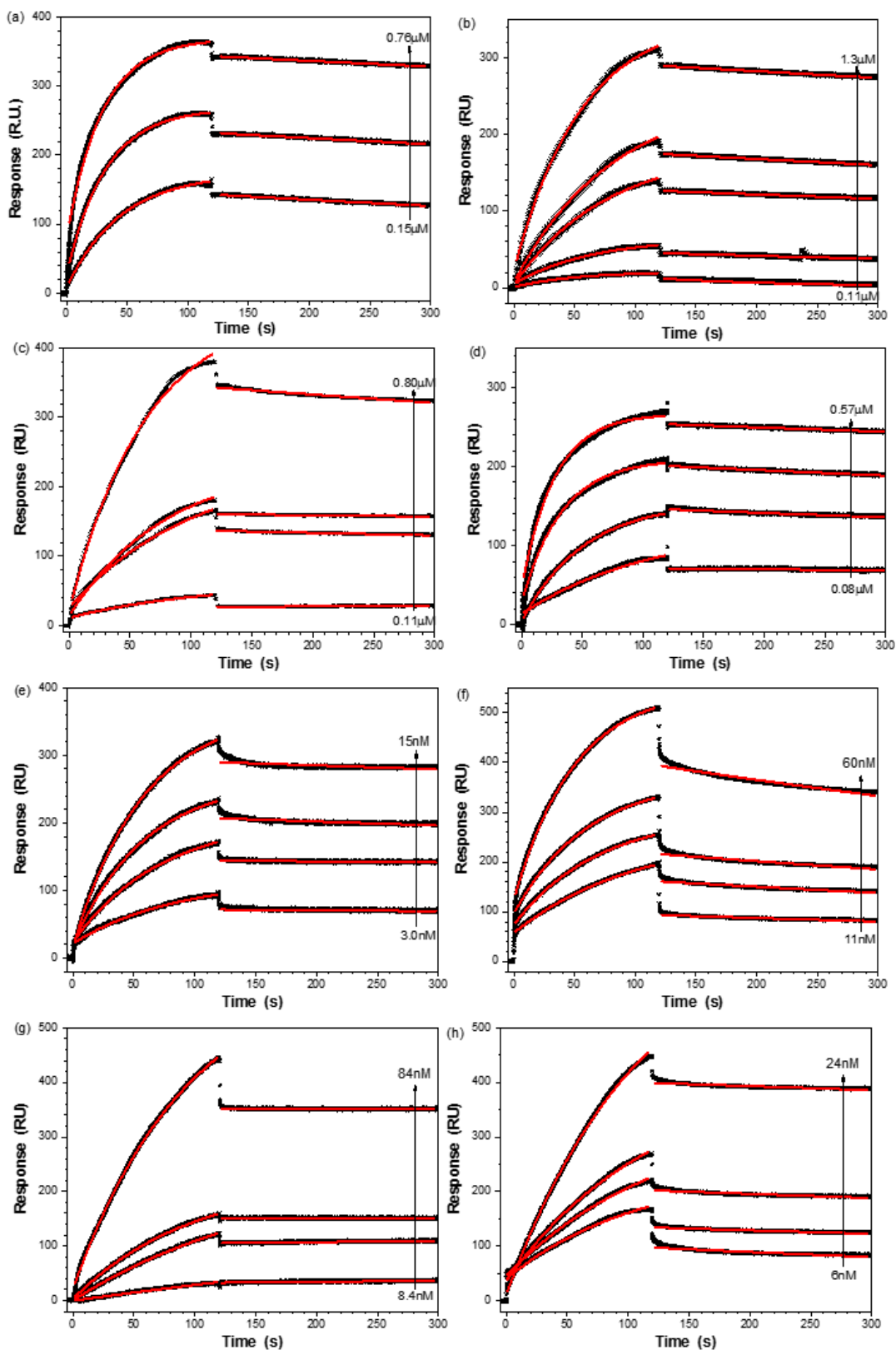


**Figure 4.18.** SPR sensorgrams of FL-CN<sub>x</sub> films interaction with (a-d) HSA and (e-h) Fib. (a,e) FL-CN<sub>x</sub>-00 (b, f) FL-CN<sub>x</sub>-10(c, g) FL-CN<sub>x</sub>-20 (d, h) FL-CN<sub>x</sub>-30.

For biomolecular interactions, the  $k_a$  measures the recognition between 2 binding partners, whereas the  $k_d$  measures the strength and stability of the binding complex. The  $k_a$  and  $k_d$  values for the FL-CN<sub>x</sub> films prepared with different %N<sub>2</sub> plasma discharge gas are shown in Figure 4.19. The  $k_d$  values for the different FL-CN<sub>x</sub> films interacting with both HSA and Fib are on the order of  $10^{-4} \text{ s}^{-1}$ , and the  $k_d$  value for each protein on a specific film are within a factor of 2. The  $k_d$  values are very stable, and the half-life ( $\tau_{1/2}$ ) calculated by Equation 4.1 is approximately 1.6 h for a  $k_d = 10^{-4} \text{ s}^{-1}$ .

$$\tau_{1/2} = \frac{\ln 2}{k_d} \quad (4.1)$$

The  $k_a$  for the protein interactions with the FL-CN<sub>x</sub> surface showed a more significant dependence on both the protein and the FL-CN<sub>x</sub> surface. The  $k_a$  for the HSA interaction showed an approximate 3-fold decrease from the FL-CN<sub>x</sub>-00 film to the FL-CN<sub>x</sub>-10 film. The  $k_a$  for the FL-CN<sub>x</sub>-20 film is very similar to the FL-CN<sub>x</sub>-10 film, but a 3-fold increase in  $k_a$  was observed for the FL-CN<sub>x</sub>-30 film. On the other hand, the  $k_a$  measured for Fib had an approximate 4-fold decrease for the FL-CN<sub>x</sub>-10 film compared to the FL-CN<sub>x</sub>-00 film. The  $k_a$  is approximately 10-fold larger for the Fib compared to the HSA. The  $k_a$  for FL-CN<sub>x</sub>-20 film decreased approximately 2.5-fold, and the FL-CN<sub>x</sub>-30 film increased by approximately 4-fold compared to the FL-CN<sub>x</sub>-20 minimum.

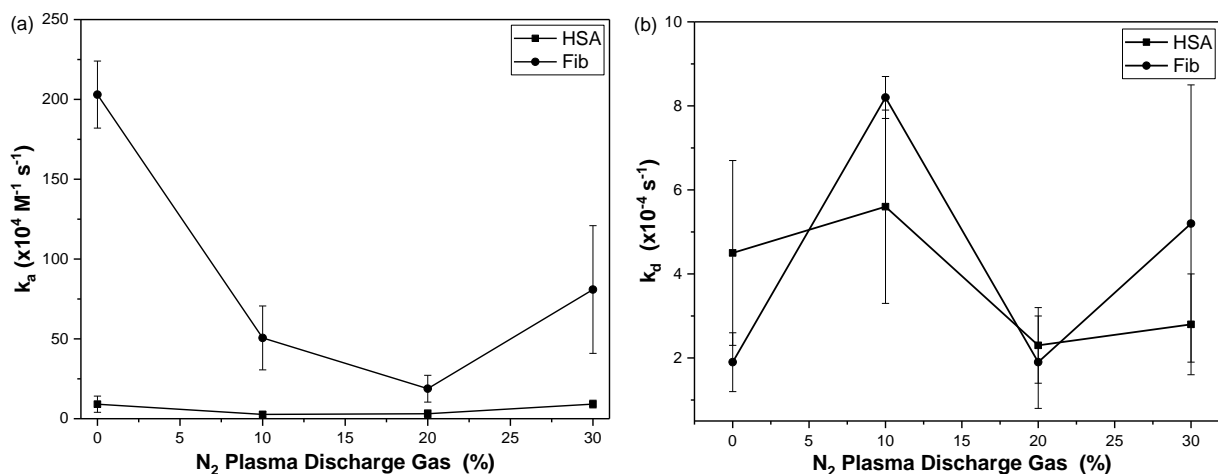


**Figure 4.19.** SPR kinetics for HSA and Fib for the FL-CN<sub>x</sub> films prepared with different %N<sub>2</sub> plasma discharge gas. (a)  $k_a$  (b)  $k_d$ .

The SPR kinetic results indicate that the  $k_a$  drives the protein surface interaction, and the incorporation of some nitrogen in the a-C matrix changes the protein/surface interaction. In general, the  $k_a$  for Fib is much larger compared to HSA (20-fold difference FL-CN<sub>x</sub>-00 film). The

$k_a$  for Fib is approximately 15-fold larger compared to the HSA interaction with the FL-CN<sub>x</sub>-10 film. However, the  $k_a$  for the FL-CN<sub>x</sub>-20 film was reduced to a 6-fold difference between Fib and HSA, but this difference increased to 9-fold difference for the FL-CN<sub>x</sub>-30 film. These differences were still lower compared to the FL-CN<sub>x</sub>-00 film.

The  $k_a$  values for each protein appear to have a correlation to the contact angle values of the FL-CN<sub>x</sub> films, as shown in Figure 4.20.

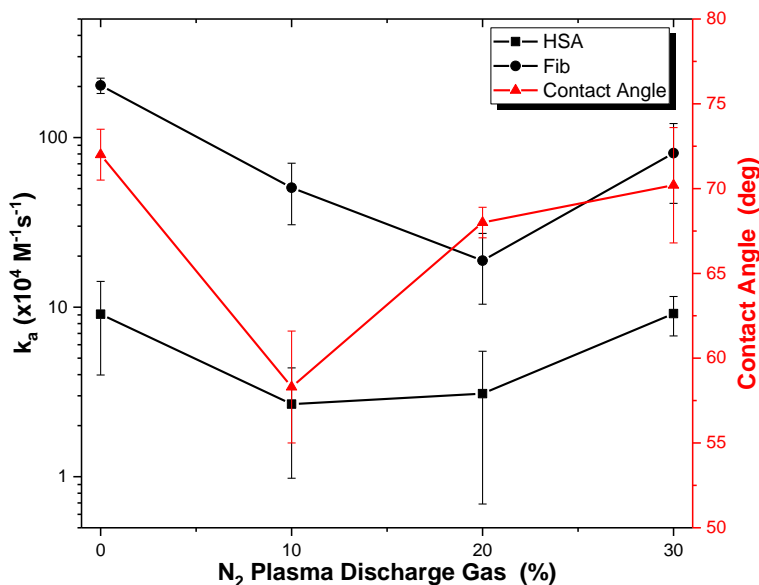


**Figure 4.20.** Comparison of the  $k_a$  kinetics of Fib and HSA with the wettability of the FL-CN<sub>x</sub> films prepared with different %N<sub>2</sub> plasma discharge gas.

Both HSA and Fib adsorption onto chemically-modified silica surfaces were found to have a strong correlation with the surface wettability.<sup>217</sup> The Fib was found to adsorb more on hydrophobic surfaces, which is a general “rule of thumb”, but it was further found that the Fib adsorption had a correlation with the surface chemistry present. It was found that the Fib adsorption increased for surfaces with the presence of sulfur (sulfonates), but the Fib adsorption decreased with the presence of nitrogen (amine groups) (chemical composition was evaluated from XPS). A detailed correlation for HSA adsorption and surface chemistry was not studied. Both proteins will adsorb onto both hydrophilic and hydrophobic surfaces, but they both preferentially adsorb onto hydrophobic surfaces.<sup>218</sup> In another study, competitive binding studies found that Fib had a higher affinity to surfaces compared to HSA, regardless of the surface wettability.<sup>219</sup> However, increasing the Fib:HSA ratio to 1:10, which is approximately similar to ratios found in plasma, the Fib adsorbed onto the surface decreased for all surfaces, with the exception of the most hydrophilic

surface. They found that the surface adsorption of Fib was independent of the Fib:HSA ratio, and the Fib was close to 100% adsorbed.

HSA is considered to be noninteracting towards platelets, and surfaces containing HSA bound layers have been found to contain less platelet adhesion. Figure 4.21 shows the Fib binding on the FL-CN<sub>x</sub>-00 film, as well as the same surface pre-treated with HSA (1200 RU immobilized). The untreated surface shows the typical association kinetics of Fib and the FL-CN<sub>x</sub> surface, and the dissociation kinetics shows approximately 1750 RU (1.75 ng/mm<sup>2</sup>) remaining on the surface after the 2 min injection. The dissociation of the Fib is very slow and the Fib/FL-CN<sub>x</sub> interaction is very stable. The same concentration of Fib was then injected over a HSA saturated surface (1200 RU), and the resulting sensorgram looks very similar a bulk refractive index shift. The association kinetics is very fast and reaches equilibrium quickly. At the end of the injection, the signal quickly dissociated and the baseline shifted by 20 RU, indicating that approximately 20 pg/mm<sup>2</sup> of Fib remained on the surface. Compared to the untreated FL-CN<sub>x</sub> surface, the HSA-treated sample reduced the Fib capacity on the surface by 88-fold. It is unclear from this measurement on whether the Fib adsorbed to the FL-CN<sub>x</sub> surface (pinholes in the HSA film), or whether the Fib adsorbed to the HSA layer. Regardless, quantitative  $k_a/k_d$  measurements revealed the significance of the initial protein binding layer and its protective nature towards Fib binding and the possible longevity of the film in a serum environment.

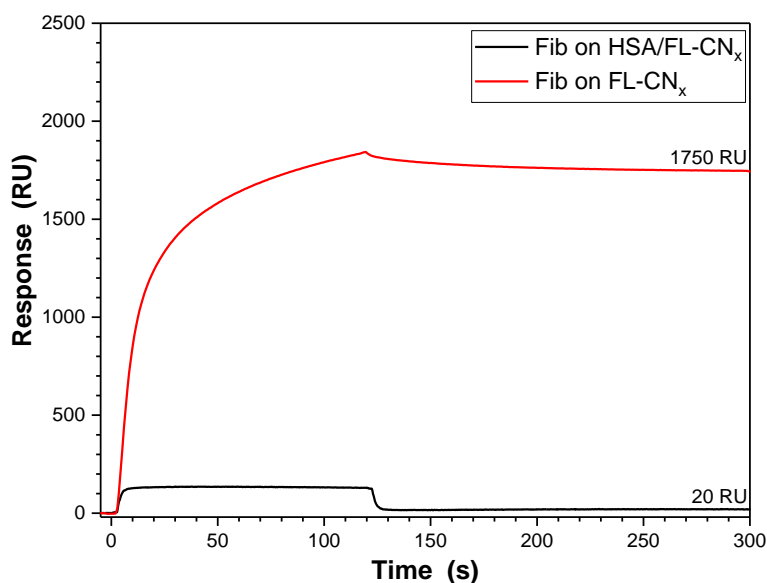


**Figure 4.21.** SPR sensorgrams of Fib (500 nM) binding to FL-CN<sub>x</sub>-00 film for the unmodified surface (red) and HSA saturated FL-CN<sub>x</sub>-00 surface (1200 RU HSA immobilized).

### 4.1.3.2. Scanning Transmission X-ray Spectroscopy (STXM)

STXM measurements had been successfully applied to measuring HSA and Fib binding onto polymer blend films.<sup>220-222</sup> This technique was applied to study the protein binding onto the FL-CN<sub>x</sub> surfaces and relate the film's electronic structure with the protein binding. The C-Kedge, N-Kedge, and O-Kedge NEXAFS spectra for the FL-CN<sub>x</sub> films are shown in Figure 4.22 and the electronic states observed are summarized in Table 4.9. Integration of the carbon, nitrogen and oxygen signals shown in Figure 4.22(d) reveals that the addition of N<sub>2</sub> into the plasma discharge gas increases the at.%N to 25-27%, while the at.%O is approximately constant at 9-11%.

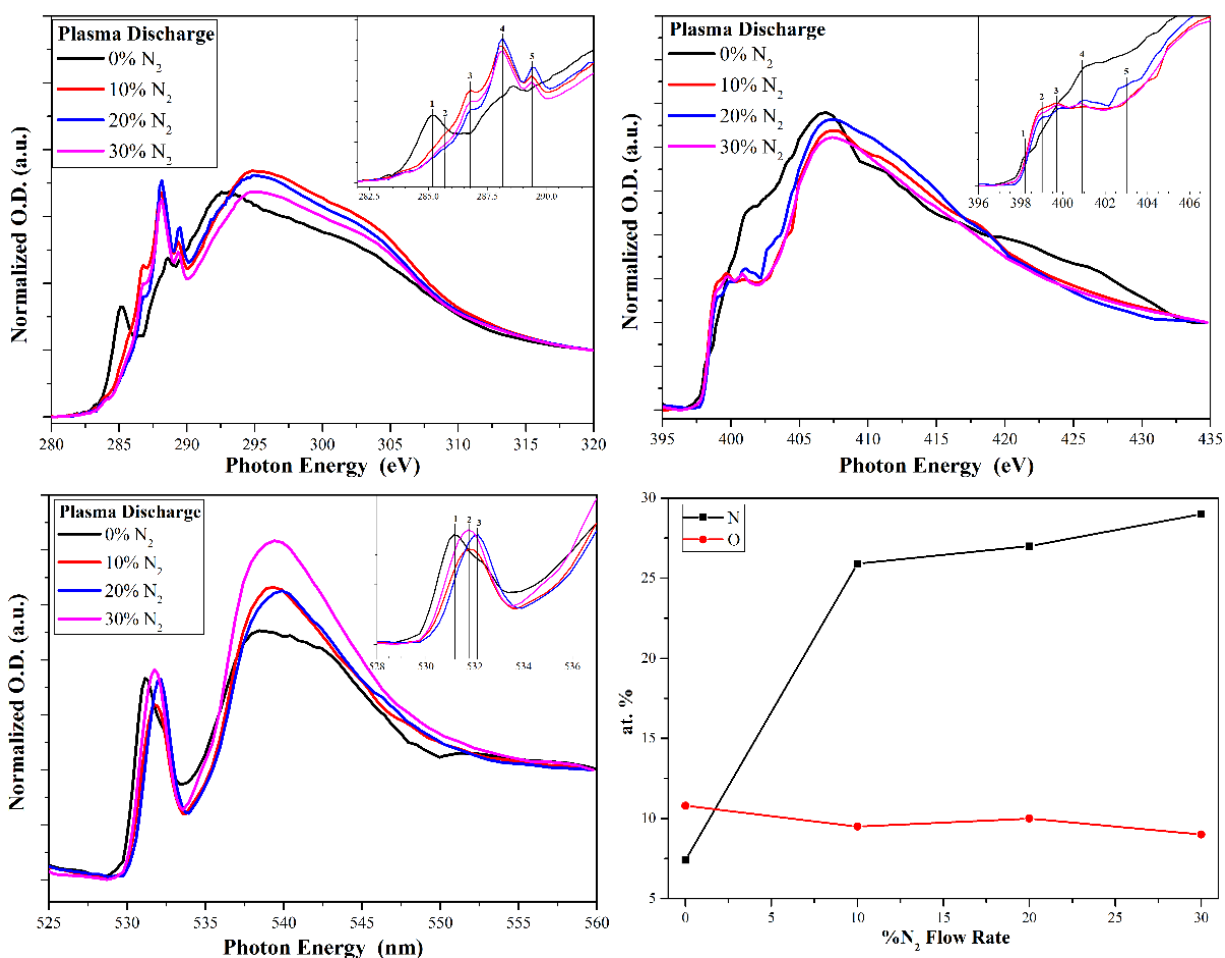


**Figure 4.22.** NEXAFS for (a) C1s (b) N1s (c) O1s for FL-CN<sub>x</sub> films prepared with different N<sub>2</sub>/Ar plasma discharge gas ratios. (d) The at.% of N and O within the films are determined by the integrated area ratios for different films.

The NEXAFS spectra shown in Figure 4.22 are given in optical density (OD) so that the prominent bands for a given film are proportional to the C-C, C-N, C-O bonding. The N-Kedge

NEXAFS spectrum shown in Figure 4.22(b) identified 3-major  $\pi^*$  resonance bands as pyridinic (N1), pyrrolic (N2), and graphitic-N (N3) centered at 398.7 eV, 399.9 eV, and 401.2 eV, respectively.<sup>223</sup> In addition, the FL-CN<sub>x</sub>-20 film shows an additional band at approximately 403 eV which is attributed to an oxidize graphitic-like N site. A broad band centered at approximately 405eV for the FL-CN<sub>x</sub>-00 film shifts to 407 eV for the FL-CN<sub>x</sub>-10 to FL-CN<sub>x</sub>-30 films and corresponds to the  $\sigma^*$  resonance.

The O-Kedge NEXAFS spectra shown in Figure 4.22(c) show 2 prominent features located at 531-532 eV and 539-540 eV corresponding to the  $\pi^*(C=O)$  resonance and  $\sigma^*$  resonance. It is interesting to note that the O-edge shifts upon high nitrogen incorporation into the a-C network, and the  $\pi^*$  resonances appear to be a convolution of 2 bands which most likely correspond to different O-containing functional groups (carboxyl oxygen, ketones, etc). Although it is expected that a higher concentration of O-containing functional groups are present on the surface, EELS measurements on low N-containing films made from the deposition chamber found small amounts of oxygen throughout film, but the concentration was higher near the surface.<sup>103</sup>

The C-Kedge NEXAFS spectra for the FL-CN<sub>x</sub> films are shown in Figure 4.22(a). The 0%N<sub>2</sub> prepared FL-CN<sub>x</sub> film shows prominent bands located at 285.1 eV, 288.5 eV, and 293 eV which are assigned to aromatic carbon ( $1s \rightarrow \pi^*(C=C)$ ) and carboxylic acid ( $1s \rightarrow \pi^*(C=O)$ ), and  $1s \rightarrow \sigma^*(C=C)$  transitions, respectively. With the addition of high at.%N to the film matrix, a new prominent shoulder appears at 285.6 eV(C1), and 3 discrete bands centered at 286.7 eV (C2), 288.1eV (C3), and 289.4 eV (C4) appear in the  $\pi^*$  resonance region. In addition, the broad  $1s \rightarrow \sigma^*$  band increases in overall band intensity and the major band shifts to approximately 295 eV for high nitrogen containing films. The C1 band is assigned to N-incorporated aromatic rings (pyridinic rings). The C2 band has been assigned to  $sp^2(C=N)$  bonding in a-CN<sub>x</sub> films<sup>224</sup>, oligonucleotide heterocyclic rings<sup>225</sup>, peptides,<sup>226</sup> and  $sp(C\equiv N)$ <sup>190, 224</sup>. However, the observed  $C\equiv N$  bands in Raman or FTIR studies for FL-CN<sub>x</sub> films deposited onto PTFE was not observed. Other oxygen-containing functional groups resonances ( $\pi^*C=O$ ) also occur in this region.<sup>190</sup> The C3 resonance band can be assigned to a  $sp^3(C-N)$ . The ( $\pi^*N-C=O$ ) transition has been commonly found in the amide backbone of peptides and protein materials.<sup>222, 226</sup> The C4 resonance band has been attributed can be attributed to  $sp^2(C=N)$  in pyridinic rings,<sup>224</sup> or ring systems containing multiple N, similar to that found in nucleotide heterocyclic rings,<sup>225</sup> or tryptophan peptide side chains.<sup>226</sup>

**Table 4.9.** NEXAFS bands for C1s, N1s, and O1s for FL-CN<sub>x</sub> films prepared with different %N<sub>2</sub> plasma discharge gas.

	Energy (eV)				Assignment
	FL-CN <sub>x</sub> -00	FL-CN <sub>x</sub> -10	FL-CN <sub>x</sub> -20	FL-CN <sub>x</sub> -30	
<b>C1s</b>					
<b>1</b>	285.1	285.1	285.1	285.0	1s(C <sub>ring</sub> )→π* <sub>C=C</sub>
<b>2</b>	--	285.6	285.6	285.6	1s(C-N) <sub>ring</sub> →π* <sub>C=C</sub>
<b>3</b>	286.5	286.7	286.7	286.7	1s(C-C) fused ring→π* <sub>C8</sub> (tryptophan side chain)
<b>4</b>	288.5	288.1	288.1	288.1	1s(C=O)→π* <sub>COOH</sub> ; 1s(C=O) →π* <sub>O=C-N</sub>
<b>5</b>	--	289.4	289.4	289.4	1s(C=N)→π* <sub>N-C=N</sub> ; 1s(C=N)→π* <sub>N-CO-N</sub>
<b>6</b>	293	295	295	295	1s→σ* (C-C); 1s→σ* (C-N)
<b>N1s</b>					
<b>1</b>	398.1	--	--	--	1s→π* <sub>C-N=C</sub> (pyridinic N)
<b>2</b>	399.0	399.0	399.0	399.0	1s→π* <sub>C-N=C</sub> (pyridinic N),(multiple N)
<b>3</b>	399.9	399.8	399.9	399.8	1s→π*pyrrole-type
<b>4</b>	401.1				1s→π* <sub>graphitic N</sub> ; , 1s→π* <sub>N-C=O</sub>
<b>5</b>	--	--	403.0	--	1s→π* <sub>N2</sub>
<b>6</b>	406.7	407.3	407.4	407.4	1s→σ*
<b>O1s</b>					
<b>1</b>	531.2		--	--	1s→π* <sub>C=O</sub> (ketone)
<b>2</b>		531.8		531.8	1s→π* <sub>C=O</sub> + 1s→π* <sub>O-C=O</sub> (carboxyl)
<b>3</b>	532.3		532.1		1s→π* <sub>O-C=O</sub> (carboxyl)
<b>4</b>	538.9	539.5	539.9	539.6	1s→σ*

The FL-CN<sub>x</sub>-10 film was exposed to HSA for 2 minutes, rinsed and dried. The C1s, N1s, and O1s NEXAFS spectra of the HSA-treated FL-CN<sub>x</sub>-10 film, HSA, and the untreated FL-CN<sub>x</sub>-10 film are shown in Figure 4.23. NEXAFS mapping using STXM typically involves each pixel of the stack to be fit to known NEXAFS reference spectra by a singular value decomposition method, which is an optimized method of least square analysis.<sup>227</sup> In addition, each reference material should ideally have a distinguishable unique band signature that is not found in other reference materials. In Figure 4.23(a), the C1s NEXAFS spectrum for the FL-CN<sub>x</sub>-10 film has an unique bands centered at 286.7 eV and 289.4 eV. However, the major bands found in the HSA spectrum are the 1s(C<sub>ring</sub>)→π\*<sub>C=C</sub> and 1s(C=O) →π\*<sub>O=C-N</sub> centered at 285.1 eV and 288.1 eV, respectively, are also present in the FL-CN<sub>x</sub>-10 film spectrum. It would be difficult to distinguish between the HSA and the FL-CN<sub>x</sub>-10 film using the bands found in the C1s spectrum.

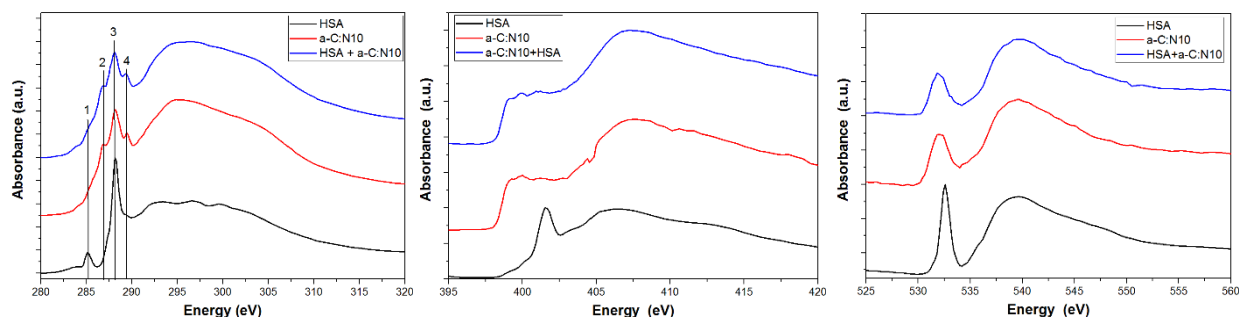


**Figure 4.23.** NEXAFS of HSA immobilized on FL-CN<sub>x</sub> film prepared with 10% N<sub>2</sub> plasma discharge gas. (a) C1s (b) N1s (c) O1s. An HSA solution (0.1mg/mL in PBS, pH7.4) was dropped onto the FL-CN<sub>x</sub> film for 2-3min, gently rinsed with PBS, then water, and then dried.

The N1s NEXAFS spectra of the HSA-treated FL-CN<sub>x</sub> surface, untreated FL-CN<sub>x</sub>-10 film, and HSA are shown in Figure 4.23(b). The major band found in HSA consists of the  $1s \rightarrow \pi^*_{N-C=O}$  amide band located at 402.1 eV. Unfortunately, the FL-CN<sub>x</sub>-10 film also has a small feature in this region, so this band is not suitable for distinguishing between the HSA and the FL-CN<sub>x</sub>-10 film. Similarly, The O1s NEXAFS spectrum for HSA shown in Figure 4.23(c) is centered at 532.5 eV, but the FL-CN<sub>x</sub>-10 film band is broad and slightly shifted at 532.4 eV. However, the HSA-coated FL-CN<sub>x</sub>-10 film spectrum has very similar lineshape to the untreated FL-CN<sub>x</sub>-10 film, and it would be very difficult to distinguish between HSA signal and FL-CN<sub>x</sub> signal.

Overall, the major bands found in the FL-CN<sub>x</sub> films (Table 4.9) also overlap with the HSA bands, so the STXM NEXAFS imaging technique was determined to be not suitable. The possible exception could be the FL-CN<sub>x</sub>-00 film. In this case, the major band in the C1s NEXAFS spectrum is the  $1s(C=O) \rightarrow \pi^*_{COOH}$  band centered at 288.5 eV, which is 0.4 eV higher compared to the  $1s(C=O) \rightarrow \pi^*_{O=C-N}$  band centered at 288.1 eV found in HSA. With careful energy calibration of the beamline, it may be possible to image the HSA on the FL-CN<sub>x</sub>-00 film. However, the other drawback for this technique would be the small spectral signature of HSA (2-4 nm) for a single layer compared to the thicker FL-CN<sub>x</sub> film (approximately 100 nm). The HSA signal could be enhanced by depositing a thinner FL-CN<sub>x</sub> film, as the STXM technique has been able to measure single layer graphene.<sup>228</sup> Unfortunately, the synchrotron facility experienced disruptions, several peer reviewed shifts were lost and additional beamtime could not be secured through the peer review process in the following cycle. It was ultimately decided to discontinue this part of the research.

## 4.2. Metal Free a-C:N Films

### 4.2.1. Verification of Metal-Free a-C:N Deposition

The original plasma assisted graphite sputter chamber was built with spare parts. Although the chamber worked very well, there were some fundamental design flaws in which lead to the incorporation of metals into the amorphous carbon films. These included improperly shielded metal components, lack of a N<sub>2</sub>(l) trap on the vacuum line to reduce backflow contamination, etc. An attempt to correct these measures on the original sputtering chamber was made, but a multi-user environment made it difficult to keep the deposition chamber clean and operational.

A new deposition chamber was designed, and details are summarized in Section 3.1.2. However, the W filament was placed further away from the substrate as to not heat the sample during film deposition. The deposition temperature (estimated using an infrared temperature gun) was approximately less than 50-70° C. Therefore, the deposited films were a-C:N type film. The verification of the metal-free a-C:N films were assessed with  $\mu$ -XRF and XPS survey scans and are shown in Figure 4.24.

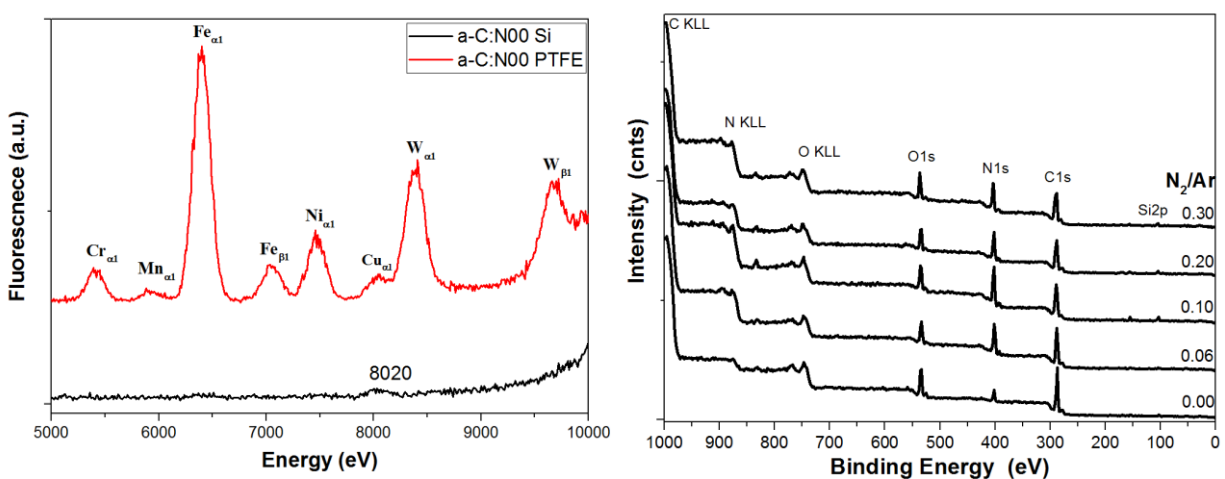


**Figure 4.24.** (a)  $\mu$ -XRF of a-C:N-00 prepared film deposited on Si from new chamber is compared to the FL-CN<sub>x</sub>-00 film prepared from the old chamber. (b) XPS survey scans for the a-C:N films deposited on Si shows no additional metals co-deposited into a-C:N films.

The  $\mu$ -XRF spectrum of the a-C:N-00 is compared to the FL-CN<sub>x</sub>-00 film prepared from the original deposition chamber. The FL-CN<sub>x</sub>-00 film was found to contain the highest amount of metals, but the  $\mu$ -XRF spectrum for the a-C:N-00 films prepared in the new chamber does not show any metal fluorescence. Similarly, XPS survey scan measurements for a-C:N films prepared in the new chamber show the major elements present were C, N, O, and a small amount of Si was

also present. It was unclear if the source of the Si was a result of Si etched off the substrate surface during the deposition process or coming from the pyrex plasma chamber. It was also possible that there was Si contaminated particles on the surface from cutting the samples for XPS measurements.

#### 4.2.2. a-C:N Film Characterization on Au Substrate

The “metal-free” a-C:N films were prepared in a new chamber, and prepared in the new chamber at a lower temperature. In addition, an Fe-doped a-C:N-00 (a-C:N-00Fe) was also prepared in order to investigate any effects from the Fe during film deposition. The AFM, Raman spectroscopy, and contact angle measurement results for the different a-C:N films are summarized in Table 4.10. The surface topography of the a-C:N films was measured with AFM and shown in Figure 4.25. The films were very smooth and revealed a small nano-cluster morphology on the surface. There was not a significant difference in  $R_{RMS}$  surface roughness which varied from 1.8-2.3 nm for the metal free a-C:N films. The a-C:N-00Fe film had a slightly higher  $R_{RMS}$  roughness value of 2.7 nm, but it was not statistically significant.

**Table 4.10.** Film Characterization of metal-free a-C:N films prepared with different  $N_2\%$  plasma discharge gas and deposited on Au sensor surfaces.

a-C:N Films	AFM <sup>1</sup>	Raman Spectroscopy <sup>2</sup>			Contact Angle <sup>3</sup>
	$R_{RMS}$ (nm)	G-Band ( $cm^{-1}$ )	D- Band ( $cm^{-1}$ )	$I_D/I_G$ <sup>4</sup>	(Deg)
a-C:N-00-Fe	2.7 ( $\pm 0.3$ )	1561 (156)	1350 (229)	0.51 (0.04)	56.2 ( $\pm 1.8$ )
a-C:N-00	2.2 ( $\pm 0.2$ )	1558 (143)	1309 (301)	0.70 (0.11)	55.9 ( $\pm 1.7$ )
a-C:N-05	2.1 ( $\pm 0.1$ )	1550 (135)	1348 (368)	1.41 (0.09)	49.5 ( $\pm 1.3$ )
a-C:N-10	2.3 ( $\pm 0.4$ )	1548 (145)	1348 (326)	1.26 (0.09)	51.8 ( $\pm 1.3$ )
a-C:N-20	2.3 ( $\pm 0.1$ )	1550 (140)	1353 (372)	1.10 (0.08)	51.7 ( $\pm 1.1$ )
a-C:N-30	1.8 ( $\pm 0.4$ )	1558 (157)	1360 (358)	0.88 (0.12)	56.1 ( $\pm 1.0$ )

<sup>1</sup>  $R_{RMS}$  values were taken from  $2 \mu m \times 2 \mu m$  areas over  $n = 4-5$  areas.

<sup>2</sup> FWHM values given in brackets.

<sup>3</sup> Contact angles were taken from  $n = 5$  measurements.

<sup>4</sup> Standard error calculated from peak height ratio given in brackets.

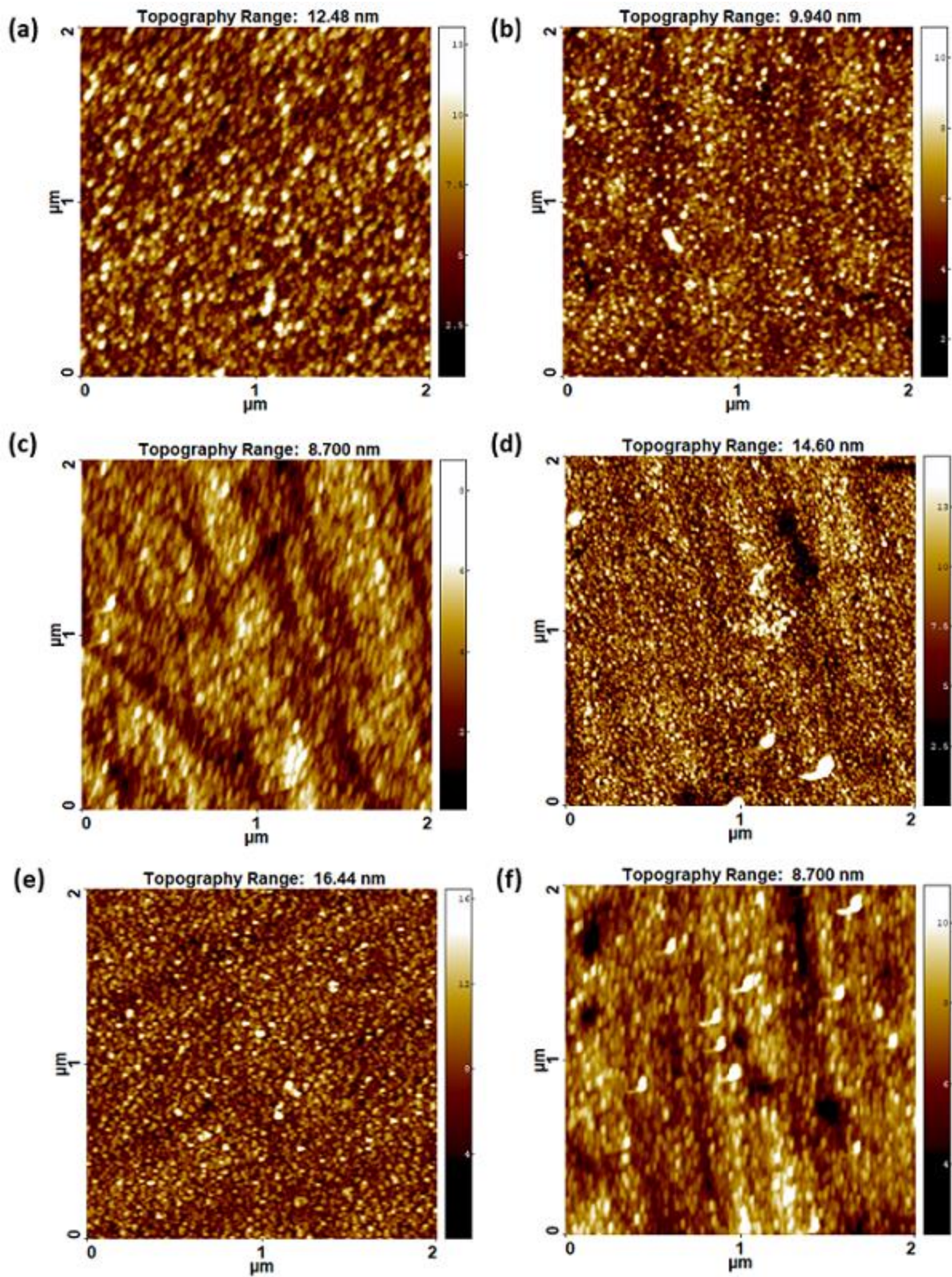


**Figure 4.25.** AFM topography images of a-C:N films prepared with different amounts of N<sub>2</sub> plasma discharge gas: (a) a-C:N-00Fe (b) a-C:N-00; (c) a-C:N-05; (d) a-C:N-10; (e) a-C:N-20, (f) a-C:N-30. Images are 2 μm x 2 μm.

The Raman spectra for the Fe-doped and “metal-free” a-C:N films are shown in Figure 4.26(a), and the band positions and widths are summarized in Table 4.10. The G-band and D-bands were deconvoluted according to Ferrari.<sup>172, 176</sup> Comparing the Fe-doped and “metal-free” a-C:N films, the G-band for the Fe-doped a-C:N film was upshifted slightly to 1561 cm<sup>-1</sup> compared to the 1558 cm<sup>-1</sup> for the “metal-free” a-C:N film. However, the I<sub>D</sub>/I<sub>G</sub> peak intensity ratio was smaller for the Fe-doped a-C:N film (0.51) compared to the “metal-free” a-C:N film (0.70). This would suggest that the addition of the Fe within the plasma reduced the amount of 6-membered aromatic clusters within the film matrix. The G-band for the a-C:N-05 film down-shifted to 1550 cm<sup>-1</sup>, indicating a slight increase in %sp<sup>3</sup> character in the film and the I<sub>D</sub>/I<sub>G</sub> peak intensity increased to 1.39 suggesting more order and 6-membered aromatic clusters within the film. The a-C:N-10 film had a slight G-band downshift to 1548 cm<sup>-1</sup> and slight I<sub>D</sub>/I<sub>G</sub> ratio decrease to 1.26. Further addition of %N<sub>2</sub> plasma discharge gas for the a-C:N-20 and a-C:N-30 films showed slight upshifts for the G-band to 1550 cm<sup>-1</sup> and 1558 cm<sup>-1</sup>, respectively. However, the I<sub>D</sub>/I<sub>G</sub> ratio declined to 1.10 and 0.88 for the a-C:N-20 and a-C:N-30 films.

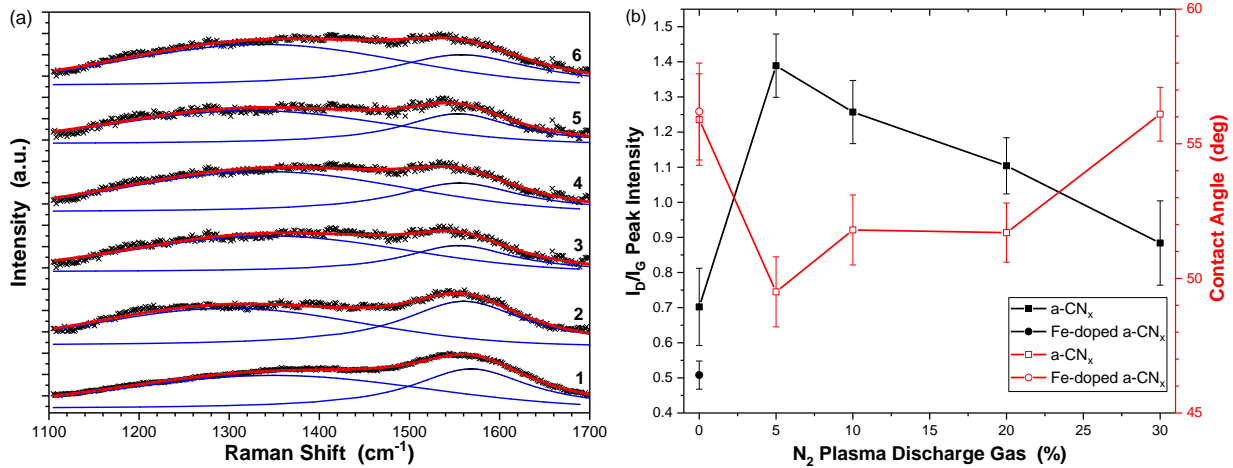


**Figure 4.26.** (a) Raman measurements ( $\lambda_{\text{ex}} = 514.5$  nm) of a-C:N-00Fe (1) and metal-free (2-6) a-C:N films prepared with different %N<sub>2</sub> plasma discharge gas. (2) a-C:N-00; (3) a-C:N-05; (4) a-C:N-10; (5) a-C:N-20; (6) a-C:N-30. (b) The I<sub>D</sub>/I<sub>G</sub> peak intensity ratio and the contact angle measurements for the Fe-doped and “metal free” a-C:N films.

The wettability of the different a-C:N films was assessed by static sessile contact angle measurements. Contact angle measurements using Millipore water on the different surfaces are shown in Figure 4.26(b). The a-C:N films prepared in the “metal-free” apparatus have a much lower contact angle compared to the FL-CN<sub>x</sub> films prepared in original chamber and described in Section 4.1. However, the contact angle for the a-C:N films showed a similar trend. The

introduction of N<sub>2</sub> into the plasma discharge gas showed a decrease in contact angle from 55.9° to 49.5° for the a-C:N-00 and a-C:N-05 films, respectively. The a-C:N-10 film had a slight increase in the water contact angle to 51.8°. The a-C:N-20 and a-C:N-30 films showed a further increase in the water contact angles of 51.7° and 56.1°, respectively. The a-CN-00Fe film showed a very similar water contact angle of 56.2° compared to the 55.9° value obtained for the a-C:N-00 film. This suggested that the addition of Fe into the a-C:N matrix did not significantly change the surface energy of the a-C:N film.

The XPS survey scans and UPS workfunction measurements of the sputtered a-C:N films are summarized in Table 4.11. It should be noted that there was a small amount of Au detected from the survey scans. It was possible that this was due to small pinholes within the a-C:N films, but it was later determined that the Ar<sup>+</sup> ion sputtering gun was not sputtering samples evenly and hot spots were evident in other samples. Therefore, the presence was not necessarily from pinholes in the films. The XPS survey scans of sputtered films showed a large incorporation of nitrogen into the a-C matrix, even for the lowest value of % N<sub>2</sub> in the plasma discharge gas. The N/C and O/C ratios as a function of %N<sub>2</sub> plasma discharge is shown in Figure 4.27(a). The N/C ratio initially has a large increase with the introduction of N<sub>2</sub> into the plasma discharge gas, and it plateaus around N/C = 0.6-0.7. The O/C ratio was small for the a-C:N-00 film (O/C = 0.02), but it increased to a range of O/C = 0.05-0.08 for the N-containing a-C:N films. The amount of at.% O is relatively low within the films (1.9-4.4 at.%) compared to the surface values (10-12 at.% O).

**Table 4.11.** XPS and UPS measurements of a-C:N films prepared on Au substrate.

a-C:N Film	XPS <sup>a</sup>						UPS <sup>b</sup>	
	at.% C	at.% N	at.% O	at.% Fe	at.% Au	N/C	O/C	Workfunction (eV)
a-C:N-00Fe	81.8	12.1	4.0	1.3	Au	0.15	0.05	4.1
a-C:N-00	91.6	6.5	1.9	--		0.07	0.02	4.2
a-C:N-05	63.5	33.1	3.3	--	0.1	0.52	0.07	4.8
a-C:N-10	60.4	35.1	4.1	--	0.4	0.58	0.07	4.6
a-C:N-20	54.7	40.7	4.4	--	0.1	0.74	0.08	4.1
a-C:N-30	59.4	37.0	3.1	--	0.5	0.62	0.05	4.2

<sup>a</sup> Relative errors in XPS area measurements are approximately 5-10%.

<sup>b</sup> Relative energy resolution for He(I) source used in UPS measurements is 0.02 eV.

The high-resolution XPS measurements of the C1s, N1s and O1s regions are shown in Figure 4.27 and summarized in Table 4.12.

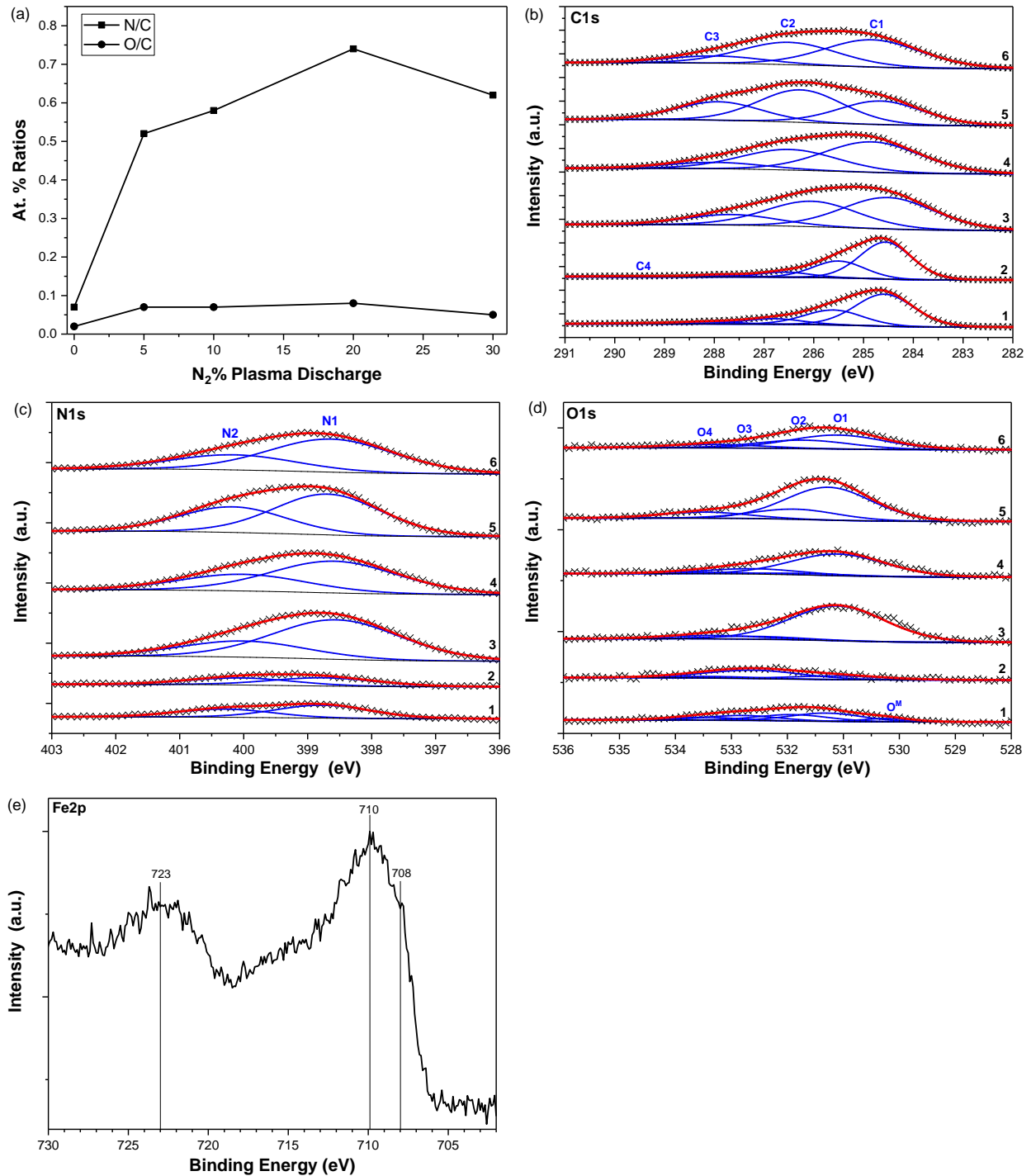


**Figure 4.27.** High resolution XPS of the a-C:N films prepared with different % $\text{N}_2$  plasma discharge gas. (1) a-C:N-00Fe (2) a-C:N-00 (3) a-C:N-05 (4) a-C:N-1 (5) a-C:N-20 (6) a-C:N-30. (a) The at.% ratios of N/C and O/C as a function of plasma discharge gas during film preparation. High resolution XPS spectra were collected for (b) C1s; (c) N1s; (d) O1s; (e) Fe2p.

**Table 4.12.** Peak deconvolution of high resolution XPS measurements of a-C:N films prepared with different %N<sub>2</sub> plasmas discharge gas.

<b>(a) C1s<sup>a</sup></b>								
a-C:N Film	C1 C=C, C-H Ar-N (eV)	At.%	C2 C=N; C-O (eV)	At.%	C3 C-N; C=O (eV)	At.%	C4 COOH (eV)	At.%
a-C:N-00Fe	284.6 (1.4)	57.1	285.6 (1.4) 286.8 (1.4)	27.2 10.0	288.0 (1.4)	4.0	289.3 (1.4)	1.8
a-C:N-00	284.6 (1.2)	59.2	285.5 (1.2) 286.6 (1.2)	27.0 8.3	287.9 (1.2)	3.8	289.5 (1.2)	1.7
a-C:N-05	284.8 (2.1)	51.0	286.4 (2.1)	36.0	288.0 (2.1)	13.0		
a-C:N-10	284.8 (2.3)	53.0	286.5 (2.3)	35.9	288.0 (2.3)	11.1		
a-C:N-20	284.7 (2.0)	31.6	286.3 (2.0)	43.6	287.9 (2.0)	24.8		
a-C:N-30	284.8 (2.3)	47.9	286.5 (2.3)	39.3	288.0 (2.3)	12.8		
<b>(b) N1s<sup>a</sup></b>								
	N1 Pyridinic N (eV)	At.%	N2 Pyrrolic N (eV)	At.%				
a-C:N-00Fe	398.8 (1.8)	61.3	400.3 (1.8)	38.7				
a-C:N-00	398.7 (2.0)	53.9	400.0 (2.0)	46.1				
a-C:N-05	398.5 (2.3)	71.0	400.0 (2.3)	29.0				
a-C:N-10	398.6 (2.3)	65.6	400.0 (2.3)	34.4				
a-C:N-20	398.6 (2.0)	61.4	400.2 (2.0)	38.6				
a-C:N-30	398.6 (2.3)	68.6	400.2 (2.1)	31.4				
<b>(c) O1s<sup>a</sup></b>								
	O1 Quinone (eV)	At.%	O2 C=O (eV)	At. %	O3 C-O-C (eV)	At.%	O4 C-O;Ar-OH (eV)	At.%
a-C:N-00Fe <sup>M</sup>	531.3 (1.5)	33.5	531.9 (1.5)	25.7	532.8 (1.5)	20.2	533.5 (1.5)	11.8
a-C:N-00	531.1 (2.0)	26.1	531.7 (2.0)	0.5	532.6 (2.0)	61.7	533.3 (2.0)	11.7
a-C:N-05	531.1 (2.0)	50.1	531.7 (2.0)	32.9	532.6 (2.0)	0.0	533.3 (2.0)	17.0
a-C:N-10	531.1 (2.0)	71.8	531.7 (2.0)	5.2	532.6 (2.0)	18.0	533.3 (2.0)	4.9
a-C:N-20	531.3 (1.8)	66.6	531.9 (1.8)	20.6	532.8 (1.8)	0.3	533.5 (1.8)	12.5
a-C:N-30	531.1 (2.0)	53.9	531.7 (2.0)	32.7	532.6 (2.0)	0.0	533.3 (2.0)	13.4

<sup>a</sup> Standard deviation for C1s, N1s, and O1s areas are approximately 0.8 at.%, 1.1 at.%, 1.6 at.%, respectively.

\*FWHM peak widths are shown in brackets.

<sup>M</sup> An additional peak located at 530.2 eV (1.0 eV, 8.8 at.%O) was deconvoluted from Fe<sub>x</sub>O<sub>y</sub> presence in film.

The C1s region shown in Figure 4.27(b) shows a peak envelope centered near 285 eV which broadens significantly with nitrogen incorporation. The binding energies for both carbon-

oxygen and carbon-nitrogen functional groups are very similar. Deconvolution between the different binding groups is very difficult unless a well calibrated instrument and good standards are used. When standards are not available, peak deconvolution can be performed on one sample, and the optimized peak deconvolution can be used for the remaining samples. The C1s region for the a-C:N-00 and a-C:N-00Fe samples were deconvoluted into 5 peaks. The C1 centered at 284.6 eV which is attributed to graphitic  $sp^2$  carbon. A second peak centered at 285.6 eV (C1b) has been attributed to aromatic carbons containing  $sp^2$ -nitrogen.<sup>186</sup> The C2 peak centered at 286.6 eV is attributed to  $sp^2$  bonded nitrogen, C-OH and C-O-C groups. The C3 peak centered at 287.8 eV is attributed to C=O and O=C-N groups. The C4 group centered at 289.5 eV is attributed to the COOH functional group. The a-C:N-00 and a-C:N-00Fe peak positions and FWHM peak widths were very similar. The nitrogen containing a-C:N films were deconvoluted into 3 main peaks. The C1 peak shifted to higher energy and broadened with nitrogen incorporation into the a-C matrix.<sup>229</sup> The C2 peak was centered at 286.4 ( $\pm 0.1$ ) eV and the peak area increased to  $> 30$  at.%C. This peak is attributed to the aromatic carbon containing  $sp^2$ -nitrogen. This peak shifted from the from that observed in the a-C:N-00 film, possibly due to the large nitrogen incorporation in the films. The C3 peak was centered at 288.0 ( $\pm 0.1$ ) eV is attributed to  $sp^3$ -nitrogen from amide functional groups.

The asymmetric N1s peaks shown in Figure 4.27(c) is centered at 399 eV and can be deconvoluted into 2 major peaks: N1 peak located at 398.6 ( $\pm 0.1$ ) eV is associated with 2-fold coordinated  $sp^2$ -hybridized N (pyridinic N) and the N2 peak centered at 400.1 ( $\pm 0.2$ ) eV is attributed to 3-fold coordinated  $sp^2$ -hybridized N (pyrrolic N). There was no apparent peak or shoulder located in the 401 eV region like that observed in the FL-CN<sub>x</sub> samples.

The O1s XPS region shown in Figure 4.27(d) was deconvoluted into 4 peaks<sup>188</sup>: (1) O1 is located at 531.2 ( $\pm 0.1$ ) eV and is associated with quinone-type structure, (2) O2 is located around 531.8 ( $\pm 0.1$ ) eV and it is associated with carbonyls, (3) O3 located at approximately 532.7 ( $\pm 0.1$ ) eV is associated with C-O-C structure, O4 is located at approximately 533.4 ( $\pm 0.1$ ) eV and is associated with COOH and phenols. There was no peak or shoulder around 535 eV which is associated with adsorbed water. Overall, the amount of oxygen within the a-C:N films was very low. For the a-C:N-00Fe film, and additional peak located at 530.2 eV is associated with the presence of Fe<sub>x</sub>O<sub>y</sub>.

The high resolution Fe2p spectrum shown in Figure 4.27(e) shows asymmetric bands centered at 710 eV (Fe2p<sub>3/2</sub>) and 723 eV (Fe2p<sub>1/2</sub>). There is also a shoulder at 708 eV. Multiple

Fe-oxides are known to exist within samples and quantifying the different Fe-oxides is difficult and can lead to erroneous interpretation.<sup>196</sup> Qualitatively, the Fe2p spectrum is similar to that observed for FeO, which has a band center of symmetry is 709.5 eV).<sup>198, 200</sup> It is also possible for the presence of Fe<sub>3</sub>O<sub>4</sub> (magnetite) which contains a mixture of Fe<sup>2+</sup> and Fe<sup>3+</sup> ions. The Fe2p XPS spectrum for FL-CN<sub>x</sub>-00 showed the presence of Fe<sup>3+</sup>. The a-C:N-00Fe sample showed the presence of more Fe<sup>2+</sup>, but it is known that Ar<sup>+</sup> sputtering can reduce iron oxides.<sup>230</sup>

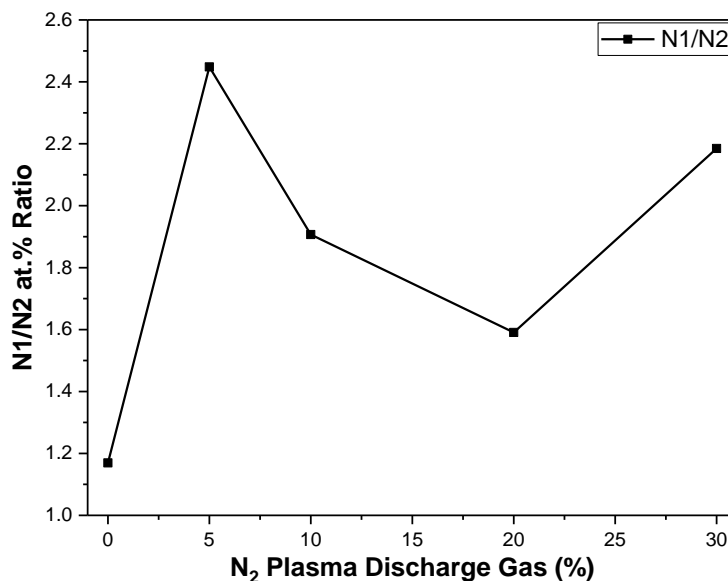


**Figure 4.28.** The N1/N2 at.% peak ratio from N1s spectral deconvolution as a function of a-C:N films prepared with different %N<sub>2</sub> plasma discharge gas.

The UPS of the a-C:N films are shown in Figure 4.29. UPS uses low energy electrons (He<sup>I</sup> = 21.22 eV) to induce the photoemission of electrons from the valence band region. The use of low energy excitation photons provides a very shallow penetration depth (<2-3 nm), so this technique reveals the electronic surface structure and is highly surface sensitive. In addition to the valence band structure acquisition, the electronic workfunction ( $\Phi$ ) (referred to as surface potential for non-metals) can also be determined from the spectrum by measuring the difference of the Fermi level and the low kinetic energy electron cut-off and subtracting this value from the incident photon energy. The  $\Phi$  is very sensitive to surface structure (different metal crystal faces have different  $\Phi$  values), doping-levels, and changes in the surface dipoles. The  $\Phi$  values as a function of the %N<sub>2</sub> in the plasma discharge is shown in Figure 4.29(b). The initial incorporation of nitrogen into the a-C matrix increased the  $\Phi$  value for the a-C:N-05 film. However, further incorporation of nitrogen

into the film by increasing the %N<sub>2</sub> plasma discharge gas decreased the  $\Phi$  value for the a-C:N films.

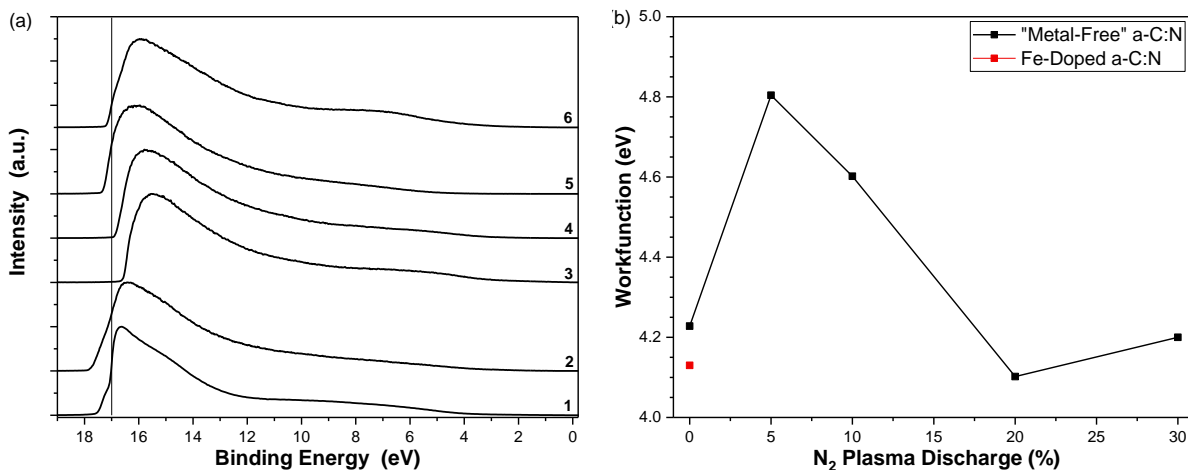


**Figure 4.29.** (a) UPS ( $\text{He}^I = 21.22 \text{ eV}$ ) spectra of the Fe-doped (1) and metal-free (2-6) a-C:N films prepared with different %N<sub>2</sub> plasma discharge gas. (1) a-C:N-00Fe (2) a-C:N-00 (3) a-C:N-05% (4) a-C:N-10 (5) a-C:N-20 (6) a-C:N-30. (b) The  $\Phi$  of each a-C:N film calculated from the secondary electron cut-off.

#### 4.2.3. SPR of a-C:N Protein Interactions

SPR sensor chips with the a-C:N films were made with the new deposition chamber. The a-C:N films did not contain any metals co-deposited in the films, and they were prepared at lower temperatures compared to the FL-CN<sub>x</sub> films. A Biorad XPR36 instrument became available in the SSSC which provided a unique experimental feature in that the platform contained 6 independent flow channels that could be rotated both horizontally and vertically. This allows for 36 sensorgrams to be measured during one sample cycle. The basic layout of the Biorad Proteon XPR36 sensor chip was shown in Figure 1.3 (pg. 7).

The a-C:N films were deposited onto clean Au sensor chips. The SPR reflectance curves of a cleaned Au sensor chip and a representative a-C:N-10 film are shown in Figure 4.30. The clean Au sensor surface has a minimum (SPR dip) at approximately 12 pixel units, whereas the addition of the a-C:N film shifts the SPR dip minimum to approximately 5 pixel units. This shift represents a change in refractive index at the surface (correlated to an increase in mass), and it confirms the presence of the a-C:N film.

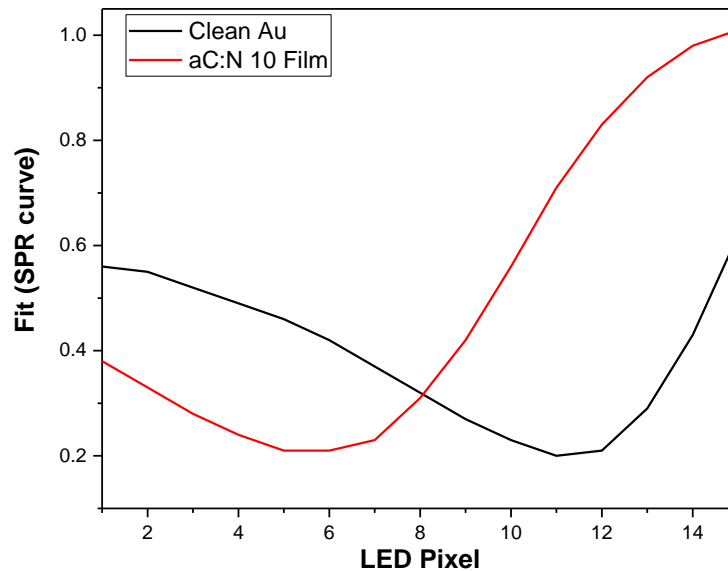


**Figure 4.30.** Representative SPR reflectance curves of cleaned Au sensor chip and a-C:N film.

The Proteon XPR36 instrument has 6 independent flow channels that run simultaneously. A “reference” channel was created in the vertical direction of channel 6 by flowing casein or BSA over the flow cells to “block” the active sites on the a-C:N surface. The sensorgrams shown in Figure 4.31 show how the casein or BSA injection over the a-C:N reference channel saturates the surface with over 2000 RU of protein. Both proteins are commonly used for blocking non-specific binding sites in biochemical methods like Western blots. The resulting protein-coated reference surface provided a suitable reference that has minimal interaction with HSA and Fib and will provide correction for minor refractive index changes between the running buffer and the analyte protein solutions. If present, minor non-specific binding interactions may also be subtracted.

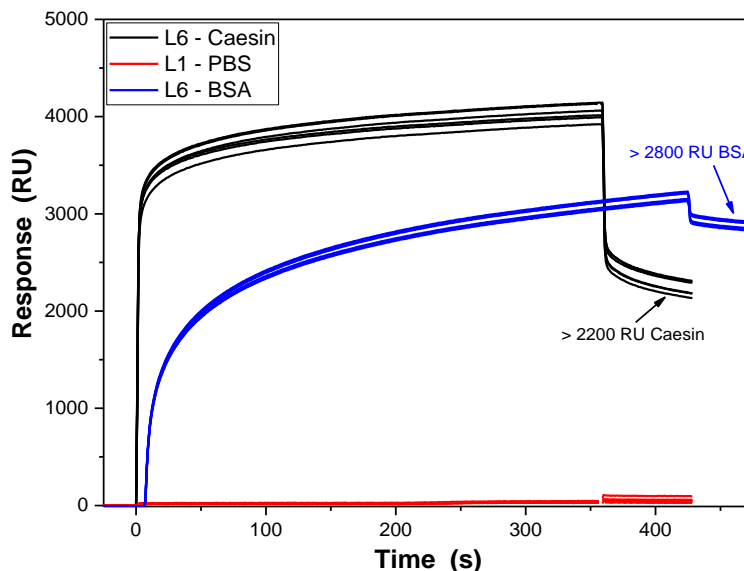


**Figure 4.31.** SPR sensorgrams of using casein and BSA to block non-specific binding sites to be used as a suitable reference surface.

An example HSA sensorgram concentration series is shown in Figure 4.32 for an a-C:N-10 film. The HSA 2-fold dilution concentration series (0-178 nM) flows over the horizontal channels (1-6), where L1 is an “active” a-C:N surface and L6 is the BSA coated “reference” surface are shown in Figure 4.32(a-b), respectively. The HSA sensorgram profile shown in Figure 4.32(a) is a combination of the HSA interaction with the a-C:N-10 surface, the refractive index of the different concentration of HSA solution, and the instrument drift. The HSA sensorgram profile for the L6 reference channel shown in Figure 4.32(b) shows a much lower response profile and lineshape. The lineshape is very close to a rectangular box, which indicates a minimal non-specific interaction with HSA and more dominated by the bulk-refractive index changes between the HSA solution and the running buffer. Figure 4.32(c) shows the resulting sensorgrams after the reference (L6) sensorgrams are subtracted from the a-C:N-10 active surface (L1) for the HSA concentration profile. This HSA sensorgram profile is corrected for the bulk refractive index shift from the HSA solutions as well as any minimal non-specific binding interaction. Finally, the sensorgrams shown in Figure 4.32(d) are double-referenced sensorgrams after subtracting the HSA concentration sensorgrams with a “blank buffer” sensorgram (0 nM HSA). This corrected the sensorgrams for any instrumental drift that may be present during measurements.

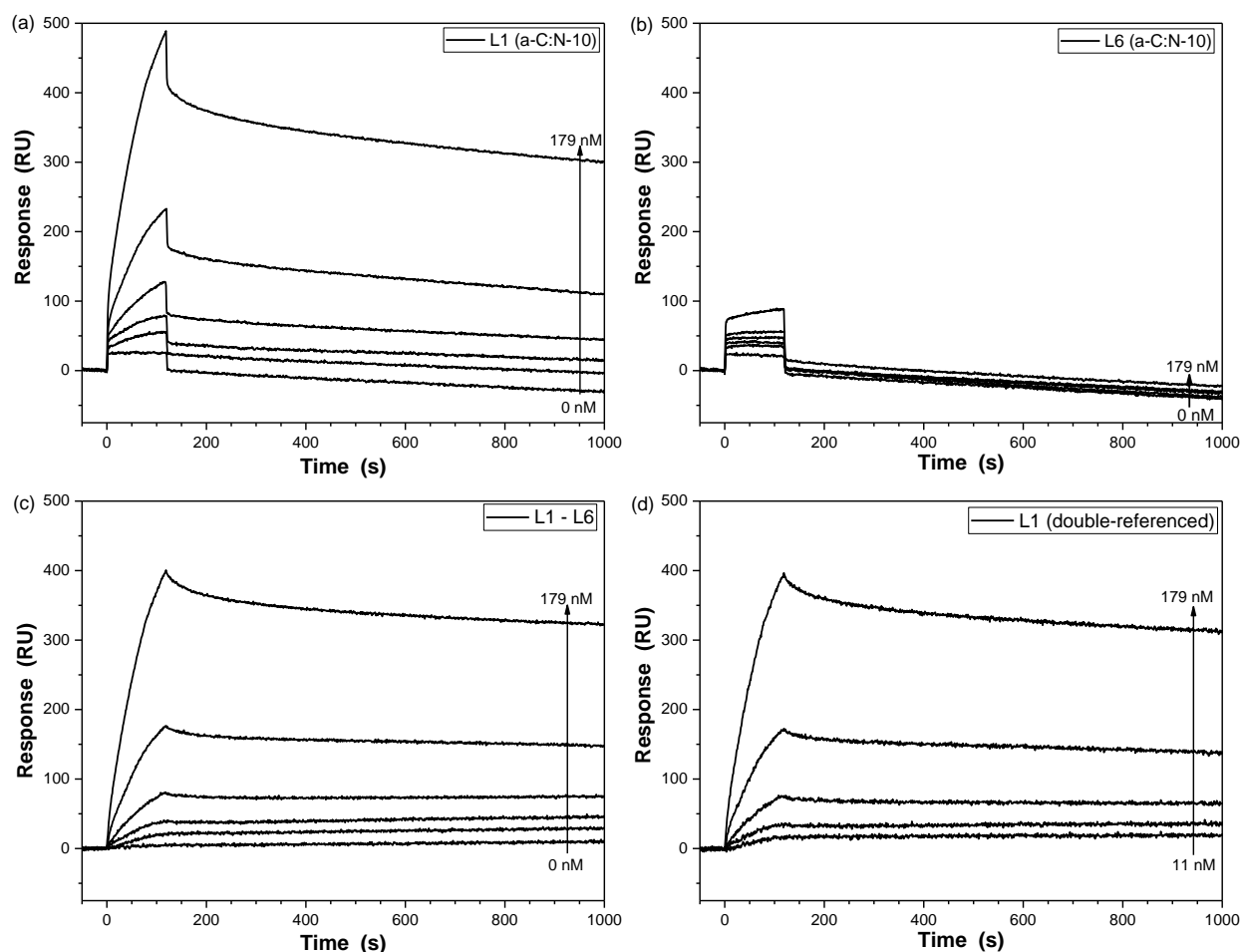


**Figure 4.32** SPR sensorgrams for HSA (0-179 nM) interaction with a-C:N-10 film. (a) HSA sensorgrams over the a-C:N-10 surface (L1) (b) HSA sensorgrams over the BSA-coated reference surface shown in Figure 4.31. (c) HSA “reference” subtracted sensorgrams (L1-L6) will correct for refractive index changes from protein solutions (d) double reference subtracted sensorgrams after subtracting the “buffer blank”(A6). This concentration profile sensorgrams are ready for kinetics modelling.

The SPR sensorgrams of HSA and Fib interaction with a-C:N films prepared with different %N<sub>2</sub> plasma discharge gas are shown in Figure 4.33. The SPR sensorgrams are double referenced, and within a typical sensorgram the PBS running buffer is flowed over the surface prior to the analyte injection. The response value is close to 0 and stable. At the start of the analyte injection (t = 0 s), the instrument switches from the running buffer to the analyte solution and there is an observed increase in response (increase in refractive index at the surface) which corresponds to an increase in mass at the surface during this association phase. At the end of the association phase (t = 120 s), the system is switched back to the running buffer and marks the beginning of the dissociation phase. A slow decrease in the response is associated with the protein desorption from the surface.

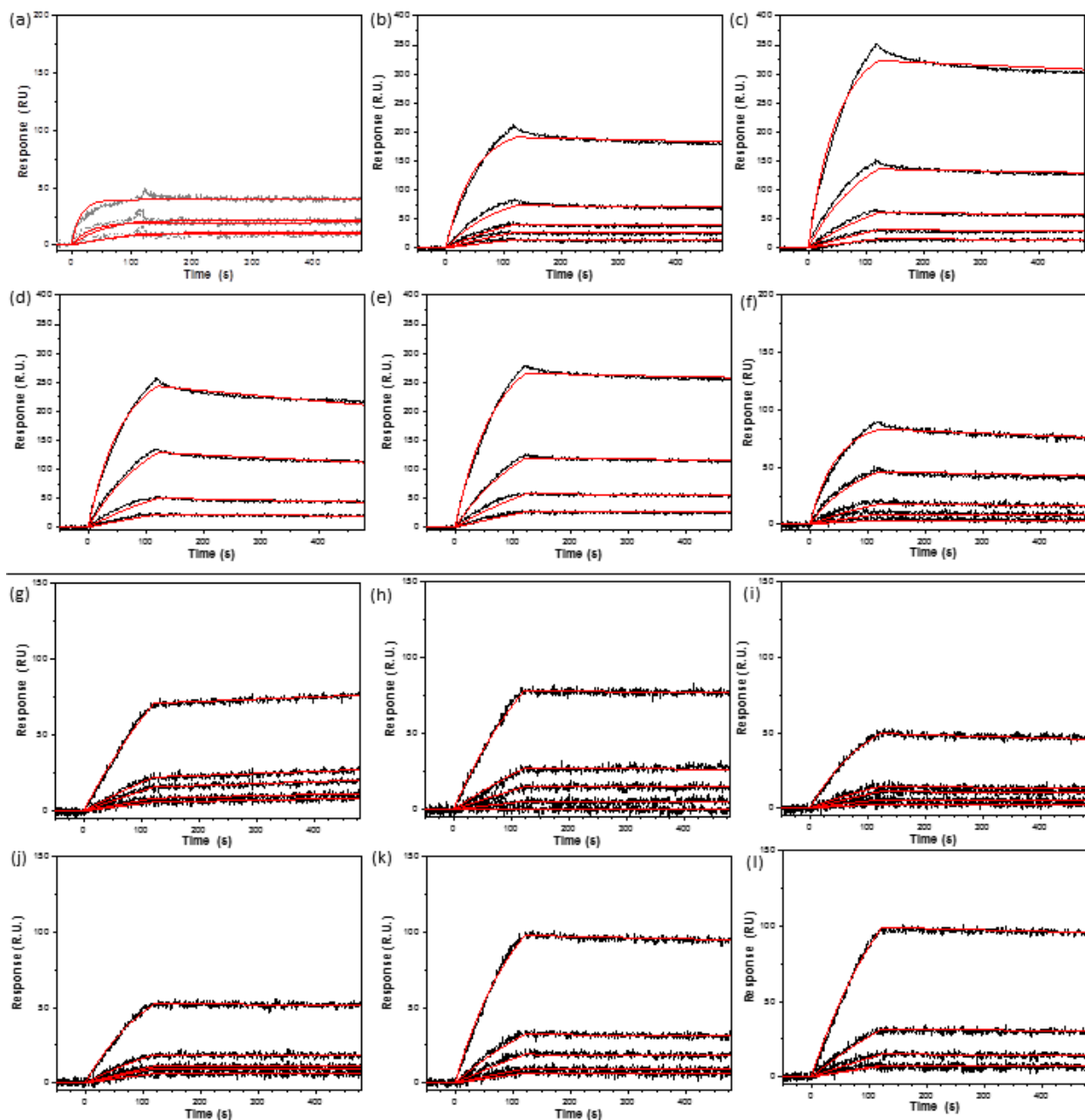


**Figure 4.33.** SPR sensorgrams of HSA (top) and Fib (bottom) interaction with a-C:N surfaces prepared with different %N<sub>2</sub> plasma discharge. HSA solutions (179 nM, 1X PBS, pH 7.4) were diluted 2-fold, and injected for 2 min at 30  $\mu\text{L min}^{-1}$ , followed by a 5-10 min dissociation. Fib (7.5 nM, 1X PBS pH 7.4) was diluted 2-fold and injected under the same conditions as HSA. Sensorgrams were evaluated with a 1:1 Langmuir model to determine kinetic parameters. (a,g) a-C:N-00; (b,h) a-C:N-05; (c,i) a-C:N-10; (d,j) a-C:N-20; (e,k) a-C:N-30; (f,l) a-C:N-00Fe.

The sensorgrams for the different a-C:N films interaction with HSA and Fib were fit to a 1:1 Langmuir binding model and summarized in Table 4.13. The  $k_a$  measures the recognition between 2 binding partners, whereas the  $k_d$  measures the strength and stability of the binding

complex. In general, the  $k_a$  (Fib) >  $k_a$  (HSA) by an order of magnitude, and the  $k_d$  values for both HSA and Fib measured on the same a-C:N film were the same magnitude and within statistical error of each other.

**Table 4.13.** Binding Kinetics<sup>a</sup> of HSA and Fib onto a-C:N Films.

a-C:N Film	$k_a$ ( $\times 10^5 \text{ M}^{-1} \text{ s}^{-1}$ )	$k_d$ ( $\times 10^{-4} \text{ s}^{-1}$ )	$K_D$ (nM)	$\chi^2$
<b>(a) HSA</b>				
a-C:N-00-Fe	2.2 ( $\pm 0.1$ )	2.0 ( $\pm 0.6$ )	0.9 ( $\pm 0.3$ )	3.1 ( $\pm 0.3$ )
a-C:N-00 <sup>b</sup>	3.1 ( $\pm 0.6$ )	4.6 ( $\pm 2.5$ )	1.5 ( $\pm 1.0$ )	2.6 ( $\pm 0.6$ )
a-C:N-05	1.2 ( $\pm 0.1$ )	1.5 ( $\pm 0.7$ )	1.3 ( $\pm 0.7$ )	12.1 ( $\pm 2.5$ )
a-C:N-10	1.1 ( $\pm 0.1$ )	1.6 ( $\pm 0.3$ )	1.5 ( $\pm 0.2$ )	20.2 ( $\pm 1.8$ )
a-C:N-20	1.8 ( $\pm 0.3$ )	0.6 ( $\pm 0.4$ )	0.3 ( $\pm 0.2$ )	45.3 ( $\pm 25.2$ )
a-C:N-30	1.8 ( $\pm 0.2$ )	0.8 ( $\pm 0.1$ )	0.5 ( $\pm 0.1$ )	9.6 ( $\pm 1.8$ )
<b>(b) Fib</b>				
a-C:N-00-Fe	16.6 (6.2)	3.7 (1.8)	0.3 ( $\pm 0.21$ )	3.0 ( $\pm 0.6$ )
a-C:N-00 <sup>b</sup>	15.0 (3.5)	3.0 (2.4)	0.22 ( $\pm 0.2$ )	1.8 ( $\pm 0.1$ )
a-C:N-05	7.5 (0.4)	0.6 (0.6)	0.1 ( $\pm 0.1$ )	3.3 ( $\pm 0.1$ )
a-C:N-10	12.8 (0.7)	1.1 (0.7)	0.1 ( $\pm 0.1$ )	2.4 ( $\pm 0.1$ )
a-C:N-20	10.1 (0.4)	0.9 (0.3)	0.1 ( $\pm 0.03$ )	2.5 ( $\pm 0.1$ )
a-C:N-30	11.5 (0.2)	0.6 (0.2)	0.1 ( $\pm 0.02$ )	2.6 ( $\pm 0.1$ )

<sup>a</sup> 1:1 Langmuir Model was used to determine the binding kinetics. Values are averages from 3-5 measurements (standard deviations are given in brackets).

<sup>b</sup> A 1:1 Langmuir Model with a drifting baseline was used to model binding kinetics. The drift was fitted locally, and well below the recommended < 0.05 RU/s drift.

The kinetic data is grouped in an isoaffinity plot ( $k_d$  vs  $k_a$ ) shown in Figure 4.34. Isoaffinity plots are useful for visualization of the different binding interactions on a single plot. Overall, the  $K_D$  values for Fib are stronger compared to HSA for a given a-C:N surface. However, the  $K_D$  values are very similar for the different a-C:N surfaces. The  $K_D$  values for HSA interaction do not show a significant difference for the a-C:N-00, a-C:N-05, and a-C:N-10 surfaces. However, the  $K_D$  values decrease (stronger affinity) for the a-C:N-20 and a-C:N-30 surfaces. In general, it would be difficult to distinguish differences in the a-C:N films prepared with different %N<sub>2</sub> plasma discharge gas if using only binding affinity values alone.

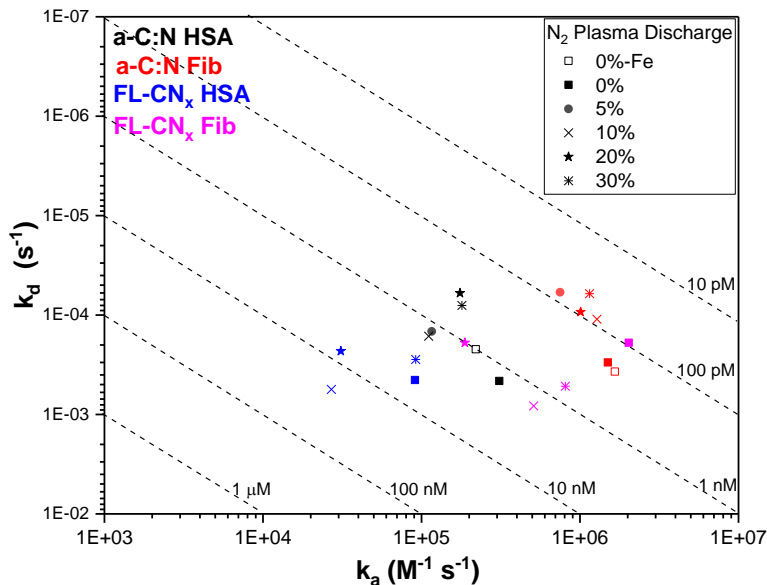


**Figure 4.34.** Isoaffinity plot for the HSA (black) and Fib (red) for a-C:N films prepared with different %N<sub>2</sub> plasma discharge gas. The kinetic parameters for FL-CN<sub>x</sub> interaction with HSA (blue) and Fib (purple) are also shown.

The  $k_a$  values as function of a-C:N films show that the  $k_a$  (Fib) is larger than  $k_a$  (HSA) by at least 5 times. The addition of nitrogen into the a-C matrix shows an initial decrease in the  $k_a$  by a factor of 2-2.5 time for both HSA and Fib, indicating that both proteins show a slower recognition towards the a-C:N-05 film compared to the a-C:N-00 film. The  $k_a$  for the a-C:N-10 film increased by approximately 2 times for Fib, but was similar to the a-C:N-05 film for HSA. Further addition of nitrogen in the a-C matrix for the a-C:N-20 and a-C:N-30 films did not alter the  $k_a$  value for Fib as it remained fairly constant. However, the  $k_a$  for HSA did increase slightly.

The  $k_d$  values for both Fib and HSA in the  $10^{-5}$ - $10^{-4}$  s<sup>-1</sup> and are very similar for each a-C:N film. The protein/surface interaction is very stable, regardless of a-C:N film, and corresponding  $t_{1/2}$  for the protein/surface complex with a  $k_d$  of  $0.5$ - $1 \times 10^{-4}$  s<sup>-1</sup> is approximately 1.9-3.9 hr. The a-C:N-00 film had the highest  $k_d$  value at  $4.7 \times 10^{-4}$  s<sup>-1</sup> and  $3.0 \times 10^{-4}$  s<sup>-1</sup> for HSA and Fib, respectively. The a-C:N-05 film had a lower  $k_d$  values of  $1.5 \times 10^{-4}$  s<sup>-1</sup> and  $0.6 \times 10^{-4}$  s<sup>-1</sup> for HSA and Fib, respectively. The  $k_d$  value for HSA remained relatively the same at  $1.6 \times 10^{-4}$  s<sup>-1</sup> whereas the  $k_d$  value for Fib increased slightly to  $1.1 \times 10^{-4}$  s<sup>-1</sup> for the a-C:N-10 film. Further addition of nitrogen into the a-C matrix for the a-C:N-20 and a-C:N-30 films decreased the HSA  $k_d$  to  $0.6$ - $0.8 \times 10^{-4}$  s<sup>-1</sup>, and the Fib  $k_d$  also decreased to  $0.9$ - $0.6 \times 10^{-4}$  s<sup>-1</sup>.

The incorporation of Fe into the plasma discharge gas was done for the a-C:N-00Fe film. The amount of Fe incorporated into the film was 1.2 at.% Fe, and it was present as Fe(III) oxides

according to XPS measurements. The comparison of the  $k_a$  value for the a-C:N-00 and a-C:N-00Fe interaction with HSA and Fib is shown in Figure 4.35. The  $k_a$  values for both HSA and Fib are not statistically significant for both a-C:N-00 and a-C:N-00Fe, and it can be concluded that the small amount of Fe(III) oxides did not change the protein binding on the a-C:N surface.

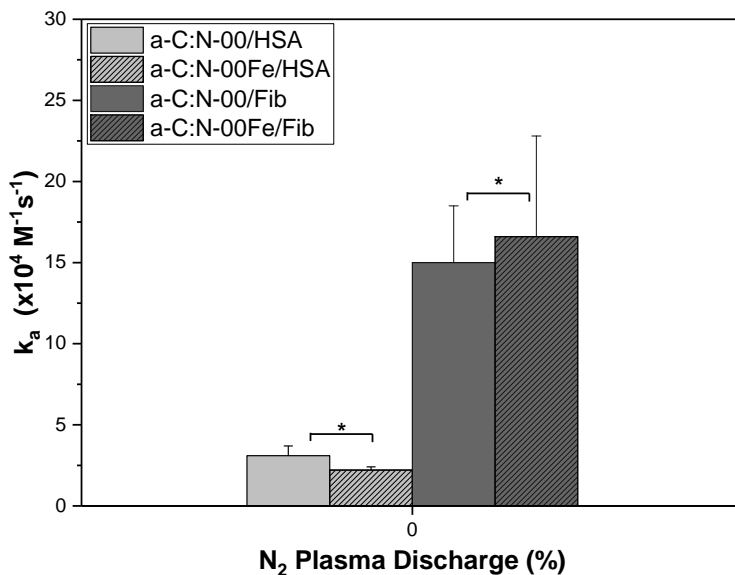


**Figure 4.35.** The comparison of  $k_a$  values for a-C:N-00 and a-C:N-00Fe film interaction with HSA and Fib.

#### 4.2.4. a-C:N Protein Interaction Discussion

SPR measurements allowed the evaluation of the  $k_a$  and  $k_d$  of model blood proteins HSA and Fib for a-C:N films prepared with different %N<sub>2</sub> plasma discharge gas. The SPR results showed that the initial binding of HSA and Fib was a reversible interaction, though they had very strong binding affinity. Overall, the  $k_d$  did not vary significantly for HSA and Fib for a specific a-C:N film. The  $k_d$  value had a range of  $1\text{-}5 \times 10^{-4} \text{ s}^{-1}$  for a-C:N films prepared with a-C:N-00 to a-C:N-10 films. This indicates that the protein:surface complex is very stable. The a-C:N-20 and a-C:N-30 films had a slightly lower  $k_d$  value that was in the range of  $5\text{-}10 \times 10^{-5} \text{ s}^{-1}$ . The SPR results show that the protein:surface interaction is not irreversible interaction, but it forms an extremely stable protein:surface complex that corresponds to a  $t_{1/2}$  of approximately 1.9-3.7 hr.

The  $k_a$  of the protein interaction with an a-C:N surface plays a significant role in the overall  $K_D$  of the protein:surface interaction. The initial addition of nitrogen into the a-C matrix showed a modest decrease in the  $k_a$  value, indicating that the recognition rate for both proteins slowed down with nitrogen incorporation into the a-C matrix. Since the  $k_d$  values are very similar for both proteins and assuming that most plasma proteins will have similar  $k_d$  profiles, proteins will initially

populate the surface based on its recognition kinetics, as well as the size and concentration of the protein in plasma. Although the  $k_a$  was lower for HSA compared to Fib, the HSA:Fib ratio in plasma is approximately 13:1 and it has a higher diffusion coefficient. It is therefore plausible that the reason for the HSA surface concentrations observed by other studies is due to its size and plasma concentration. It is relatively small enough to adsorb in uncoated regions that may be more difficult for larger proteins such as Fib to effectively adsorb. The larger saturation of nitrogen found in the a-C:N-20 and a-C:N-30 films showed a larger  $k_a$  value and increased recognition rate for both HSA and Fib. This along with a very low  $k_d$  value indicates that the protein adsorption layer is very stable.

The  $k_a(\text{Fib}) > k_a(\text{HSA})$  was similarly observed for the FL-CN<sub>x</sub> film interactions. This trend was also observed for HSA and Fib interactions with different metal oxide nanoparticles.<sup>162</sup> Fib has  $k_a = 3\text{-}7 \times 10^6 \text{ M}^{-1} \text{ s}^{-1}$  for interaction with TiO<sub>2</sub> and CeO<sub>2</sub> surfaces. These values are similar magnitude compared to the a-C:N films. The HSA kinetic interactions with TiO<sub>2</sub> and CeO<sub>2</sub> had  $k_a = 2\text{-}3 \times 10^4 \text{ M}^{-1} \text{ s}^{-1}$  and were fit with a 1:1 Langmuir interaction with conformational change, as previous spectroscopic measurements in the same lab indicated that HSA underwent a conformational change.<sup>163</sup> Other studies have suggested that HSA adsorption followed a one-step process.<sup>231</sup> However, the time needed for HSA to unfold and spread will likely be surface dependent, and it is currently unknown for the a-C:N films in this research. The higher concentration HSA sensorgrams shown in Figure 4.33 do show deviations from the 1:1 Langmuir fit to the raw data, suggesting a second process occurring. However, there is no significant deviation occurring between the raw and fitted data for the lower concentration sensorgrams, so this could be a possible concentration dependent effect causing an unknown biphasic process. It is possible that the increase in surface density at higher concentrations causes lateral interactions with neighbors, or it is possible that solution-based HSA are interacting with adsorbed HSA. At this time, there is not enough information to confidently fit the data with a more complex kinetic model.

The  $k_a$  values follow a similar trend to the contact angle measurements in that the  $k_a$  value decreases for both HSA and Fib as the a-C:N films become more hydrophilic (a-C:N-05 and a-C:N-10 films). The  $k_a$  value then increased when the a-C:N films become more hydrophobic when more nitrogen saturates in the a-C matrix (a-C:N-20 and a-C:N-30 films). Proteins will adsorb to surfaces through a combination of electrostatic and hydrophobic interactions on the surface.

However, the proteins generally show stronger affinity towards more hydrophobic surfaces.<sup>119</sup> The stronger affinity towards more hydrophobic surfaces therefore is heavily influenced by its  $k_a$ , or rate of recognition.

The  $I_D/I_G$  intensity ratio from Raman spectroscopy measurements initially increased and the film contains more 6-membered ring clusters and more order within the film which corresponded with a decrease in the  $k_a$  for both HSA and Fib. The average cluster size is slightly larger and more ordered, suggesting a slight increase in long range order in the film crystallinity may decrease its recognition kinetic rate with proteins.

The UPS measurements on the a-C:N films showed variation of  $\Phi$  for the a-C:N films prepared with different %N<sub>2</sub> plasma discharge gas. The a-C:N-05 film showed an increase in the  $\Phi$  value, but the a-C:N films prepared with larger %N<sub>2</sub> plasma discharge gas had lower  $\Phi$  values. The increase in  $\Phi$  value for the a-C:N-05 film appears to correlate with a decrease in the  $k_a$  value obtained in the SPR measurements, whereas  $\Phi$  values for the a-C:N-10 to a-C:N-30 films lowered while the  $k_a$  values increased. The relation of surface  $\Phi$  and surface functional groups on multiwall carbon nanotubes found that the  $\Phi$  value increased with the addition of oxygen-functional groups on the surface.<sup>232</sup> the addition of surface functional groups and nitrogen incorporation likely disrupts the  $\pi$ -conjugation at the surface and introduces surface dipole moments. The larger  $\Phi$  value for the a-C:N-05 film indicates that the surface structure has more surface dipole moments compared to the other a-C:N films.

In general, the a-C:N films had an order of magnitude larger  $k_a$  values for both HSA and Fib compared to the FL-CN<sub>x</sub> films. The FL-CN<sub>x</sub> films were prepared at higher temperatures that helps anneal the films and give them a more fullerene-like property. The differences in the 2 types of a-C are not that straightforward. The a-C:N films are more hydrophilic compared to the FL-CN<sub>x</sub> films, so the hydrophobic character of the given surface is significant, but not the driving factor for protein adsorption kinetics. It is most likely a complex combination of film properties that contribute to the attractiveness of adsorption for proteins. There are properties from the Raman measurements that are different for the 2 types of a-C films. The G-band peak position for the FL-CN<sub>x</sub> films were upshifted to the 1566-1575 cm<sup>-1</sup> region compared to 1550-1558 cm<sup>-1</sup> region found in the a-C:N films. This suggests that the FL-CN<sub>x</sub> films were more graphitic-like, containing less sp<sup>3</sup> character compared to the a-CN<sub>x</sub> films. Another distinguishing feature extracted from the Raman microscopy measurements is that the D-band FWHM peak widths were >300-370 cm<sup>-1</sup> for

the a-C:N films compared to the D-band FWHM peak widths of 210-280  $\text{cm}^{-1}$  for the FL-CN<sub>x</sub> films. The D-band represents the number of different 6-fold sp<sup>2</sup> aromatic rings clusters and the larger FWHM represents a larger distribution of 6-fold sp<sup>2</sup> aromatic ring clusters in the a-C:N films compared to the FL-CN<sub>x</sub> films.

The a-C:N-00 film and the a-C:N-00Fe films did not show statistically significant differences in  $k_a$  values for HSA and Fib surface interactions. There was a small amount of Fe (1.3 at.%) incorporated into the a-C matrix that appeared to be mainly FeO, but it is possible that Fe<sub>2</sub>O<sub>3</sub> may also be present. Additional film properties from AFM, Raman, XPS, UPS, and contact angle measurements were very similar for the “metal-free” and Fe-incorporated films. It can therefore be implied that the metal incorporation found in the FL-CN<sub>x</sub> films did not alter the FL-CN<sub>x</sub> films regarding protein binding kinetic interactions. However, it is also highly stressed that if any additional contaminants are observed, no matter the concentration, they should be removed as to avoid any lingering questions.

## CHAPTER 5 - CONCLUSIONS

### 5.1. Summary

A SPR assay was successfully developed to investigate the initial binding kinetics of HSA and Fib to a-C surfaces using 2 different commercially available SPR instruments. Nitrogen incorporation into the a-C films was varied by changing the %N<sub>2</sub> plasma discharge gas during film deposition. Different commercial SPR instruments provide the same results for biomolecular interaction assays. They differ in the instrumentation design, liquid delivery, and user experience. The BiacoreX instrument is an entry level instrument that provides 2 serial flow channels. The assay developed on this instrument for the FL-CN<sub>x</sub> films used a single flow channel and instrument drift was corrected by subtracting a “blank” buffer. Sensorgrams were fit using a 1:1 Langmuir model showing that the  $k_a$  values for the different FL-CN<sub>x</sub> films depended on the %N<sub>2</sub> plasma discharge gas during film deposition. The  $k_d$  values were very similar for all FL-CN<sub>x</sub> films and for both proteins ( $2-8 \times 10^{-4} \text{ s}^{-1}$ ). This indicated that the driving force for the protein adsorption was the protein recognition kinetics. The FL-CN<sub>x</sub> sensor films were characterized with Raman spectroscopy, AFM, and contact angle measurements. The change in  $k_a$  for Fib interaction showed a similar trend to the hydrophobic character of the surface, where an increase in the hydrophilic character of the FL-CN<sub>x</sub> film correlated with a decrease in the  $k_a$  value for Fib. On the other hand, the hydrophobic character of the FL-CN<sub>x</sub> film was not as dependent for the  $k_a$  for HSA interaction. Raman spectroscopy measurements showed that the I<sub>D</sub>/I<sub>G</sub> intensity ratio showed an increase with the nitrogen incorporation into the FL-CN<sub>x</sub> films, but then decreased for the FL-CN<sub>x</sub> film. A similar trend was observed for the  $k_a$ (HSA), where it decreased with nitrogen incorporation into the film, but the  $k_a$ (HSA) for FL-CN<sub>x</sub>-30 increased.

It was hoped that STXM measurements could help correlate the FL-CN<sub>x</sub> electronic structure with protein adsorption. STXM experiments allow high resolution chemical imaging (30 nm pixel size) along with its ability to measure under a liquid environment. However, the C1s, N1s, and O1s NEXAFS spectra for the FL-CN<sub>x</sub> films contained peaks that were very similar peak positions to the protein. It was very difficult to create image profiles differentiating the protein signal and the FL-CN<sub>x</sub> substrate. In addition, the transmission mode also provides the signal for the total FL-CN<sub>x</sub> film (~100nm) as well the protein layer (2-10 nm). Because the synchrotron beamtime was secured through peer-review process, the time allotted was not enough to improve

on the original experimental design, and more time could not be secured through the peer review process, so this experiment was terminated.

The metals incorporated into the FL-CN<sub>x</sub> films using the original deposition chamber were determined to be in oxide form. The major metal observed from  $\mu$ -XRF measurements was Fe, and the Fe content decreased proportionally with the increase in N<sub>2</sub>/Ar plasma discharge gas ratio. The Fe-oxides were further investigated using XPS, Fe L-edge XANES, and ESR, and indicated that the metal oxides did not interact/couple with a-C surroundings. The Fe2p high resolution XPS measurements showed that the oxidation state of Fe was dependent on the N<sub>2</sub>/Ar plasma discharge gas ratio. The FL-CN<sub>x</sub>-00 film contained mainly Fe<sub>2</sub>O<sub>3</sub> near the surface, but introduction of %N<sub>2</sub> plasma discharge during film preparation showed higher amounts of FeO near the surface. The Fe L-edge XANES spectra showed variations for the different FL-CN<sub>x</sub> films, and changes in the surface and bulk electronic structure for a given FL-CN<sub>x</sub> film. The ESR results also showed that the Fe<sup>3+</sup> existed in different symmetry environments, which also suggested different types of iron oxides.

A new plasma deposition chamber was successfully designed and constructed to produce “metal-free” a-C:N films, and verified from  $\mu$ -XRF and XPS measurements. The a-C:N films were prepared with different %N<sub>2</sub> plasma discharge gas were deposited onto SPR sensor surfaces at lower temperatures (50-70 °C) compared to the FL-CN<sub>x</sub> films (195±15 °C). The SPR measurements performed on the Proteon XPR36 instrument allowed a full concentration series to be completed in a single injection. The HSA and Fib interactions with the different a-C:N surfaces were modeled using a 1:1 Langmuir model. The  $k_d$  values for both HSA and Fib were similar for the a-C:N surfaces, and the a-C:N-00 to a-C:N-10 films were comparable ( $1-5 \times 10^{-4} \text{ s}^{-1}$ ), whereas a-C:N-20 and a-C:N-30 films were slightly lower ( $k_d = 0.6-0.9 \times 10^{-4} \text{ s}^{-1}$ ). The  $k_a(\text{Fib})$  was larger by an order of magnitude compared to  $k_a(\text{HSA})$  for a given a-C:N surface. Nitrogen incorporation into the a-C:N-05 film decreased  $k_a$ , but a continual increase to the %N<sub>2</sub> plasma discharge gas during film deposition actually increased the  $k_a(\text{Fib})$  and  $k_a(\text{HSA})$ . Correlation of the changes in  $k_a$  with a-C:N film property was not apparent, and the protein initial binding kinetics with a given surface is likely a combination of several properties. The decrease in  $k_a$  for the a-C:N film was correlated with an increase in the hydrophilic character of the surface, as well as an increase in I<sub>D</sub>/I<sub>G</sub> intensity ratio from Raman spectroscopy measurements, and increase in the pyridinic/pyrrolic at.% ratio within the film, and an increase in the  $\Phi$  value.

The incorporation of Fe into the a-C:N-00 film matrix was done by purposely adding a small % Fe target to the graphite target, resulting in 1.3 at.%Fe incorporation into the a-C:N matrix. The initial binding kinetics for HSA and Fib from SPR measurements did not show a statistically significant difference in the  $k_a$  value between the a-C:N-00 and a-C:N-00Fe films. This showed that the small amount of iron oxide did not change the binding kinetics. In addition, other a-C:N film properties measured from AFM, Raman spectroscopy, contact angle measurements, XPS, and UPS were very similar. Ultimately, trace impurities should be eliminated from the a-C:N films, regardless of their reactivity.

The success of a potential biocompatible device is likely to be significantly influenced by the protein layer that is deposited onto the biomaterial interface. How this protein layer interacts with cellular materials such as endothelial cells in synthetic vascular grafts, or platelet adhesion during thrombosis events will play a role for the suitability of a potential biomaterial. In addition, the dynamic changes of the protein layer that may occur *in vivo* are still not well understood. However, the SPR assay developed in this work may provide new insights towards the initial protein adsorption onto the a-C interface, the stability of the protein layer, and how this protein layer interacts with other plasma proteins. In addition, the SPR assay may also study additional surface properties and environmental factors that may influence the protein layer stability may also be studied. Ultimately, better understanding towards the major factors for creating a stable protein layer at the biomaterial interface will ultimately aid in the design of better biomaterials and biocompatible devices.

## **5.2. Proposed Future Work**

The development of an SPR assay for initial protein binding kinetics onto a-C surfaces provides several interesting research directions. For example, recent publications showed different chemical routes to change the functional groups on carbon film surface.<sup>156</sup> The ability to change the functional groups on the a-C:N surface in different vertical flow channels using the Proteon XPR36 instrument allows real-time measurements on the changes in surface functional groups on the same sensor surface in a single concentration series. Other types of experiments may include passivating the a-C:N surface with different surface densities and measure changes in the initial binding kinetics of the heavier proteins kininogen, Factor VII, etc. that are implicated in the Vroman effect and the potential removal of smaller proteins like HSA.

The relaxation/conformational changes in the protein spreading on the a-C:N surface can be measured using AFM imaging techniques. Newer AFM instrumentation has the ability of video rate imaging speed, and protein/DNA binding has been observed. Other imaging techniques such as tip-enhanced Raman spectroscopy combines the imaging capabilities of AFM with Raman spectroscopy. This technique could correlate the Raman spectrum of the a-C:N surface with the protein adsorption. It may also be possible to measure the secondary structure of the adsorbed protein by deconvolution of the protein's amide I band. Other surface sensitive techniques such as time of flight-secondary ion mass spectrometry allow surface imaging (10 nm depth) via mass spectrometry fragments. This technique also has sub-50 nm pixel resolution, which could provide very high resolution imaging at the interface.

## REFERENCES

1. Ratner, B. D.; Hoffman, A. J.; Schoen, F. J.; Lemons, J. E., Biomaterials Science: A Multidisciplinary Endeavor. In *Biomaterials Sciences: An Introduction to Materials in Medicine*, Ratner, B. D.; Hoffman, A. J.; Schoen, F. J.; Lemons, J. E., Eds. Elsevier Academic Press: San Diego, 2004; pp 1-10.
2. Carew, E. O.; Cooke, F. W.; Lemons, J. E.; Ratner, B. D.; Vesely, I.; Vogler, E. A., Properties of Materials. In *Biomaterials Science: An Introduction to Materials in Medicine*, 2nd ed.; Ratner, B. D.; Hoffman, A. J.; Schoen, F. J.; Lemons, J. E., Eds. Elsevier Academic Press: San Diego, 2004; pp 23-66.
3. Biological Evaluation of Medical Devices - Part 1: Evaluation and Testing Within a Risk Management Process. 5th ed.; International Organization of Standardization: Switzerland, 2018; Vol. ISO 10993-1:2018, p 41.
4. ISO 10993-4:2017 - Biological Evaluation of Medical Devices Part 4: Selection of Tests for Interactions with Blood. 3 ed.; International Organization for Standardization: Switzerland, 2017; p 69.
5. Zhang, M., Biocompatibility of Materials. In *Biomaterials and Tissue Engineering*, Shi, D., Ed. Springer: New York, 2004; pp 83-144.
6. Vroman, L., When Blood Is Touched. *Materials (1996-1944)* **2009**, 2 (4), 1547-1557.
7. Paul, L.; Sharma, C. P., Preferential adsorption of albumin onto a polymer surface: An understanding. *Journal of Colloid and Interface Science* **1981**, 84 (2), 546-549.
8. Haley, M. M.; Brand, S. C.; Pak, J. J., Carbon Networks Based on Dehydrobenzoannulenes: Synthesis of Graphdiyne Substructures. *Angewandte Chemie International Edition in English* **1997**, 36 (8), 836-838.
9. Robertson, J., Amorphous carbon. *Adv. Phys.* **1986**, 34 (4), 317-374.
10. Silva, S. R. P., *Properties of Amorphous Carbon*. INSPEC: United Kingdom, 2003; p 367.
11. Robertson, J., Diamond-like Amorphous Carbon. *Materials Science and Engineering R* **2002**, 37, 129-281.
12. Hainsworth, S. V.; Uhure, N. J., Diamond like carbon coatings for tribology: production techniques, characterisation methods and applications. *International Materials Reviews* **2007**, 52 (3), 153-174.
13. Ferrari, A. C.; Robertson, J., Raman spectroscopy of amorphous, nanostructured, diamond-like carbon, and nanodiamond. *Philosophical Transactions of the Royal Society of London. Series A: Mathematical, Physical and Engineering Sciences* **2004**, 362 (1824), 2477-2512.
14. Ferrari, A. C., Non-destructive Characterization of Carbon Films. In *Tribology of Diamond-Like Carbon Films: Fundamentals and Applications*, Donnet, C.; Erdemir, A., Eds. Springer: 2008; p 25.
15. Grill, A., Diamond-like carbon coatings as biocompatible materials - an overview. *Diamond and Related Materials* **2003**, 12 (2), 166-170.
16. Sanchez-Lopez, J. C.; Fernandez, A., Doping and Alloying Effects on DLC Coatings. In *Tribology of Diamond-Like Carbon Films: Fundamentals and Applications*, Donnet, C.; Erdemir, A., Eds. 2008; pp 311-337.

17. Fu, R. K. Y.; Mei, Y. F.; Shen, L. R.; Siu, G. G.; Chu, P. K.; Cheung, W. Y.; Wong, S. P., Molybdenum-carbon film fabricated using metal cathodic arc and acetylene dual plasma deposition. *Surf. Coat. Technol.* **2004**, *186* (1-2), 112-117.
18. Fu, R. K. Y.; Mei, Y. F.; Fu, M. Y.; Liu, X. Y.; Chu, P. K., Thermal stability of metal-doped diamond-like carbon fabricated by dual plasma deposition. *Diamond and Related Materials* **2005**, *14* (9), 1489-1493.
19. Adelhelm, C.; Balden, M.; Rasinski, M.; Lindig, S.; Plocinski, T.; Welter, E.; Sikora, M., Investigation of metal distribution and carbide crystallite formation in metal-doped carbon films (a-C:Me, Me = Ti, V, Zr, W) with low metal content. *Surf. Coat. Technol.* **2011**, *205* (19), 4335-4342.
20. Balden, M., Characterization of nano-structured W-, Ti-, V-, and Zr-doped carbon films. *Thin Solid Films* **2011**, *519* (12), 4032-4036.
21. Lin, Y.-H.; Lin, H.-D.; Liu, C.-K.; Huang, M.-W.; Chen, Y.-C.; Chen, J.-R.; Shih, H. C., Annealing effect on the structural, mechanical and electrical properties of titanium-doped diamond-like carbon films. *Thin Solid Films* **2009**, *518* (5), 1503-1507.
22. Zou, C. W.; Wang, H. J.; Feng, L.; Xue, S. W., Effects of Cr concentrations on the microstructure, hardness, and temperature-dependent tribological properties of Cr-DLC coatings. *Applied Surface Science* **2013**, *286*, 137-141.
23. Wang, D.-Y.; Weng, K.-W.; Chang, C.-L.; Guo, X.-J., Tribological performance of metal doped diamond-like carbon films deposited by cathodic arc evaporation. *Diamond and Related Materials* **2000**, *9* (3), 831-837.
24. Dimigen, H.; Klages, C.-P., Microstructure and wear behavior of metal-containing diamond-like coatings. *Surface and Coatings Technology* **1991**, *49* (1), 543-547.
25. Kinoshita, H.; Ikuta, R.; Murakami, S., Deposition and field-emission characterization of electrically conductive nitrogen-doped diamond-like amorphous carbon films. *J. Vac. Sci. Technol., A* **2004**, *22*, 1857-1861.
26. Kundoo, S.; Saha, P.; Chattopadhyay, K. K., Electron field emission from nitrogen and sulfur-doped diamond-like carbon films deposited by simple electrochemical route. *Materials Letters* **2004**, *58* (30), 3920-3924.
27. Liu, D.; Zhang, S.; Ong, S. E.; Benstetter, G.; Du, H., Surface and electron emission properties of hydrogen-free diamond-like carbon films investigated by atomic force microscopy. *Materials Science & Engineering, A: Structural Materials: Properties, Microstructure and Processing* **2006**, *A426* (1-2), 114-120.
28. Kwok, S. C. H.; Wang, J.; Chu, P. K., Surface energy, wettability, and blood compatibility of phosphorus doped diamond-like carbon films. *Diamond and Related Materials* **2005**, *14* (1), 78-85.
29. Neidhardt, J.; Hultman, L.; Broitman, E.; Scharf, T. W.; Singer, I. L., Structural, mechanical and tribological behavior of fullerene-like and amorphous carbon nitride coatings. *Diamond and Related Materials* **2004**, *13* (10), 1882-1888.
30. Palacio, J. F.; Bull, S. J.; Neidhardt, J.; Hultman, L., Nanoindentation response of high performance fullerene-like CN<sub>x</sub>. *Thin Solid Films* **2005**, *494* (1-2), 63-68.

31. Cui, F. Z.; Qing, X. L.; Li, D. J.; Zhao, J., Biomedical investigations on CN<sub>x</sub> coating. *Surface and Coatings Technology* **2005**, *200* (1-4), 1009-1013.
32. Maitz, M. F.; Gago, R.; Abendroth, B.; Camero, M.; Caretti, I.; Kreissig, U., Hemocompatibility of low-friction boron-carbon-nitrogen containing coatings. *J. Biomed. Mater. Res. Part B Appl. Biomater.* **2006**, *77* (1), 179-187.
33. Kwok, S. C. H.; Wan, G. J.; Ho, J. P. Y.; Chu, P. K.; Bilek, M. M. M.; McKenzie, D. R., Characteristics of phosphorus-doped diamond-like carbon films synthesized by plasma immersion ion implantation and deposition (PIII and D). *Surf. Coat. Technol.* **2007**, *201* (15), 6643-6646.
34. Hasebe, T.; Shimada, A.; Suzuki, T.; Matsuoka, Y.; Saito, T.; Yohena, S.; Kamijo, A.; Shiraga, N.; Higuchi, M.; Kimura, K.; Yoshimura, H.; Kuribayashi, S., Fluorinated diamond-like carbon as antithrombogenic coating for blood-contacting devices. *Journal of Biomedical Materials Research, Part A* **2006**, *76A* (1), 86-94.
35. Hasebe, T.; Yohena, S.; Kamijo, A.; Okazaki, Y.; Hotta, A.; Takahashi, K.; Suzuki, T., Fluorine doping into diamond-like carbon coatings inhibits protein adsorption and platelet activation. *J. Biomed. Mater. Res., Part A* **2007**, *83A* (4), 1192-1199.
36. Cutiongco, E. C.; Li, D.; Chung, Y.-W.; Bhatia, C. S., Tribological Behavior of Amorphous Carbon Nitride Overcoats for Magnetic Thin-Film Rigid Disks. *Journal of Tribology* **1996**, *118* (3), 543-548.
37. Bae, J.-H.; Cho, J., Structural, morphological, and mechanical properties of amorphous carbon and carbon nitride thin films deposited by reactive and ion beam assisted laser ablation. *Journal of Materials Science* **1999**, *34* (5), 1093-1098.
38. Franceschini, D. F.; Achete, C. A.; Freire, F. L., Internal stress reduction by nitrogen incorporation in hard amorphous carbon thin films. *Applied Physics Letters* **1992**, *60* (26), 3229-3231.
39. Du, C.; Su, X. W.; Cui, F. Z.; Zhu, X. D., Morphological behaviour of osteoblasts on diamond-like carbon coating and amorphous C-N film in organ culture. *Biomaterials* **1998**, *19* (7-9), 651-658.
40. Tessier, P. Y.; Pichon, L.; Villechaise, P.; Linez, P.; Angleraud, B.; Mubumbila, N.; Fouquet, V.; Straboni, A.; Milhet, X.; Hildebrand, H. F., Carbon nitride thin films as protective coatings for biomaterials: Synthesis, mechanical and biocompatibility characterizations. *Diamond and Related Materials* **2003**, *12* (3-7), 1066-1069.
41. Kwok, S. C. H.; Yang, P.; Wang, J.; Liu, X.; Chu, P. K., Hemocompatibility of nitrogen-doped, hydrogen-free diamond-like carbon prepared by nitrogen plasma immersion ion implantation-deposition. *Journal of Biomedical Materials Research, Part A* **2004**, *70A* (1), 107-114.
42. Wang, C.; Yang, S. R.; Li, H. X.; Zhang, J. Y., Elastic properties of a-C : N : H films. *Journal of Applied Physics* **2007**, *101* (1), 6.
43. Hellgren, N.; Johansson, M. P.; Broitman, E.; Hultman, L.; Sundgren, J.-E., Role of nitrogen in the formation of hard and elastic thin films by reactive magnetron sputtering. *Physical Review B* **1999**, *59* (7), 5162-5169.

44. Neidhardt, J.; Czigany, Z.; Hultman, L., Superelastic fullerene-like carbon nitride coatings synthesized by reactive unbalanced magnetron sputtering. *Surf. Eng.* **2003**, *19* (4), 299-303.
45. Broitman, E.; Hellgren, N.; Wänstrand, O.; Johansson, M. P.; Berlind, T.; Sjöström, H.; Sundgren, J. E.; Larsson, M.; Hultman, L., Mechanical and tribological properties of CN<sub>x</sub> films deposited by reactive magnetron sputtering. *Wear* **2001**, *248* (1), 55-64.
46. Ceramic Materials. In *Handbook of Materials For Medical Devices*, Davis, J. R., Ed. ASM International: Materials Park, OH, 2003; pp 148-49.
47. Allen, M.; Myer, B.; Rushton, N., In vitro and in vivo investigations into the biocompatibility of diamond-like carbon (DLC) coatings for orthopedic applications. *J.Biomed.Mater.Res.* **2001**, *58* (3), 319-328.
48. Du, C.; Su, X. W.; Cui, F. Z.; Zhu, X. D., Morphological behavior of osteoblasts on diamond-like carbon coating and amorphous C-N film in organ culture. *Biomaterials* **1998**, *19* (7-9), 651-658.
49. Jones, M. I.; McColl, I. R.; Grant, D. M.; Parker, K. G.; Parker, T. L., Protein adsorption and platelet attachment and activation, on TiN, TiC, and DLC coatings on titanium for cardiovascular applications. *J.Biomed.Mater.Res.* **2000**, *52* (2), 413-421.
50. Li, D. J.; Niu, L. F., Influence of N atomic percentages on cell attachment for CN<sub>x</sub> coatings. *Bulletin of Materials Science* **2003**, *26* (4), 371-375.
51. Dearnaley, G.; Arps, J. H., Biomedical applications of diamond-like carbon (DLC) coatings: A review. *Surface and Coatings Technology* **2005**, *200* (7), 2518-2524.
52. Hauert, R., A review of modified DLC coatings for biological applications. *Diamond and Related Materials* **2003**, *12* (3-7), 583-589.
53. Chu, P. K., Bioactivity of plasma implanted biomaterials. *Nuclear Instruments & Methods in Physics Research, Section B: Beam Interactions with Materials and Atoms* **2006**, *242* (1-2), 1-7.
54. Yamazaki, K.; Litwak, P.; Tagusari, O.; Mori, T.; Kono, K.; Kameneva, M.; Watach, M.; Gordon, L.; Miyagishima, M.; Tomioka, J.; Umezu, M.; Outa, E.; Antaki, J. F.; Kormos, R. L.; Koyanagi, H.; Griffith, B. P., An implantable centrifugal blood pump with a recirculating purge system (Cool-Seal system). *Artif Organs* **1998**, *22* (6), 466-474.
55. Andrade, J.; Hlady, V., Protein adsorption and materials biocompatibility: A tutorial review and suggested hypotheses. In *Advances in Polymer Science*, Springer Berlin / Heidelberg: 1986; Vol. 79, pp 1-63.
56. Norde, W.; Horbett, T. A.; Brash, J. L., Proteins at interfaces III: Introductory overview. In *ACS Symp. Ser.*, American Chemical Society: 2012; Vol. 1120, pp 1-34.
57. Brash, J. L., Protein surface interactions and biocompatibility: A forty year perspective. In *ACS Symp. Ser.*, American Chemical Society: 2012; Vol. 1120, pp 277-300.
58. Norde, W., My voyage of discovery to proteins in flatland ...and beyond. *Colloids and Surfaces B: Biointerfaces* **2008**, *61* (1), 1-9.

59. Reviakine, I.; Jung, F.; Braune, S.; Brash, J. L.; Latour, R.; Gorbet, M.; van Oeveren, W., Stirred, shaken, or stagnant: What goes on at the blood–biomaterial interface. *Blood Rev.* **2017**, *31* (1), 11-21.
60. Bokros, J. C., Carbon biomedical devices. *Carbon* **1977**, *15* (6), 353-371.
61. Stanley, J.; Klawitter, J.; More, R., 26 - Replacing joints with pyrolytic carbon. In *Joint Replacement Technology*, Revell, P. A., Ed. Woodhead Publishing: 2008; pp 631-656.
62. Hauert, R.; Thorwarth, K.; Thorwarth, G., An overview on diamond-like carbon coatings in medical applications. *Surface and Coatings Technology* **2013**, *233*, 119-130.
63. Ma, W. J.; Ruys, A. J.; Mason, R. S.; Martin, P. J.; Bendavid, A.; Liu, Z.; Ionescu, M.; Zreiqat, H., DLC coatings: Effects of physical and chemical properties on biological response. *Biomaterials* **2007**, *28* (9), 1620-1628.
64. Narayan, R. J., Nanostructured diamondlike carbon thin films for medical applications. *Materials Science & Engineering, C: Biomimetic and Supramolecular Systems* **2005**, *C25* (3), 405-416.
65. Santos, M.; Bilek, M. M. M.; Wise, S. G., Plasma-synthesised carbon-based coatings for cardiovascular applications. *Biosurface and Biotribology* **2015**, *1* (3), 146-160.
66. Barragan, P.; Herbst, F.; Kalachev, A., The BioDiamond and BioDiamond F Stents. In *Handbook of coronary stents*, 3rd ed.. ed.; Serruys, P. W.; Kutryk, M. J. B., Eds. London : M. Dunitz Malden, Mass., USA : Distributed in the USA by Blackwell Science: London : Malden, Mass., USA, 2000; pp 29-40.
67. Gutensohn, K.; Beythien, C.; Bau, J.; Fenner, T.; Grewe, P.; Koester, R.; Padmanaban, K.; Kuehnl, P., In Vitro Analyses of Diamond-like Carbon Coated Stents: Reduction of Metal Ion Release, Platelet Activation, and Thrombogenicity. *Thrombosis Research* **2000**, *99* (6), 577-585.
68. Airoidi, F.; Colombo, A.; Tavano, D.; Stankovic, G.; Klugmann, S.; Paolillo, V.; Bonizzoni, E.; Briguori, C.; Carlino, M.; Montorfano, M.; Liistro, F.; Castelli, A.; Ferrari, A.; Sgura, F.; Di Mario, C., Comparison of diamond-like carbon-coated stents versus uncoated stainless steel stents in coronary artery disease. *The American Journal of Cardiology* **2004**, *93* (4), 474-477.
69. Meireles, G. C. X.; Abreu, L. M. d.; Forte, A. A. d. C.; Sumita, M. K.; Sumita, J. H.; Aliaga, J. D. C. S., Randomized Comparative Study of Diamond-like Carbon Coated Stainless Steel Stent versus Uncoated Stent Implantation in Patients with Coronary Artery Disease. *Arquivos Brasileiros de Cardiologia* **2007**, *88* (4), 343-347.
70. Antonucci, D.; Bartorelli, A.; Valenti, R.; Montorsi, P.; Santoro, G. M.; Fabbicocchi, F.; Bolognese, L.; Loaldi, A.; Trapani, M.; Trabattoni, D.; Moschi, G.; Galli, S., Clinical and angiographic outcome after coronary arterial stenting with the carbostent. *The American Journal of Cardiology* **2000**, *85* (7), 821-825.
71. Bartorelli, A. L.; Trabattoni, D.; Montorsi, P.; Fabbicocchi, F.; Galli, S.; Ravagnani, P.; Grancini, L.; Cozzi, S.; Loaldi, A., Aspirin alone antiplatelet regimen after intracoronary placement of the Carbostent™: The Antares study. *Catheterization and Cardiovascular Interventions* **2002**, *55* (2), 150-156.
72. Visconti, G.; Focaccio, A.; Tavano, D.; Airoidi, F.; Briguori, C., The CID Chrono™ cobalt–chromium alloy carbofilm-coated coronary stent system. *International Journal of Cardiology* **2011**, *149* (2), 199-204.
73. Meens, H. J. M.; Horvers, R. A. M., The GENIC DYLYN stent. In *Handbook of Coronary Stents, Fourth Edition*, CRC Press: 2001; pp 98-100.

74. De Scheerder, I.; Szilard, M.; Yanming, H.; Ping, X. B.; Verbeken, E.; Neerinck, D.; Demeyere, E.; Coppens, W.; Van De Werf, F., Evaluation of the biocompatibility of two new diamond-like stent coatings (Dylyn™) in a porcine coronary stent model. *J. Invasive Cardiol.* **2000**, *12* (8), 389-394.
75. Riezebos, R.; Ronner, E.; Kiemeneij, F.; Laarman, G. J., A prospective multicentre registry of the procedural and long-term clinical and angiographic results of stent implantation using a Dylyn coated coronary stent system. *Int. J. Cardiovasc. Interventions* **2004**, *6* (3-4), 137-141.
76. Ando, K.; Ishii, K.; Tada, E.; Kataoka, K.; Hirohata, A.; Goto, K.; Kobayashi, K.; Tsutsui, H.; Nakahama, M.; Nakashima, H.; Uchikawa, S.; Kanda, J.; Yasuda, S.; Yajima, J.; Kitabayashi, H.; Sakurai, S.; Nakanishi, K.; Inoue, N.; Noike, H.; Hasebe, T.; Sato, T.; Yamasaki, M.; Kimura, T., Prospective multi-center registry to evaluate efficacy and safety of the newly developed diamond-like carbon-coated cobalt-chromium coronary stent system. *Cardiovascular Intervention and Therapeutics* **2017**, *32* (3), 225-232.
77. Mountfort, K.; Carrié, D.; Valgimigli, M.; Sardella, G.; Banai, S.; Romaguera, R.; Stella, P., Meeting the Unmet - The Cre8 Polymer-free Drug-eluting Stents Technology: Proceedings of a satellite symposium held at EuroPCR on May 20th - 23rd 2014 in Paris. *Interventional cardiology (London, England)* **2014**, *9* (3), 184-189.
78. Yamazaki, K.; Saito, S.; Nishinaka, T.; Kurosawa, H.; Nakatani, T.; Kobayashi, J.; Kitamura, S.; Matsumiya, G.; Yoshiki, S.; Nishimura, T.; Niinami, H.; Kyo, S., 517: Japanese Clinical Trial Results of an Implantable Centrifugal Blood Pump &#x201c;EVAHEART&#x201d. *The Journal of Heart and Lung Transplantation* **2008**, *27* (2), S246.
79. Yamazaki, K.; Saito, S.; Kihara, S.; Tagusari, O.; Kurosawa, H., Completely pulsatile high flow circulatory support with a constant-speed centrifugal blood pump: mechanisms and early clinical observations. *General Thoracic and Cardiovascular Surgery* **2007**, *55* (4), 158-162.
80. Motomura, T.; Kelly, B., Surgical Techniques for Implanting the EVAHEART 2 Double Cuff Tipless Inflow Cannula. *ASAIO J* **2018**.
81. Motomura, T.; Tuzun, E.; Yamazaki, K.; Tatsumi, E.; Benkowski, R.; Yamazaki, S., Preclinical Evaluation of the EVAHEART 2 Centrifugal Left Ventricular Assist Device in Bovines. *ASAIO J* **2018**.
82. Vallana, F.; Rinaldi, S.; Calletti, P.; Nguyen, A.; Piwnica, A., Pivot Design in Bileaflet Valves. *ASAIO J* **1992**, *38* (3), M600-M606.
83. Misawa, Y.; Saito, T.; Konishi, H.; Oki, S.-i.; Kaminishi, Y.; Sakano, Y.; Morita, H.; Aizawa, K., Clinical experience with the Bicarbon heart valve prosthesis. *Journal of Cardiothoracic Surgery* **2007**, *2* (1), 8.
84. Azarnoush, K.; Laborde, F.; de Riberolles, C., The Sorin Bicarbon over 15 years clinical outcomes: Multicentre experience in 1704 patients. *Eur. J. Cardio-thorac. Surg.* **2010**, *38* (6), 759-766.
85. Misawa, Y.; Muraoka, A.; Ohki, S.; Aizawa, K.; Kawahito, K.; Saito, T.; Sato, H.; Takazawa, I.; Kurumisawa, S.; Akutsu, H.; Sugaya, A., Fifteen-year experience with the Bicarbon heart valve prosthesis in a single center. *Journal of Cardiothoracic Surgery* **2015**, *10* (1).
86. Meer, A. L. v. d.; James, N. L.; Edwards, G. A.; Esmore, D. S.; Rosenfeldt, F. L.; Begg, J. D.; Woodard, J. C., Initial In Vivo Experience of the VentrAssist Implantable Rotary Blood Pump in Sheep. *Artificial Organs* **2003**, *27* (1), 21-26.

87. James, N. L.; van der Meer, A. L.; Edwards, G. A.; Snelling, S. R.; Begg, J. D.; Esmore, D. S.; Woodard, J. C., Implantation of the VentrAssist Implantable Rotary Blood Pump in Sheep. *ASAIO Journal* **2003**, *49*, 454-458.
88. Angelini, G. S. F., (GB), Pistolesi, Claudio (Siena, IT) Heart valve prosthesis. 5236448, 1993.
89. Binner, J.; Hogg, P.; Sweeney, J., Carbon For Implants. In *Advanced Materials 1991-1992: I. Source Book*, Binner, J.; Hogg, P.; Sweeney, J.; Butler, N., Eds. Elsevier Science Publishers Ltd.: Oxford, UK, 1991; p 56.
90. Unsworth, W.; Angelini, G. D.; Pistolesi, C. Heart Valve Prosthesis. US005693090A, 1997.
91. Roy, R. K.; Lee, K.-R., Biomedical applications of diamond-like carbon coatings: A review. *Journal of Biomedical Materials Research Part B: Applied Biomaterials* **2007**, *83B* (1), 72-84.
92. Ma, W.; Ruys, A. J.; Zreiqat, H., 16 - Diamond-like carbon (DLC) as a biocompatible coating in orthopaedic and cardiac medicine. In *Cellular Response to Biomaterials*, Di Silvio, L., Ed. Woodhead Publishing: 2009; pp 391-426.
93. Greenwald, S. E.; Berry, C. L., Improving vascular grafts: the importance of mechanical and haemodynamic properties. *The Journal of Pathology* **2000**, *190* (3), 292-299.
94. Esquivel, C. O.; Blaisdell, F. W., Why small caliber vascular grafts fail: a review of clinical and experimental experience and the significance of the interaction of blood at the interface. *J Surg Res* **1986**, *41* (1), 1-15.
95. Burkel, W. E., The challenge of small diameter vascular grafts. *Med Prog Technol* **1988**, *14* (3-4), 165-175.
96. Vandencastele, N.; Nisol, B.; Viville, P.; Lazzaroni, R.; Castner, D. G.; Reniers, F., Study of plasma modified-PTFE for biological applications: relationship between protein resistant properties, plasma treatment, surface composition and surface roughness. *Plasma processes and polymers (Print)* **2008**, *5* (7), 661-671.
97. Vasilets, V. N.; Hermel, G.; Konig, U.; Werner, C.; Muller, M.; Simon, F.; Grundke, K.; Ikada, Y.; Jacobasch, H. J., Microwave CO<sub>2</sub> plasma-initiated vapor phase graft polymerization of acrylic acid onto polytetrafluoroethylene for immobilization of human thrombomodulin. *Biomaterials* **1997**, *18* (17), 1139-1145.
98. Imbert, E.; Poot, A. A.; Figdor, C. G.; Feijen, J., Expression of leukocyte adhesion molecules by endothelial cells seeded on various polymer surfaces. *J.Biomed.Mater.Res.* **2001**, *56* (3), 376-381.
99. Koveker, G. B.; Graham, L. M.; Burkel, W. E.; Sell, R.; Wakefield, T. W.; Dietrich, K.; Stanley, J. C., Extracellular matrix preparation of expanded polytetrafluoroethylene grafts seeded with endothelial cells: influence on early platelet deposition, cellular growth, and luminal prostacyclin release. *Surgery* **1991**, *109* (3 Pt 1), 313-319.
100. Miyata, T.; Conte, M. S.; Trudell, L. A.; Mason, D.; Whittemore, A. D.; Birinyi, L. K., Delayed exposure to pulsatile shear stress improves retention of human saphenous vein endothelial cells on seeded ePTFE grafts. *J Surg Res* **1991**, *50* (5), 485-493.

101. Rosenman, J. E.; Kempczinski, R. F.; Pearce, W. H.; Silberstein, E. B., Kinetics of endothelial cell seeding. *J Vasc Surg* **1985**, 2 (6), 778-784.
102. Vasquez, S.; Achete, C. A.; Borges, C. P.; Franceschini, D. F.; Freire, J. F. L.; Zanghellini, E., Structure and properties of a-C:H films deposited onto polymeric substrates. *Diamond Relat. Mater.* **1997**, 6 (5-7), 551-554.
103. Vasilets, V. N.; Hirose, A.; Yang, Q.; Singh, A.; Sammynaiken, R.; Foursa, M.; Shulga, Y. M., Characterization of doped diamond-like carbon films deposited by hot wire plasma sputtering of graphite. *Applied Physics A: Materials Science & Processing* **2004**, 79 (8), 2079-2084.
104. Hamilton, T.; Wilks, R. G.; Yablonskikh, M. V.; Yang, Q.; Foursa, M. N.; Hirose, A.; Vasilets, V. N.; Moewes, A., Determining the sp<sup>2</sup>/sp<sup>3</sup> bonding concentrations of carbon films using X-ray absorption spectroscopy. *Can.J.Phys.* **2008**, 86 (12), 1401-1407.
105. Hamilton, T.; Foursa, M.; Hirose, A.; Moewes, A., X-ray absorption of nitrogen-doped amorphous carbon films for determining sp<sup>2</sup>/sp<sup>3</sup> bonding concentrations. *Radiat.Phys.Chem.* **2006**, 75 (11), 1613-1616.
106. Srinivasan, S.; Tang, Y.; Li, Y. S.; Yang, Q.; Hirose, A., Ion beam deposition of DLC and nitrogen doped DLC thin films for enhanced haemocompatibility on PTFE. *Applied Surface Science* **2012**, 258 (20), 8094-8099.
107. Boccafoschi, F.; Chevallier, P.; Sarkissian, A.; Mantovani, D., Haematological performances of carbon coated PTFE by plasma-based deposition. *Mater.Sci.Forum* **2010**, 638-642 (Pt. 1, THERMEC 2009), 512-517.
108. Khatir, S.; Hirose, A.; Xiao, C., Coating diamond-like carbon films on polymer substrates by inductively coupled plasma assisted sputtering. *Surf. Coat. Technol.* **2014**, 253, 96-99.
109. Khatir, S.; Hirose, A.; Xiao, C., Characterization of physical and biomedical properties of nitrogenated diamond-like carbon films coated on polytetrafluoroethylene substrates. *Diamond Relat. Mater.* **2015**, 58, 205-213.
110. Matsuo, H.; Kanasugi, K.; Ohgoe, Y.; Hirakuri, K. K.; Fukui, Y., Biocompatibility of a-C:H film coating for synthetic vascular graft. *Diamond and Related Materials* **2009**, 18 (5-8), 1031-1034.
111. Nakatani, T.; Imai, Y.; Fujii, Y.; Goyama, T.; Ozawa, S., Novel DLC Coating Technique on an Inner-wall of Extended Polytetrafluoroethylene Vascular Grafts Using Methane Plasma Produced by AC HV Discharge. *Journal of Photopolymer Science and Technology* **2018**, 31 (3), 373-377.
112. Chu, P. K., Plasma surface treatment of artificial orthopedic and cardiovascular biomaterials. *Surface and Coatings Technology* **2007**, 201 (9-11), 5601-5606.
113. Yang, P.; Huang, N.; Leng, Y. X.; Yao, Z. Q.; Zhou, H. F.; Maitz, M.; Leng, Y.; Chu, P. K., Wettability and biocompatibility of nitrogen-doped hydrogenated amorphous carbon films: Effect of nitrogen. *Nucl.Instrum.Methods Phys.Res., Sect.B* **2006**, 242 (1-2), 22-25.
114. Foursa, M. Plasma-assisted deposition of nitrogen-doped amorphous carbon films onto polytetrafluoroethylene for biomedical applications. 2007.

115. Srinivasan, S.; Yang, Q.; Vasilets, V. N. In *Nitrogen doped diamond like carbon thin films on ptfе for enhanced hemocompatibility*, Nanostructured Materials and Nanotechnology II - 32nd International Conference on Advanced Ceramics and Composites, Daytona Beach, FL, Daytona Beach, FL, 2009; pp 233-242.
116. Haynes, C. A.; Norde, W., Globular proteins at solid/liquid interfaces. *Colloids and Surfaces B: Biointerfaces* **1994**, 2 (6), 517-566.
117. Rabe, M.; Verdes, D.; Seeger, S., Understanding protein adsorption phenomena at solid surfaces. *Advances in Colloid and Interface Science* **2011**, 162 (1), 87-106.
118. Silva-Bermudez, P.; Rodil, S. E., An overview of protein adsorption on metal oxide coatings for biomedical implants. *Surface and Coatings Technology* **2013**, 233, 147-158.
119. Elwing, H. B.; Li, L.; Askendal, A. R.; Nimeri, G. S.; Brash, J. L., Protein Displacement Phenomena in Blood Plasma and Serum Studied by the Wettability Gradient Method and the Lens-on-Surface Method. In *Proteins at Interfaces II*, American Chemical Society: 1995; Vol. 602, pp 138-149.
120. Lord, M. S.; Foss, M.; Besenbacher, F., Influence of nanoscale surface topography on protein adsorption and cellular response. *Nano Today* **2010**, 5 (1), 66-78.
121. Rechendorff, K.; Hovgaard, M. B.; Foss, M.; Zhdanov, V. P.; Besenbacher, F., Enhancement of Protein Adsorption Induced by Surface Roughness. *Langmuir* **2006**, 22 (26), 10885-10888.
122. Lord, M. S.; Cousins, B. G.; Doherty, P. J.; Whitelock, J. M.; Simmons, A.; Williams, R. L.; Milthorpe, B. K., The effect of silica nanoparticulate coatings on serum protein adsorption and cellular response. *Biomaterials* **2006**, 27 (28), 4856-4862.
123. Mughal, M. Z.; Lemoine, P.; Lubarsky, G.; Maguire, P. D., Protein adsorption on nano-patterned hydrogenated amorphous carbon model surfaces. *Mater. Des.* **2016**, 97, 239-248.
124. Ekblad, T.; Liedberg, B., Protein adsorption and surface patterning. *Current Opinion in Colloid & Interface Science* **2010**, 15 (6), 499-509.
125. Sommerfeld, J.; Richter, J.; Niepelt, R.; Kosan, S.; Keller, T. F.; Jandt, K. D.; Ronning, C., Protein adsorption on nano-scaled, rippled TiO<sub>2</sub> and Si Surfaces. *Biointerphases* **2012**, 7 (1-4), 55.
126. Talbot, J.; Tarjus, G.; Van Tassel, P. R.; Viot, P., From car parking to protein adsorption: an overview of sequential adsorption processes. *Colloids and Surfaces A: Physicochemical and Engineering Aspects* **2000**, 165 (1), 287-324.
127. Norde, W.; Giacomelli, C. E., Conformational changes in proteins at interfaces: From solution to the interface, and back. *Macromolecular Symposia* **1999**, 145 (1), 125-136.
128. Schmitt, A.; Varoqui, R.; Uniyal, S.; Brash, J. L.; Pusineri, C., Interaction of fibrinogen with solid surfaces of varying charge and hydrophobic—hydrophilic balance: I. Adsorption isotherms. *Journal of Colloid and Interface Science* **1983**, 92 (1), 25-34.

129. Brash, J. L.; Uniyal, S.; Pusineri, C.; Schmitt, A., Interaction of fibrinogen with solid surfaces of varying charge and hydrophobic—hydrophilic balance: II. Dynamic exchange between surface and solution molecules. *Journal of Colloid and Interface Science* **1983**, *95* (1), 28-36.
130. Kwok, K. C.; Yeung, K. M.; Cheung, N. H., Adsorption Kinetics of Bovine Serum Albumin on Fused Silica: Population Heterogeneities Revealed by Single-Molecule Fluorescence Microscopy. *Langmuir* **2007**, *23* (4), 1948-1952.
131. Norde, W.; Giacomelli, C. E., BSA structural changes during homomolecular exchange between the adsorbed and the dissolved states. *Journal of Biotechnology* **2000**, *79* (3), 259-268.
132. Castner, D. G.; Ratner, B. D., Biomedical surface science: Foundations to frontiers. *Surface Science* **2002**, *500* (1-3), 28-60.
133. Kempson, I. M.; Hwu, Y.; Prestidge, C. A., Probing Protein Association with Nano- and Micro-Scale Structures with ToF-SIMS. In *Proteins at Interfaces III State of the Art*, American Chemical Society: 2012; Vol. 1120, pp 709-729.
134. Feng, L.; Andrade, J. D., Protein adsorption on to low-temperature isotropic carbon 4. Competitive adsorption on carbon and silica studied by two-dimensional electrophoresis. *Colloids and Surfaces B: Biointerfaces* **1995**, *4* (6), 313-325.
135. Wojciechowski, P.; Ten Hove, P.; Brash, J. L., Phenomenology and mechanism of the transient adsorption of fibrinogen from plasma (Vroman effect). *Journal of Colloid and Interface Science* **1986**, *111* (2), 455-465.
136. Hirsh, S. L.; McKenzie, D. R.; Nosworthy, N. J.; Denman, J. A.; Sezerman, O. U.; Bilek, M. M. M., The Vroman effect: Competitive protein exchange with dynamic multilayer protein aggregates. *Colloids and Surfaces B: Biointerfaces* **2013**, *103*, 395-404.
137. Sperling, C.; Fischer, M.; Maitz, M. F.; Werner, C., Blood coagulation on biomaterials requires the combination of distinct activation processes. *Biomaterials* **2009**, *30* (27), 4447-4456.
138. Xu, L.-C.; Bauer, J. W.; Siedlecki, C. A., Proteins, platelets, and blood coagulation at biomaterial interfaces. *Colloids and Surfaces B: Biointerfaces* **2014**, *124*, 49-68.
139. Sivaraman, B.; Latour, R. A., The relationship between platelet adhesion on surfaces and the structure versus the amount of adsorbed fibrinogen. *Biomaterials* **2010**, *31* (5), 832-839.
140. Zhang, L.; Casey, B.; Galanakis, D. K.; Marmorat, C.; Skoog, S.; Vorvolakos, K.; Simon, M.; Rafailovich, M. H., The influence of surface chemistry on adsorbed fibrinogen conformation, orientation, fiber formation and platelet adhesion. *Acta Biomater.* **2017**, *54*, 164-174.
141. Sivaraman, B.; Latour, R. A., The Adherence of platelets to adsorbed albumin by receptor-mediated recognition of binding sites exposed by adsorption-induced unfolding. *Biomaterials* **2010**, *31* (6), 1036-1044.
142. Sivaraman, B.; Latour, R. A., Time-Dependent Conformational Changes in Adsorbed Albumin and Its Effect on Platelet Adhesion. *Langmuir* **2012**, *28* (5), 2745-2752.

143. Feng, L.; Andrade, J. D., Protein adsorption on low-temperature isotropic carbon: I. Protein conformational change probed by differential scanning calorimetry. *J. Biomed. Mater. Res.* **1994**, *28* (6), 735-743.
144. Feng, L.; Andrade, J. D., Protein adsorption on low-temperature isotropic carbon. II. effects of surface charge of solids. *Journal of Colloid And Interface Science* **1994**, *166* (2), 419-426.
145. Feng, L.; Andrade, J. D., Protein adsorption on low temperature isotropic carbon. III. Isotherms, competitiveness, desorption and exchange of human albumin and fibrinogen. *Biomaterials* **1994**, *15* (5), 324-333.
146. Feng, L.; Andrade, J. D., Protein adsorption on low temperature isotropic carbon: V. How is it related to its blood compatibility? *Journal of Biomaterials Science, Polymer Edition* **1995**, *7* (5), 439-452.
147. Logothetidis, S.; Gioti, M.; Lousinian, S.; Fotiadou, S., Haemocompatibility studies on carbon-based thin films by ellipsometry. *Thin Solid Films* **2005**, *482* (1-2), 126-132.
148. Logothetidis, S., Hemocompatibility of carbon based thin films. *Diamond Relat.Mater.* **2007**, *16* (10), 1847-1857.
149. Lousinian, S.; Logothetidis, S., Optical properties of proteins and protein adsorption study. *Microelectronic Engineering* **2007**, *84* (3), 479-485.
150. Mitsakakis, K.; Lousinian, S.; Logothetidis, S., Early stages of human plasma proteins adsorption probed by Atomic Force Microscope. *Biomolecular Engineering* **2007**, *24* (1), 119-124.
151. Berlind, T.; Tengvall, P.; Hultman, L.; Arwin, H., Protein adsorption on thin films of carbon and carbon nitride monitored with in situ ellipsometry. *Acta Biomater.* **2011**, *7* (3), 1369-1378.
152. Berlind, T.; Furlan, A.; Czigany, Z.; Neidhardt, J.; Hultman, L.; Arwin, H., Spectroscopic ellipsometry characterization of amorphous carbon and amorphous, graphitic and fullerene-like carbon nitride thin films. *Thin Solid Films* **2009**, *517* (24), 6652-6658.
153. Mrksich, M.; Sigal, G. B.; Whitesides, G. M., Surface Plasmon Resonance Permits in Situ Measurement of Protein Adsorption on Self-Assembled Monolayers of Alkanethiolates on Gold. *Langmuir* **1995**, *11* (11), 4383-4385.
154. Mrksich, M.; Whitesides, G. M., Using Self-Assembled Monolayers To Understand The Interactions Of Man-Made Surfaces With Proteins And Cells. *Annu. Rev. Biophys. Biomol. Struct.* **1996**, *25*, 55-78.
155. Sigal, G. B.; Mrksich, M.; Whitesides, G. M., Effect of Surface Wettability on the Adsorption of Proteins and Detergents. *Journal of American Chemical Society* **1998**, *120*, 3464-3473.
156. Lockett, M. R.; Weibel, S. C.; Phillips, M. F.; Shortreed, M. R.; Sun, B.; Corn, R. M.; Hamers, R. J.; Cerrina, F.; Smith, L. M., Carbon-on-Metal Films for Surface Plasmon Resonance Detection of DNA Arrays. *J. Am. Chem. Soc.* **2008**, *130* (27), 8611-8613.
157. Akasaka, H.; Gawazawa, N.; Suzuki, T.; Nakano, M.; Ohshio, S.; Saitoh, H., Evaluation of protein adsorption on hydrogenated amorphous carbon films by surface plasmon resonance phenomenon. *Diamond Relat.Mater.* **2010**, *19* (10), 1235-1239.

158. Akasaka, H.; Takeda, A.; Suzuki, T.; Nakano, M.; Ohshio, S.; Saitoh, H., Fibrinogen and lysozyme adsorption on amorphous carbon film surface detected by multilayer device from the back side of the film. *Diamond Relat. Mater.* **2011**, *20* (2), 213-216.
159. Zou, S.; Schatz, G. C., Silver nanoparticle array structures that produce giant enhancements in electromagnetic fields. *Chem. Phys. Lett.* **2005**, *403* (1), 62-67.
160. Walkowiak, B.; Kochmanska, V.; Jakubowski, W.; Okroj, W.; Kroliczak, V., Interaction of body fluids with carbon surfaces. *Journal of Wide Bandgap Materials* **2002**, *9* (4), 231-242.
161. Li, X.; Husson, S. M., Adsorption of dansylated amino acids on molecularly imprinted surfaces: A surface plasmon resonance study. *Biosensors and Bioelectronics* **2006**, *22* (3), 336-348.
162. Canoa, P.; Simón-Vázquez, R.; Popplewell, J.; González-Fernández, Á., A quantitative binding study of fibrinogen and human serum albumin to metal oxide nanoparticles by surface plasmon resonance. *Biosensors and Bioelectronics* **2015**, *74*, 376-383.
163. Simón-Vázquez, R.; Lozano-Fernández, T.; Peleteiro-Olmedo, M.; González-Fernández, Á., Conformational changes in human plasma proteins induced by metal oxide nanoparticles. *Colloids and Surfaces B: Biointerfaces* **2014**, *113*, 198-206.
164. Chung, K.; Rani, A.; Lee, J.-E.; Kim, J. E.; Kim, Y.; Yang, H.; Kim, S. O.; Kim, D.; Kim, D. H., Systematic Study on the Sensitivity Enhancement in Graphene Plasmonic Sensors Based on Layer-by-Layer Self-Assembled Graphene Oxide Multilayers and Their Reduced Analogues. *ACS Appl. Mater. Interfaces* **2015**, *7* (1), 144-151.
165. Singh, M.; Holzinger, M.; Tabrizian, M.; Winters, S.; Berner, N. C.; Cosnier, S.; Duesberg, G. S., Noncovalently functionalized monolayer graphene for sensitivity enhancement of surface plasmon resonance immunosensors. *J. Am. Chem. Soc.* **2015**, *137* (8), 2800-2803.
166. Zhang, J.; Sun, Y.; Wu, Q.; Zhang, H.; Bai, Y.; Song, D., A protein A modified Au-graphene oxide composite as an enhanced sensing platform for SPR-based immunoassay. *Analyst (Cambridge, U. K.)* **2013**, *138* (23), 7175-7181.
167. Zen, F.; Karanikolas, V. D.; Behan, J. A.; Andersson, J.; Ciapetti, G.; Bradley, A. L.; Colavita, P. E., Nanoplasmonic Sensing at the Carbon-Bio Interface: Study of Protein Adsorption at Graphitic and Hydrogenated Carbon Surfaces. *Langmuir* **2017**, *33* (17), 4198-4206.
168. Worley, C. G.; Linton, R. W., Removing sulfur from gold using ultraviolet/ozone cleaning. *Journal of Vacuum Science & Technology A: Vacuum, Surfaces, and Films* **1995**, *13* (4), 2281-2284.
169. Ansar, S. M.; Ameer, F. S.; Hu, W.; Zou, S.; Pittman, C. U.; Zhang, D., Removal of Molecular Adsorbates on Gold Nanoparticles Using Sodium Borohydride in Water. *Nano Letters* **2013**, *13* (3), 1226-1229.
170. Yuan, M.; Zhan, S.; Zhou, X.; Liu, Y.; Feng, L.; Lin, Y.; Zhang, Z.; Hu, J., A Method for Removing Self-Assembled Monolayers on Gold. *Langmuir* **2008**, *24* (16), 8707-8710.
171. Feng, R. F.; Gerson, A.; Ice, G.; Reininger, R.; Yates, B.; McIntyre, S., VESPERS: A beamline for combined XRF and XRD measurements. *Aip Conf Proc* **2007**, *879*, 872-874.

172. Ferrari, A. C.; Robertson, J., Interpretation of Raman spectra of disordered and amorphous carbon. *Phys.Rev.B: Condens.Matter Mater.Phys.* **2000**, *61* (20), 14095-14107.
173. Ferrari, A. C.; Rodil, S. E.; Robertson, J., Interpretation of infrared and Raman spectra of amorphous carbon nitrides. *Phys.Rev.B: Condens.Matter Mater.Phys.* **2003**, *67* (15), 155306/1-155306/20.
174. Rodil, S. E.; Ferrari, A. C.; Robertson, J.; Milne, W. I., Raman and infrared modes of hydrogenated amorphous carbon nitride. *J.Appl.Phys.* **2001**, *89* (10), 5425-5430.
175. Ferrari, A. C.; Rodil, S. E.; Robertson, J., Resonant Raman spectra of amorphous carbon nitrides: the G peak dispersion. *Diamond Relat.Mater.* **2003**, *12* (3-7), 905-910.
176. Ferrari, A. C.; Robertson, J., Raman spectroscopy of amorphous, nanostructured, diamond-like carbon, and nanodiamond. *Philos.Trans.R.Soc.London, Ser.A* **2004**, *362* (1824), 2477-2512.
177. Casiraghi, C.; Ferrari, A. C.; Robertson, J., Raman spectroscopy of hydrogenated amorphous carbons. *Physical Review B: Condensed Matter and Materials Physics* **2005**, *72* (8), 085401/1-085401/14.
178. Elman, B. S.; Shayegan, M.; Dresselhaus, M. S.; Mazurek, H.; Dresselhaus, G., Structural characterization of ion-implanted graphite. *Physical Review B* **1982**, *25* (6), 4142-4156.
179. Dresselhaus, M. S.; Dresselhaus, G., Light scattering in graphite intercalation compounds. In *Light Scattering in Solids III: Recent Results*, Cardona, M.; Güntherodt, G., Eds. Springer Berlin Heidelberg: Berlin, Heidelberg, 1982; pp 3-57.
180. Kleinsorge, B.; Ferrari, A. C.; Robertson, J.; Milne, W. I.; Waidmann, S.; Hearne, S., Bonding regimes of nitrogen in amorphous carbon. *Diamond Relat. Mater.* **2000**, *9* (Copyright (C) 2011 American Chemical Society (ACS). All Rights Reserved.), 643-648.
181. Muhl, S.; Méndez, J. M., A review of the preparation of carbon nitride films. *Diamond and Related Materials* **1999**, *8* (10), 1809-1830.
182. Liang, C. Y.; Krimm, S., Infrared Spectra Of High Polymers III. Polytetrafluoroethylene And Polychlorotrifluoroethylene. *J. Chem. Phys.* **1956**, *25* (3), 563-571.
183. Starkweather, H. W.; Ferguson, R. C.; Chase, D. B.; Minor, J. M., Infrared-Spectra Of Amorphous And Crystalline Poly(tetrafluoroethylene). *Macromolecules* **1985**, *18* (9), 1684-1686.
184. Starkweather, H. W.; Ferguson, R. C.; Chase, D. B.; Minor, J. M., Infrared spectra of amorphous and crystalline poly(tetrafluoroethylene). *Macromolecules* **1985**, *18* (9), 1684-1686.
185. Beamson, G.; Briggs, D., *High resolution XPS of organic polymers : the Scienta ESCA300 database*. Wiley: Chichester [England] ;, 1992.
186. Susi, T.; Pichler, T.; Ayala, P., X-ray photoelectron spectroscopy of graphitic carbon nanomaterials doped with heteroatoms. *Beilstein Journal of Nanotechnology* **2015**, *6*, 177-192.
187. Rodil, S. E.; Muhl, S., Bonding in amorphous carbon nitride. *Diamond and Related Materials* **2004**, *13* (4), 1521-1531.

188. Brender, P.; Gadiou, R.; Rietsch, J.-C.; Fioux, P.; Dentzer, J.; Ponche, A.; Vix-Guterl, C., Characterization of Carbon Surface Chemistry by Combined Temperature Programmed Desorption with in Situ X-ray Photoelectron Spectrometry and Temperature Programmed Desorption with Mass Spectrometry Analysis. *Analytical Chemistry* **2012**, *84* (5), 2147-2153.
189. Grosvenor, A. P.; Kobe, B. A.; McIntyre, N. S., Studies of the oxidation of iron by water vapour using X-ray photoelectron spectroscopy and QUASES™. *Surface Science* **2004**, *572* (2-3), 217-227.
190. Urquhart, S. G.; Ade, H., Trends in the Carbonyl Core (C 1S, O 1S)→ $\pi^*_{C=O}$  Transition in the Near-Edge X-ray Absorption Fine Structure Spectra of Organic Molecules. *Journal of Physical Chemistry B* **2002**, *106*, 8531-8538.
191. Pireaux, J. J.; de Meulemeester, R.; Roberfroid, E. M.; Gregoire, C.; Chtaib, M.; Novis, Y., Excimer laser ( $\lambda = 193$  nm) versus Al K $\alpha$  x-ray damages on polymer surfaces: an XPS (core and valence levels) analysis of polytetrafluoroethylene, polypropylene and polyethylene. *Nucl. Instrum. Methods Phys. Res., Sect. B* **1995**, *105* (1-4), 186-91.
192. Chen, Z. Y.; Zhao, J. P.; Yano, T.; Ooie, T., Valence band electronic structure of carbon nitride from x-ray photoelectron spectroscopy. *Journal of Applied Physics* **2002**, *92* (1), 281-287.
193. Deslattes, R. D.; Kessler, E. G.; Indelicato, P.; de Billy, L.; Lindroth, E.; Anton, J., X-ray transition energies: new approach to a comprehensive evaluation. *Reviews of Modern Physics* **2003**, *75* (1), 35-99.
194. Peignon, M. C.; Cardinaud, C.; Turban, G., Etching processes of tungsten in SF6-O2 radio-frequency plasmas. *Journal of Applied Physics* **1991**, *70* (6), 3314-3323.
195. Katrib, A.; Hemming, F.; Wehrer, P.; Hilaire, L.; Maire, G., The multi-surface structure and catalytic properties of partially reduced WO3, WO2 and WC + O2 or W + O2 as characterized by XPS. *Journal of Electron Spectroscopy and Related Phenomena* **1995**, *76*, 195-200.
196. Biesinger, M. C.; Payne, B. P.; Grosvenor, A. P.; Lau, L. W. M.; Gerson, A. R.; Smart, R. S. C., Resolving surface chemical states in XPS analysis of first row transition metals, oxides and hydroxides: Cr, Mn, Fe, Co and Ni. *Applied Surface Science* **2011**, *257* (7), 2717-2730.
197. McIntyre, N. S.; Zetaruk, D. G., X-ray photoelectron spectroscopic studies of iron oxides. *Analytical Chemistry* **1977**, *49* (11), 1521-1529.
198. Grosvenor, A. P.; Kobe, B. A.; Biesinger, M. C.; McIntyre, N. S., Investigation of multiplet splitting of Fe 2p XPS spectra and bonding in iron compounds. *Surface and Interface Analysis* **2004**, *36* (12), 1564-1574.
199. Droubay, T.; Chambers, S. A., Surface-sensitive Fe2p photoemission spectra for  $\alpha$ -Fe2O3(0001): The influence of symmetry and crystal-field strength. *Physical Review B* **2001**, *64* (20).
200. Yamashita, T.; Hayes, P., Analysis of XPS spectra of Fe2+ and Fe3+ ions in oxide materials. *Applied Surface Science* **2008**, *254* (8), 2441-2449.
201. Crocombette, J. P.; Pollak, M.; Jollet, F.; Thromat, N.; Gautier-Soyer, M., X-ray-absorption spectroscopy at the Fe L2,3 threshold in iron oxides. *Physical Review B* **1995**, *52* (5), 3143-3150.

202. Pellegrain, E.; Hagelstein, M.; Doyle, S.; Moser, H. O.; Fuchs, J.; Vollath, D.; Schuppler, S.; James, M. A.; Saxena, S. S.; Niesen, L.; Rogojanu, O.; Sawatzky, G. A.; Ferrero, C.; Borowski, M.; Tjernberg, O.; Brookes, N. B., Characterization of Nanocrystalline  $\gamma$ -Fe<sub>2</sub>O<sub>3</sub> with Synchrotron Radiation Techniques. *physica status solidi (b)* **1999**, 215 (1), 797-801.
203. Kuiper, P.; Searle, B. G.; Rudolf, P.; Tjeng, L. H.; Chen, C. T., X-ray magnetic dichroism of antiferromagnet Fe<sub>2</sub>O<sub>3</sub>: The orientation of magnetic moments observed by Fe 2p x-ray absorption spectroscopy. *Physical Review Letters* **1993**, 70 (10), 1549-1552.
204. von der Heyden, B. P.; Roychoudhury, A. N.; Tyliczszak, T.; Myneni, S. C. B., Investigating nanoscale mineral compositions: Iron L-3-edge spectroscopic evaluation of iron oxide and oxy-hydroxide coordination. *Am. Miner.* **2017**, 102 (3), 674-685.
205. Ewels, P.; Sikora, T.; Serin, V.; Ewels, C. P.; Lajaunie, L., A Complete Overhaul of the Electron Energy-Loss Spectroscopy and X-Ray Absorption Spectroscopy Database: eelsdb.eu. *Microsc. microanal.* **2016**, 22 (3), 717-724.
206. Peak, D.; Regier, T., Direct Observation of Tetrahedrally Coordinated Fe(III) in Ferrihydrite. *Environ. Sci. Technol.* **2012**, 46 (6), 3163-3168.
207. Miedema, P. S.; de Groot, F. M. F., The iron L edges: Fe 2p X-ray absorption and electron energy loss spectroscopy. *J. Electron Spectrosc. Relat. Phenom.* **2013**, 187, 32-48.
208. von der Heyden, B. P.; Roychoudhury, A. N.; Mtshali, T. N.; Tyliczszak, T.; Myneni, S. C. B., Chemically and Geographically Distinct Solid-Phase Iron Pools in the Southern Ocean. *Science* **2012**, 338 (6111), 1199.
209. Leedahl, B.; Boukhalov, D. W.; Kurmaev, E. Z.; Kukharenko, A.; Zhidkov, I. S.; Gavrilov, N. V.; Cholakh, S. O.; Le, P. H.; Luo, C. W.; Moewes, A., Bulk vs. Surface Structure of 3d Metal Impurities in Topological Insulator Bi<sub>2</sub>Te<sub>3</sub>. *Scientific Reports* **2017**, 7 (1), 5758.
210. Broitman, E.; Gueorguiev, G. K.; Furlan, A.; Son, N. T.; Gellman, A. J.; Stafström, S.; Hultman, L., Water adsorption on fullerene-like carbon nitride overcoats. *Thin Solid Films* **2008**, 517 (3), 1106-1110.
211. Demichelis, F.; Rong, X. F.; Schreiter, S.; Tagliaferro, A.; De Martino, C., Deposition and characterization of amorphous carbon nitride thin films. *Diamond and Related Materials* **1995**, 4 (4), 361-365.
212. Bilek, M. M.; Bax, D. V.; Kondyurin, A.; Yin, Y.; Nosworthy, N. J.; Fisher, K.; Waterhouse, A.; Weiss, A. S.; dos Remedios, C. G.; McKenzie, D. R., Free radical functionalization of surfaces to prevent adverse responses to biomedical devices. *Proc Natl Acad Sci U S A* **2011**, 108 (35), 14405-10.
213. Goldfarb, D.; Bernardo, M.; Strohmaier, K. G.; Vaughan, D. E. W.; Thomann, H., Characterization of Iron in Zeolites by X-band and Q-Band ESR, Pulsed ESR, and UV-Visible Spectroscopies. *Journal of the American Chemical Society* **1994**, 116 (14), 6344-6353.
214. Angel, B. R.; Vincent, W. E. J., Electron Spin Resonance Studies of Iron Oxides Associated with the Surface of Kaolins. *Clays and Clay Minerals* **1978**, 26 (4), 263-272.

215. Heijboer, W. M.; Battiston, A. A.; Knop-Gericke, A.; Haevecker, M.; Mayer, R.; Bluhm, H.; Schloegl, R.; Weckhuysen, B. M.; Koningsberger, D. C.; de Groot, F. M. F., In-Situ Soft X-ray Absorption of Over-exchanged Fe/ZSM5. *J. Phys. Chem. B* **2003**, *107* (47), 13069-13075.
216. de Smit, E.; Swart, I.; Creemer, J. F.; Hoveling, G. H.; Gilles, M. K.; Tyliczszak, T.; Kooyman, P. J.; Zandbergen, H. W.; Morin, C.; Weckhuysen, B. M.; de Groot, F. M. F., Nanoscale chemical imaging of a working catalyst by scanning transmission X-ray microscopy. *Nature (London, U. K.)* **2008**, *456* (7219), 222-225.
217. Wojciechowski, P. W.; Brash, J. L., Fibrinogen and albumin adsorption from human blood plasma and from buffer onto chemically functionalized silica substrates. *Colloids Surf., B* **1993**, *1* (2), 107-117.
218. Wertz, C. F.; Santore, M. M., Effect of Surface Hydrophobicity on Adsorption and Relaxation Kinetics of Albumin and Fibrinogen: Single-Species and Competitive Behavior. *Langmuir* **2001**, *17* (10), 3006-3016.
219. Rodrigues, S. N.; Gonçalves, I. C.; Martins, M. C. L.; Barbosa, M. A.; Ratner, B. D., Fibrinogen adsorption, platelet adhesion and activation on mixed hydroxyl-/methyl-terminated self-assembled monolayers. *Biomaterials* **2006**, *27* (31), 5357-5367.
220. Leung, B. O.; Brash, J. L.; Hitchcock, A. P., Characterization of biomaterials by soft X-ray spectromicroscopy. *Materials* **2010**, *3*, 3911-3938.
221. Leung, B. O.; Hitchcock, A. P.; Cornelius, R.; Brash, J. L.; Scholl, A.; Doran, A., X-ray spectromicroscopy study of protein adsorption to a polystyrene-poly(lactide) blend. *Biomacromolecules* **2009**, *10* (7), 1838-45.
222. Leung, B. O.; Wang, J.; Brash, J. L.; Hitchcock, A. P., Imaging hydrated albumin on a polystyrene-poly(methyl methacrylate) blend surface with X-ray spectromicroscopy. *Langmuir* **2009**, *25* (23), 13332-5.
223. Gago, R.; Abrasonis, G.; Jimenez, I.; Moller, W., Growth mechanisms and structure of fullerene-like carbon-based thin films: superelastic materials for tribological applications. In *Trends in Fullerene Research*, Nova Science Publishers, Inc.: 2007.
224. Lopez, S.; Dunlop, H. M.; Benmalek, M.; Tourillon, G.; Wong, M. S.; Sproul, W. D., XPS, XANES and ToF-SIMS characterization of reactively magnetron-sputtered carbon nitride films. *Surface and Interface Analysis* **1997**, *25* (5), 315-323.
225. Samuel, N. T.; Lee, C.-Y.; Gamble, L. J.; Fischer, D. A.; Castner, D. G., NEXAFS characterization of DNA components and molecular-orientation of surface-bound DNA oligomers. *Journal of Electron Spectroscopy and Related Phenomena* **2006**, *152* (3), 134-142.
226. Kaznatcheyev, K.; Osanna, A.; Jacobsen, C.; Plashkevych, O.; Vahtras, O.; Agren, H.; Carravetta, V.; Hitchcock, A. P., Inner-shell Absorption Spectroscopy of Amino Acids. *Journal of Physical Chemistry A* **2002**, *106*, 3153-3168.
227. Koprinarov, I. N.; Hitchcock, A. P.; McCrory, C. T.; Childs, R. F., Quantitative Mapping of Structured Polymeric Systems Using Singular Value Decomposition Analysis of Soft X-ray Images. *The Journal of Physical Chemistry B* **2002**, *106* (21), 5358-5364.

228. Iyer, G. R. S.; Wang, J.; Wells, G.; Guruvenket, S.; Payne, S.; Bradley, M.; Borondics, F., Large-Area, Freestanding, Single-Layer Graphene–Gold: A Hybrid Plasmonic Nanostructure. *ACS Nano* **2014**, *8* (6), 6353-6362.
229. Neidhardt, J.; Hultman, L.; Czigany, Z., Correlated high resolution transmission electron microscopy and X-ray photoelectron spectroscopy studies of structured CN<sub>x</sub> (0 < x < 0.25) thin solid films. *Carbon* **2004**, *42* (12-13), 2729-2734.
230. Choudhury, T.; Saied, S. O.; Sullivan, J. L.; Abbot, A. M., Reduction of oxides of iron, cobalt, titanium and niobium by low-energy ion bombardment. *Journal of Physics D: Applied Physics* **1989**, *22* (8), 1185-1195.
231. Roach, P.; Farrar, D.; Perry, C. C., Interpretation of protein adsorption: surface-induced conformational changes. *Journal of the American Chemical Society* **2005**, *127* (22), 8168-8173.
232. Ago, H.; Kugler, T.; Cacialli, F.; Salaneck, W. R.; Shaffer, M. S. P.; Windle, A. H.; Friend, R. H., Work Functions and Surface Functional Groups of Multiwall Carbon Nanotubes. *The Journal of Physical Chemistry B* **1999**, *103* (38), 8116-8121.